A systematic approach for developing and manufacturing fruit simulators

A thesis presented in partial fulfilment of the requirements for the degree of

Doctor of Philosophy

In

Food Engineering

Massey University

Palmerston North, New Zealand

Huijian Huang

2022

Abstract

Due to the high cost, variable nature and seasonal availability of fruit, conducting large scale experiments for research purposes is not easy. A fruit simulator is a physical tool that mimics the mechanistic features and properties of the targeted fruit; hence, it can be used as a replacement for the fruit in research experiments. This study focuses on developing simulators for heat transfer experiments, especially in horticultural produce precooling.

A framework for developing the simulator was established based on the importance of each mechanistic feature. Depending on the application's needs, the simulator can mimic different length scale levels of the targeted fruit, such as the individual fruit, the bulk stacking of the fruit or sub-units of the fruit (e.g., a punnet/bag of table grapes). The scale level determines whether certain mechanistic features are important and affects the values of the thermal properties that must be matched. For example, a simulator that mimics a punnet of fruit with enclosed air pockets has an effective thermal conductivity and volumetric heat capacity that includes contributions from the thermal properties of the fruit and air, which provides more room for material selection.

Based on this framework, a systematic approach for the simulator manufacture and material selection was developed. Three different simulators were developed based on the framework: kiwifruit, apple and table grape simulators. The comparison of a simulator and real fruit precooling trials showed good agreement, validating the approach and demonstrating the feasibility of using simulators in postharvest research. The kiwifruit simulator was validated at different experimental scale levels, from individual kiwifruit to multiple kiwifruit boxes containing numerous individual kiwifruit simulators (which reflected pallet scale precooling).

During the simulator development, the concept of a time-scaled approach was identified and was explored. In theory, if the volumetric heat capacity of a simulator becomes smaller while the Bi of the simulator remains the same, the heating/cooling time of the simulator in an experiment will decrease proportionally according to the Fourier number (Fo). This approach was validated via the three simulators developed in this study. The validation of the simulators confirms the feasibility of this time-scaled concept. This approach has a significant advantage in reducing the experimental time and easing the material selection process for the simulator manufacture.

In the table grape simulator development, a process of using CT scans of the bulk packaged system to study the bulk shape and effective properties of the fruit subunits (bags) were developed,

where the bulk shape and effective thermal properties of a bag of table grape were determined based on the process. A set of bag shaped fruit simulators was then manufactured with equivalent bulk thermal conductivity and used to validate the bulk simulator approach by comparison of cooling rates with real fruit.

Overall, this study has successfully developed a generalised heat transfer simulator development framework. In addition, this study validated the feasibility and applicability of the time-scaling approach, which could be helpful for any future experiments. Furthermore, this study has developed a process to use CT scanning to determine a bulk object's bulk shape and effective property.

The outcomes of the work pave the way for carrying out postharvest and packaging optimisation experimental trials with reduced variability, greater ease and without seasonal constraints. The simulator development framework provides a basis for further expansion of these concepts into other applications beyond the heat transfer focus that they were developed for in this work.

Acknowledgement

I cannot express my gratitude enough to my supervisors, Professor John Bronlund, Dr. Mark Tunnicliffe and Dr. Young-Min Shim, and I truly appreciate their support. Without them, none of my work would be possible. In addition, I am incredibly grateful that Professor John Bronlund has taught and mentored me for almost a decade since I was a graduate student. I have learned not only technical skills from him but also critical thinking, flexibility in handelling difficult situations, and many more.

I would also like to thank my teammate Dr Jamal Olatunji, Dr Justin O'Sullivan, Dr Nicolas Tapia, Dr. Aiman Jamsari, Peter Jefferey, and many more from CPRR (now called MAF Digital Lab). A special thanks to Professor Andrew East, the project manager of the Fiberboard Packaging Design Project - MAUX1302, for funding this project and providing feedback and guidance.

Equally, I would like to thank my friends and family, especially my wife, mum, and late dad, without whom I would not have the courage to take this PhD challenge.

Last but not less, I would like to acknowledge my God. I believe that I would not be able to finish my thesis without His help, as Proverbs 1:7 "the fear of the Lord is the beginning of knowledge, but fools despise wisdom and instruction".

Table of Contents

List of Figure

List of tables

Nomenclature

Symbol	Description	Unit
A	Surface area	m^2
c	Heat capacity	$J\ kg^{-1}K^{-1}$
D	Mass transfer coefficient	$m\ s^{-1}$
D'	Diffusivity	m^2/s
D^d	Effective diffusion tensor	$m^2\ s^{-1}$
D_{eq}	Equivalent diameter	m
g	Gravitational acceleration	$m^2\ s^{-1}$
G	Irradiation	$W\ m^{-2}$
h	Heat transfer coefficient	$W\ m^{-2}\ K^{-1}$
H_{vap}	Latent heat of the water	$J\ kg^{-1}$
J	Radiosity	$W\ m^{-2}$
k_m	mass transfer coefficient	$kg\ m^{-2}s^{-1}Pa^{-1}$
K	Permeability	m^2
n	Node	
M	Molar mass	$g\ mol^{-1}$
P	Pressure	Pa
R	Gas constant	$J\ mol^{-1}\ K^{-1}$
T	Temperature	K
t	Time	s
u	Velocity	$m\ s^{-1}$
V	Volume	m^3
L	Characteristic length	m
x	Distance	m

Dimensionless Number	Description	Equation
Bi	Biot number	hL/λ
Da	Darcy number	K/L^2
F	View factor	$\sum F_i$
F_c	Forchheimer coefficient	
Fo	Fourier number	$\alpha t/L^2$
Nu	Nusselt number	hL/λ
pd	Partial fraction	
Pr	Prandtl number	$c\mu/\lambda$
Re	Reynolds number	$\rho uL/\mu$
Ra	Rayleigh number	$\rho\beta\Delta TL^3g/\alpha$
Ra_m	Darcy-Rayleigh number	$RaDa$
S	A function of source	
Sh	Sherwood number	$\lambda_{air}L/D'_{air}$
Y	Fractional unaccomplished temperature	$(T-T_i)/(T_{amb}-T_i)$

Greek	Description	Unit
α	Thermal diffusivity	$m^2\ s^{-1}$
β	Thermal expansion constant	K^{-1}
ρ	Density	$kg\ m^{-3}$
λ	Thermal conductivity	$W\ m^{-1}\ K^{-1}$
τ	Stress tensor	Pa
ε	Emissivity	
σ	Stefan–Boltzmann constant	$W\ m^2\ K^{-1}$
μ	Dynamic viscosity	$Pa \cdot\ s$

Subscript	Description
m	Source of mass
u	Source of momentum
h	Source of energy
ref	Reference
f	Fluid phase
s	Solid-phase
eff	Effective
sf	Solid and fluid phase
sim	Simulator
amb	Ambient
$conv$	Convective
p	Particle
air	Air
$skin$	Skin

Abbreviation	Description
HCT	Half cooling time
MAD	Maximum absolute difference
CI	Confident interval
TSF	Time scale factor

Chapter 1. Introduction

1.1 Background

1.1.2 The need for research on simulator development

Precooling is a standard postharvest treatment method used to preserve the quality and improve the shelf life of horticultural produce (Brosnan & Sun, 2001). It involves the large scale removal of field heat from the harvested crop to slow respiration. Precooling is an ongoing research topic, as many different variables can affect the overall cooling performance (Pathare et al., 2012). There are several ways that precooling performance can be improved. These include air/liquid flow optimisation, the design of packaging and pallet stacking. Recent reviews have shown that increasing effort has been put into the package design to enhance precooling (Pathare et al., 2012; Redding et al., 2016; Zhao et al., 2016). A small change in a package design can significantly improve forced air cooling, which is one of the most common precooling methods (Allais & Alvarez, 2001; Emond et al., 1996; Lambrinos et al., 1997). Excessive or inappropriate vent openings can dramatically reduce the packaging strength and lead to package and produce damage. A good vent design can significantly improve the precooling efficiency while maintaining the package strength (Castro, Vigneault, & Cortex, 2004a). In order to improve the precooling performance in any way, pallet-scale (or even greater scale) experiments are needed. However, large scale experiments are generally expensive, logistically challenging and contain considerable experimental variation (Ambaw et al., 2013; Smale, 2004; Zou, Opara, & McKibbin, 2006b).

Conducting a large scale experiment with horticultural produce is generally difficult and expensive. First, most horticultural products are seasonal, which means experiments can only be conducted at specific times of the year. Second, the physiology of the horticultural produce will change over time, together with its physical properties. This leads to considerable experimental variation (Vigneault, Castro, & Cortez, 2005a). As a result, the horticultural produce is generally not suitable for reuse for more than one experiment. Third, using the real horticultural produce for experiments is expensive, due to the large quantity of fruit needed. For example, a single pallet fruit trial might need a ton of fruit. These are the typical difficulties associated with using real horticultural produce in experiments. As such, the number of large scale experiments that can be

feasibly done is limited, and methods are required to screen designs or configurations before finalising experimental protocols.

Because of the rapid growth of computational power, numerical modelling has become a popular approach to reduce the number of large scale experiments needed (Ambaw et al., 2013; Pathare et al., 2012). However, a numerical model contains various assumptions and simplifications, which need to be experimentally validated (Vigneault, Castro, & Cortez, 2005a). Therefore, experiments are sometimes unavoidable. A numerical model should not be considered as a replacement of the experiment, but rather supplementary information to confirm understanding or screen designs and configurations.

Using produce simulators as a replacement for real horticultural produce in an experiment could provide advantages. In the context of this work, a produce simulator is a physical model that simulates certain aspects of the horticultural produce and can be used as a replacement for the real product in experiments. Several studies have been done on this concept (Redding et al., 2016; Vigneault, Castro, & Cortez, 2005a). An example is tylose, which was first introduced by Riedel (1960) and is used as a meat simulator for chilling, freezing and thawing experiments (Pham, 2014). A gel of 25% tylose in water has similar thermal properties to meat and can simulate heat transfer behaviour (Icier & Ilicali, 2005; Llave et al., 2016; Pham, 2014). One limitation of tylose is that its high water content means that drying can occur. This changes its properties, and so there is a limit to the life of the simulators made from it. Apart from tylose gel, there is no well-known material that can be used for a large scale experiment in horticultural produce. Research groups tend to develop specific produce simulators to fulfil their particular needs (Alvarez & Flick, 1999b; Alvarez, Bournet, & Flick, 2003; Vigneault, Castro, & Cortez, 2005a). Therefore, this study is to develop a framework for simulator development that can be used as a guideline by other researchers to develop task-specific simulators in the future.

1.1.3 The kiwifruit industry in New Zealand

Due to geographic isolation, food export is one of the major factors contributing to the New Zealand economy (Carson & East, 2017). In 2019, New Zealand exported more than 6.2 billion NZD worth of horticultural products, which is 10% of the total merchandise exports and 2% of the New Zealand GDP (FreshFacts, 2017; Statistics New Zealand, 2019). Within the horticultural exports,

kiwifruit is one of the major horticultural produces. As a result, kiwifruit was selected as the initial horticultural produce target in this work for simulator development. Forced air cooling was the primary focus as it is the most common precooling method used in the kiwifruit industry (O'Sullivan, 2016).

1.2 Main goals and objectives

This research's main goals were to a) develop a simulator or simulators for kiwifruit forced air cooling optimisation, and b) generalise the development method of the kiwifruit simulator into a standard framework for future simulator development.

In order to achieve the goals, the objectives were:

1. To develop an understanding of the heat transfer mechanisms occurring during forced air cooling, and then identify the corresponding properties a simulator must have, to be effective,
2. To develop a systematic approach for material selection that can match the required properties, and then develop a systematic fabrication process that is suitable for the selected material,
3. To fabricate and validate the developed simulator prototype,
4. To generalise the process into a simulator development framework and then validate the framework via developing a new simulator for a different horticultural product.

Chapter 2. Literature review

This chapter will first review the current precooling technology, demonstrating the need for continuous improvement. Following this, mathematical models of precooling studies are reviewed, and the advantages and limitation of this approach for identifying ways to improve performance will be discussed. From the discussion, the need for a produce simulator is identified, and state of the art will be reviewed. Although the review focuses on horticultural produce, some parts are applicable to other food systems if such a food simulator is needed.

2.1 Precooling

It is well-known that temperature management is one of the essential factors influencing the shelf-life of horticultural produce and that precooling is one of the most important unit operations to achieve this (Brosnan & Sun, 2001; Pathare et al., 2012; Zhao et al., 2016). A few hours delay in precooling can significantly decrease the produce's marketable value (Ambaw, Fadiji, & Opara, 2021; Ferrua, 2007).

A comprehensive review on precooling has been done by Brosnan and Sun (2001), who categorise precooling methods into six approaches; room cooling, ice cooling, hydrocooling, vacuum cooling, cryogenic cooling and forced air cooling.

2.1.1 Room cooling

Room cooling is the method that requires the minimum amount of preparation. It can be as simple as placing palletised produce in a refrigerated room (Figure 2-1). Inside the room, air movement is mainly driven by the evaporator fan and natural convection (Delele et al., 2009), which means the air movement is relatively low. As a result, this method generally has a slow cooling rate and is not suitable for produce that needs rapid cooling (Fordham & Briggs, 1985, pp. 178-179).

Figure 2-1, Typical room cooling (O'Sullivan et al., 2014)

The cooling rate and uniformity of this method can be optimised by improving package design, stacking configuration, and the evaporator fans position (Brosnan & Sun, 2001). Interestingly, recent studies have shown an interest in utilising this method in a refrigerated container (instead of a refrigerated room), as it could significantly simplify the logistics process (Defraeye et al., 2015a; Defraeye et al., 2015b; Defraeye et al., 2016).

2.1.2 Ice cooling

Ice cooling is a traditional precooling method, which applies direct contact between the ice and the produce (Figure 2-2). In a palletised condition, ice can be injected inside the package but only if the package is treated to be waterproof (Gillies & Toivonen, 1995). This kind of package is generally more expensive (Thompson, 1996). This method has the advantage of minimising moisture loss (Gillies & Toivonen, 1995), but the disadvantage of a) poor temperature control, which leads to chilling injury, and b) encouraging plant diseases, as contamination could occur (Wills et al., 2007). This precooling method's temperature control can be optimised via altering the ice particles size or combining it with hydrocooling (Vigncaull, Goycttc, & Raghavan, 1995).

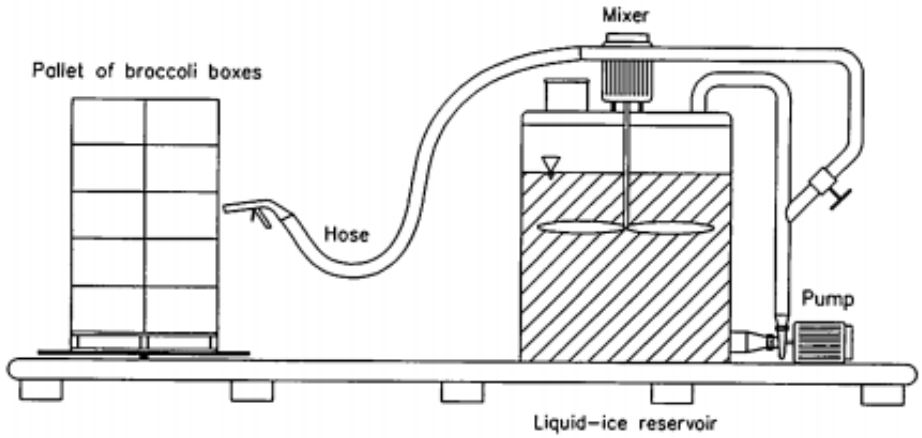

Figure 2-2, Typical ice cooling system (Vigncaull, Goycttc, & Raghavan, 1995)

2.1.3 Hydrocooling

Like ice cooling, Hydrocooling utilises direct contact with the coolant (in this case, chilled water) to remove field heat from the produce (Figure 2-3). It has similar advantages and disadvantages to ice cooling, except it provides better temperature management (Vigneault, Bartz, & Sargent, 2000). This method can be optimised via controlling the water flow rate and the capacity of the process is limited by the water reservoir (Thompson, 1996). It is generally applied to bulk fruit prior to packing.

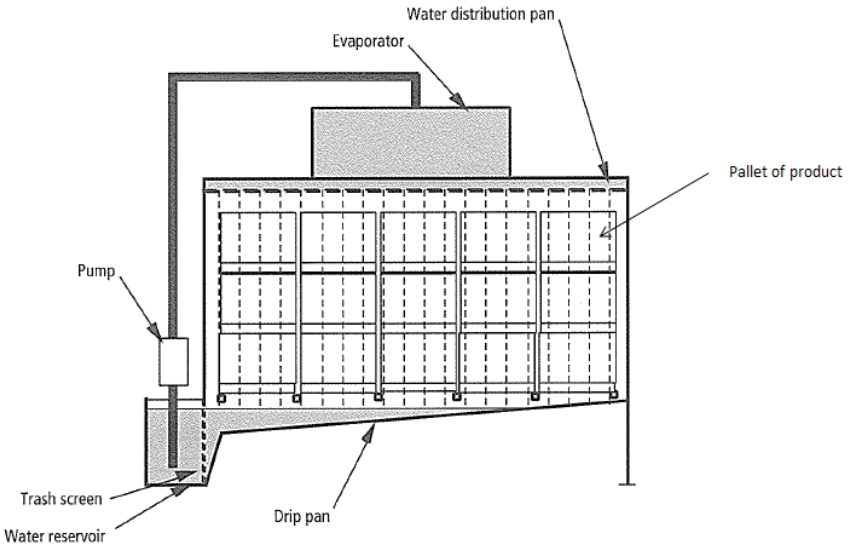

Figure 2-3, Typical hydrocooling system, adopted from Thompson (1996)

2.1.4 Vacuum cooling

Vacuum cooling is achieved by promoting evaporation on the produce surface; hence lowering the produce temperature via removing the latent heat. This method is generally conducted inside a vacuum chamber (Figure 2-4), which has single or multiple vacuum pumps, and a refrigeration unit. This method is thirteen times faster than the conventional room cooling method (Ozturk & Ozturk, 2009), and it is particularly favourable for porous or leafy products (He et al., 2004; Ozturk & Ozturk, 2009; Turk & Celik, 1992). However, this method requires expensive equipment and is not suitable for produce that are pressure sensitive (He et al., 2004; Ryall, 1972). It also incurs considerable moisture loss (Turk & Celik, 1992), which means a reduction in the saleable weight. This method's performance can be optimised via improving package design (Turk & Celik, 1992) or controlling the pressure reduction in the system (Ozturk & Ozturk, 2009).

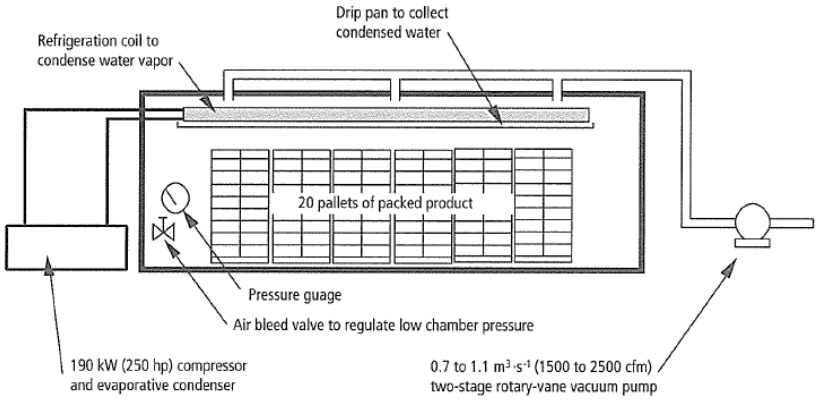

Figure 2-4, Typical vacuum cooling system (Thompson, 1996)

2.1.5 Cryogenic cooling

Cryogenic cooling applies cryogenic substances, such as liquid nitrogen or dry ice to cool the produce. Many research has been done on this precooling method (IGI Global, 2015), but it is still not a typical commercial practice, mainly due to the high capital and operational costs (Brosnan & Sun, 2001).

2.1.6 Forced air cooling

Forced air cooling was first developed at 1960 and it is now the most commonly used method to cool fruit (Thompson, 1996; Zhao et al., 2016), due the low cost and high flexibility (Allais &

Alvarez, 2001). Arrays of palletised produce are placed in a refrigerated room (Figure 2-5), where tarpaulins are used to cover the gaps. A fan is then used to create a pressure drop across the pallets, forcing the refrigerated air to flow through the produce; hence, achieving cooling. Water loss can be a major issue with this method, but it is resolved by utilising a polylined package system (section 2.1.6.1) or waxing the produce (Thompson, 1996).

Figure 2-5, A typical forced air cooling system (O'Sullivan et al., 2014)

Many factors can be manipulated to optimise this method, such as the package design, pallet format, or refrigerated air condition (Pathare et al., 2012). However, since this method is the most common, research on optimisation of this method has become increasingly popular (Redding et al., 2016).

2.1.6.1 Package

Of the many factors that can be manipulated to improve forced-air cooling, package optimisation is one of the most effective but dilemmatic approaches. Increased total open area (package vent size) can improve the produce cooling rate but it must not compromise the package strength (Castro, Vigneault, & Cortex, 2004a). Researchers have continuously carried out work in this area (Pathare et al., 2012).

Overall, two classes of package system are used; open and closed package systems. An open package system means refrigerated air can flow through the stack of produce, such as apple boxes and strawberry punnets (Figure 2-6 A and B), with direct contact between the air and the fruit or

primary package surface. Produce in this system is generally cooled relatively fast (Ngcobo et al., 2013c). In a closed package system, the produce is enclosed by a barrier (polyliner). Examples of closed systems are kiwifruit and grape boxes (Figure 2-6 C and D). Closed package systems can greatly minimise moisture loss, providing better quality produce, but the encapsulation of the produce slows down the cooling rate (Burdon & Lallu, 2011; Ngcobo et al., 2013a). Generally, plastic liners (such as HDPE liners) are used to enclose the produce. The polyliner can be intact, micro-perforated or large hole (~ 2 mm diameter) perforated formats (Ngcobo, Opara, & Thiart, 2012a). Although a small amount of refrigerated air might be able to flow through perforated liners, the effect on heat transfer is insignificant (Ngcobo et al., 2012; Ngcobo et al., 2013c). Therefore, packages using perforated liners are still considered as closed package systems.

A) B)

C) D)

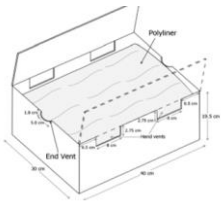

Figure 2-6, Examples of Open package systems; A) apple box (Tanner, 1998), B) strawberry punnet (Ferrua & Singh, 2009c) and Closed package system C) kiwifruit box (O'Sullivan, 2016) , D) grape box (Delele et al., 2012)

2.2 Mathematical modelling of precooling

Researchers tend to utilise the modelling approach to optimise the precooling process due to the low cost, it being logistically easy and providing a controllable environment for comparison of designs (Defraeye et al., 2015; Zhao et al., 2016).

Understanding the heat transfer mechanism is important for a model development. Therefore, this section will first review the important heat transfer mechanisms, and then discuss the possible

modelling approaches. The development of physical simulators requires similar simplification to what is done during mathematical modelling, so valuable insights can be found by comparing different approaches. Finally, the limitations of modelling are reviewed.

2.2.1 The heat transfer mechanism

Five possible heat transfer modes can occur during precooling. These are conduction, convection, radiation, evaporation/condensation (mass transfer) and heat generation through fruit respiration (Dehghannya, Ngadi, & Vigneault, 2010; Zhao et al., 2016).

As mentioned (section 2.1.6.1) there are two types of package system, open and closed. The heat transfer mechanism within these package systems can be different. Tanner (1998) summarised the possible heat transfer pathways as follows:

- Open package system (Figure 2-7 A)
    a) Heat and mass transfer due to the airflow
    b) Internal conduction inside the product
    c) Forced or free convection on the surface of the product
    d) Evaporation or condensation of water vapour on the surface of the product
    e) Surface to surface radiation (product to product or product to packaging material)
    f) Conduction via thermal contact between product to adjacent material (another product or package material)
    g) Heat production due to respiration
    h) Moisture transfer within the package
    i) Internal conduction inside package material
    j) Evaporation or condensation of water vapour on the surface of package material
- Closed package system (Figure 2-7 B)
    a) Heat and mass transfer external to the product stack
    b) Internal conduction inside the product

c) Free convection on the surface of the product

d) Evaporation or condensation of water vapour on the surface of the product

e) Surface to surface radiation

f) Conduction via thermal contact between product to adjacent material

g) Heat production due to respiration

h) Moisture transfer within the package

i) Internal conduction inside package material

j) Forced or free convection on the outside surface of the packaging material

k) Evaporation or condensation of water vapour on the surface of package material

l) Conduction via thermal contact between the product and the polyliner

m) Free convection on the surface of polyliner internal surface

n) Forced and free convection on the surface of polyliner external surface

a)

b)

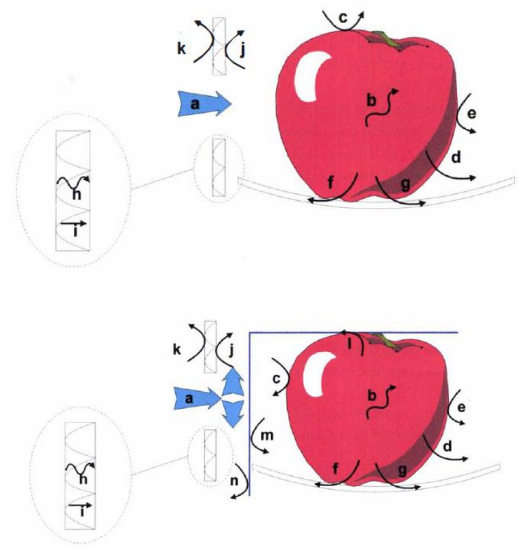

Figure 2-7, Conceptual heat transfer pathways of a) open and b) closed package system (Tanner, 1998)

Although all the mentioned heat transfer pathways might occur, only some of the pathways are important to be considered. Models simulating forced-air cooling of the product were reviewed as summarised in

Table 2-1. Models generally consider product internal conduction (b) and surface convection (c). Evaporation/condensation (d) and respiration (g) are considered in some models, and radiation (e) is generally not considered. Models generally do not consider conduction via thermal contact between products (f). One main reason for that is due to the limitation of computational power, where a considerable computational cost is incurred by making the products touch in the geometry (O'Sullivan, 2016). The other reason is conduction via thermal contact is generally insignificant in an open package system (Van der Sman, 2008). However, the study of Ben Amara, Laguerre, and Flick (2004) and Laguerre, Amara, and Flick (2006) showed that the conduction via thermal contact can be significant when the air velocity is lower than 1 $m\ s^{-1}$.

Note that only a few models (7 and 10 in

Table 2-1) simulate the precooling of a closed package system. These models generally consider the effect of internal radiation is insignificant. The sensitivity analysis included for model 10 shows that radiation inside the package system has an insignificant effect (O'Sullivan, 2016). Also, O'Sullivan (2016)believed that the effect of evaporation/condensation could be neglected, as the purpose of a closed package system (using polyliner) is to minimise the moisture transfer (O'Sullivan et al., 2016a). However, Dincer (1995) study suggests that the effect of radiation and evaporation/condensation can be important when the air flow is less than 2.5 $m\ s^{-1}$, which means when the effect of forced convection is relatively low. This can be confirmed by the experimental observations from other studies (Ben Amara, Laguerre, & Flick, 2004; Laguerre, Amara, & Flick, 2006; Laguerre et al., 2008; Laguerre, Benamara, & Flick, 2010). Also, Ngcobo, Opara, and Thiart (2012a) reported the observation of condensation on the internal polyliner surface, which suggests evaporation/condensation might have occurred inside the polyliner package during precooling.

Table 2-1, Heat transfer mechanisms included in validated forced-air cooling models from the past

	Package system	Conduction	Convection	Evaporation / condensation	Radiation	Respiration
1	Open	Included	Forced	Included	Not included	Not included
2	Open	Included	Forced and free	Included	Not included	Included
3	Open	Included	Forced and free	Not included	Not includedf	Included
4	Open	Included	Forced	Not included	Not included	Included
5	Open	Included	Forced	Included	Not included	Not included
6	Open	Included	Forced	Not included	Not included	Included
7	Closed	Included	Forced and free	Included	Not included	Included
8	Open	Included	Forced and free	Not included	Not included	Included
9	Open	Included	Forced	Included	Not included	Included
10	Closed	Included	Forced and free	Not included	Not included	Not included

Reference list: 1 = Alvarez and Trystram (1995); 2 = Amos (1995); 3 = Tanner et al. (2002a); Tanner, Cleland, and Opara (2002b); Tanner, Cleland, and Robertson (2002c); 4 = Zou, Opara, and McKibbin (2006a, 2006b); 5 = Ferrua and Singh (2009a, 2009b, 2009c); 6 = Dehghannya, Ngadi, and Vigneault (2008, 2011, 2012); 7 = Delele et al. (2012); 8 = Delele et al. (2013, 2013a); 9 = Han et al. (2015); Han et al. (2017); Han et al. (2018); 10 = O'Sullivan (2016)

2.2.2 Modelling approaches

There are three types of mathematical modelling approaches used for precooling. These are direct numerical simulation (DNS), porous medium simulation and a zonal approach (Dehghannya, Ngadi, & Vigneault, 2010).

2.2.2.1 The generic equations for DNS

The DNS approach considers each individual item of produce, where the detail of each individual item of produce is included in the model geometry. In general, the movement and temperature of the fluid in a mathematical model is governed by the continuity equation (Equation 2-1), momentum equation (Equation 2-2) and energy equation (Equation 2-3), where g is gravitational constant, ρ is density, u is velocity, τ is the stress tensor, c is specific heat capacity, and T is temperature. S_m , S_u and S_h are the source of mass, momentum and energy (Tu, Yeoh, & Liu,

2008). The subscripts i and j represent the Cartesian direction. When the fluid has Newtonian rheology, the viscosity of the fluid is constant and the flow is incompressible (Ma < 0.3), the momentum equation can be simplified (Equation 2-4) into the Navier-Stokes equations, where μ is viscosity (Tu, Yeoh, & Liu, 2008). If free convection needed to be considered, then the equation Buossinesq approximation or ideal gas expression needs to be added (see Equation 2-5 and Equation 2-6), where β is the thermal expansion, M is the molar mass and R is the ideal gas constant. The subscript ref means at the reference point. The Buossinesq approximation is less computational intensive, but the ideal gas expression is more appropriate for large temperature differentials (Norton, Tiwari, & Sun, 2013). If mass transfer is considered in the model, then an extra equation (Equation 2-7) is needed to describe the movement of that species (Norton, Tiwari, & Sun, 2013).

Modified Navier-Stokes models and simplified boundary layer models have been developed to reduce computational expense, such as Reynolds average Navier Stokes model (RANS) and k-ε model to model the fluid on the boundary. However, precaution needs to be taken when choosing the model, as an inappropriate model can provide wrong predictions (Defraeye et al., 2012; Defraeye, Verboven, & Nicolai, 2013a).

Continuity equation

$$\frac{\partial \rho}{\partial t} + \nabla(\rho u_i) = S_m \qquad \text{Equation 2-1}$$

Momentum equation

$$\frac{\partial}{\partial t}(\rho u) + u\nabla(\rho u) = \nabla(\tau) + \rho g + S_u \qquad \text{Equation 2-2}$$

Energy equation

$$\frac{\partial}{\partial t}(\rho c T) + \nabla(\rho u_i c T) = \nabla(\lambda \nabla \mathrm{T}) + S_h \qquad \text{Equation 2-3}$$

Navier-Stokes equation

$$\frac{\partial}{\partial t}(\rho u) + \nabla\left(\rho u_i u_j\right) = -\nabla \mathrm{P} + \mu\nabla(\nabla u) + \rho g + S_u \qquad \text{Equation 2-4}$$

Buossinesq approximation

$$\rho = \rho_{ref}[1 - \beta(T - T_{ref})] \qquad \text{Equation 2-5}$$

Idea gas expression

$$\rho = \frac{P_{ref} M}{RT} \qquad \text{Equation 2-6}$$

Mass transfer equation

$$\frac{\partial C}{\partial t} + \nabla(\rho u C) = \nabla(D\nabla \mathrm{C}) + S_c \qquad \text{Equation 2-7}$$

The Fourier equation is generally used to describe the temperature change in the solid phase of the model (Equation 2-8), where the heat source S_h term could be the respiration heat of the product (Zhao et al., 2016). The boundary conditions (Equation 2-9) can include convection, surface to surface radiation and evaporation/condensation, where ε is the emissivity, σ is the Stefan-Boltzmann constant, G is the irradiation, and H_{vap} is the latent heat (COMSOL Multiphysics; Norton, Tiwari, & Sun, 2013). The irradiation term can be expressed as a summation of radiosity (Equation 2-10), where F is the view factor and J is the radiosity (COMSOL Multiphysics).

Fourier equation

$$\frac{\partial}{\partial t}(T) = \nabla(\frac{\lambda_p}{\rho c}\nabla \mathrm{T}) + S_h \qquad \text{Equation 2-8}$$

Boundary condition

$$-\lambda_p \nabla \mathrm{T_s} = \varepsilon(G - \sigma T_s^4) + n\lambda_a \nabla \mathrm{T} + H_{vap} n D \nabla \mathrm{C} \qquad \text{Equation 2-9}$$

Summation of radiosity

$$G = \sum_{i=1}^{n} F_i J_i \qquad \text{Equation 2-10}$$

Fick's equation is generally used to describe the mass transfer of moisture inside the solid phase, as shown in Equation 2-11, and the boundary condition can be expressed as Equation 2-12, where the driving force $(C_{amb} - C_s^*)$is not limited to any fixed units, but dependent on the unit of the mass transfer coefficient k_m. C_s^* is a function of C_s and could be the same or different units from C_s but it will be consistent with C_{amb}.

Fick's equation

$$\frac{\partial C}{\partial t} = \nabla(D\nabla \mathrm{C}) + S_c \qquad \text{Equation 2-11}$$

Boundary condition

$$-\nabla \mathrm{C} = k_m(C_{amb} - C_s^*) \qquad \text{Equation 2-12}$$

2.2.2.2 The generic equations for the porous medium approach

In large scale simulations, DNS is extremely computational intensive and takes a long time to solve (Norton, Tiwari, & Sun, 2013). Porous medium simulation is a simplified approach, which assumes the modelling object to be a porous medium. This can reduce the computational power required to solve the model, but the drawback is in neglecting the internal detail of the bulk object (Verboven et al., 2006). Instead of being interested in the individual produce temperature and local airflow field, average air flows within the product stack and volume averaged temperature are considered. In order to have a meaningful airflow average, the averaging volume needs to be large enough compared to the individual product (Figure 2-8). Therefore, this approach requires the characteristic length of the product to be much smaller than the characteristic length of the overall system (the averaging volume). It means the package to product length ratio needs to be large (P/p ratio). Researchers tend to use the P/p ratio of greater than 10 as a threshold before the porous media approach is used (Dehghannya, Ngadi, & Vigneault, 2010; Ferrua & Singh, 2008) although Van der Sman (2002) showed that the ratio can be as low as 6.6.

Figure 2-8, Dependence of average value on averaging volume (Whitaker, 1969)

The fluid movement is governed by the continuity equation (Equation 2-1) and Darcy's law equation. Depending on the conditions, different Darcy's law equations are used (Verboven et al., 2006). At low velocity, Darcy's equation is appropriate (Equation 2-13), where k is the permeability of the porous medium, and the u is the velocity averaged over the porous medium. At high velocity (turbulent flow), the Darcy-Forchheimer equation (Equation 2-14) should be used, where the F_c is the Forchheimer coefficient, which is a semi empirical number. When the fluid is in a confined environment, such as packages of product, then the Brinkman-Forchheimer-Darcy equation (Equation 2-15) should be used.

Darcy's equation

$$-\nabla \mathrm{P} = \frac{\mu}{K} u \qquad \text{Equation 2-13}$$

Darcy-Forchheimer equation

$$-\nabla \mathrm{P} = \frac{\mu}{K} u - \frac{F_c \rho}{K^{0.5}} u\,|u| \qquad \text{Equation 2-14}$$

Brinkman-Forchheimer-Darcy equation

$$-\nabla \mathrm{P} = \frac{\mu}{K} u - \frac{F_c \rho}{K^{0.5}} u\,|u| + \mu_{eff} \nabla(\nabla \mathrm{u}) \qquad \text{Equation 2-15}$$

In terms of energy balance, there are two situations that need to be considered; whether the fluid inside the porous medium is in thermal equilibrium with the solid phase or not (Verboven et al., 2006). If the fluid and solids are in local thermal equilibrium, then the overall porous medium can be approximated as a single effective material (Equation 2-16), where D^d is the effective diffusion tensor, which describes the intermixing of hot and cold fluid due to the tortuous flow pattern at the microscopic scale and subscript f , means the fluid phase (Das, Mukherjee, & Muralidhar, 2018). If the fluid and solid phase does not reach thermal equilibrium, then two equations (Equation 2-17 and Equation 2-18) are needed to describe the energy balance of the fluid and the solid, where p is the volume fraction of the described phase, subscript s means solid phase and subscript sf means the interface between solid and fluid.

Single-phase model

$$(\rho c)_{eff} \frac{\partial T}{\partial t} + (\rho c)_f \, u\nabla = \nabla\big(\nabla(\lambda_{eff} + D^d)\, T\,\big) + S_h \qquad \text{Equation 2-16}$$

Two-phase model

$$(p\rho c)_f \frac{\partial T_f}{\partial t} + (p\rho c)_f \, u\nabla \mathrm{T_s} = \nabla\big(\nabla \lambda_{ff} T_f\big) + A_{sf} h_{sf}\big(T_s - T_f\big) + p_f S_h \qquad \text{Equation 2-17}$$

$$(p\rho c)_s \frac{\partial T_s}{\partial t} + (p\rho c)_s \, u\nabla = \nabla(\nabla \lambda_{ss} T_s) + A_{sf} h_{sf}(T_f - T_s) + p_s S_h \qquad \text{Equation 2-18}$$

Similarly, two conditions can be defined for the mass transfer in the porous medium; saturated and non-saturated (Equation 2-19 to Equation 2-21), where D means the mass diffusivity (Das, Mukherjee, & Muralidhar, 2018).

Single-phase model

$$\frac{\partial C}{\partial t} + \nabla \mathrm{u} = D\nabla\,(\nabla \mathrm{C}) + S_c \qquad \text{Equation 2-19}$$

Two-phase model

$$\frac{\partial C_f}{\partial t} + u\nabla \mathrm{C_f} = D\nabla(\nabla \mathrm{C_f}) + A_{sf} k_{m\ sf}\left(C_s^* - C_f\right) + p_f S_c \qquad \text{Equation 2-20}$$

$$\frac{\partial C_s}{\partial t} + u\nabla \mathrm{C} = D\nabla(\nabla \mathrm{C_s}) + A_{sf} k_{m\ sf}\left(C_s^* - C_f\right) + p_f S_c \qquad \text{Equation 2-21}$$

2.2.2.3 Zonal approach

A zonal approach is achieved by dividing a system into subdivisions, and instead of modelling the whole system, each subdivision is modelled (Figure 2-9). Zones can be divided based on the produce position inside the package (Tanner et al., 2002a) or it can be divided equally based on the package dimension (Olatunji, 2018). This approach requires much less computing effort, which can be combined with an iterative optimisation method for product design (East & Smale, 2008). The drawback of this is the decoupling of the energy equations and the fluid flow equations (Dehghannya, Ngadi, & Vigneault, 2010), where energy and flow equations need to be solved separately.

Figure 2-9, Illustration of zonal approach, where (A), (B) and (C) are the necessary sub-models governing the zone condition and the intra and intra zone transfer, respectively (Tanner et al., 2002a).

2.2.3 Limitations of mathematical models

Ideally, models should consider all the relative governing equations and solved either analytically or by using finite discrete numerical methods. This ideal situation can rarely be achieved. Solving all models analytically is not currently possible, as the mathematical approaches to solving some equations are not known. For example, the analytical solution of Navier–Stokes equation remains as one of the seven Clay Mathematics Institute millennium problems (Clay Mathematics Institute, 2018). Solving models with infinitesimally fine discretisation is also not currently an option, due to

computational power limitations. A model is generally solved with a mesh scale involving millions of elements and time steps of 0.01 to 0.001 of the simulated time (Table 2-2).

Long computational times are a common issue with the modelling approach. Nowadays the computational time of a model is still generally twice as long as the prediction time (Table 2-2). Study 20 in Table 2-2, which is one of the most recent studies (2018), took 50 hours (computational time) to solve the model, which predicts the product temperature over 30 hours (prediction time). Simplification of models could be an option to reduce the computational time (Delele et al., 2013), however, erroneous simplifications due to lack of knowledge can lead to incorrect predictions (Roy & Oberkampf, 2011).

Model prediction are not always reliable, as models generally contains three type of errors; model form errors, model input errors and numerical approximation errors (Oberkampf & Roy, 2010). The summation of these errors can be as large as 30% in a simple one dimensional steady state model, and therefore, model validation is a standard protocol for any model development (Oberkampf & Roy, 2010).

Table 2-2, Model simulation details over the last decade

#	Study purpose	Product	Model details						Solution method				
			Dimensions	App.	SS / T	scale	t_{sim} (hr)	Feat.	Mesh x10^6	Time step (s)	Iterations	PC spec.	$t_{comp.}$ (hr)
1	Ventilated package design	Sphere	3	DNS	SS	Single package	N/A	CFD	0.99		220	One core processor (2.20GHz)	0.58
2	Ventilated package design	Sphere	2	DNS	T	Single package	2	CFD HT MT	0.15			Dual core processor (3.00GHz) 32GB RAM	0.91
3	Ventilated package design	Sphere	3	DNS	SS	Single package	N/A	DE CFD	0.45-1.2			One core processor (3.21GHz) 4GB RAM	9-20
4	Analytical solution study	No specify	1		T	Single product	Fo =2.5	HT	N/A	N/A	N/A		
5	Ventilated package design	Straw-berry	3	DNS	T	Multi packages	2	CFD HT MT	2.9	15	20	One core processor (2.20GHz)	>2
6	Cool store optimisation	Sphere	3	PM	T	Cool room	20	CFD HT MT	1.2	1	50	One core processor (3.21 GHz) 4GB RAM	20
7	Cool store optimization	Chicory root	3	PM	T	Cool room		CFD HT MT	1.6			One core processor (3.21 GHz) 4GB RAM	
8	Ventilated package design	Sphere	3	DNS	T	Single package	2	CFD HT	2	0.005		Quad core processor (2.60GHz) 8GB RAM	16
9	Ventilated package design	Sphere	3	PM	SS	Pallet	N/A	CFD	1.4		12000	Normal processor (3.20GHz)	60
10	Air flow pattern study	Apple	2	DNS	T	Two apples	60	CFD HT		0.05			
11	Cool store optimisation	Not specify	3	PM	T	Refer container	30	CFD HT	0.14-0.16	0.1-60	30	Dual core processor (1.6 GHz) 1GB Ram	
12	Thermal fumigation optimisation	Sphere	3	DNS	SS	Cool room	N/A	CFD MT	3.2	10	50	Quad core processor (3.00GHz) 8GB RAM	17
13	Ventilated package design	Sphere/ orange	3	DNS	T	Palletized layer	12	CFD HT	5.4-5.6	60		12 core processor (2.66GHz) 48GB RAM	40
14	Ventilated package design	Sphere/ orange	3	DNS	T	3 palletized layer	16	CFD HT		180	50	Due core processor (2.93GHz) 8GB RAM	9-28
15	Ventilated package design	Table grape	3	PM	T	Cool room	27	CFD HT MT	4.61			Due core processor (2.93GHz) 8GB RAM	22

16	Cooling method evaluation	Oranges / sphere	3	DNS	T	Multi packages	20	CFD HT	4.1-7.2	60		12 core processor (2.66GHz) 48GB RAM	48
17	Ventilated package design	Kiwifruit	3	DNS	T	Palletised layer	12	CFD HT	7.6	60	20	Quad core processor (3.20GHz) 8GB RAM	20
18	Ventilated package design	Apple/ sphere	3	DNS	T	Singe package	20	CFD HT MT	0.32	60	20	Due core processor (3.10GHz) 4GB RAM	
19	Ventilated package design	Apple/ sphere	3	DNS	T	Single package	12	CFD HT	3.89 -4.05	150		Quad core processor (3.40GHz) 32GB RAM	96
20	Ventilated package design	Apple/ sphere	3	DNS	T	Palletized layer	20	CFD HT MT	5.5	60	20	16 core processor (2.53GHz) 32GB RAM	30
21	Cool chain optimization	Sphere	3	DNS	T	Pallet	1056	CFD HT	26	60			
22	Air flow pattern study	Sphere	3	DNS	T	Box	8	CFD HT	3.1	240	20	192 GB RAM	70
23	Cool chain optimization	Box	3	PM	T	Boxes		CFD HT	0.15				

Note: **D** = dimension; App. = approach; SS = steady state; T= transient; feat. = feature; math= mathematic; itera. = iteration; CFD = computational fluid dynamic; HT = heat transfer; MT = mass transfer; DE = discrete element method; Num = numerical solution; Ana = analytical solution; PM = porous medium approach; PC spec. = computer specification reference list:

1 = Ferrua and Singh (2008); 2 = Dehghannya, Ngadi, and Vigneault (2008, 2011, 2012); 3 = Delele et al. (2008); 4 = Cuesta and Lamúa (2009); 5 = Ferrua (2007); Ferrua and Singh (2009a, 2009b, 2009c, 2009d); 6 = Delele et al. (2009a); 7= Delele et al. (2009); 8 = Tutar, Erdogdu, and Toka (2009); 9 = Moureh, Tapsoba, and Flick (2009a, 2009b); 10 = Martins et al. (2011); 11 = Tanaka et al. (2012); 12 = Delele et al. (2012a); 13 = Defraeye et al. (2013); Defraeye et al. (2014); 14 = Delele et al. (2013, 2013a); 15 = Delele et al. (2012); 16 = Defraeye et al. (2015a); Defraeye et al. (2015b); Defraeye et al. (2016); 17 = O'Sullivan et al. (2016b); O'Sullivan et al. (2017); 18 = Han et al. (2015); Han et al. (2017); 19 = Berry et al. (2016); 20 = Han et al. (2018); 21 = Wu et al. (2018); Wu and Defraeye (2018); 22 = Curto[1] et al. (2021); 23= So et al. (2021)

2.3 Simulator development (physical models)

Although mathematical modelling can be used as an alternative to experimental work, computational limitations, modelling uncertainties and the ultimate need for validation mean that experimental work is still required. A small scale experiment, such as an individual product or a package of product can be conducted in a relatively simple manner, but large scale experiments, such as pallet size (Delele et al., 2013) or refrigerated container size (Tanner & Amos, 2002), are generally expensive, logistically difficult, and have low replicability (Redding et al., 2016; Vigneault & Castro, 2005; Zhao et al., 2016). This low reproducibility can be attributed to the natural variation of the product physical properties and product position. Studies have reported the difficulty in obtaining identical product for comparison (Chuntranuluck, 1995; Ferrua & Singh, 2009b). Gruyters et al. (2018) showed that the variation in product shape can significantly affect the stacking of the product; hence, providing different heat transfer conditions. In addition, the degradation of the product can change the product properties, introducing further variability into the experiment (Vigneault & Castro, 2005). Furthermore, conducting large experiments generally requires significant labour and resources. Availability of the product can sometimes be a problem, especially the horticultural produce, which is available only seasonally (Redding et al., 2016).

A simulator can be a partial solution to overcome those issues by providing a replacement for the real product in an experiment. For example, Tylose was introduced by Riedel (1960) as a material with similar thermal properties to meat. Therefore it became one of the most common meat simulators for studies investigating the heating and cooling of meat (Anderson & Singh, 2005; Icier & Ilicali, 2005; Llave et al., 2016; Tremeac, Hayert, & Le-Bail, 2008). A simulator is not a replacement for mathematical modelling or experiments with real fruit, but an assisting tool. Simulators can provide more stable and controllable properties and can be used at any time. It can be thought of as a physical version of mathematical models.

This section will first review the relevant properties of horticultural produce for simulator development, and then the state of the art. The properties of the developed simulators will be compared with the real produce.

2.3.1 Relevant produce properties

The Fourier equation can model the heat transfer of the product cooling with an appropriate boundary condition (Equation 2-8 and Equation 2-9), which means the relevant properties are:

- Thermal conductivity (λ), density (ρ) and specific heat capacity (c) – for conduction
- Shape – for convection and conduction
- Respiration heat - for the heat generated by respiration
- Moisture content (MC) and skin permeability (k_s) – for evaporation and condensation
- Skin emissivity (ε) – for radiation

This study focusses on horticultural produce, and the properties of typical produce are reviewed (Table 2-3). In general, a typical horticultural product has:

- Thermal conductivity =~ 0.51 $(W\ m^{-1}\ K^{-1})$
- Density = ~1118 $(kg\ m^{-3})$
- Specific heat capacity = ~3820 $(J\ kg^{-1}K^{-1})$
- Respiration heat = ~150 $(mW\ kg^{-1})$
- Moisture content = ~ 83%
- Skin emissivity = 0.90 - 0.98 (Chen, 2015; Hellebrand, Beuche, & Linke, 2001; Hellebrand et al., 2001a; López et al., 2012)

Although the mentioned properties are identified as being relevant to the simulator development, Redding et al. (2016) argued the only essential properties to match are the size, shape, thermal diffusivity (Equation 2-22) and Biot Number (Equation 2-23), Bi. Thermal diffusivity is one of the parameters in the Fourier equation (Equation 2-8) that governs the rate of internal conduction. Biot Number is a ratio of external to internal heat transfer resistances of an object. Biot numbers much greater than 1 means the convection is so significant that the surface temperature of the object is the same as the ambient. Biot number much smaller than 1 means the internal heat transfer resistance is so small that the object has uniform temperature and heat transfer to the

surface from the ambient is limiting. Simulating these parameters means λ , ρc (volumetric specific heat capacity)and hL need to be matched, where hL can be matched by mimicking the size and shape of the produce (Acevedo, Sánchez, & Young, 2007).

$$\alpha = \frac{\lambda}{\rho c}$$ Equation 2-22

$$Bi = \frac{hL}{\lambda}$$ Equation 2-23

Table 2-3, Summary of selected horticultural produce properties

Produce	MC $wt\%$	ρ[1] $kg\ m^{-3}$	c $J\ kg^{-1}\ K^{-1}$	λ $W\ m^{-1}\ K^{-1}$	Respiration $mW\ kg^{-1}$	k_s $ng\ kg^{-1}\ s^{-1}\ Pa^{-1}$ [a] $\mu g\ m^{-2}\ s^{-1}\ Pa^{-1}$ [b]
Apples	83.93	790-840	3720-4020	0.371-0.481	6.8-103.8	42[a]
Apricots	86.35	1003	3870	0.375	15.5-155.2	
Avocados	74.27	1054	3670	0.429[1]	183.3-1029.1	
Bananas	74.26	1044	3560	0.462-0.475[1]	37.3-242.5	
Blueberries	84.61	990[3]	3830	0.539[3]	6.8-259	2.19[b]
Cherries	86.13-80.76	1049	3730-3850		17.5-210.5	
Figs	79.11		3700		23.5-281.8	
Kiwifruit	80.0-86.0 [11]	996[7]	3830-3950	0.542-0.577[8]	8.3-57.3	7.40-24.68 [b9]
Grapefruit	90.89		3960		34.9-64.5	81[a]
Table gapes	81.30-80.56	1055-1115[13]	3400-3710	0.497-0.549 [4, 12]	3.9-114.4	123[a]
Lemons	87.4	1032[2]	3940	0.592[2]	15.5-59.2	
Limes	88.26	1030[2]	3930	0.595[2]	7.8-134.8	2.08[b]
Mangos	81.71	1083	3740	0.562 [2]	133.4-356.0	2.22[b]
Nectarines	86.28	990[4]	3860	0.585		
Olives	79.99		3760		64.5-180.9	
Oranges	82.3	1085	3810	0.554[1]	9.2-107.7	1.72[b]

Produce	MC $wt\%$	ρ[1] $kg\ m^{-3}$	c $J\ kg^{-1}\ K^{-1}$	λ $W\ m^{-1}\ K^{-1}$	Respiration $mW\ kg^{-1}$	k_s $ng\ kg^{-1}\ s^{-1}\ Pa^{-1}$ [a] $\mu g\ m^{-2}\ s^{-1}\ Pa^{-1}$ [b]
Peaches	87.66	1044	3910	0.581[1]	12.1-361.3	572[a]
Pears	83.81	1070	3800	0.595	7.8-266.7	0.686[a]
Pineapples	86.5	983[2]	3850	0.567[2]	22.3-185.7	
Plums	85.2	1090	3830	0.540-0.551[1]	7.6-71.1	136[a]
Raspberries	86.57		3960		52.4-727.4	
Strawberries	91.57	900[4]	4000	0.462[4]	36.4-625.6	13.6[b]
Average	83.8	1080.1	3820	0.508	150.0	

reference list : No superscript = Ashrae (2010); 1 = food properties handbook (Ahmed & Rahman, 2009b; Panagiotis, Magdalini, & Mohammad Shafiur, 2009; Singh, Ferruh, & Mohammad Shafiur, 2009); 2 = Ikegwu and Ekwu (2009); 3 = from Marai, Ferrar, and Civelli (2012); 4 = Sweat (1974); 5 = Akhijahani and Khodaei (2013); 6 = Valente et al. (1996); 7 = Razavi and Parvar (2007); 8 = O'Sullivan (2016); 9 = Montanaro et al. (2012), 10 = Oliveira et al. (2012); 11= Hosseinzadeh, Feyzollahzadeh, and Afkari (2013) 12 = Bingol et al. (2008) 13 = Rolle et al. (2015)

2.3.2 State of the art

The existing food and produce simulators reported in the literature were reviewed (

Table 2-4). Overall, four formats of simulator can be found, gel simulators (i.e. Tylose gel object), material filled simulators (i.e. apple simulator), solid object simulators (i.e. PVC sphere) and heat element simulators (i.e. cheese simulator). Although a range of horticultural produce simulators have been developed, no generalised systematic process has been proposed for their design. Also, the developed simulators tend to be unique and only suitable for the study context that they were developed for.

Table 2-4, A summary of previous simulators reported in the literature

#	Simulator/materials	k $W\ m^{-1}\ K^{-1}$	ρcp $kJ\ m^{-3}K^{-1}$	Shape	Application	Remarks
1	23-25% Tylose gel object[1-6]	0.48-0.53	3883	Any	Food thawing study	
2	Tylose filled the aluminium cylinder with wetted cloth surface[7]	0.48-0.53	3883	Cylinder	Validation of chilling time prediction model	Allows evaporation
3	Composite of guar gel with expanded polystyrene or aluminium [8]	Varied	Varied	Any	Validation of thermal conductivity prediction model	
4	Wetted/ dry plaster [9, 10, 11]	0.5	N/A	Cylinder	Validation of the chilling temperature profile	Allows evaporation
5	Combination set of sphere[12]	N/A	N/A	Sphere	Heat transfer mechanism inside pack bed	Allows heating, radiation and convection
6	Hollow PVC sphere [13, 14, 15, 16]	~ 0.02	N/A	Sphere	Air flow study	
7	Gel-filled polymer sphere [16, 17, 18, 19]	0.52	4153	Sphere	Ventilated package design	Can be 4% gelatine gel [17], 1.5% - 3% agar gel [16, 19] or 3% carrageen gel [18]
8	Water filled polymer sphere, [20, 21,]	0.52	4153	Sphere	Ventilated package design	Free convection of the water might occur inside the sphere
9	PVC sphere[22]	0.68	1857	Sphere	Ventilated package design	
10	Acrylic sphere[23]	0.21	1731	Sphere	Empirical model development	
11	Carrageenan gel sphere[25]	0.95	4153	Sphere	Validation of palletised cooling model	Allows evaporation

12	Aluminium avocado[26]	N/A	N/A	Avocado	Calculate heat transfer coefficient	
13	Grape box simulator[27]	N/A	N/A	Slab	Study heat transfer coefficient	The simulator provides constant heat, and the heat transfer coefficient is obtained at steady-state conditions.
14	Kiwifruit simulator[28]	N/A	N/A	Sphere	Simulate dry matter concentration for equipment calibration	Made of gelatine gel composite
15	Fruit texture simulator[29]	N/A	N/A	N/A	Simulate fruit texture	Made of calcium alginate or calcium low methoxyl pectate
16	Apple simulator[30]	0.45	3442	Apple	Cool chain monitoring	Made of polyamide shell filled with agar expand polystyrene composite
17	Cheese simulator [31]	0.35	N/A	Cylinder	Validated palletised cheese storage model	The simulator is made of plaster and able to provide heat to simulate the respiration effect

reference list: 1 = Pham ; 2 = Bonacina et al. (1974); 3 = Chuntranuluck, Wells, and Cleland (1998a); 4 = Cleland (1977); 5 = Llave et al. (2016); 6 = Tremeac, Hayert, and Le-Bail (2008); 7 = Chuntranuluck, Wells, and Cleland (1998a); 8 = Carson (2002); 9 = Le Page et al. (2009); 10 = Laguerre, Benamara, and Flick (2010); 11 = Laguerre, Remy, and Flick (2009); 12 = Ben Amara, Laguerre, and Flick (2004); 13 = Laguerre et al. (2008a); 14 = Laguerre, Amara, and Flick (2006); 15 = Allais and Alvarez (2001); 16 = Castro, Vigneault, and Cortex (2004a); 17 = Laguerre et al. (2008); 18 = Allais, Alvarez, and Flick (2006); 19 = Maul et al. (1997); 20 = Emond et al. (1996); 21 = Delele et al. (2013); 22 = Castro, Vigneault, and Cortex (2004, 2004a); Castro, Vigneault, and Cortez (2005); Vigneault and Goyette (2002); Vigneault and Castro (2005); Vigneault, Castro, and Cortez (2005a); Vigneault et al. (2007); 23 = Minh, Perry, and Bennett (1969); 24 = Alvarez and Flick (1999a, 1999b); Alvarez, Bournet, and Flick (2003); 25 = Alvarez and Trystram (1995); 26 = Valente et al. (1996); 27 = Frederick and Comunian (1994); 28 = Ang (2014); 29 = Wood (1975); 30 = Defraeye et al. (2017); 31 = Pham, Moureh, and Flick (2018)

2.3.2.1 Gel simulators

Gel simulators are where gel material is utilised to make the simulator. Gel materials used include 4% gelatine gel (4%), agar gel (1.5% -3%),or Tylose (23-25%). Making simulators from gel materials requires high moisture content, which allows a closer match of the thermal properties to the horticultural produce as produce generally has a high moisture content (Ashrae, 2010). In addition, the high water content allows the simulation of moisture transfer to a certain degree (Anderson & Singh, 2005). It should be noted that gel materials generally have yield points of 20 to 100 kPa depending on the gel type and concentration (Hershko & Nussinovitch, 1996), whereas oranges, one of the relatively firm horticultural products, has a yield point of 29 kPa (Ihueze & Mgbemena, 2017). This suggests that gel materials are rigid enough to simulate the palletised stacking of produce. If the gel material is stacked in a manner that can cause damage, it means the stacking is also likely to damage the real produce. The drawback of using this type of simulator is the low durability of the gel material. Ang (2014) found that microbial activity can occur within the gel after a few months; even when heavily dosed with antimicrobial chemicals. Anderson and Singh (2005) found that the water loss of the tylose gel was an irreversible process, which means the thermal properties of the simulator could also change over time, limiting their useful life

2.3.2.2 Material filled simulator

The material filled simulators consist of at least two components, the shell and the filling, where the filling can be air, water or gel, and the shell has the function of shaping and protecting the simulator. Different filling materials can be used depending on the application. For example, hollow PVC spheres are commonly used for studies of airflow patterns, where the thermal properties of the simulator are not necessary (Alvarez & Flick, 1999b). Water or gel material filling is used when the simulator needs to match the thermal properties of real produce (Defraeye et al., 2017; Delele et al., 2013; Laguerre et al., 2008). One of the most recent simulators of this type is the apple simulator developed by Defraeye et al. (2017), which is used as a monitoring tool during fruit shipping/transport, where the instantaneous temperature of the simulator can be a proxy for other produces inside the same package (Figure 2-10).

Compared to the gel simulator, the material filled simulator provides better durability and stability and may prevent moisture loss. However, the presence of the shell material could mean extra

thermal resistance or a potential thermal bridge around the surface of the simulator. A stack of this type of simulator could have different heat transfer pathways than a stack of real produce.

Figure 2-10, Apple simulator from Defraeye et al. (2017)

2.3.2.3 Solid object simulator

Simulators made of solid material can be classified as solid object simulators. Examples include the PVC sphere simulator, avocado aluminium simulator or the plaster simulator. This type of simulator is generally durable and stable. However, this type of simulator is unlikely to fully match the thermal properties of real produces due to material limitations. No common inert material can be found that matches the required thermal conductivity (~ 0.5 $W\ m^{-1}\ K^{-1}$) and volumetric specific heat capacity (~ 3800 $kJ\ m^{-3}K$). This is because horticultural produce generally contain a high percentage of water (section 2.3.1), and water is a substance with unusually high specific heat capacity due to hydrogen bonding (Stokely et al., 2010). High-density polythene could match the thermal conductivity, but it has a lower volumetric specific heat capacity (Redding et al., 2016). Stainless steel is one of the few materials that could match the volumetric specific heat (Stankus et al., 2008) due to leveraging its high density, but the thermal conductivity is significantly over the required thermal conductivity. Therefore, this simulator can only provide an abstraction for relative heat transfer applications.

Nevertheless, this type of simulator is still useful. Valente et al. (1996) developed an aluminium avocado to study the heat transfer coefficient of avocado under forced convection conditions. Plaster simulators were used to simulate the steady-state conditions that food experiences inside a fridge so that the important heat transfer mechanisms can be studied (Laguerre, Remy, & Flick, 2009; Laguerre, Benamara, & Flick, 2010). Note that the thermal conductivity of plaster is similar

to horticultural produce (~ 0.5 $W\ m^{-1}\ K^{-1}$), but not the volumetric specific heat (Ashrae, 2010). PVC sphere simulators were used in the study of Vigneault and Castro (2005) for horticultural package design, where useful scientific findings were obtained (Dehghannya, Ngadi, & Vigneault, 2008; Vigneault, Goyette, & De Castro, 2006; Vigneault & de Castro, 2006a; Vigneault et al., 2007; Vigneault, Thompson, & Wu, 2009). In those studies, the simulators were utilised to construct a rig for the package design testing (Figure 2-11). Interestingly, Vigneault and Castro (2005) proposed an empirical parameter called the cooling rate index, which is a ratio of the simulator cooling rate to water cooling rate. The researchers believed that this cooling rate index is an important parameter to empirically predict the cooling time of a given package design.

This concept was explored further by Redding et al. (2016), who proposed the possibility of chilling time scaling. Redding et al. (2016) utilised a simple one-dimensional analytical model to demonstrate the linear relationship between the cooling time and the volumetric specific heat capacity. Thus, the chilling time of a product can be estimated by multiplying the chilling time of an unmatched simulator with the ratio of the simulator to actual product volumetric specific heat capacities.

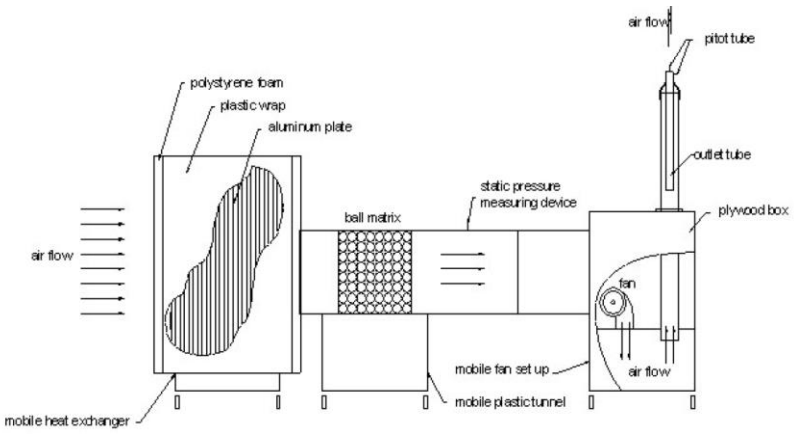

Figure 2-11, Package testing rig in Vigneault et al. (2007) study

2.3.2.4 Heating element simulator

Simulators with embedded heat elements are generally used in steady-state conditions. In this scenario, heat removed by a given heat transfer mode is equal to the heat produced by the heating element, and therefore the effect of heat transfer mode can be studied (Ben Amara, Laguerre, & Flick, 2004). The common application of this simulator is to determine the heat transfer coefficient (Equation 2-24), where h is the overall heat transfer coefficient, A is the area

of the simulator, $\dot{Q}$ is the constant heat provided by the element, $T_{sim.s}$ is the surface temperature of the simulator and T_{amb} is the ambient temperature (Ben Amara, Laguerre, & Flick, 2004; Frederick & Comunian, 1994; Laguerre, Amara, & Flick, 2006).

$$h = \frac{\dot{Q}}{A(T_{sim.s} - T_{amb})} \qquad \text{Equation 2-24}$$

Ben Amara, Laguerre, and Flick (2004) utilised a set of spheres, including spheres with embedded heating elements, to study pack beds' heat transfer mechanism in steady-state conditions (Figure 2-12). As the heating sphere was surrounded (stacked) by other hollow spheres (low thermal conductivity), convection is the major heat transfer mode removing the heat from the sphere, and therefore the convective heat transfer coefficient can be determined. When a brass sphere ($k = 126\ W\ m^{-1}K^{-1}$) is next to the heating sphere; some heat can be lost via air convection and brass sphere conduction. As the surrounding spheres are printed with black painted (emissivity = 0.97), the radiation heat transfer becomes significant (whereas the original material had emissivity =0.12). The authors found that at low air velocity (0.11 $m\ s^{-1}$), conduction and radiation play essential roles in the heat transfer mechanisms (an additional 25% and 39%, respectively). This finding can be translated to the cooling or heating of stacked food.

Figure 2-12, The simulators setup of Ben Amara, Laguerre, and Flick (2004) study to understand the heat transfer mechanism inside a packed bed at steady state conditions

The grape simulator (Figure 2-13) in Frederick and Comunian (1994) study was used to estimate grape punnets' overall heat transfer coefficient in convection conditions. The simulator consisted of an aluminium box (including lid for the shape), mica (for the volumetric heat capacity) and

nichrome wire (for heating). The weak point of this simulator is the empty space inside the box that allows free convection, introducing errors in the result (Frederick & Comunian, 1994). Making a grape punnet instead of individual grapes is similar to the idea of the porous media approach in mathematical modelling.

Figure 2-13, The grape simulator in Frederick and Comunian (1994) study

The cheese simulator (Figure 2-14) used by Pham, Moureh, and Flick (2018) is also for steady-state conditions, but the heating element was to mimic the heat released due to the respiration of camembert cheese. This simulator was used to validate a cheese cool storage model. As the rate of respiration (in the simulator) was controllable and the properties (such as shape, thermal properties, and others) of the simulator were constant throughout the storage period, the simulator provided good data for the model validation.

Figure 2-14, The cheese simulator in the Pham, Moureh, and Flick (2018) study

2.4 Summary and remarks

In this review, the methods of precooling were reviewed. Continuous optimisation is needed for each method to improve rates, uniformity, and cooling efficiency. A better package design seems to be one of the most influential and popular optimisation approaches, as a slight modification to the package can result in significant improvements. Modelling is one of the most favoured

approaches for researchers to explore how to improve precooling performance. It provides controllable testing environments and requires minimal logistics and planning. However, the computational time of models is still generally long, and validation experiments are still needed due to the limitations of modelling and to ensure the underlying assumptions are appropriate. This reinforces the need for simulators to aid modelling and experimental studies.

It is worthy of mentioning that not many studies have focussed on optimising closed package systems. As a result, the heat transfer mechanisms of a closed package system is not clear. Contradicting results have been reported from different studies.

Although a few simulators have been developed in different studies, a systematic development approach is not available. Also, most of the developed simulators are designed for a small-scale experiment, whereas a full scale of simulator experiment is rarely found. In the review of Redding et al. (2016), some guidelines were proposed; however, they are not extensive. The next chapter will continue this discussion and attempt to develop a systematic framework for simulator development.

Chapter 3. A conceptual framework for simulator development

A need for a simulator has been identified, but no systematic approach has been previously proposed in the literature. This chapter explains a basic conceptual framework for simulator development. The development of both physical and mathematical simulations share similarities in that they reduce complexity by neglecting some modes of heat transfer. For this reason, the conceptual framework for simulator development was developed by considering the existing modelling approaches of direct numerical simulation (DNS), porous medium and zonal models. The physical simulator design conceptual framework adapts these approaches by considering the different possible scales leading to individual, bulk, and semi-bulk simulators. The heat transfer modes that can be included in each simulator type are discussed.

3.1 Direct Numerical Simulation as an analogy to individual simulators

The DNS modelling approach considers the heat transfer characteristics of each product during the heating or cooling process. The geometry and packing of each fruit in the system are included, and air gaps within which natural or forced convection may occur. The concept of DNS models can be transferred directly into individual physical simulator development. Generally, for the air phase, models need to consider both fluid dynamics and heat transfer for a representative simulation, which requires solving the computationally intensive Naiver-Stokes equations. However, a physical model – a simulator, can accommodate the airflow by matching the product's geometry and allowing the presence of air gaps.

The general Fourier's equation (Equation 2-8) applies for positions inside the fruit. As such, an individual simulator design needs to reproduce conductive heat transfer within it (Equation 2-8). The S_h is the respiration term which generates heat. In some designs, this has been included from a heating element embedded inside the simulator.

The boundary conditions in a DNS can consider conduction, convection, radiation and evaporation and can be written as Equation 3-1. The equations suggest that an individual simulator could require the inclusion of up to five heat transfer modes if the correct thermal response between real and simulated fruit are to be matched. These include conduction to the fruit surface, and either conduction away from the surface into the surrounding air, convection into a well mixed air space, radiation and evaporation.

$$\frac{\partial}{\partial t}(\rho cT) = \nabla(\lambda \nabla \mathrm{T}) + S_h \qquad \text{Equation 2-8}$$

$$-\lambda_p \nabla \mathrm{T_s} = \lambda_{eff} \nabla \mathrm{T} + h_{conv}(T_{amb} - T_s) + \varepsilon \sum_{j=1}^{n} F_i \sigma (T_i^4 - T_s^4) + H_{vap} k_m (P_{amb} - P_s) \qquad \text{Equation 3-1}$$

3.1.1 Simulator feature – conductive heat transfer mode

Two types of conduction can happen during cooling (section 2.2.1), product internal conduction, which is described by the governing equation (Equation 2-8), and the conduction (fruit to fruit or fruit to package) via thermal contact to other media, which is described by the term $\lambda_{eff} \frac{\partial T}{\partial x}$ in the boundary condition (Equation 3-1).

3.1.1.1 Internal conduction

The thermal conductivity (λ), density (ρ), and heat capacity (c) are the essential thermal properties governing the internal conduction as defined in the Fourier equation. The volumetric specific heat capacity is the multiplication of density and specific heat capacity. The mass times heat capacity (or volume times volumetric heat capacity) describes how much energy the object must gain to increase its temperature by 1°C. In general, matching the product shape (and therefore distance in each dimension), thermal conductivity and the volumetric heat capacity can match the internal conduction that will occur in real fruit.

Simplification can be made when heat transfer is limited at the surface (and rapid within the produce). In such a case, the internal gradients in the product are low, and the product can be considered to have a uniform temperature. In the case of convective external boundary conditions, this condition can be quantified using the Biot number (Bi), a dimensionless number quantifying the ratio of the body's internal and external heat transfer resistances (Equation 2-23). A similar Bi-like number could be evaluated, including other surface heat transfer modes on the right-hand side of Equation 3-1 (e.g. radiation), and the discussion below is still relevant.

$$Bi = \frac{hL}{\lambda} \qquad \text{Equation 2-23}$$

Bi smaller than 0.1

When Bi is smaller than 0.1, the external resistance is much greater than internal resistance, and therefore the temperature profile of the body would be more toward a uniform value (Krantz, 2007, p. 159). The possible conditions for this Bi number could be products in a well-insulated package during cooling or horticultural products under room cooling conditions. In this case, the thermal conductivity of the object is less important as the heat transfer is restricted by the external heat transfer. Therefore, the simulator only needs to match the volumetric heat capacity to simulate the internal heat accumulation. Typically, horticultural produce have a volumetric heat capacity of ~4125 $kJ\ m^{-3}K^{-1}$ (section 2.3.1), and steel or gel materials can potentially match this value (Defraeye et al., 2017; Stankus et al., 2008)

Bi smaller larger 10

When Bi is greater than ten, the internal resistance is much greater than the external resistance. Therefore, the object's surface temperature is close to the ambient temperature. A possible scenario to fulfil this Bi number condition is a well-ventilated package during forced-air cooling. In this case, only the thermal diffusivity (ratio of thermal conductivity and volumetric heat capacity) is important for the internal conduction. A typical horticultural product has a thermal diffusivity of approximately 1.2 x10^{-7} m^2s^{-1} (section 2.3.1). Gel materials and PTFE could potentially match this value (Pan et al., 2017).

Bi between 0.1 to 10

When the Bi number is between 0.1 to 10, external and internal thermal resistances are of similar magnitude, and therefore it is important to match both the thermal conductivity and volumetric heat capacity. Typically, the horticultural product has a thermal conductivity of ~ 0.5 $W\ m^{-1}\ K^{-1}$ and volumetric heat capacity of ~4125 $kJ\ m^{-3}\ K^{-1}$. Only limited materials can match both these values (Redding et al., 2016).

Gel materials could potentially be the only option for matching both values. The downside of using gel materials for the simulator is the relatively short lifetime. The microbial degradation of the gel or moisture loss could change the thermal properties of the simulator, providing inconsistent

experimental results (Ang, 2014; Maul et al., 1997). Selecting a non-gel base material that matches thermal conductivity and volumetric heat capacity is difficult.

Redding et al. (2016) proposed a time-scaling approach, which only requires matching the thermal conductivity of the product, thus easing the difficulty of the material selection process. The author also used a simple analytical model to indicate the linearity between cooling rate and volumetric heat capacity. Therefore, the time can be scaled to account for a mismatch of the simulator's volumetric heat capacity compared to the produce. For example, if a simulator matches the thermal conductivity of the product, but the volumetric heat capacity is two times less, then the simulator should theoretically cool or be heated two times faster than the real product. This hypothesis is sensible. If the boundary heat flux is in a consistent condition, the volumetric heat capacity (Mc in Equation) is linearly relative to the cooling rate ($\frac{\partial T}{\partial t}$ in Equation). Further discussion and validation of this hypothesis is given in Chapter 5.

3.1.1.2 Conduction via thermal contact

When two objects are in contact, heat can be transferred via the contact area. Simulators might need to mimic the deformation of the product in contact to match the contact area and, therefore, the extent of conductive heat transfer. This requires matching the mechanical properties and geometry of the product.

Generally, numerical models tend to ignore this heat transfer pathway (Han et al., 2018; O'Sullivan et al., 2016a) due to limitations in computational power. Tanner (1998) believed that the contact resistance between two solid objects is generally large, and therefore heat transfer would be more favourable through other pathways, such as convection. Van der Sman (2008) performed a scaling analysis and proved that heat conduction via thermal contact is not a significant heat transfer pathway. Furthermore, the study of Laguerre, Amara, and Flick (2006) indicates that when the ratio between the product and nearby medium (air) thermal conductivity ratio is less than 100, the heat flow is close to a parallel pathway (Figure 3-1 a). As the ratio increases, the heat flow converges to the contact area (Figure 3-1 b). Horticultural products generally have a thermal conductivity of 0.5 $W\ m^{-1}K^{-1}$, and air has a thermal conductivity of 0.025 $W\ m^{-1}K^{-1}$Error! Bookmark not defined., which results in a ratio of 25 (smaller than 100). This agrees the other studies suggesting conduction via thermal contact are insignificant for horticultural product cooling.

a) b)

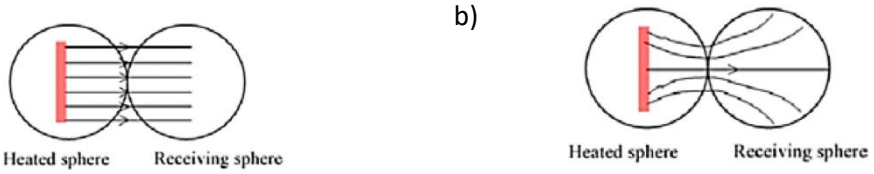

Figure 3-1, Heat flow pathway for high product to medium thermal conductivity ratio (a) and low ratio (b), adapted from Laguerre, Amara, and Flick (2006)

3.1.2 Simulator feature – Convective heat transfer mode

The term, $h_{conv}(T_{amb} - T_s)$, in the boundary equation (Equation 3-1) describes the convective heat transfer over the product's surface into a surrounding bulk media. The heat transfer coefficient, h_{conv}, is an approximation of fluid flow effect on the objects surface heat transfer. Typically, matching the object's shape mimics the heat transfer coefficient (Acevedo, Sánchez, & Young, 2007).

The convection mechanisms in the open package and closed package systems are different. In an open package system, air can flow through and interact with the products. In a closed system, the air is restricted by barriers and cannot interact with the products. The convection inside an open system is generally forced convection, and the convection inside a closed package system is generally free convection due to the buoyancy force generated by the temperature gradient. Regardless of system type, convection can be mimicked by matching the product shape and reproducing the shape and constrictions in the air spaces. For example, Acevedo, Sánchez, and Young (2007) used a grape shaped aluminium simulator to determine the surface heat transfer coefficient of a package of the grape inside an enclosed system when free convection occurred. Valente et al. (1996) used an avocado shaped aluminium simulator to determine avocado's surface convective heat transfer coefficient under forced air cooling.

Convection is generally important for product cooling. In an open package system, the surface convection on the product is important, and the heat transfer coefficient can be determined by the empirical model (Equation 3-2) given by Laguerre, Amara, and Flick (2006). The external convection on the package surface is important in a closed package system, and the internal free convection could also be important. The importance of this internal convection can be determined via the Rayleigh-Darcy number (Ra_m; Equation 3-3 to Equation 3-5). If the number is greater than

$4\pi^2$, natural convection would be significant inside the package system (Nield, 2013). Within Equation 3-3, L is the characteristic length of the package.

$$Nu = \frac{hL}{\lambda_{air}} = 1.56Re^{0.42}\,\mathrm{Pr}^{1/3} \qquad \text{Equation 3-2}$$

$$Ra_m = Ra \times Da = K\,\frac{g\beta\Delta TL}{v\,\alpha_{air}} \qquad \text{Equation 3-3}$$

$$K = \frac{D_{eq}^2\,p^2}{180(1-p)^2} \qquad \text{Equation 3-4}$$

$$D_{eq} = 6\frac{V_p}{A_p} \qquad \text{Equation 3-5}$$

3.1.3 Simulator feature – Radiative heat transfer mode

The term, $\varepsilon \sum_{j=1}^{n} F_i\sigma(T_i^4 - T_s^4)$, in the boundary equation (Equation 3-1) represents the radiative heat transfer mode. This indicates that if radiation is important, the simulator needs to match the emissivity (ε), the product surface temperature (T_s) and the view factor (F) to simulate the radiation effect. The emissivity of the simulator can be matched via surface modification, such as painting the surface (Ben Amara, Laguerre, & Flick, 2004). The surface temperature of the simulator will be matched by default if the simulator is faithful to the overall heat transfer mechanisms. The view factor, which defines how much heat is transferable via radiation to the nearby visible objects, can be simulated by matching the product shape and packing arrangement.

Radiation is generally considered insignificant during produce precooling (section 2.2.1). Feng and Han (2012) mathematically proved that two equal size contacting spheres only have a view factor of 0.07. The view factor of two unconnected spheres with an obstacle in between has an even lower value, which reflects the view factor of the products packed inside a package. As the product is closely packed and the temperature gradient between the adjacent products is small, the effect of radiation should be minimal.

3.1.4 Simulator feature – Evaporative heat transfer mode

3.1.4.1 Open package system

The term, $H_{vap}\,k_m(P_{amb} - P_s)$ governs the evaporation effect into a surrounding bulk media. To include it, the simulator would have to allow for moisture evaporation into the surrounding air.

The mathematical term indicates that the evaporation effect of the simulator can be simulated by matching the effective mass transfer coefficient (k_m) and the moisture pressure deficit, ($P_{amb} - P_s$). The latent heat (H_{vap}) will be matched if the evaporating substance is water. The effective mass transfer coefficient consists of two components (Equation 3-6), the air film mass transfer coefficient (k_{air}) and the skin mass transfer coefficient (k_{skin}), which is a derivation from the skin permeability. The air film mass transfer coefficient is a function of air velocity and object shape, which can be matched through the product geometry. The skin mass transfer coefficient can be matched by having a modified surface layer; for example, Chuntranuluck, Wells, and Cleland (1998a) used wetted cloth. The moisture pressure deficit will be matched if the simulator contains water.

$$k_m = \left(\frac{1}{k_{m_{air}}} + \frac{1}{k_{m_{skin}}}\right)^{-1} \qquad \text{Equation 3-6}$$

There are differences of opinion on the importance of product evaporation during cooling (section 2.2.1), where some studies suggested it is important (Delele et al., 2012; Ferrua & Singh, 2009a), and some studies believed it is not important (O'Sullivan et al., 2016a; Tanner et al., 2002a). To develop a better understanding, a simplified model (Model A; Figure 3-2) was built, using a one-dimensional spherical equation. The sphere centre was defined as a symmetry boundary, meaning there is no heat flux. The surface boundary was considered with convection and evaporation effects. The water vapour pressure was estimated based on temperature using the Antoine equation (Chuntranuluck, Wells, & Cleland, 1998b). The Fourier equation (Equation 2-8) was the governing equation of the object, and the model was solved by COMSOL Multiphysics v5.2.

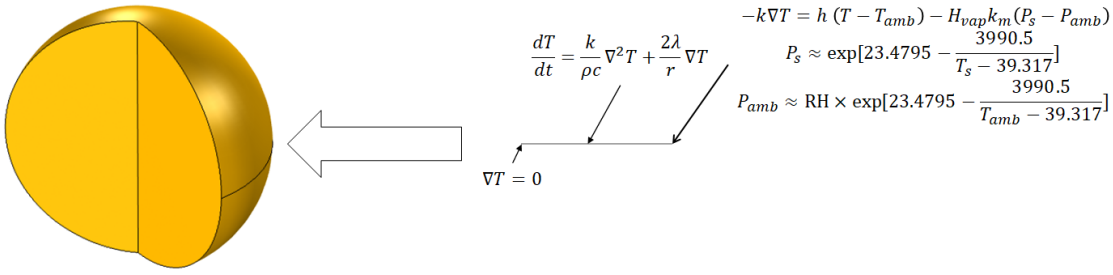

Figure 3-2, 2D simplified model to understand evaporation effects

A range of heat transfer coefficients, effective mass transfer coefficients and ambient relative humidity (RH) were tested in model A. The outcome is summarised in Figure 3-3. The 'no evaporation' scenario was used as a benchmark, where the effective mass transfer coefficient was set as zero. The maximum temperature deviation (MAD; Equation 3-7) during cooling was

calculated by subtracting the model output for each scenario to the benchmark output at each time and then finding the maximum deviation over all times. This value represents the maximum possible evaporation effect during cooling. The ratio of heat to the mass transfer coefficient ($\frac{h}{k_m}$) was used to quantify the magnitude of the evaporation effect. Overall, Figure 3-3 shows that when the heat transfer coefficient is 10^9 times greater than the mass transfer coefficient, the evaporation effect becomes insignificant (max temp dev. less than 1 °C). This is because the surface temperature of the product is cooled fast enough that the moisture pressure deficit value drops significantly, limiting the evaporation. There is no evaporation effect when RH is 100%, which is sensible and expected, as the moisture pressure deficit, in that case, is zero. 80 to 90% of RH values are typical ambient conditions found in industrial horticultural product cooling (O'Sullivan, 2016; Tanner, 1998). Under this condition, the heat to mass transfer coefficient ratio needs to be greater than 10^8 times to avoid the significant effects of evaporation (max temp dev. ~ 1 °C).

$$MAD = \max|T_{\text{bench}}(t) - T_{scenario}(t)| \qquad \text{Equation 3-7}$$

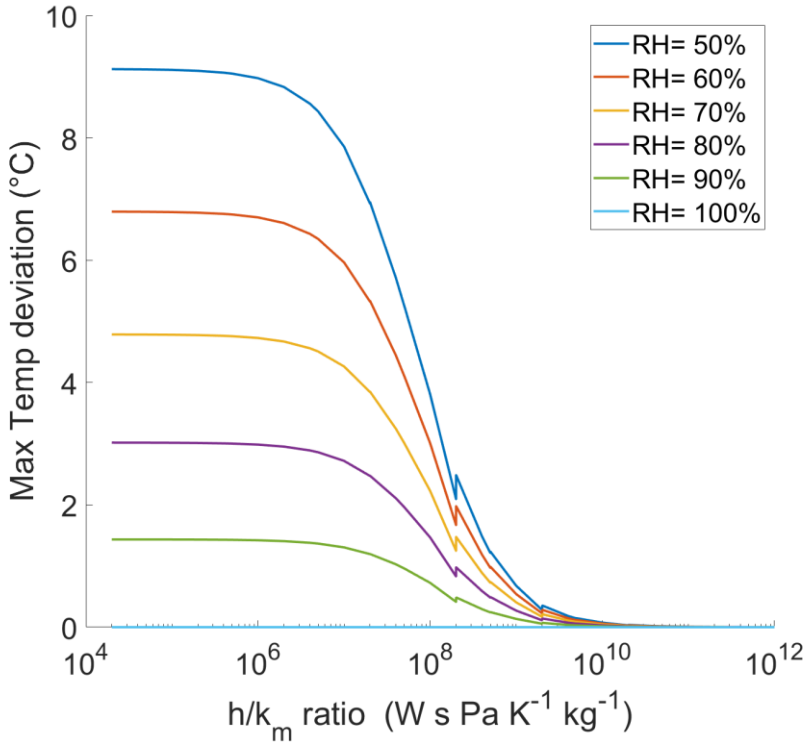

Figure 3-3, Comparisons of evaporation effect under different heat transfer coefficient condition

Since the effective mass transfer coefficient consists of the air film and skin mass transfer coefficient, the heat to mass transfer coefficient can be rearranged as Equation 3-8. Horticultural products generally have an equivalent diameter of 2 to 64 mm (Redding et al., 2016), and the air velocity in the produce precooling is 0.02 to 5 $m\ s^{-1}$ (Laguerre et al., 2008). Based on this, the heat transfer coefficient for cooling can be calculated (Equation 3-2) to be under 100 $W\ m^{-2}\ K^{-1}$, which is also reported in Ashrae (2010). As most of the horticultural products have a skin mass transfer coefficient smaller than $10^{-9}\ kg\ s^{-1}\ m^{-2} Pa^{-1}$ (Ashrae, 2010), the horticultural product during cooling, generally has $\frac{h}{k_m air}$ greater than 10^9. As a result, the evaporation is already significantly restricted by the produce skin permeability even if the air film resistant is not considered.

$$\frac{h}{k_m} = h\left(\frac{1}{k_{m_{air}}} + \frac{1}{k_{m_{skin}}}\right) = \frac{h}{k_{m_{air}}} + \frac{h}{k_{m_{skin}}} \qquad \text{Equation 3-8}$$

3.1.4.2 Closed package systems

The concept above is generalised for an open package system by considering the heat transfer coefficient. Generally, evaporation effects are considered insignificant in closed systems as the purpose of using a polyliner is to minimise moisture loss (Ngcobo et al., 2013a; O'Sullivan et al., 2016a). In order to confirm this, a simplified model was developed (Model B), evaluating the effect of evaporation (Figure 3-4). The model simulates four products (the semi-circles, Figure 3-4 left) stacked in a column inside a closed package system, where the rectangle at the bottom represents the cardboard box, and the top boundary represents a thin plastic layer covering the product. This mimics a stack of produce inside a carton package. The governing equation for temperature is Fourier's equation (Equation 2-8). The governing equation for the air phase is the continuity equation and the Naiver-Stokes equation with Boussinesq approximation for the internal natural convection (Equation 2-1 to Equation 2-3). Fick's equation is the governing equation for the mass transfer in the air phase (Equation 2-7). The concentration boundary condition for the product surface is defined as a saturated water surface, which is the maximum possible for evaporation (Equation 3-9); The temperature boundary condition for the product surface was defined as

Equation 3-10 and Equation 3-11; The velocity boundary condition for the product surface was defined as no-slip wall, which means equal to zero. The external surface of the package was defined as constant 0 °C and saturated vapour concentration at 0°C (the top and bottom boundary), and the side boundary was defined as no flux. Evaporation effects can be tested by comparing the model without latent heat. The model is solved by COMSOL Multiphysics v5.2 using 2D axisymmetric rotational (8098 mesh elements were created).

Equation 2-1 to 2-3, and 2-7, correspond to the conservation of mass, momentum, energy and vapour in the air space.

$$\frac{\partial \rho}{\partial t} + \nabla(\rho u_i) = 0 \qquad \text{Equation 2-1}$$

$$\frac{\partial}{\partial t}(\rho u_i) + \nabla\left(\rho u_i u_j\right) = \nabla(\tau_i) + \rho g_{i_u} \qquad \text{Equation 2-2}$$

$$\frac{\partial}{\partial t}(\rho c T) + \nabla(\rho u_i c T) + \nabla\left(E_{vap}\, \rho u C\right) = \nabla(\lambda \nabla T) \qquad \text{Equation 2-3}$$

$$\frac{\partial C}{\partial t} + \nabla(\rho u C) = \nabla(D \nabla \mathrm{C}) \qquad \text{Equation 2-7}$$

Fourier's law (Equation 2-8) applies within the fruit.

$$\frac{\partial}{\partial t}(\rho c T) = \nabla(\lambda \nabla T) \qquad \text{Equation 2-8}$$

At the fruit surface and the top and bottom boundaries, the water vapour concentration is assumed to be at the saturated water vapour pressure, as given by ideal gas law (equation 3-10). Both top and bottom temperature were set to be 0 °C.

$$C = \frac{P_{sat}}{R\, T} \qquad \text{Equation 3-9}$$

The heat conducted to the fruit surface is equal to the lost of heat due to evaporation or heat transfer into the air.

$$\lambda \nabla T = H_{vap} D\, \nabla C + \lambda_{eff} \nabla T \qquad \text{Equation 3-10}$$

The left and right boundaries were symmetry (Equation 3-11)

$$\nabla T = 0; \nabla \rho u = 0; \nabla C = 0 \qquad \text{Equation 3-11}$$

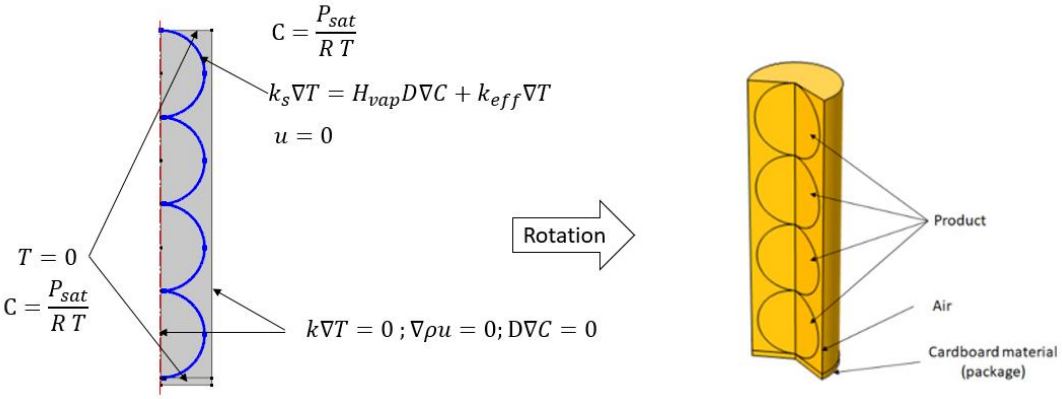

Figure 3-4, Simplified model for evaporation comparison

Figure 3-5 shows the predicted volume average temperature of the product with and without evaporative cooling. In general, the maximum temperature deviation incurred by ignoring evaporation is less than 0.5 °C. Thus, under conditions that are optimal for evaporation inside a closed package system, product temperature has a minimal effect from evaporative cooling. These results agree with the conclusions from O'Sullivan et al. (2016a).

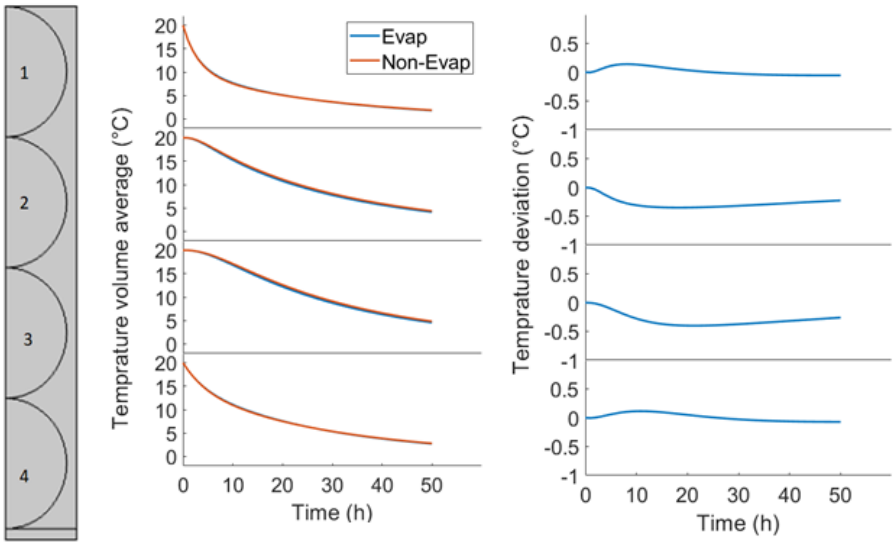

Figure 3-5, Comparing the effect of evaporation on product temperature in a closed package system

3.1.5 Simulator feature –respiration of heat

The term S_h in the governing equation (Equation 2-8) accounts for the heat generated by product respiration. Although many studies have included respiration heat in their models (section 2.2.1), researchers generally agree that the effect of respiration heat is insignificant during rapid cooling

(O'Sullivan et al., 2016a; Tanner et al., 2002a). Including respiration heat in a mathematical model is relatively simple, but it would be challenging to include this in a physical model. Electrical components need to be embedded into the simulator, to provide the heat, and fine-tuning is needed to make the heating rate vary as a function of temperature (Pham, Moureh, & Flick, 2018) as in fruit, the respiration rate is temperature-dependent (Ashrae, 2010).

3.2 Porous medium approach as an analogy of a bulk simulator

The porous medium approach to modelling considers the fruit to be a bulk volume with effective properties (such as a stack or a package of products). The development of the porous medium modelling approach is also transferable to the development of a bulk simulator. However, the implications of bulk simulator development are different, depending on the type of package system being considered.

In an open package system, air can flow through the product or within stacks inside the package. Mathematically, the airflow can be averaged based on Darcy's law (Equation 2-13 to Equation 2-15). This averaging is dependent on the air permeability, which is a function of product diameter and the porosity of the stack (Verboven et al., 2006). Matching these parameters is equivalent to developing an individual simulator, and therefore bulk simulators do not offer advantages for open package systems. Producing a bulk simulator with equivalent resistance to airflow results in a continuous phase with similar dimensions to the fruit, and therefore the properties must match the fruit as discussed for the direct simulation approach in Section 3.1. Furthermore, the position of the fruit phase and overall dimensions of the bulk system would be fixed, and the use of the simulator would be much less flexible.

In a closed package system, air cannot flow through the product stack. As the air velocity is equal or close to zero inside the package (Equation 2-16), the energy equation of the porous medium approach can be simplified into the Fourier equation (Equation 3-12) with consideration of effective thermal properties, indicating the possibility of a bulk simulator with effective properties. Evidence for this can be found from the study of Amos (1995), where the Fourier's equation with the effective properties was used to predict cooling in an unvented apple box and reasonable predictions were obtained. Although internal natural convection could be significant (O'Sullivan et al., 2016a), a slight adjustment to the effective value can be made to compensate for this (Becker

& Fricke, 1996; Tanner et al., 2002a). However, if the adjustment cannot account for the internal heat transfer mechanisms, a bulk simulator would not be viable.

$$(\rho c)_{eff}\frac{\partial T}{\partial t} + \cancel{(\rho c)_f u \frac{\partial T}{\partial x_i}}^{0} = \frac{\partial}{\partial x_i}\left(\frac{\partial(\lambda_{eff} + \cancel{D_t}^{0})\,T}{\partial x_i}\right) + S_h \qquad \text{Equation 3-12}$$

3.2.1 Package to product length ratio (P/p ratio)

The P/p ratio is a useful parameter in evaluating the feasibility of the porous medium approach in modelling (Ferrua & Singh, 2008). Typically, the ratio needs to be at least 6.6 (Van der Sman, 2002) to be appropriate to distribute the air phase throughout the bulk and model the system using effective properties.

The effective volumetric heat capacity and thermal conductivity are the important parameters governing the temperature profile of the bulk simulator. The effective volumetric heat capacity can be accurately predicted based on volume fraction (Equation 3-13), and it is not a function of the P/p ratio. However, the geometry can affect the effective thermal conductivity (Carson et al., 2003), which means the P/p ratio can affect it. To understand the effect of the P/p ratio on bulk simulator design, a simplified model (Model C) was developed based on the Fourier equation (Figure 3-6). The model assumed an array of infinitely long cylinders (2D circles) stacked inside an enclosed space, where the array dimension can be varied from one by one (P/p=1) to twenty by twenty (P/p=20). Heat transfer occurred by conduction through both the product and air phases with point contact between adjacent circles.

The volume fraction of the geometry remained constant regardless of the array size, and therefore the effective volumetric heat capacity remained constant. The side boundaries were defined as insulation, and the top and bottom boundaries were defined as having constant temperatures of 20 °C and 0 °C, respectively. The diameter of the cylinder (the circle in 2D) was defined as 30 mm (point touching), which is the middle range of typical produce size (Redding et al., 2016). The thermal conductivity of the individual product was defined as 0.51 $W\ m^{-1}K^{-1}$, and the volumetric heat capacity was defined as 4152.3 $kJ\ m^{-3}\ K^{-1}$, which are the typical thermal properties of horticultural produce (see section 2.3.1.). The model was solved in COMSOL Multiphysics using the stationary solver to predict the steady-state heat transfer through the system. Although a 3D model of stacked spheres would be a more appropriate description of a stack of produce, the

result from this 2D simulation reflected what occurs in 3D and required significantly reduced computational time.

Equation 3-14 shows how the volumetric heat capacity was calculated where pd is the volume fraction of the product phase.

$$(\rho c)_{eff} = \rho c_1 \times pd + \rho c_2 \times (1 - pd)$$ Equation 3-13

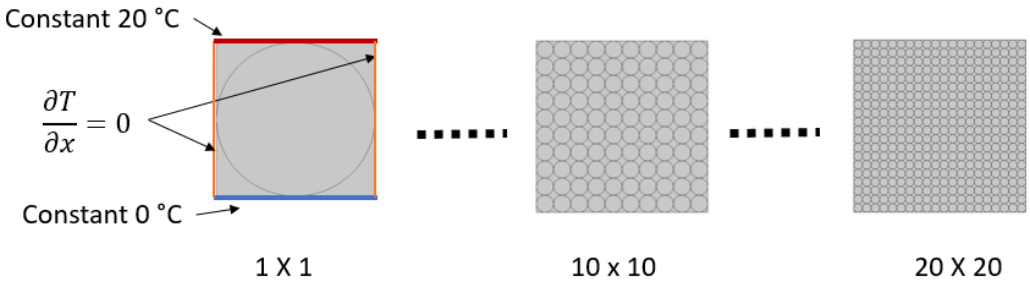

Figure 3-6, Model C system summary

The apparent effective thermal conductivity occurring in the model can be calculated based on the definition of thermal conductivity as applied to the whole bulk system (Equation 3-14), the heat flow (ϕ) per characteristic length (L) per temperature gradient (ΔT) where the heat flow can be calculated by averaging the heat flow on each boundary node (Equation 3-15).

$$\lambda_{eff} = \frac{\phi}{L\,\Delta T}$$ Equation 3-14

$$\phi = W \int_0^L q_n dx$$ Equation 3-15

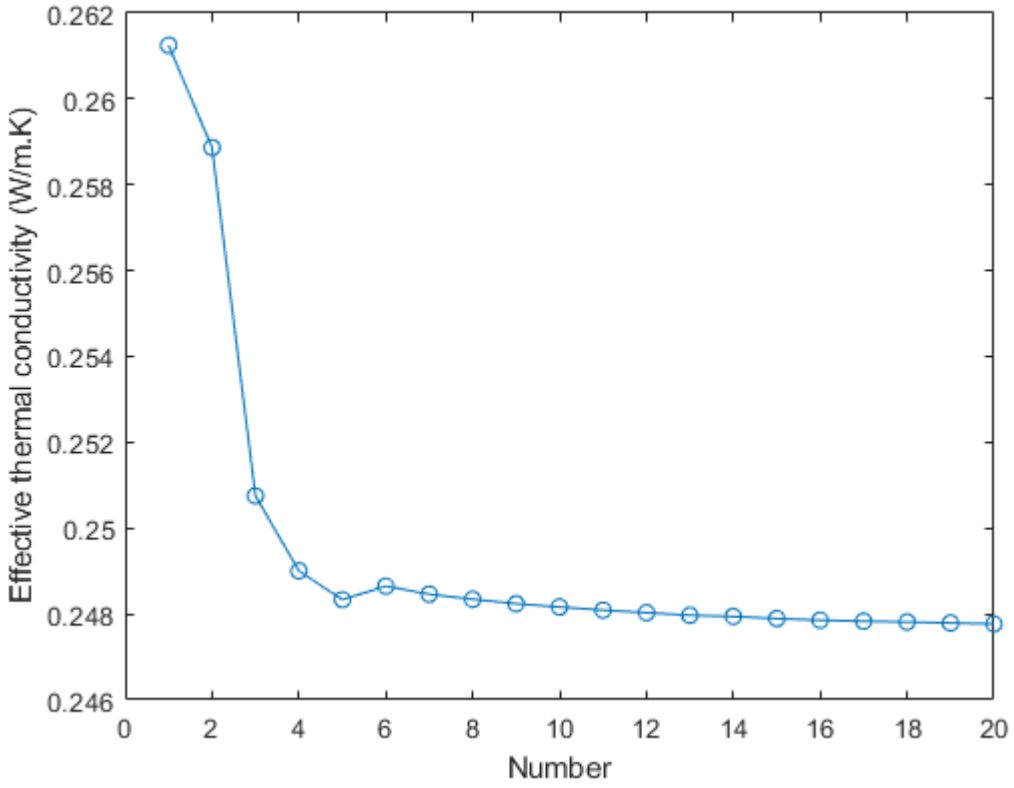

Figure 3-7, Change of effective apparent thermal conductivity at different P/p ratios

Figure 3-7 shows the apparent effective thermal conductivity of the model geometry as a result of different P/p ratios. Figure 3-7 shows that the effective thermal conductivity starts converging to a constant value at P/p ratios greater than 7, which agrees with the findings of Van der Sman (2002). However, the overall change from the ratio of 1 to the ratio of 20 is only 0.02 $W\ m^{-1}\ K^{-1}$, which is less than the natural product variation(O'Sullivan, 2016). The sensitivity analysis of O'Sullivan (2016) shows that this thermal conductivity variation has minimal effect on the overall product cooling process.

To better understand the effect of the P/p ratio on effective thermal conductivity, a second model was developed (Model D; Figure 3-8) for the dynamic cooling of bulk produce. This model consisted of two components, the non-porous medium model (NPM), which adapts the geometry from model C, and the porous medium model (PM), a region with effective properties. The effective volumetric heat capacity of the system was estimated based on Equation 3-13, and the effective thermal conductivity used the maximum and minimum effective thermal conductivity value from Figure 3-7 (0.261 and 0.248 $W\ m^{-1}\ K^{-1}$, respectively). The top and side boundaries

were defined as no flux, and the bottom boundary was defined as constant at 0 °C. Unsteady state cooling rates were predicted in each case using COMSOL Multiphysics.

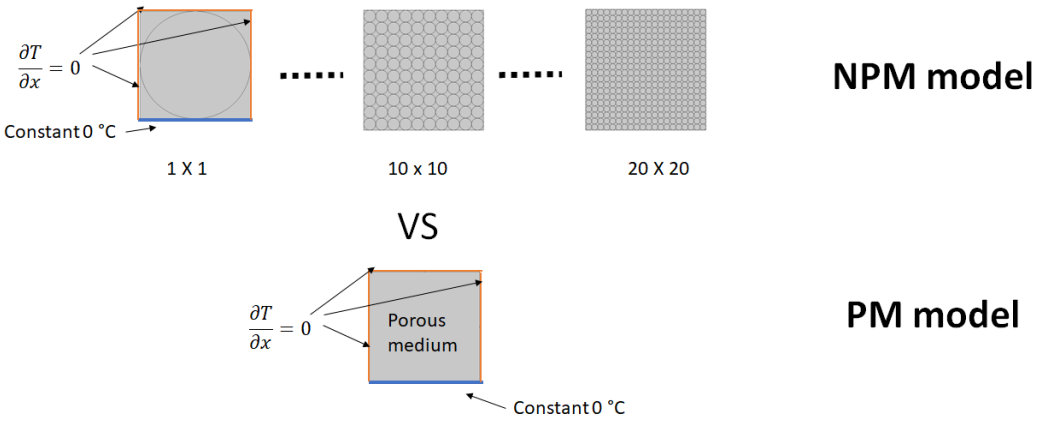

Figure 3-8, Model D system summary

Figure 3-9 compares the effect of the P/p ratio on porous medium approach error. Again, the maximum temperature deviation during the cooling was calculated (see 3.1.4). The temperature of each circle centre in the NPM model and corresponding position in the PM model were compared. The maximum temperature deviation was calculated from the overall maximum difference between these positions throughout the cooling period. As expected, the maximum temperature deviation is unstable before P/p is less than 5 but comes relatively consistent after P/p reaches 7. Although the maximum temperature deviation could be as big as 2.2 °C when the P/p ratio is less than 5, this temperature error could sometimes be acceptable depending on the purpose of the study (Getahun et al., 2017). Also, a temperature difference of 2.2°C in a large-scale experiment could be considered insignificant given that the experimental variation is already large (Olatunji et al., 2017; Olatunji, Shim, & East, 2019). Based on this argument, the critical P/p ratio is not considered at a particular value, but the acceptable tolerance associated with the ratio.

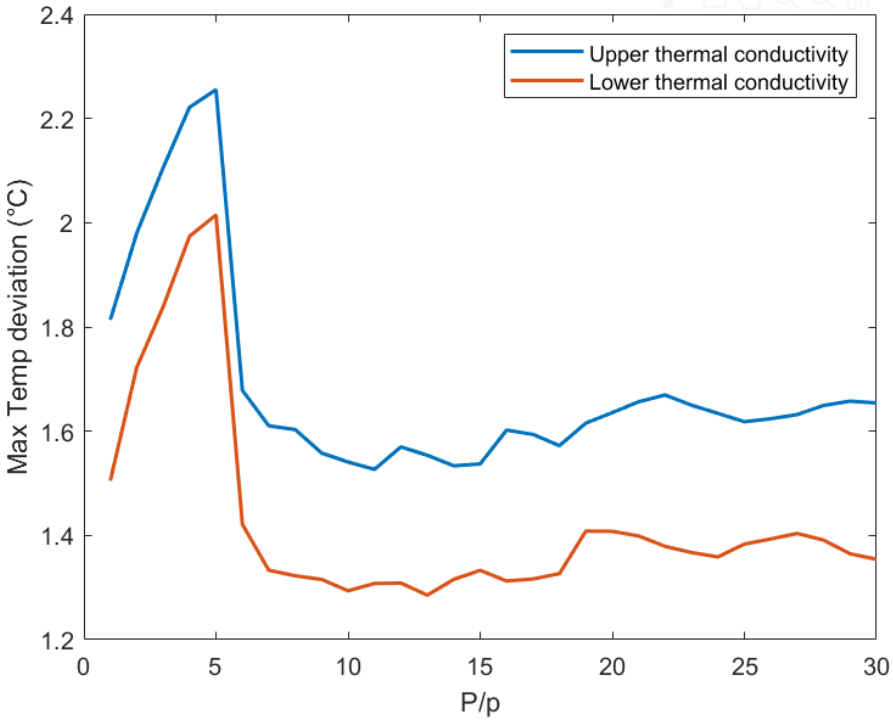

Figure 3-9, Comparison of the effect of P/p ratio effect on PM model error

3.3 Zonal approach

A zonal model is an intermediate approach between the DNS and porous medium approaches. This approach is suitable for developing simulators for multi-level packaging systems (Figure 3-10), such as the packaging of grapes or blueberries. In these systems, the product is packed into a subunit (e.g., clamshell or bag), and multiple of these are then packed into a larger cardboard package. These small sub-units can then be looked at as zones, which are in turn considered as mini-bulk simulators. As a result, simulating convection and radiation in the air gaps between zones become possible. In developing the subunit simulators, the considerations discussed in section 3.2 around effective bulk properties, P/p ratio and external shape should be considered. Pragmatic decisions on the shape of each 'zone' must also be made. Flexibility can be developed by creating uniformly sized subunits that pack together (as would occur in packed punnets), wherein other circumstances it may be necessary to make subunits with a varying shape that stack together in well-defined orders to match the real system (as would occur in bags of grapes for example).

Figure 3-10, Examples of multi-level package systems (Ngcobo et al., 2013a)

3.4 Approach selection

Table 3-1 summarises the heat transfer features of each approach. An individual simulator can include all (or most) heat transfer modes, whereas bulk and zonal simulators can only include some of the heat transfer features. Figure 3-11 shows an overall flowchart proposed for aiding decision-making during simulator development. The framework can be divided into three components, approach selection, heat transfer mode selection and time scale or gel-based simulator selection. This framework was developed for product cooling, but the approach and basic structure could be adapted to other scenarios where simulators could be useful.

Table 3-1, Summary of three approaches on each heat transfer mode

Heat transfer mode	Individual	Bulk	Zonal	Properties
Conduction	Yes	Yes	Yes	ρC & λ
Convection	Yes	No	Partially	Shape
Radiation	Yes	No	Partially	ε, T_s & $shape$
Evaporation	Yes	No	No	D_{eff}, WC
Respiration	Yes	Yes	Yes	Heating element

The logic for the approach to selection starts by identifying whether the product to be simulated is packed in a closed or open system. If it is an open system, then the simulator needs to be in an individual form to account for the airflow through and around the product, as discussed in 3.2. If

the package system is closed where the contents can be divided into closed sub-units and the convection and radiation between the subunits are important, then the zonal simulator approach can be considered. A bulk simulator can be considered if the system cannot be divided into subunits and the convection and radiation between the subunits are not important. To confirm the relevance of the bulk or zonal approaches, the importance of the internal detail of the stacked produce needs to be evaluated. The key considerations are the contribution of internal natural convection, radiation and evaporation to heat transfer within the bulk. It is known that internal radiation and evaporation inside a closed package system is insignificant (see section 3.1). Therefore, the importance of the internal detail is based on the Rayleigh-Darcy number. If the Rayleigh-Darcy number is greater than $4\pi^2$, then the internal free convection is significant, and the simulator needs to be an individual format. If the number is less than $4\pi^2$, then internal free convection is insignificant, and the acceptability of temperature error based on the P/p ratio must be considered, (refer to Figure 3-9). If the likely error is acceptable, then bulk or zonal simulator approaches can be adopted.

As already discussed, an individual simulator can include conduction, convection, radiation evaporation and respiration heat transfer features, whereas a bulk simulator can only include conduction, convection and respiration, and zonal simulators can partially include internal convection and radiation between subunits. Conduction and convection are always important for simulators. For an individual simulator in an open system, the decisions are based on Bi number (as discussed in section 3.1.1.1). However, if the package is a closed system, thermal conductivity and volumetric heat capacity need to be considered. In theory, the Bi number simplification concept (section 3.11) should be applied on the external bulk package, where the bulk package of the product is considered as an effective object. In order to maintain this external Bi number of the package, the thermal conductivity of the individual simulator needs to be consistent with the targeted product to result in the same effective thermal conductivity of the bulk package. As the thermal conductivity of the individual simulator needs to be matched, the volumetric heat capacity will also need to be matched at any Bi number conditions. As a result, for the individual simulator in a closed package system, the thermal conductivity and volumetric heat capacity always need to be matched.

Typically, a horticultural product has high water content (Ashrae, 2010), and therefore the thermal properties are similar to water, the volumetric heat capacity of ~ 4125 $kJ\ m^{-3}\ K^{-1}$ and thermal

conductivity of ~ 0.5 $W\ m^{-1}\ K^{-1}$ (section 2.3.1). Water is a special substance with high heat capacity due to its hydrogen bonded molecular structure (Silverstein, Haymet et al. 2000), and it is difficult to select a common stable material with similar values. As discussed (section 3.1.1), if the Bi number of the condition is lower than 0.1, the simulator design only needs to match the volumetric heat capacity, which means stainless steel could be potentially used (Stankus et al., 2008); if the Bi number is greater than 10, the simulator only needs to match the ratio of thermal conductivity and volumetric heat capacity (thermal diffusivity), which means PTFE can potentially match this value in fruit (Pan et al., 2017). When the Bi number is greater than 0.1 but smaller than 10, thermal conductivity and heat capacity need to be matched, which is challenging for material selection.

Gel-based materials could be potential options as they contain high percentages of water, and, indeed, many gel-based simulators can be found in the literature (section 2.3.2). However, gel-based simulators are generally less durable and stable (as discussed in section 3.1.1.1). Therefore, time-scaling approaches are an alternative of matching both thermal properties where durability and long-term stability are required.

For bulk and zonal simulators, the effective thermal properties need to be matched (as discussed in section 3.2). The inclusion of significant volumes of air in the bulk material allows a wider range of materials that could be suitable for simulator design. Typically, the volume fraction of bulk products is ~50%, which results in the effective thermal conductivity being ~ 0.25 $W\ m^{-1}\ K^{-1}$ (parallel thermal conductivity model), and volumetric heat capacity in fruit is ~ 2062 kJ/m^{3}K (Equation 3-13). PTFE or PTFE composites could be potential materials to achieve these properties.

Individual simulators need to match the individual shape, and bulk or zonal simulators need to match the external bulk shape. Matching the shape for a simulator is relatively easy, which can be done mechanically (such as milling or routing). Radiation is generally not important (as discussed in section 3.1.3), but the surface emissivity, temperature, and shape need to be matched if it is important. As mentioned, most common materials have similar emissivity to horticultural products (section 2.3.1), and the surface temperature would be matched by default if the simulator behaviour is faithful to the heat transfer mechanism.

Only individual simulators allow the inclusion of evaporation. The importance of the evaporation effect is dependent on the package system (open), RH and h/k_m ratio (as discussed in section 3.1.4). If evaporation is important, the simulator would most likely need to be a gel base material

with a modified external skin layer such as the system used by Chuntranuluck, Wells et al. (1998) in their simulator. The literature generally agreed that the respiration of heat is not important during product cooling (section 2.2), but if it is important, a controlled heating element can be embedded into the simulator to match the release of the heat of respiration (Pham, Moureh, & Flick, 2018).

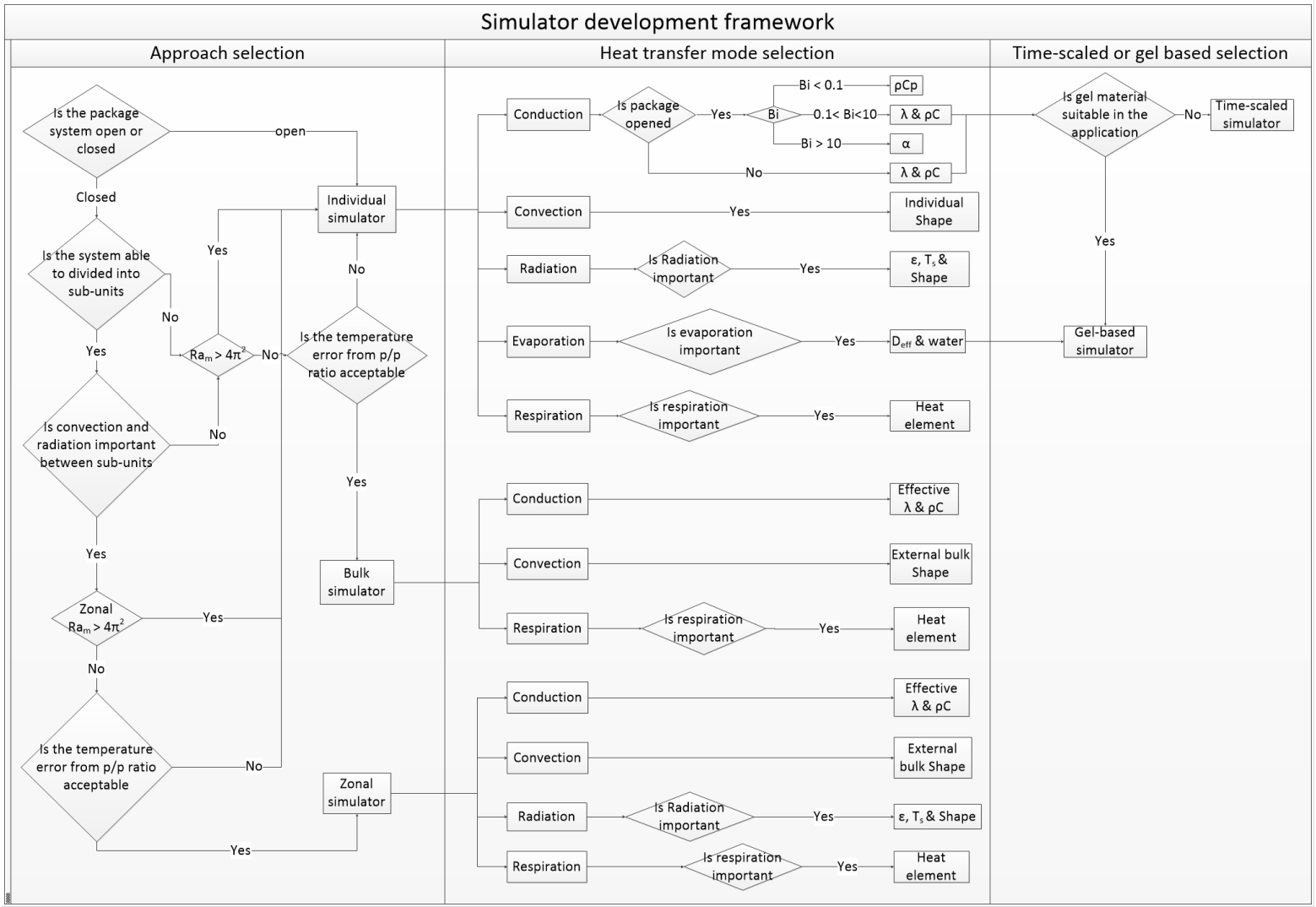

Figure 3-11, Simulator development framework flowchart

3.5 Summary and remarks

Overall, this chapter discussed the heat transfer mechanisms considered in the numerical simulation development into physical simulator development. Each heat transfer mode during cooling was analysed, and the important properties were determined. A systematic flow chart was proposed for using the development framework. Although this framework was constructed for product cooling applications, it is believed that it can be extended to other applications.

This framework will be demonstrated in subsequent chapters by application to different precooling fruit systems, where different approaches to simulator development are appropriate.

It is also important to note that many simulators are generally needed for the optimisation process, such as a box, a pallet, or multiple simulators. Therefore, material selection and the manufacturing process is important to a simulator design, which will be discussed in the following chapter.

Chapter 4. Simulator manufacturing and design

The previous chapter presented a framework for simulator development. As mentioned previously, a large number of simulators are generally required to conduct packaging or precooling operation optimisation experiments. This chapter will discuss the material selection process and potential manufacturing techniques. Simulator prototyping will then be discussed, and an example will be demonstrated.

4.1 Material selection

In the material selection process, the relevant properties for the cooling application simulator are thermal conductivity and volumetric heat capacity, and therefore only these two parameters are the focus of this section. Other essential parameters were discussed in chapter 2 and 3 and can be matched via other methods.

Table 2-1 summarises the required thermal properties for typical precooling applications in horticultural produce for each simulator approach.

Table 4-1, Required thermal conductivity and volumetric heat capacity.

Simulator approach	Thermal conductivity $(W\ m^{-1}K^{-1})$	Volumetric heat capacity $(kJ\ m^{-3}K^{-1})$
Individual	~ 0.5	~ 4125
Bulk/ zonal	~ 0.25	~ 2062
Time scaled individual	~ 0.5	N/A
Time scaled bulk	~0.25	N/A

In order to help material selection, an iterative computational program was developed to enable visual comparison of material properties and for their binary combinations in a systematic way (Figure 4-1). A data list of materials with their thermal conductivity and volumetric heat capacity were used as inputs into the program. Commercial materials (single-phase) are considered first, as simulators are preferred to be made from uniform single-phase materials using various manufacturing methods such as milling, turning, casting, and other methods. If no matched material is found, then multiphase material (combinations) are considered. Iteration of material combinations and the volume fraction of each phase is conducted. The effective volumetric heat capacity (equation 3-14; in chapter 3) and the possible thermal conductivity values are calculated for each combination at each ratio, based on Maxwell-Eucken (Equation 3-13 and Equation 4-2) and the effective medium models (Equation 4-3) (Rahman & Al-Saidi, 2009). The Maxwell-Eucken model represents the combination of materials needed to have a continuous phase (matrix) and a spherical dispersed phase, where the dispersed phase must be well separated so that there is no continuous bridging between spheres. As a result, the manufacturing process needs to fulfil these requirements if the material combinations are found based on the Maxwell-Eucken model. The effective medium model assumes the fillers can be irregular and connect with another dispersed phase material. Likewise, the manufacturing process needs to be matched accordingly. This material selection algorithm can be modified and applied to other properties (if simulators are to be developed for other applications) by substituting the appropriate database and effective properties prediction models.

$$\lambda_{eff} = \lambda_c \left(\frac{1 - 2vp_d}{1 + 2vp_d}\right) \qquad \text{Equation 4-1}$$

Where

$$v = \frac{\lambda_c - \lambda_d}{2\lambda_c + \lambda_d}$$ Equation 4-2

$$\sum_{i=1}^{n} \frac{\lambda_e - \lambda_i}{\lambda_i + 2\lambda_e} = 0$$ Equation 4-3

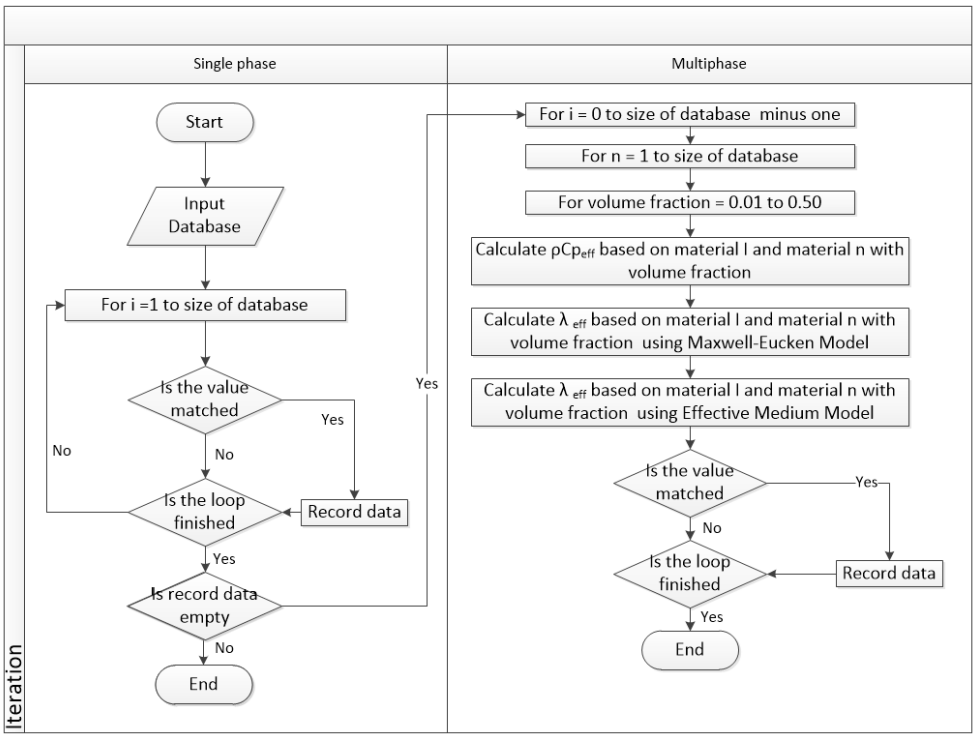

Figure 4-1, The material selection algorithm

Figure 4-2 and Figure 4-3 demonstrates the application of the selection algorithm. The input material (Appendix G) database was developed based on the free source website, MatWeb (2016), which provides commercial materials specifications. However, the provided value needs to be confirmed before being used for design purposes. Each dot in Figure 4-2 represents one material. The colour of the dot represents the material type corresponding to the graph legend. Similarly, each dot in Figure 4-3 represents one material combination, and the colour of the dot represents the material type for the continuous phase material. The cross with the label 'individual' represents the required properties range of an individual simulator for precooling application, where the value is based on typical horticultural products shown in Table 2-3 (in chapter 2). Likewise, the cross labelled 'bulk' represents the possible range of a bulk fruit simulator.

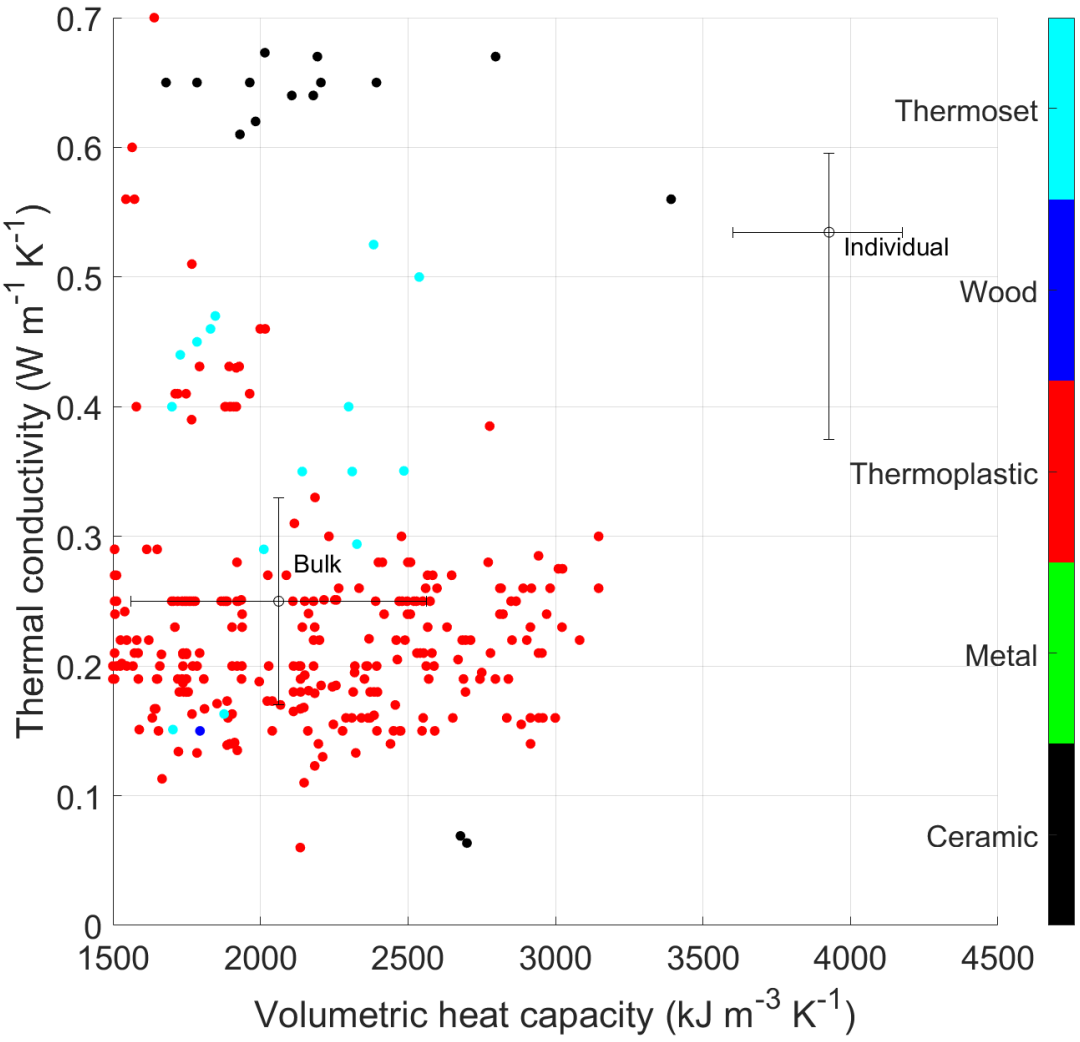

Figure 4-2, Demonstration of the selection of single-phase materials

Overall, no readily available commercial material is suitable for use in the individual simulator, but some materials could possibly be used for bulk simulators (See appendix A). They are mostly thermoplastic polymers. This suggests that injection moulding or casting could be a potential manufacturing method. As discussed in chapter 3, although water-based materials, such as tylose gel, match an individual simulator's thermal properties, gel-based materials are not considered in this project because they are less durable and stable (section 2.3.2.1), and the manufacturing and material costs could be high.

Since no suitable individual materials were found that match the needs of individual simulators, the combination algorithm (multiphase selection) was used. Similarly, each dot in Figure 4-3

represents one combination at a particular iterated volume fraction value with the particular prediction model. The colour represents the material type of the continuous phase.

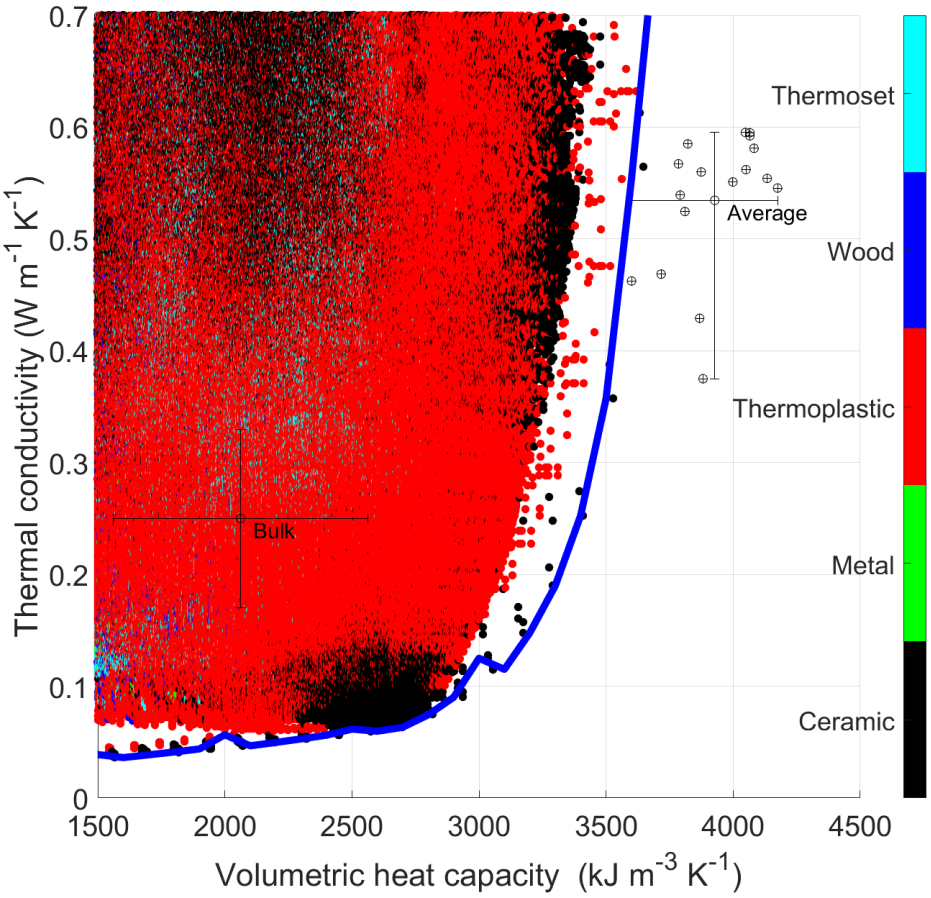

Figure 4-3, Demonstration of the material combination algorithm

One potential combination can be used for the individual simulator, which combines ceramic material with metal, which is vermiculite combined with 40% (vol) tungsten carbide (Goodfellow, UK). With the Maxwell-Eucken models dispersed structure, the combination could potentially have a thermal conductivity of 0.56 $W\ m^{-1}\ K^{-1}$ and volumetric heat capacity of 3646 $kJ\ m^{-3}\ K^{-1}$. These values are reasonably close to the thermal properties of strawberries(0.46 $W\ m^{-1}\ K^{-1}$; 3600 $kJ\ m^{-3}\ K^{-1}$) and banana (0.43 $W\ m^{-1}\ K^{-1}$ and 3716 $kJ\ m^{-3}\ K^{-1}$). The thermal properties of relevant produce were summarised previously in Table 2-3. Although this combination could be a potential material for the produce simulator, the effective properties still do not match kiwifruit and grapes, which are the targeted produce in this project. Also, both materials are generally in particle form, which means the potential manufacturing process is sintering, and the project does not have the capability of sintering manufacture. There are approximately 1.8 million potential

combinations across different materials, combined ratio and combination structures (different models, Maxwell-Eucken and effective medium models). As shown in Figure 4-3, most of the combinations use thermoplastic or thermoset materials as a continuous phase. This extensive list of combinations has not been screened for bulk simulators, as the list is too large and potential single-phase materials have already been identified in Figure 4-2.

The blue line in Figure 4-3 indicates a boundary where thermal property combinations become limited. Within the 5 million combinations, only a few combinations lie outside this line. In general, a material's thermal conductivity is positively proportional to the material's heat capacity at the atomic scale (Kittel, 2005), which means a low thermal conductivity material generally has a low specific heat capacity. Water is an unusual material, having relatively low thermal conductivity but unusually high heat capacity due to hydrogen bonding. Most food products, especially horticultural products, have high water content, which inherit the low thermal conductivity and high volumetric heat capacity properties. Finding a non-water-based material that matches these properties is very difficult.

4.2 Prototyping

Although some potential material combinations are suitable for the simulators, the time scaled approach was taken for precooling applications. For the time scaled approach, the material selection is much simpler as just the thermal conductivity needs to be matched. The main purpose of this work was to demonstrate the applicability of the simulator development framework. Utilising the time scaled approach could a) validate the time scaled approach hypothesis and b) reduce research time for material selection. If the simulator concept is validated on a time scaled approach, the concept should also be valid for a non-time scaled approach. Also, the material combination algorithm suggests that a thermoset polymer with an appropriate filler can achieve the desired thermal conductivity value. This also means casting manufacturing techniques can be used. Compared to 3D printing, injection moulding and machining, casting was the easiest and most cost-effective approach available for this project (due to the setup and the readily available resources). 3D printing is generally slow and unstable, and the ability to control material composites is limited. Injection moulding has a high initial cost for die design and is more suitable for high volume production. Also, injection moulding a sizeable solid material would likely result in shrinking issues (more than 3% shrinkage) due to density variation with temperature and

distortion of the product's shape (Jansen, Van Dijk, & Husselman, 1998). These potential shrinkage issues would have resulted in additional investigation and study and would distract from the primary goals of the research.

For these reasons a thermoset polyester resin (Norski, New Zealand) was used with appropriate fillers to create a composite material. Aluminium powder (STM Pro, New Zealand) and Q-cell (West system 409 Microsphere Blend, West System, USA; a pure white, hollow glass bubble-based, low density filler) were used as fillers to modify the composite material's effective thermal conductivity. Datasheets for these materials are found in Appendix F.

4.2.1 Casting

Casting was used for prototyping in this research. Casting is a simple and effective approach. Using Thermoset polymers as a continuous phase allows other materials such as aluminium powder or Q-cell to be dispersed before curing. By casting, the shape can be defined in one process rather than forming a multiphase block and machining to create the appropriate shape.

As shown in Figure 4-4, resin, reaction catalyst and filler are added into a container and mixed thoroughly. This mixture is then poured into a mould to solidify. During the mixing, aeration is minimised to avoid air pockets into the final product. Tests were made using degassing (by vacuum) and pressurising the casting to reduce further the presence of air/gas pockets that would alter the thermophysical properties of the composite material. Degassing involves putting the casting into a vacuum chamber where air pockets are drawn out. Pressurisation involves compressing any entrapped air pockets so as to minimise their volume. Both tests showed no significant improvement on the final product in terms of product density.

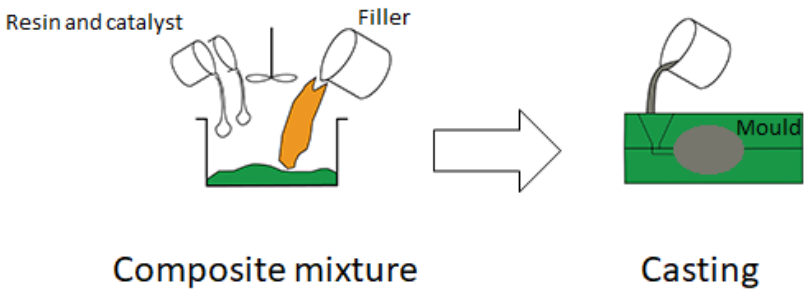

Figure 4-4, Casting process, adapted from Gunther and Mogele (2016)

4.2.1.1 Moulds

Several material and mould making techniques were tested, as listed below:

- Silicon rubber (Mold Start 15 SLOW, USA), by natural solidification process (Figure 4-5)
- PLA(UP ila, China) by 3D extrusion printing
- MDF (Lakepine MP E0, New Zealand) by CNC machining
- Rigid polyurethane foam (Formathane, New Zealand) by CNC machining
- Nylon (Precimid 1170, China) by 3D printing by selective laser sintering (SLS)

The silicon rubber mould involved first making the positive shape of the final product, which can be the existing object. In the case of making a kiwifruit simulator (see chapter 5), real kiwifruit was used as the positive object to shape the silicon rubber mould. 3D printing or other manufacturing methods can also be used to make the positive object possible. 3D printing and CNC machining approaches involve building material up or reducing material from a block based on a CAD model. This CAD model can be created from a 3D scans of the product. In the case of the table grape simulator (see chapter 6), packages of table grapes were CT scanned, and the scanned image was analysed to produce a CAD model.

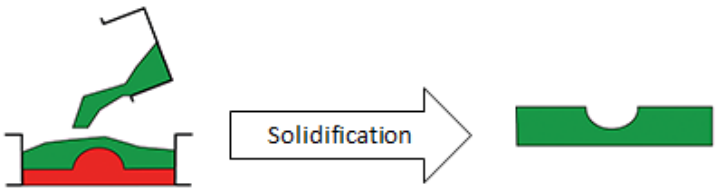

Figure 4-5, Conventional silicon rubber mould making, adapted from Gunther and Mogele (2016)

The material used for making the mould affects the difficulty in separating the solidified product from the mould (demoulding). Table 4-2 summarises the observations for the tested materials. Rubber silicon moulds took approximately 20 hours to cure fully, but products cast from this material can be demoulded easily, and the durability of the mould for repeated casting is relatively long (over 20 casts without significant deterioration). Nylon and PLA can be used for moulds if layers of paint are applied on the mould to act as release agents to ease demoulding; however, the mould's durability is relatively low. The mould making time varied depending on the complexity of

the mould and the size. Rigid polyurethane foam and MDF as mould materials resulted in poor demoulding and low durability. However, these two materials are relatively cheap, and the lead time for making these types of moulds was short. Therefore, these two materials can be considered if a one-off mould is needed.

Table 4-2, Summary of mould material and the demoulding ability

Material	Making time (hours)	Demoulding	Durability
Silicon rubber	~ 12 (curing)	Good	Ok
PLA	7 – 24 (3D printing)	Ok	Poor
MDF	0.5 – 4 (CNC machining)	Poor	Poor
Rigid polyurethane	0.5 – 4 (CNC machining)	Poor	Poor
Nylon	4-24 (SLS)	Ok	Ok

4.2.1.2 Shape

In order to capture the shape of the product, a few methods can be used. Direct copying is where the silicon rubber mixture is poured on the targeted product, and as the liquid silicon rubber solidifies the product shape, is captured. However, this method is not suitable to capture the bulk shape of a product as it also captures the voids within bulk objects. In this case, a more sophisticated method, such as 3D laser scanning or computerised tomography scanning, is needed. The shape data need to be post-processed to extract the bulk shape (more details are given in chapter 6).

4.2.2 Thermal properties measurement

As mentioned previously, the thermal conductivity and volumetric heat capacity are important for material selection. Volumetric heat capacity consists of specific heat capacity and density. Therefore, these three thermo/physical properties of the selected material were evaluated.

4.2.2.1 Thermal conductivity

An in-house made dynamic needle thermal conductivity probe was used after being calibrated with glycerine (see appendix C). The diameter of the probe was 0.8 mm, and 35 mm long (diameter to length ratio greater than 25). This needle-like probe mimics an infinite liner heat

source of zero mass, both generating heat and recording the transient heat transfer away from the material (the needle temperature). By knowing the heat input per unit length, q', ($W\ m^{-1}$) and the recorded temperature profile, the thermal conductivity of the material can be evaluated using Equation 4-4 (Ahmed & Rahman, 2009a). B is the intercept of the linearised temperature change profile (T vs. $\ln(t)$), and the slope of the profile is mathematically equal to $\frac{q'}{4\pi\lambda}$.

$$T(t) = B + \frac{q'}{4\pi\lambda}\ln(t) \qquad \text{Equation 4-4}$$

4.2.2.2 Specific heat capacity

A differential scanning calorimetry (DSC; Q2000, TA Instruments, USA) was used to obtain the materials' specific heat capacity. This method records the thermogram of heat flow (to the samples) vs sample temperature (or heating time) to achieve a linear heating rate. This recorded thermogram is compared to a known standard (generally sapphire) to evaluate the samples' specific heat capacity. In the measurement, sealed aluminium pans (Tzero, TA Instruments, USA) were used to contain the samples and sapphire was used as a standard for the calculation. The sample size was approximately 20 mg, which was sufficiently large and provided good contact with the bottom of the aluminium pan. The ramping rate was set at 2 $K\ min^{-1}$ (unless specifically mentioned) from -10 °C to 35 °C. The specific heat capacity value was evaluated from 0 °C to 30 °C, which is relevant for this project.

4.2.2.3 Density

Three methods were used to measure three different materials (mentioned below) depending on the shape of the material and the density of the materials.

Archimedes' method was used to measure the solidified polyester samples as illustrated in Figure 4-6, where the object is submerged in water, and the required force to suspend the object was measured. Based on Archimedes' principle, the volume of the object can be evaluated as Equation 4-5, where m_{H_2O} is the weight of the object submerged in water (at room temperature; 20 °C) and m_{air} is the weight of the object submerged in air. Once the object's volume is known, the object's density can be evaluated.

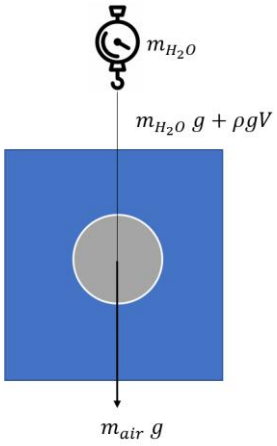

Figure 4-6, Illustration of Archimedes' method of volume measurement

$$V = \frac{m_{H_2O} - m_{air}}{\rho_{H_2O}} \qquad \text{Equation 4-5}$$

$$\rho = \frac{m}{V} \qquad \text{Equation 4-6}$$

The volume displacement method was used for measuring the density of the aluminium powder. A 10 mL measuring cylinder with a known amount of water (or other low-density fluid) were used. By adding the known weight of the powder sample into this semi-filled measuring cylinder, the incremental changein volume was recorded. As the weight of the added power is known, and the increased volume is the sample volume, the density can be evaluated.

A gas pycnometer (AccuPyc II 1340 Pycnometer, Micromeritics Instrument Corporation, USA) was used to measure the Q-cell powder's density. Based on the ideal gas law, the sample volume inside the expandable container can be evaluated based on the container's internal pressures and volume (at a fixed quantity of gas and consistent temperature). In the measurement, helium gas was used as the inert gas. A 1 cm^3 chamber size was used as the testing chamber. The initial equilibrium pressure was set at 134.4 kPa, and the equilibration rate was set at 3.5 Pa per minute. Although the Q-cell powder is a capsule of air, the crushing strength of the material is strong enough to sustain the applied pressured (Crushing strength above 10 bars See appendix F). The sample was purged by the helium gas ten times before the actual evaluation was conducted.

4.2.3 Polyester

The polyester (Norski, New Zealand) consists of two parts, the resin and the catalyst. When the catalyst is added to the resin, an exothermic reaction starts, and the resin will start solidification (curing). Depending on the curing environment, different quantities of catalysts should be added (see appendix E).

Table 4-3, Thermal properties of Norski polyester

Properties	Literature value	Manufacturing value 3	Measured value
Thermal conductivity ($W\ m^{-1}\ K^{-1}$)	0.19 1	N/A	0.157 ± 0.016 (n=6)
Specific Heat capacity ($kJ\ kg^{-1}\ K^{-1}$)	0.79 2	N/A	1.26± 0.01 (n=1)
Density ($kg\ m^{-3}$)	1100 2	1000	1194±9 (n=5)

Note : superscript 1 = Tang et al. (2012) 2 = Cecen et al. (2009) 3 = Norski Holdings Ltd.

Table 4-3 shows the literature value, manufacturing specification and the measured value of the Norski polyester. The measurements were conducted on samples cast into 50 mL Falcon tubes. For the thermal conductivity measurement, a guiding hole was created by inserting a 14-gauge needle (approximately 2 mm) in the centre of the casting object during the curing stage and extracted after the object solidified. This hole was filled with thermal paste to increase the contact between the thermal conductivity probe and the material. A small cut-off from one of the samples (4.428 g) was used for the DSC method's heat capacity analysis. The measurement range is the measured Cp value from 0 to 20°C (as experiments generally run within this temperature range). The density of the measured samples was evaluated by using Archimedes' method. All the measurements were conducted 72 hours after the curing to ensure the complete chemical reaction. Overall, the material's thermal conductivity agrees with measured value and literature, but not the specific heat capacity. This could be due to the different resin formula of the polyester, but the measured value seems reliable, as it is consistent with the composite material (see section 4.2.6) heat capacity prediction. It is noticed that both the literature and measured values were greater than

the manufacturing value, which suggests during simulator development, the validation of materials' data is necessary.

4.2.4 Aluminium powder

Aluminium powder (STM Pro, New Zealand) was selected as one of the fillers used to manipulate density and thermal conductivity. The powder has an average particle size of 45 µm (sieve 0 -2% 200 mesh and balance 325 mesh).

Table 4-4 shows the literature, manufacturer, and measured values of the aluminium powder. The thermal conductivity is not measurable as powder form, and it is also not given from the manufacturing specification. The heat capacity was measured using the DSC method described above, with 28.763 grams of sample added to the pan. The measured heat capacity was lower than the literature value, which could be to do with the purity of the powder. Nevertheless, the measured and literature values are within the same magnitude, and as long as the thermal properties of the final composite material are measured, this slight disagreement can be tolerated. The density of material has a good agreement across the measured literature and manufacturing values.

Table 4-4, Thermal properties of Aluminium Powder

Properties	Literature value	Manufacturing value [4]	Measured value
Thermal conductivity ($W\ m^{-1}\ K^{-1}$)	224-247 [1]	N/A	N/A
Specific Heat capacity ($kJ\ kg^{-1}\ K^{-1}$)	0.876 -0.899 [2]	N/A	0.78± 0.01
Density ($kg\ m^{-3}$)	2700 [3]	2700	2700±6 (n=5)

note: superscript 1 = Hust and Lankford (1984), 2 = Downie and Martin (1980), 3 = Pinto and Jiménez-Martín (2001), 4= STM Pro.

Scanning electron microscopy (SEM) was conducted on the aluminium powder to understand the shape and size of the powder. Figure 4-7 shows the SEM image of the powder. The shape of the aluminium powder is irregular, and the size of the particles agrees with the manufacturer's specification (45 µm).

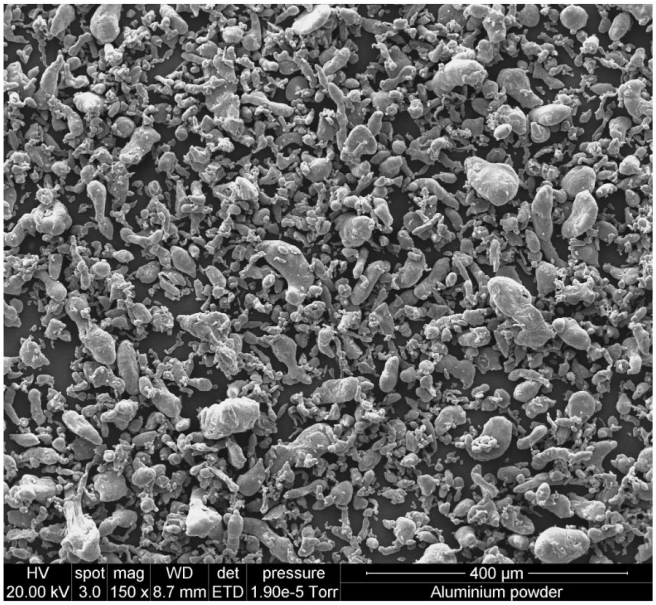

Figure 4-7, SEM image of Aluminium powder

4.2.5 Microsphere (Q-cell)

Microsphere (409 Microsphere blend, West system, USA), Q-cell, was used as one of the fillers to manipulate the density of the final composite. Table 4-5 shows the data of Q-cell. Unfortunately, there are no available thermal property data available from literature or manufacturers for this

product. It is a small spherical membrane entrapping gas. It is manufactured for use in fibreglass to occupy volume with minimal impact on weight. The heat capacity was measured using the DSC method described above with 1.456 milligrams of Q-cell added to the pan. The density was measured using a pycnometer (AccuPyc II 1340 Pycnometer, USA) using 120 milligrams of sample.

Table 4-5, Thermal properties of Q-cell

Properties	Literature value	Manufacturing value	Measured value
Thermal conductivity ($W\ m^{-1}\ K^{-1}$)	N/A	N/A	N/A
Specific Heat capacity ($kJ\ kg^{-1}\ K^{-1}$)	N/A	N/A	1.81± 0.16
Density ($kg\ m^{-3}$)	N/A	160-540	218.9 (n=5)

SEM scanning was conducted to observe the shape and size of the powder (Figure 4-8). The powder particle is perfectly spherical in the SEM image. The diameter of the Q-cell particles can be determined using MATLAB image analysis (see appendix I), and the average diameter was 61.5 µm.

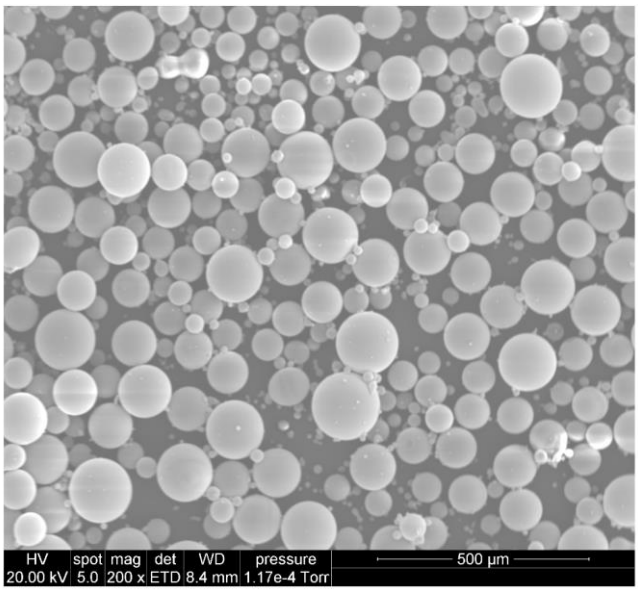

Figure 4-8, SEM image of Q-cell

4.2.6 Composites

Two types of composites were made for the project, a polyester-aluminium composite and a polyester-Q-cell composite. As the thermal conductivity, density and heat capacity are essential to the simulator, it is crucial to understand the effect of the filler volume fraction on the resulting effective properties.

For the polyester-aluminium composite, a set of three replicate samples were cast at volume fractions of 0%, 4.3%, 8.3%, 12.0% and 15.3% (0 to 40% mass fraction at increments of 10%, respectively). For the polyester-Q-cell composite a wide range of volume fractions (27 samples over the range 0 to 52%) were created. This is because the thermal properties of the Q-cell powder were not well-known. Testing more volume fractions of Q-cell in the composite could better understand the powder properties and casting behaviour. For both composite, filler, catalyst and resin were added at once, and then a mixer was used to rigorously mix the liquid component.

4.2.6.1 Thermal conductivity

The thermal conductivity was measured as described in section 4.2.3. The results are summarised in Figure 4-9. Each sample was measured three times using the thermal conductivity probe. In total nine thermal conductivity measurements were taken at each volume fraction point, except at 12% samples where only two cast samples were measured, as one of the samples was broken during the casting stage. The thermal conductivity data point at the volume fraction 24% were obtained differently, where six samples were cast, and each sample's thermal conductivity was measured (one time). This data point was the additional data point suggested by the Maxwell-Eucken model that matched the individual kiwifruit simulator's need (see chapter 5).

. As expected, the effective thermal conductivity of the composite material increases with increasing volume fraction of aluminium powder. At the same time, there was a steady decrease with increasing volume fraction of Q-cell. Some variance was observed between replicates. This is likely to be due to variances in the spatial distribution of the particles, and there is an increased chance of particle agglomeration with increased particle concentration.

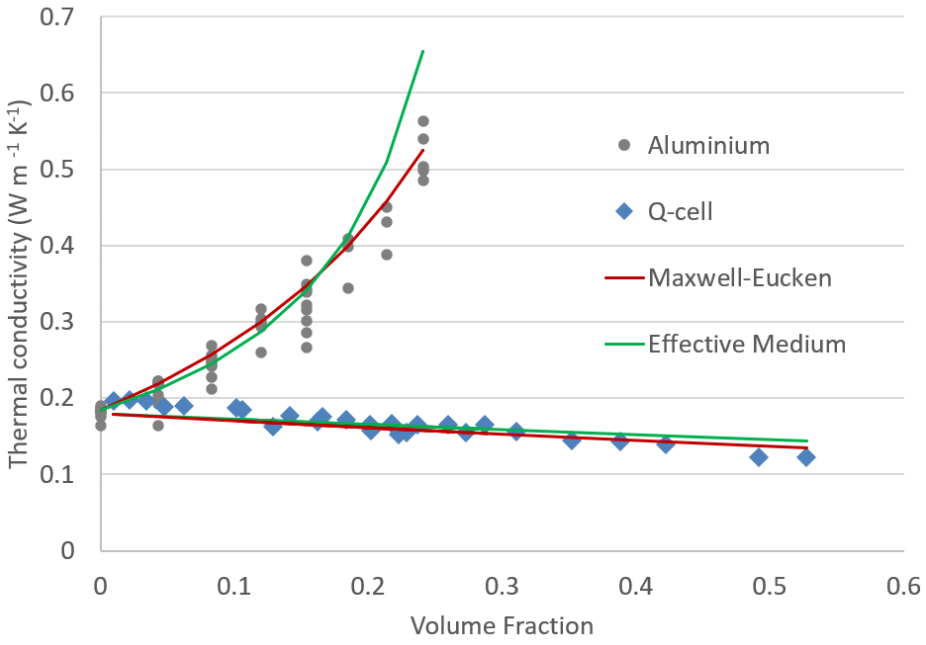

Figure 4-9, The effect of fillers volume fraction on composite effective thermal conductivity

The Maxwell-Eucken and Effective Medium Theory model predictions are both shown in Figure 4-9 for both types of composite. The Maxwell-Eucken model shows a better prediction of the effective thermal conductivity with the increasing particle volume fraction for the polyester-aluminium composite than the effective medium model, particularly at volume fractions above 0.2. This suggests good dispersion of the particles within the continuous resin phase was achieved during casting. Both models provide equally acceptable predictions for polyester Q-cell composites.

The thermal conductivity of Q-cell is unknown, and therefore it was back-calculated using Maxwell-Eucken and Effective Medium models. The estimated Q-cell thermal conductivity was 0.115 $W\ m^{-1}\ K^{-1}$ based on the Maxwell-Eucken model and 0.096 $W\ m^{-1}\ K^{-1}$ based on the Effective Medium model. These two values are relatively close. As Q-cell contains mostly air (0.025 $W\ m^{-1}\ K^{-1}$), these two calculated values are within expectations.

An individual time scaled simulator requires thermal conductivity of ~ 0.5 $W\ m^{-1}\ K^{-1}$, which can be achieved by having a polyester-aluminium composite at 24% filler volume fraction according to Figure 4-9. Samples of 24% polyester-aluminium composite were made using the Falcon tube method (as mentioned above), and a piece of the cut-off was observed under the SEM using backscattering with 20 kV accelerating voltage. Figure 4-10 a) shows the aluminium powder distribution at 100 µm, 500 µm and 1 mm scale. The white regions represent aluminium powder,

as it is a greater electron density than polyester. The dark background represents polyester. Overall, the image shows a uniform distribution of the filler, indicating the homogeneity of thermal properties. Also, the aluminium powder is not connected with nearby particles, which confirms the validity of the Maxwell-Eucken model for the prediction.

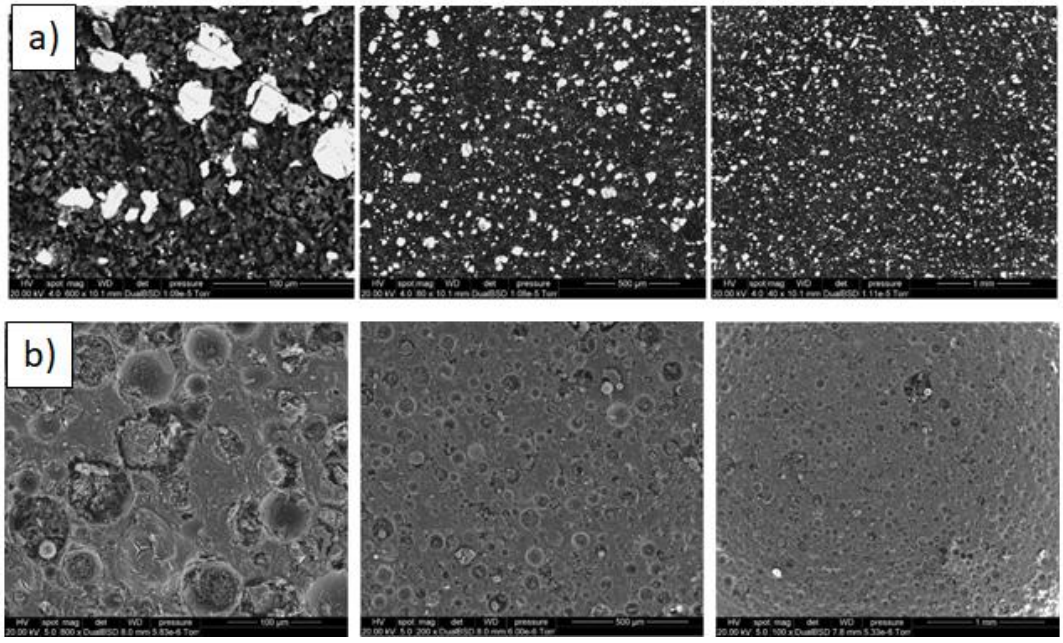

Figure 4-10, SEM picture of a) Polyester-Aluminium and b) Polyester-Q-cell composite under 100, 500 and 1000 µm scale

For a typical time scaled bulk simulator (~ 0.25 $W\ m^{-1}\ K^{-1}$), 12% (aluminium to polyester) composite would be suitable. However, the thermal conductivity of a bulk simulator could be as low as 0.14 W/m.K (such as table grape bulk simulator, see chapter 6). In this case, 52% (vol) polyester-Q-cell composite would be appropriate. Cast samples of 52% (vol) polyester-Q-cell composite were made and tested, where the measured thermal conductivity was 0.17± 0.01 W/m.K, which is slightly different from the targeted value. Given the Q-cell volume fraction is relatively high, thermal conductivity prediction models could be less sensitive in this region; slight variations from prediction could be expected. A sample of the composite was also observed under SEM. Figure 4-10 b) shows the sample at 100 µm, 500 µm and 1 mm scales. The slightly darker circular regions represent the Q-cell powder, and the light-dark background represents the polyester. Overall, the image shows a uniform distribution of the filler, indicating the homogeneity of thermal properties. Also, some Q-cell powder particles have a degree of connection with nearby particles, suggesting the Maxwell-Eucken model might be less adequate as the Q-cell ratio

increases. Nevertheless, both the Maxwell-Eucken model and Effective medium models provided reasonable predictions.

4.2.6.2 Density

The polyester-aluminium and polyester-Q-cell composite samples were also used to develop the relationship between filler volume fraction and the effective density. The sample densities were measured using the Archimedes' method as mentioned above. Equation 3-5 was used to predict each samples' effective density, where ρ is the corresponding density and pd is the volume fraction of the dispersed phase (fillers). Overall, the measurement data (scatter plot points) shows a significant agreement with the predicted values (dotted lines; R^2 close to 1).

$$\rho_{eff} = \rho_1 \times pd + \rho_2 \times (1 - pd) \qquad \text{Equation 4-7}$$

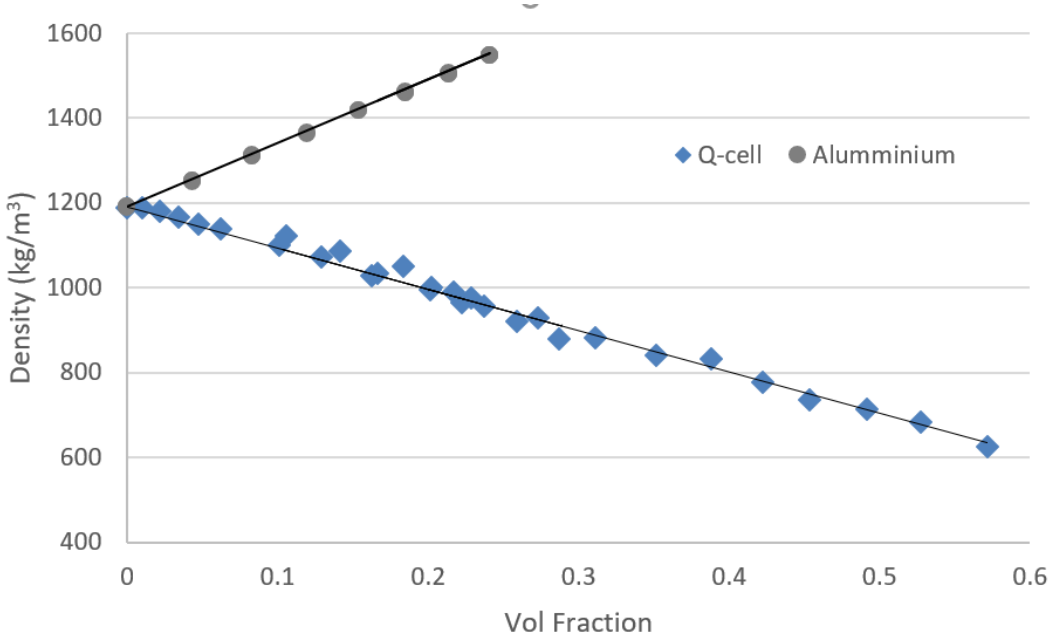

Figure 4-11, The effect of filler volume fraction on the composite's effective density

4.2.6.3 Heat capacity

Table 4-6 shows the measured and estimated heat capacity values of 24% Polyester-Aluminium and 52% Polyester Q-cell composites. The Polyester-Aluminium composite shows good agreement between measured and estimated values, whereas the estimated Polyester-Q-cell heat capacity is lower than the measured value. This slight disagreement might be due to the weight measurement tolerance of the Q-cell. Q-cell is a fine and light particle and is very difficult to

handle. Therefore, this measurement error could be carried over to the heat capacity value. However, this slight mismatch is acceptable in practice. For the time scaled simulator approach, as long as the value used in the calculation is consistent, this slight difference will be easily accounted for.

Table 4-6, Comparison of the measured and estimated heat capacity values

Material	Mass fraction	Measured Cp $(kJ\ kg^{-1}\ K^{-1})$	Estimated Cp $(kJ\ kg^{-1}\ K^{-1})$
Polyester-Aluminium (24%	41%	1.05±0.02	1.06±0.02
Polyester-Q-cell (52% vol)	16%	1.63±0.07	1.35±0.12

4.3 Summary and remarks

Overall, this chapter proposed a systematic process for material selection and developed methods for prototype development. The potential materials for the simulators and the relevant thermal properties of the materials have been discussed. These methods were used for the experimental work, and the examples are presented in the following chapters. It is believed that this systematic process and the overall simulator development framework is not limited to the cooling application simulators but can be extended to other applications if the appropriate physical properties are considered similarly.

Chapter 5. Design of individual simulators

Previous chapters have proposed a framework for simulator development. This chapter implements this framework to develop individual simulators for closed packaged kiwifruit and open packaged apples to demonstrate feasibility. As discussed in section 4.1, materials (other than water-based) are not available that have the properties to match individual fruit such as kiwifruit or apples completely. Therefore, the time scaled approach will be used.

5.1 Theory of time scaled approach

Redding et al. (2016) used a one-dimensional analytical model to demonstrate the linear relationship between the volumetric specific heat capacity and the cooling rate, proposing the concept of chilling time scaling. This concept can be generalised. As mentioned, the temperature profile of a given product can be predicted based on the Fourier Equation (Equation 5-1) with appropriate boundary conditions. Theoretically, the volumetric specific heat capacity, ρc, should have a linear relationship with the rate of temperature change, $\partial T/\partial t$, if the boundary conditions and all other properties remain consistent. Therefore, the required chilling time for a given temperature change should be time scalable based on the volumetric specific heat capacity (Equation 5-2).

$$\frac{\partial T}{\partial t} = \frac{\lambda_p}{\rho c}\nabla^2 T \qquad \text{Equation 5-1}$$

$$\frac{t_{simulator}}{t_{real}} = \frac{(\rho c)_{simulator}}{(\rho c)_{real}} \qquad \text{Equation 5-2}$$

For the third type of boundary condition (convection dominant; Equation 5-3), a constant value of Bi and temperature gradient $(T_{amb} - T_s)$ means unchanged boundary heat flux $(\lambda_p \nabla T)$. The mathematical proof of constant temperature gradient will not be demonstrated here, but this was shown by Redding et al. (2016) using an analytical model. Achieving a constant Bi number requires matching the thermal conductivity, the heat transfer coefficient and the shape of the simulator. This means a simulator that matches the thermal conductivity and shape could be used as a time scaled simulator, as the main factors affecting heat transfer coefficient (airflow distribution) would also be matched.

$$\nabla T = -\frac{hA}{\lambda}(T_{amb} - T_s) = -\frac{hL}{\lambda} \times l\,(T_{amb} - T_s) = -Bi \times l\,(T_{amb} - T_s) \qquad \text{Equation 5-3}$$

In reality, products are packed inside packages, which result in complex boundary conditions (e.g., Equation 2-9). As a result, it is mathematically challenging to justify the feasibility of the time scale approach, and therefore experimental validation is needed.

$$-\lambda \nabla T_s = \varepsilon(G - \sigma T_s^4) + n\lambda_a \nabla T + H_{vap} D \nabla C \qquad \text{Equation 2-9}$$

5.2 Closed package system application - Kiwifruit simulator

Kiwifruit are generally packed as a closed system. A standard modular bulk (MB) package of kiwifruit was used in this case study. As shown in Figure 5-1, the MB package consists of a corrugated fireboard box (0.3x0.4x0.2 m; WLH), a polyliner (10 µm thick; HDPE; folded) and 100 kiwifruit (count size 36, class A kiwifruit) randomly filled.

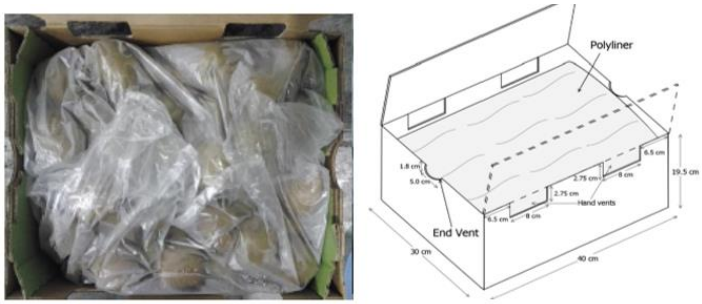

Figure 5-1, Modular bulk kiwifruit package (O'Sullivan et al., 2016a)

The thermal conductivity, specific heat capacity and density of kiwifruit were measured (Table 5-1) using the methods mentioned in Chapter 4 (thermal conductivity probe for thermal conductivity, DSC for specific heat capacity and Archimedes' method for density). The reported range for the kiwifruit specific heat capacity was measured from 0 to 20 °C, which is the typical precooling temperature range. This measured value aligns with the literature values (O'Sullivan, 2016).

Table 5-1, Thermal properties of kiwifruit

Properties	Kiwifruit
Thermal conductivity ($W\ m^{-1}K^{-1}$)	0.52±0.04 (n=26)
Specific heat capacity ($J\ kg^{-1}\ K^{-1}$)	3710±140 (n=1)
Density ($kg\ m^{-3}$)	1032±4 (n=24)

5.2.1 Simulator design and manufacture

Figure 5-2 demonstrates the utilisation of the simulator development framework, where the decision path is highlighted in green. The MB package is a closed package system, and the calculated Raleigh number (Ra_m) is greater than $4\pi^2$ (see Appendix H). This Ra_m consistent with the finding of O'Sullivan et al. (2016a), who also found that natural convection is an important heat transfer mechanism inside the modular bulk kiwifruit package. As a result of these factors, an individual simulator approach should be used.

Based on the studies of O'Sullivan (2016), only internal conduction and convection are essential. Also, based on the theoretical calculation in chapter 3, it is believed that radiation and evaporation are insignificant heat transfer pathways inside this closed package system. Therefore, the relevant properties are the shape, thermal conductivity, and volumetric heat capacity of the targeted product, kiwifruit. As discussed in chapter 4, no readily available material or material combination could be found that can match both the thermal conductivity and volumetric heat capacity. Also, water-based materials such as gel materials are not suitable for this application, as the quantity needed is large (to enable box or pallet-scale experiments), and the simulator is expected to be stable and long-lasting. As a result, the time scaled approach will be used here. Using the time scaled approach also provides an opportunity to validate the time scaled concept and reduces the complexity of prototyping. As a result of the time scaled approach, only thermal conductivity and shape will be matched.

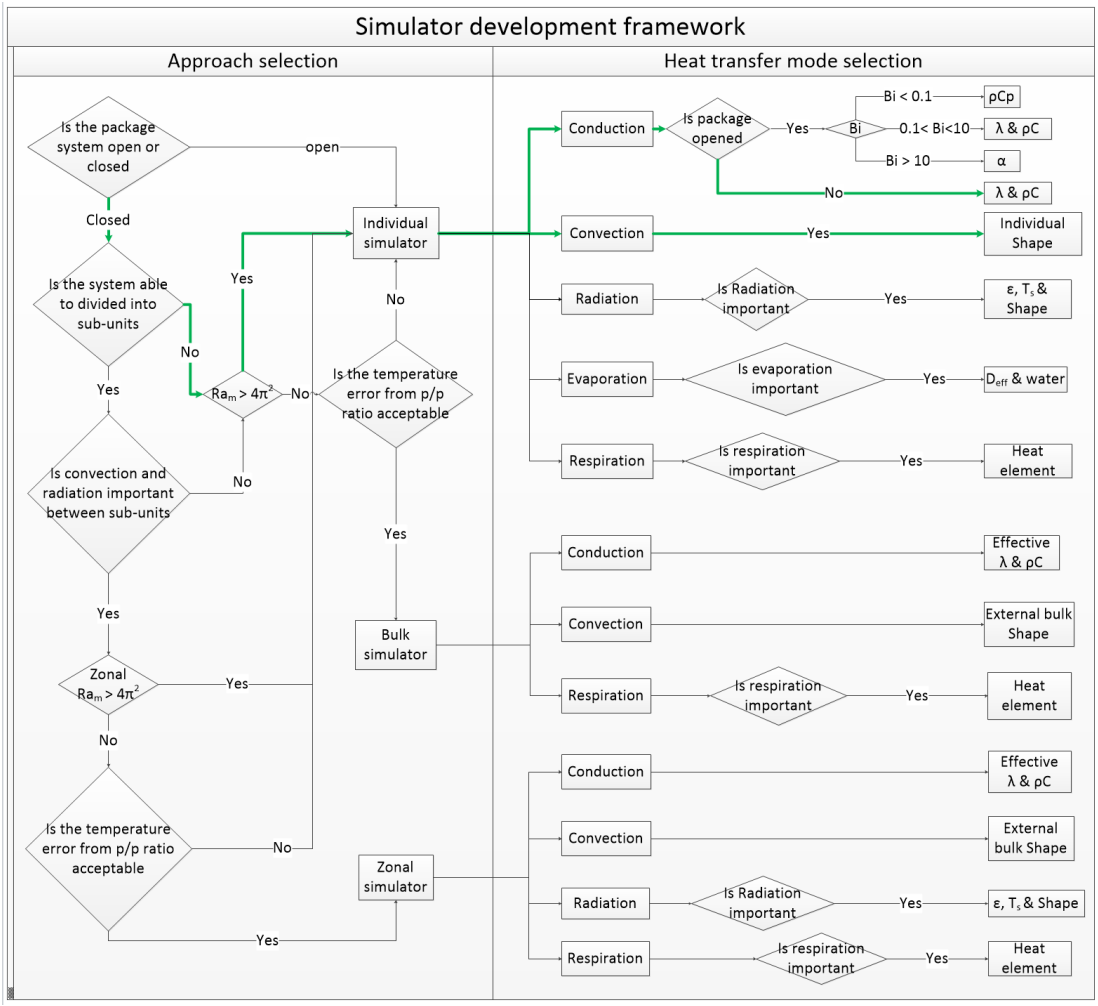

Figure 5-2, Kiwifruit simulator decision tree

Rapid prototype simulators (see Figure 5-3) were made based on the material selection framework and prototyping framework mentioned in chapter 4. Figure 4-9 suggested that 24% of aluminium-polyester composite would match the required thermal conductivity. Therefore, casting was selected as the manufacturing method using the polyester/aluminium composition. Ten moulds were made for the casting, where ten count size 36, class A kiwifruit were used, as master specimens (Mould Star 15, Smooth-On, USA; for details of the ten kiwifruit see appendix I). The detail of mould making was described in section 4.2.1. The average length, width and thickness of these ten master specimens were 61.7±2.1, 51.8±0.5, and 48.3±0.8 mm, respectively. A size 36 modular bulk package kiwifruit contains 100 kiwifruit, which means the package contains ten variants of kiwifruit shape, and each variant has ten kiwifruit simulators.

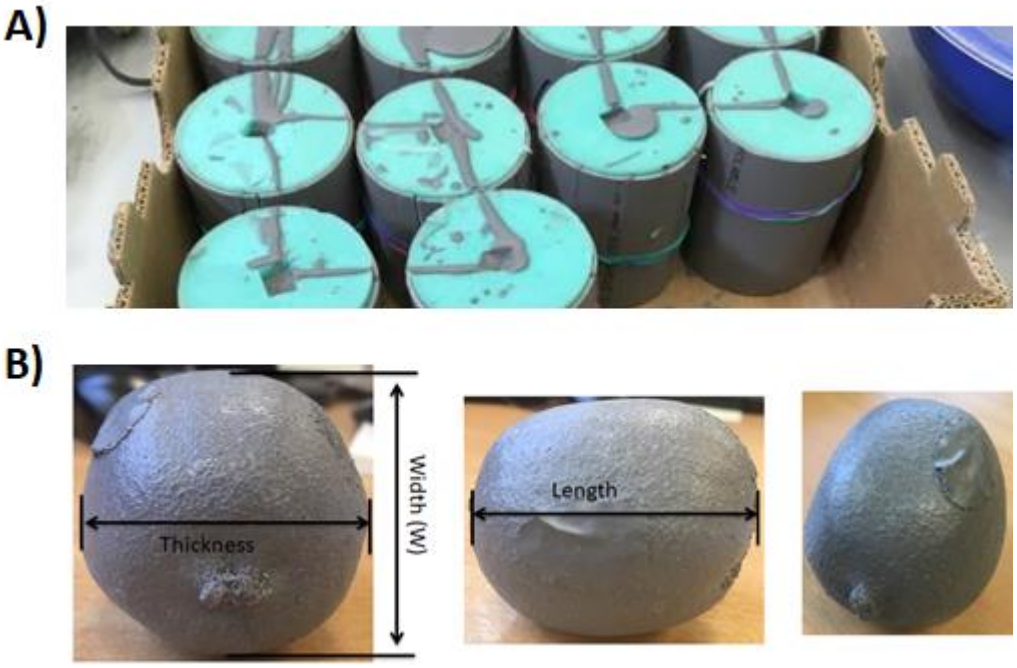

Figure 5-3, a) Simulator manufacturing process and b) Pictures of an example kiwifruit simulator

Table 5-2 shows the comparison of kiwifruit and kiwifruit simulator thermal properties, where the same measurement methods were used as described in chapter 4. Overall, the measured values agree with the expected values within uncertainty limits. Based on the values (Table 5-2), it is expected that the simulator should cool 2.46 ± 0.17 times faster (time scale factor; TSF) than real kiwifruit (Equation 5-2).

Table 5-2, Thermal properties of kiwifruit and kiwifruit simulator

Properties	Kiwifruit	Simulator
Thermal conductivity ($W\ m^{-1}K^{-1}$)	0.52±0.04 (n=26)	0.48±0.02 (n=12)
Heat capacity ($J\ kg^{-1}\ K^{-1}$)	3710±140 (n=1)	1050±20 (n=2)
Density ($kg\ m^{-3}$)	1066±3 (n=9)	1537±16 (n=64)

5.2.2 Individual scale validation

To validate the time scale approach, a fruit cooling experiment was conducted. Two kiwifruit simulators and five kiwifruit (of the same count size and dimensions) were placed on a mesh inside a wind tunnel (Figure 5-4) in a temperature-controlled room. The centre temperatures of the products were measured using thermocouples (type T, 3mm diameter). To place the

thermocouples to the centre of the simulator, a 3.5 mm guide hole was made. The depth of the hole is half of the simulator length (length refer to Figure 5-3 b; middle picture), and the hole was positioned as close to the centre of the simulator bottom as possible. Thermal paste was used to ensure good contact between the thermocouples and the material. Likewise, a guide hole was created on the kiwifruit for thermocouples instrumentation. The thermocouples were connected to a temperature logger (S2020, Grant, UK), and data were recorded every minute until the end of the experiment. The ambient temperature was set at 0 °C, and the initial temperature of the product was approximately 20 °C. The superficial air velocity was measured to be 4.31 ± 0.45 $m\ s^{-1}$ using an anemometer (TSI 9545 VelociCalc, USA), which is an average value of five measurement points evenly spaced across the wind tunnel. Although the product in this system was not packed in a closed package system, this experiment was a preliminary experiment to validate the feasibility of the time scale approach.

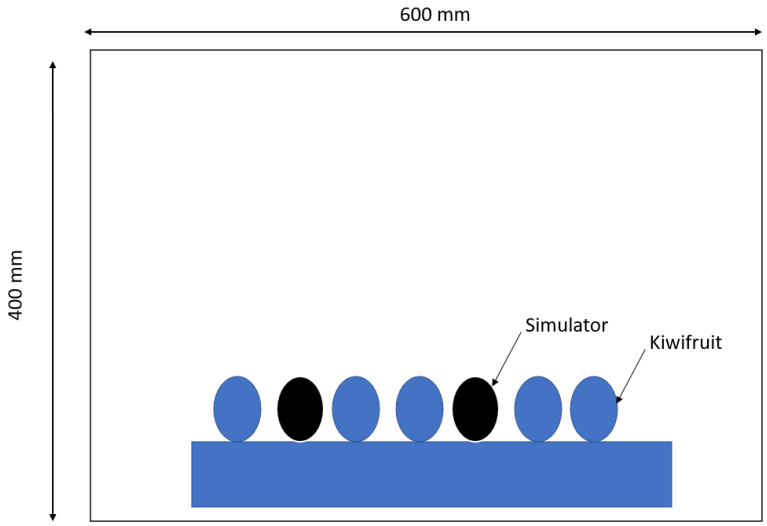

Figure 5-4, Cross-section view of experimental set up (airflow direction is into the page)

Figure 5-5 compares the fractional unaccomplished temperature change (Y) profiles between kiwifruit and the time scaled simulators. They are compared at the real-time and scaled time (equivalent Fourier number scales). On the left-hand side, the line bands represent the replicates' maximum and minimum centre temperatures, where five kiwifruit and two simulators were measured. On the right-hand side, the upper and lower values of the thermal properties were considered in the Fo calculation, and thus the line bands represent the maximum and minimum possible value. The characteristic length (L) will be the same since the kiwifruit and simulators have similar shapes and sizes and was defined as the average of the simulator's length, width, and thickness (54.0 mm). Although the thermal conductivity of kiwifruit and kiwifruit simulators have

some variation, the value was fixed at 0.50 $Wm^{-1}K^{-1}$, (the average between simulated and kiwifruit) for the Fo calculation. This will be insignificantly impact the result, as the time scaling is only based on the volumetric specific heat capacity.

As expected, the simulators cooled much faster than kiwifruit at a real time scale due to the lower thermal mass (Figure 5-4, left). Kiwifruit had a half cooling time (HCT) of 24.50 ± 1.80 minutes, whereas it was 9.75 ± 0.08 minutes for the simulator. The observed time scale factor was calculated to be 2.50 ±0.20, using Equation 5-4. This value agrees with the theoretical time scale factor discussed above (2.46 ± 0.17).

$$observed\ \ time\ scale\ factor = \frac{HCT_{t\ real}}{HCT_{t\ sim}} \qquad \text{Equation 5-4}$$

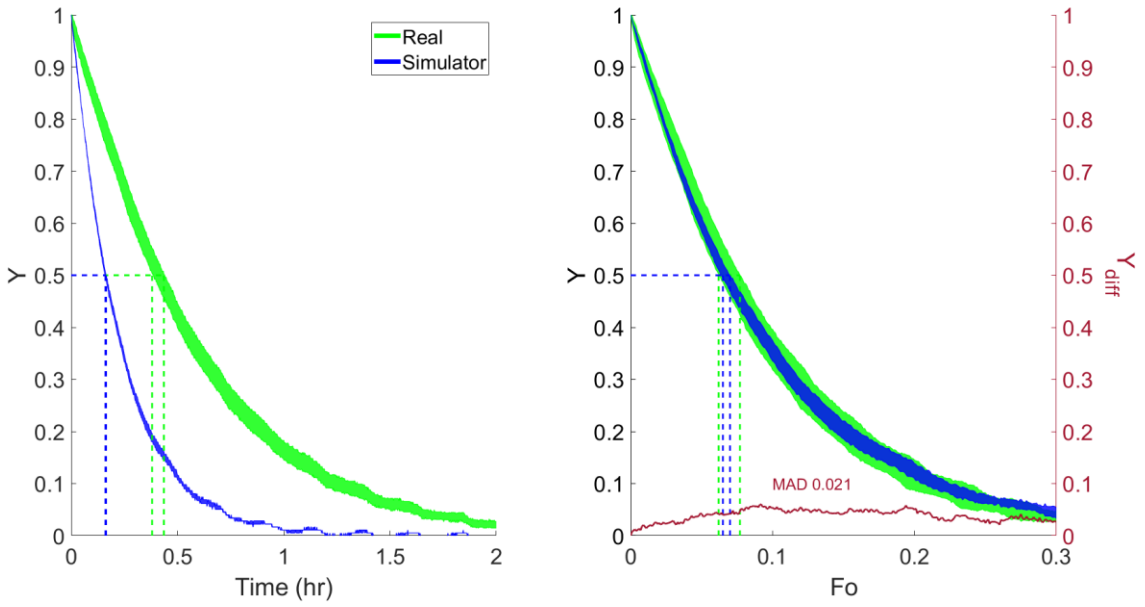

Figure 5-5, Validation results of individual kiwifruit vs simulator cooling at real-time (left) and Fo scale (right)

At Fo scale (Figure 5-5 right), the simulator temperature profile overlaps the kiwifruit temperature profile. The difference in fractional unaccomplished temperature change (Y_{diff}) (right axis; Equation 5-5) is small, and the maximum absolute difference (MAD; Equation 5-6) throughout the cooling is 0.02 (approximately a 0.4 °C difference). The HCT_{Fo} (half cooling time in Fo scale) of simulator is within the range of kiwifruit, suggesting no significant difference between the values. Overall, this suggests the simulators have similar cooling behaviour as the real kiwifruit.

$$Y_{diff} = \bar{Y}_{real} - \bar{Y}_{sim}$$ Equation 5-5

$$MAD = \max\left|Y_{dff}(t)\right|$$ Equation 5-6

Ferrua and Singh (2009c) suggested that significant amounts of heat can be lost in strawberries due to evaporation during precooling. The simulator used here does not include this heat transfer mechanism but can still provide good kiwifruit precooling simulation. Skin permeability is an important parameter restricting evaporation, and kiwifruit has similar skin permeability as strawberry. The skin permeability of strawberries is approximately 13.6 $\mu g\ m^{-2}\ s^{-1}\ Pa^{-1}$ and is 7.40-24.68 $\mu g\ m^{-2}\ s^{-1}\ Pa^{-1}$ for kiwifruit (table 2-3). The driving force for evaporation in this experiment was high and the similarity in dimensionless cooling rate observed between simulated and real fruit suggests that the evaporation effect during kiwifruit precooling is insignificant.

The boundary condition for the product is dominated by convection in this case (the third type of boundary condition). Therefore, the thermal conductivity (and so Bi) needs to be matched to ensure the time scale approach applies. The agreement between the dimensionless kiwifruit and simulator cooling dynamics shows that this was achieved. Overall, this experiment confirms the feasibility of the time scale approach on convection limited fruit cooling experiments.

5.2.2. Box scale simulator

As mentioned above, the time scale approach is expected to be feasible in a third kind of boundary condition scenario, but a closed package system involves a more complex heat transfer condition. Therefore, a box scale simulator validation was conducted. Modular bulk (MB) kiwifruit boxes were used with the fruit/simulators packed in an orderly pattern, as shown in Figure 5-6. This configuration contained 100 fruit in each box (size 36, class A).

Hundreds of time scaled kiwifruit simulators were manufactured using the method mentioned above. The kiwifruit or simulators were stacked inside the package, as shown in Figure 5-6 right. Two separate trials were conducted, one was using only kiwifruit, and the other was using only simulators. The centre temperature of sixteen kiwifruit/simulators (Figure 5-5, right) inside the box were measured every minute. The instrumentation of the simulator thermocouples is described in section 5.2.1. Electrical tape was used to secure the simulator and kiwifruit thermocouples (see appendix K). All the kiwifruit/simulator were initially equilibrated to approximately 20 °C and then

placed inside a wind tunnel for cooling. The detail of the wind tunnel can be found in O'Sullivan et al. (2016a).

After the first cooling (cooling cycle 1), the box was then equilibrated to approximately 20 °C, and then without any modification or movement of fruit within the boxes, a second cooling stage was conducted inside the wind tunnel. The cooling time for the kiwifruit MB box was approximately 20 hours and approximately 6 hours for the simulator MB box. Three replicates of the two stage cooling process were done. In each replicate fresh kiwifruit, and the simulator thermocouples were unplugged and re-instrumented.

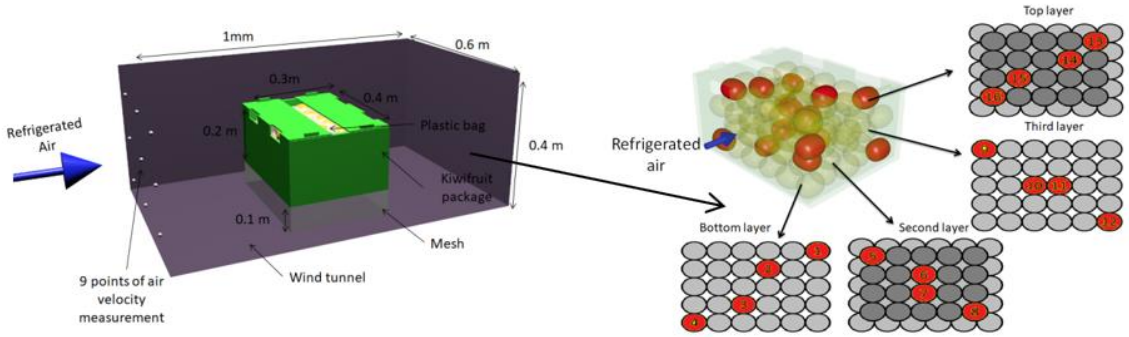

Figure 5-6, Experimental set up: the tunnel set up (left) and instrument set up (right). Red fruit/simulators represent the instrumented product.

Figure 5-7 shows the measured temperature profiles of the kiwifruit and the simulator, using the dimensionless Fo time frame. Overall, the kiwifruit has a similar temperature profile as the simulator, where the range of temperature profiles overlap, and the shape of the profiles are similar. The range shown for each temperature profile considers the replication of the results (three replicate trials, each with two cooling cycles) and the variation of thermal properties in the time scaling calculation.

Note that position 13 exhibits the most variation for kiwifruit and overlaps less with the simulator. Position 13 is at the top corner of the package, which is one of the fastest cooling positions. Usually, products near the packaging corner cool faster than other positions but are also sensitive to slight condition/positional changes (Mercier, Marcos, & Uysal, 2017).

Within the 16 positions, Y_{diff} (Equation 5-4) was calculated (right axis), and the average MAD (Maximum absolute difference, Equation 5-5) was calculated to be 0.044, which is equivalent to a 0.88 °C temperature difference (assuming T_i of 20 °C and T_{amb} of 0 °C). This 0.88 °C difference is within the measurement error of a typical type T thermocouple (Tong, 2001). Throughout the

sixteen positions, the top layer position generally has larger MAD than the other layers, and position 13 had the greatest MAD (0.112), which is equivalent to a 2°C difference. This could be due to the nature of experimental variation and uncertainties. Products on the top layer generally have a wider range of temperature profiles, which could be attributed to the flapping polyliner during the cooling and variations in polyliner/fruit contact. In addition, the stacking pattern will be slightly different each time, even though care was taken in the stacking process to be as consistent as possible. The product on the top layer would have the greatest positional offset due to the commutative positional offsets from the bottom; therefore, introducing extra error. Overall, the MAD is at an acceptable magnitude and the temperature profiles of the real product and simulator are overlapping. This validates the time scale approach for simulators in a closed package system.

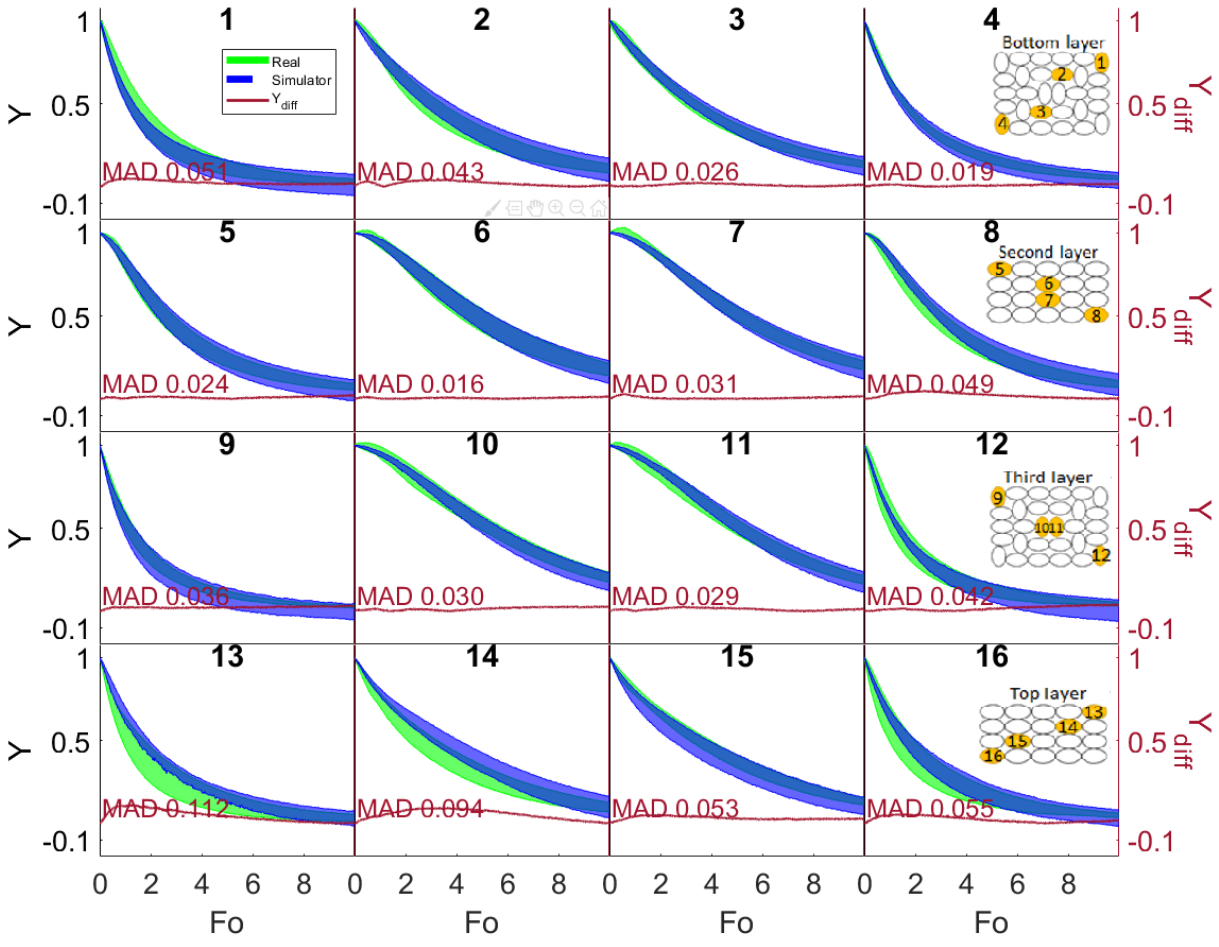

Figure 5-7, Derived temperature profiles for real and simulator kiwifruit and the average difference in Y

Further analyses were conducted based on half cooling time (HCT) of scaled time (Fo) and actual time (hr) in Figure 5-8. Overall, most of the simulator HCT_{FO} value overlap with the real product HCT_{FO}, where the error bars represent the 95% confidence interval. The HCT_{Fo} differences (Figure 5-8, left, y-axis in red) were calculated by HCT_{Fo} of real product minus simulator. The average of this HCT_{Fo} difference was -0.088 ± 0.129, which overlaps with the acceptable HCT_{Fo} difference in a controlled experiment, 0 ± 0.21 (for the detail see section 5.2.4). This means the real product had a similar cooling pattern to the simulator. On the right side of Figure 5-8, the actual HCT is compared, and the observed and time scale factor (TSF) was calculated. As mentioned in section 5.2.1, the TSF is 2.46 ± 0.17, whereas the average observed scale factor is 2.46 ± 0.14, which aligns with the theoretical scale factor.

This experiment showed that by matching the thermal conductivity and the shape, the simulator could simulate the cooling behaviour of the targeted product in a complex system, where multiple heat transfer mechanisms are involved.

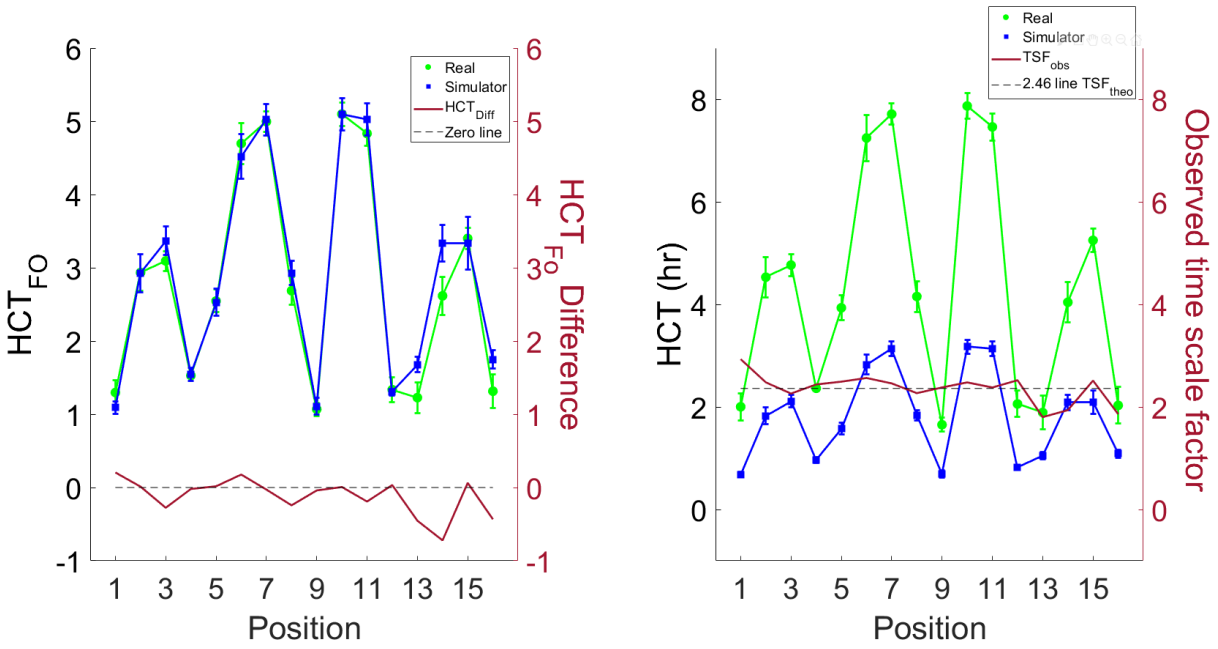

Figure 5-8, HCT of kiwifruit and simulator comparison at Fo scale (left) and actual time (right); HCT_{Fo} difference between real product and simulator (left, right axis) and observed time scaled factor (right, right axis)

5.2.3. Pallet scale cooling simulators

Although the single box scale experiment showed the feasibility of the time scaled approach, the single box scale experiment does not consider the effect of the changes in the cooling air

temperature as it passes through the stack that occurs in precooling operations. Therefore, to evaluate the feasibility of the time scaled approach on a larger scale, understanding the time scalability of the cooling air temperature is essential.

5.2.3.1. Theory

In pallet scale precooling, a fan creates a pressure drop across the pallet (see Section 2.1.6), where refrigerated air flows through the products via the package vents and headspace. Heat is transferred from the fruit in each box into the flowing air. Some heat is also transferred through the bottom of the box above into this headspace. This repeating flow pattern allows the pallet to be represented in terms of a single layer.

Consider horticultural produce (e.g. kiwifruit) packed in a row of boxes as described above. The cooling relies on the airflow above the boxes (Figure 5-9). If time scaled simulators are used instead of the horticultural produce, the air will heat up less (for the same velocity) as it passes through the layer, increasing the driving force for cooling of the next box. If the air temperature dynamics are not scalable, then the cooling of box 2 will be impacted. This potential error could further compound boxes 3 and 4. As a result, the time scale approach may not be feasible for this scenario, and therefore an investigation was undertaken to explore these dynamics.

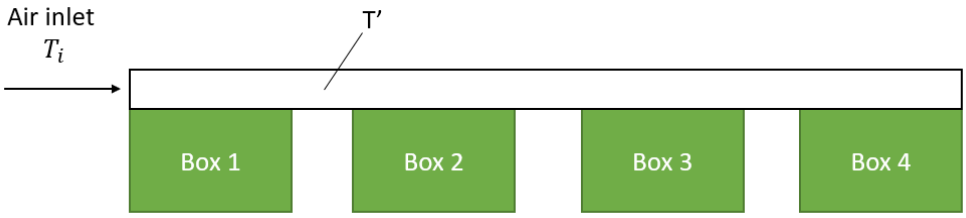

Figure 5-9, Hypothetical situation of cooling a four-box of horticultural product

The experiment outlined in section 5.2.2 showed the feasibility of the time scaled approach on a single box scale, and therefore box 1 must be time scalable. If a boundary is drawn around box 1 (Figure 5-10), a balance equation can be derived as Equation 5-7. The heat removed from box 1 must be the same as the total energy carried out by the air. The heat transfer from box 1 to the air from the fruit surface can be approximated as Equation 5-8. The rate of accumulation of heat in box 1 must be equal to the rate of energy removed via convection. Combining Equations 5-6 and 5-7 gives Equation 5-9, which is suggests that the air temperature leaving the first box is a function of air velocity, heat transfer coefficient, surface area, air temperature inlet, and the surface

temperature of box 1. If the surface temperature of box 1 is proportional to the box average temperature (Equation 5-10), if all other variables remain constant, and the temperature of box 1 is time scaled according to its thermal mass, the outlet air temperature must be time scaled accordingly.

$$\dot{m}c_{air}(T_o(t) - T_i) = V\rho c\frac{\partial T_{av}}{\partial t} \qquad \text{Equation 5-7}$$

$$hA\frac{(T_i - T_s) - (T_o - T_s)}{\ln\frac{T_i - T_{av}}{T_o - T_{av}}} = V\rho c\frac{\partial T_{av}}{\partial t} \qquad \text{Equation 5-8}$$

$$T_o = (T_i - T_s)\exp(-\frac{hA}{\dot{m}c}) - T_s \qquad \text{Equation 5-9}$$

$$T_s \propto T_{av} \qquad \text{Equation 5-10}$$

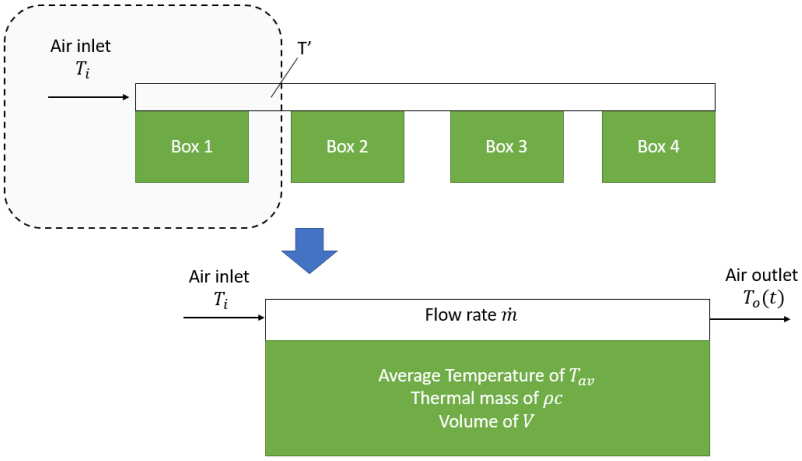

Figure 5-10, Box 1 cooling condition of the hypothetical situation

In fact, if these four boxes are placed closely, and the cooling only relies on the forced convection above, the overall cooling structure of these four boxes is not much different from a single box but with greater dimension. Therefore, the time scale approach should be feasible on this four-box scale and can be generalised to a larger scale.

In order to further test the theory and understand the limitations of the time scale approach, a two-dimensional numerical model was developed (COMSOL Multiphysics v5.2.). The layer of four MB boxes was approximated as a single uniform rectangular block, 1200 by 200 mm (as shown in Figure 5-10). The air layer was defined as 1200 by 50 mm. The inlet air temperature was defined as 0°C. The initial temperature of the block was defined as 20 °C, and the air was 0°C. The thermal

conductivity of the block was defined as 0.5 $W\ m^{-1}K^{-1}$. The air velocity (accounting for the mass flow rate) and the thermal mass of the block was defined as parameters where a range of values could be tested. The Navier-Stokes equation was used for air movement (Equation 2-4), and the energy equation (Equation 2-3) was used for air temperature. Fourier's equation (Equation 2-8) was used for the block's temperature. In order to solve this model, the geometry was meshed (4071 elements) and numerically solved using the COMSOL default solver algorithm.

Figure 5-11 shows the average temperature of the hypothetical rectangular block at high and low air velocity under real-time and scaled time conditions. The colours of the temperature lines represent different volumetric heat capacities of the block. As expected, a higher airflow rate or lower thermal mass resulted in faster cooling. When the real-time is transferred into Fo scale, all the lines overlap, regardless of thermal mass. This observation occurs in both high and low air velocity situations. This suggests that air velocity and thermal mass are not limiting factors for the time scale approach.

Figure 5-12 shows the outlet temperature of the hypothetical situation in real-time and scaled time. As expected, the time scale approach is also applied to the air so that the outlet air temperature can be time scaled according to the material thermal mass. The lower thermal mass of the material results in faster decrease of the outlet temperature in real-time, but all the lines overlapped when the time scale approach was applied.

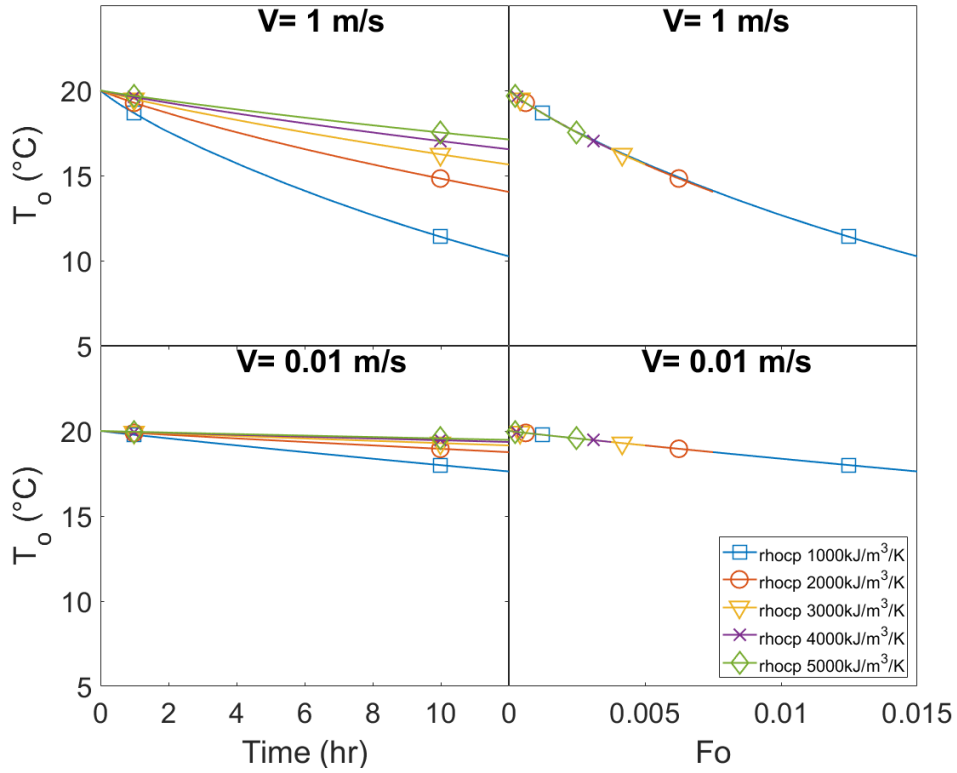

Figure 5-11, Predicted average product temperature of the hypothetical scenario at real and scaled times

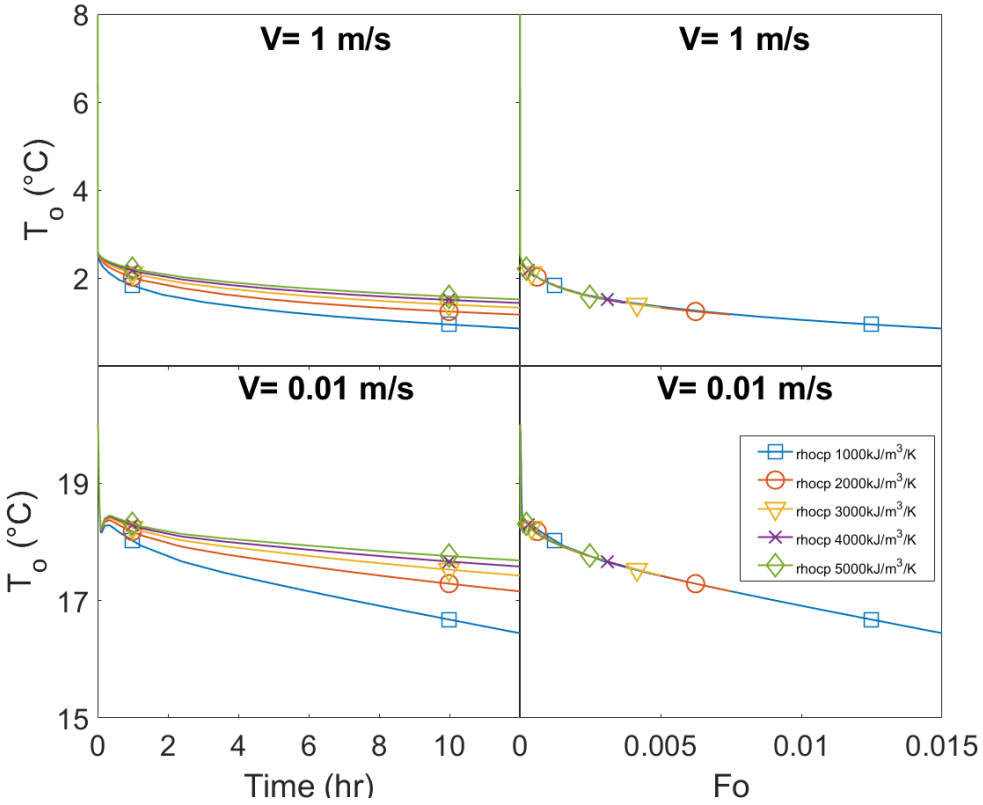

Figure 5-12, Predicted outlet temperature of the hypothetical scenario at real and scaled times

5.2.3.2. Pallet scale experimental validation of time scaling

Although both theoretical and modelling analyses indicate the feasibility and scalability of the time scale approach, experimental validation is still essential. As a result, a four-box scale cooling experiment was conducted (Figure 5-13). The boxes were positioned in a way that the cooling air must go through the boxes one by one. The surrounding surfaces of the boxes were insulated by polystyrene, allowing air to flow only through the package vent holes. There were two rows of boxes inside the precooler, the upper row and the lower row, which were filled with kiwifruit and time scaled simulators, respectively. Three trials were conducted, where the first trial was conducted at high airflow and the second and third trials were conducted at low airflow rates. Trial three was a replicate of trial two.

In the first trial, the fan speed of the precooler was set at 17.5 revolutions per second, providing a 110 Pa pressure drop (SSCSNBN002NDAA5, Honeywell, Morris Plains, USA) across the precooler. The fan speed was set at 3 revolutions per second (rps) in the second and third trials, providing a 14 Pa pressure drop across the precooler. The products had two cooling cycles (similar to the single box scale cooling). Similar to the box scale experiment (section 5.2.2), the products were cooled from approximately 20 °C to 0 °C, for the first cooling cycle. After this, the products were equilibrated to approximately 20°C before a second cooling cycling (20 to 0°C). Between the cooling cycles, no variables or product stacking was changed. The product stacking and the instrumented products positions were the same as the single box scale experiment for all eight boxes.

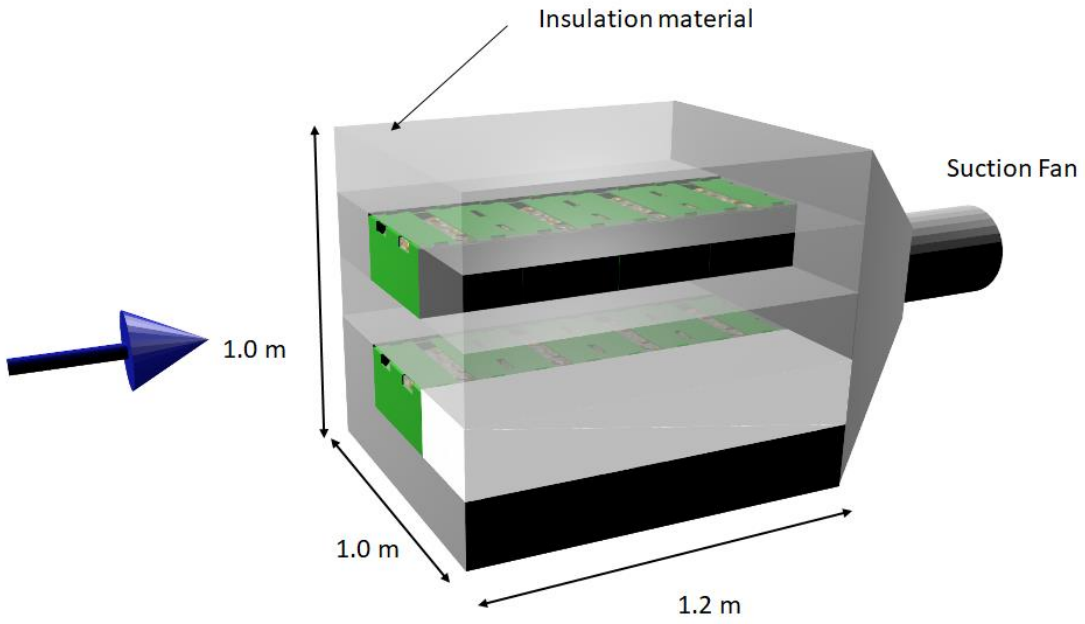

Figure 5-13, Experimental setup for four box scale cooling

Trial 1 – High air velocity

Figure 5-14 summarises the measured temperature profiles from trial 1 in scaled time. Each line represents the average temperature of the product in cycles 1 and 2. The line colours, red, green, blue, and black, represent boxes 1 to 4, respectively. The cross markers represent the kiwifruit, and the circle markers represent the simulator fruit.

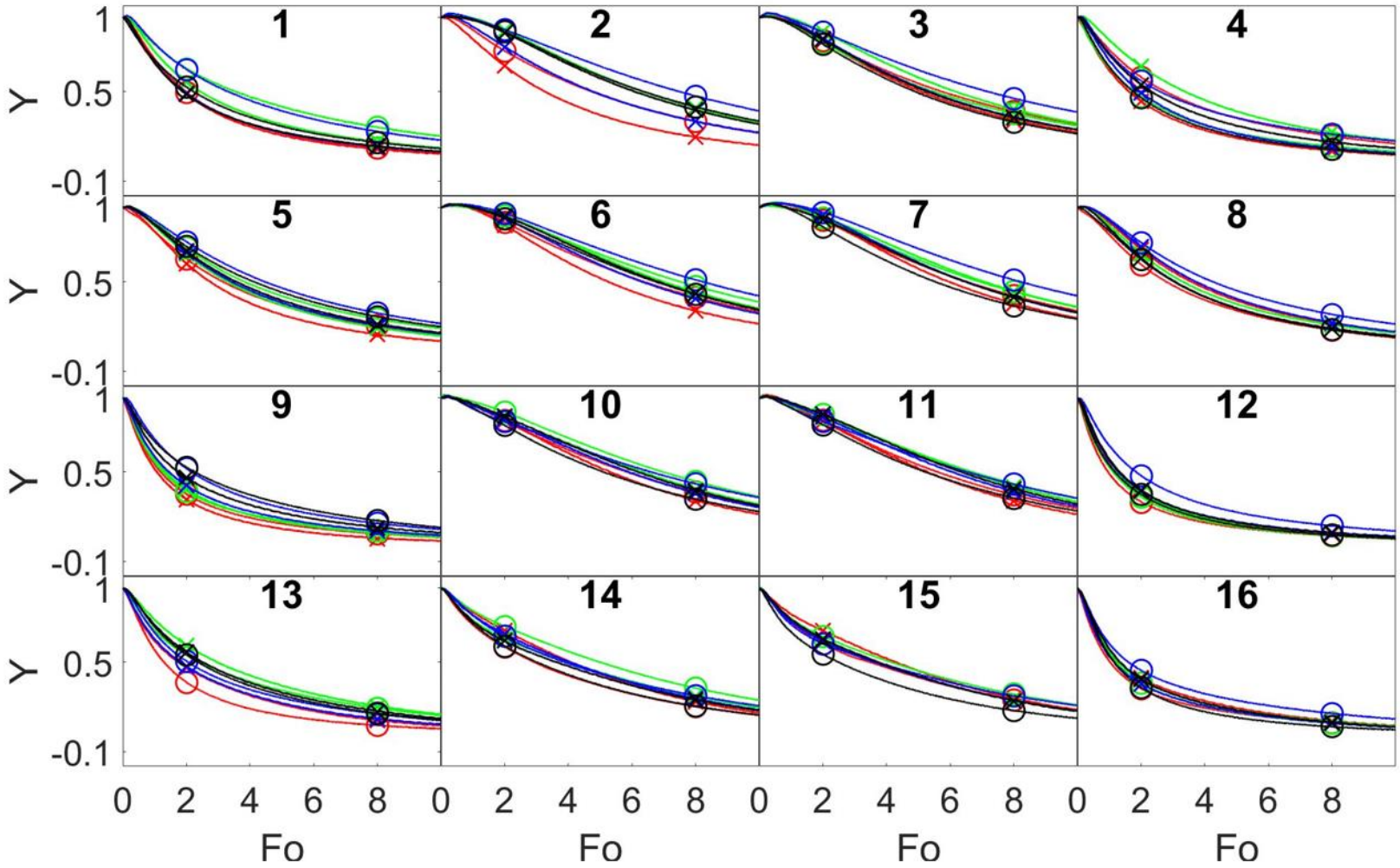

Figure 5-14, Summary of pallet layer cooling in Trial 1 (cross markers for real, circular markers for simulators; red, green, blue, and black lines represent boxes 1-4 respectively)

In general, there is no significant departure between the cross markers and circle markers in Figure 5-14, suggesting similar kiwifruit and simulator cooling behaviour at the scaled time. The MAD analysis (maximum absolute difference; Equation 5-6) in Figure 5-15 is created to assist the comparison. Overall, the MAD values generally fluctuated between 0.01 to 0.15 (equivalent to 0.2 to 3.6 °C difference), apart from position 4 in box 2. The average MAD for these 64 positions is 0.07 (equivalent to 1.7 °C). Although the MAD value is relatively large for the product in position 4 box 2, the corresponding temperature profiles (green lines in graph 4; Figure 5-14) were insignificantly different. Again, given that 16% experimental error is a typical range for a large-scale experiment (Olatunji, Shim, & East, 2019), these MAD values are acceptable.

It is interesting to point out that Figure 5-14 suggests boxes 1 to 4 had a similar cooling rate, where the red, green, blue and black lines are generally bundled together. As the airflow was directed in a way that must pass through box 1 to 4 in order, this observation suggests that the airflow was fast enough that it still able to remove a considerable amount of heat from box 4.

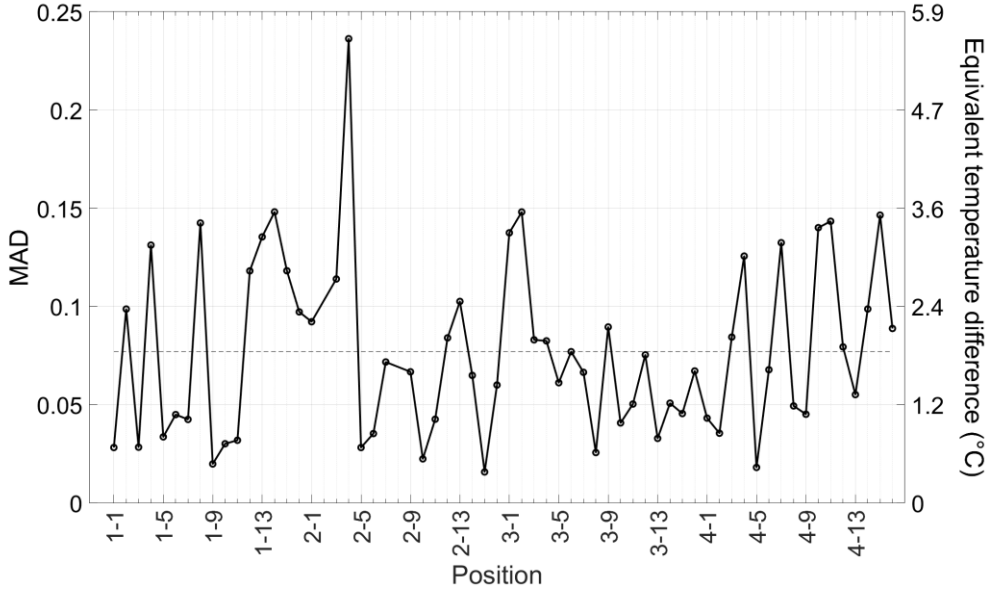

Figure 5-15, MAD analysis of Trial 1

The HCT analyses on actual time and scaling time were also conducted (Figure 5-16 and Figure 5-17), where the average HCT_{Fo} difference between real product and simulator was -0.225±0.206, and the observed scaled factor from HCT is 2.34 ± 0.13. Both values overlap with acceptable variation range, 0 ± 0.21 and 2.46 ± 0.17, respectively. Furthermore, there is no noticeable trend suggesting that the HCT_{Fo} difference increases as the product position increases, which indicates the validity of the scaling effect on the air temperature; therefore, the kiwifruit and simulators had a similar cooling profile throughout box 1 to 4. This observation indicates the validity of the time scaling effect on the air temperature, as discussed in section 5.2.3.1.

It is notable that some positions in the HCT_{Fo} analysis had considerable variation, such as position 2 in box 3 and position 6 in box 3. Comparing these positions in the actual time scale (Figure 5-17), the variation could be considerable (± 1 hour) but acceptable. This shows that the thermal properties' uncertainty could magnify the experimental variation because both the upper and lower range of the thermal properties must be considered in the Fo calculation.

It is interesting to point out that the MAD analysis suggests product in position 4 in box 2 could be a potential outliner; whereas the HCT_{Fo} analysis suggests product in position 2 box 3 has a greater HCT_{Fo} difference. This shows it is important to consider both MAD and HCT_{Fo} analysis to evaluate the difference between kiwifruit and simulator.

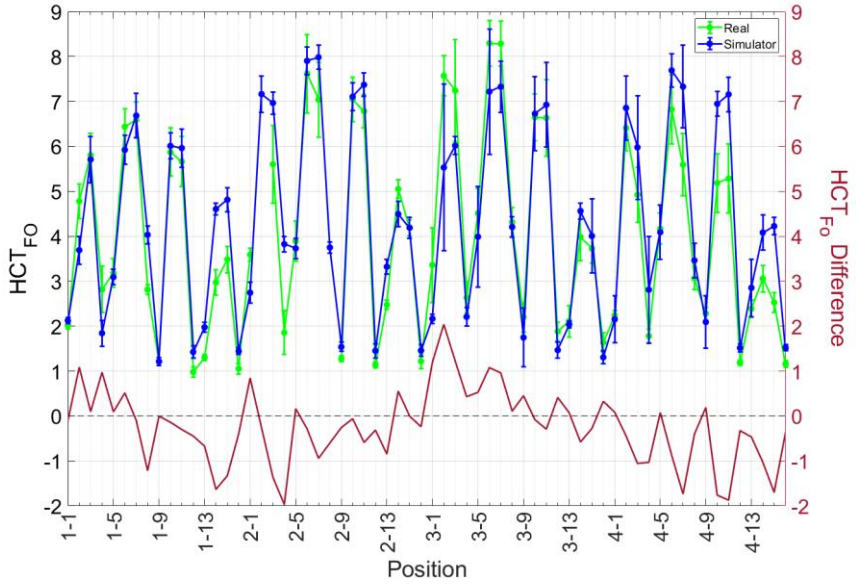

Figure 5-16, HCT_{Fo} analysis of Trial 1

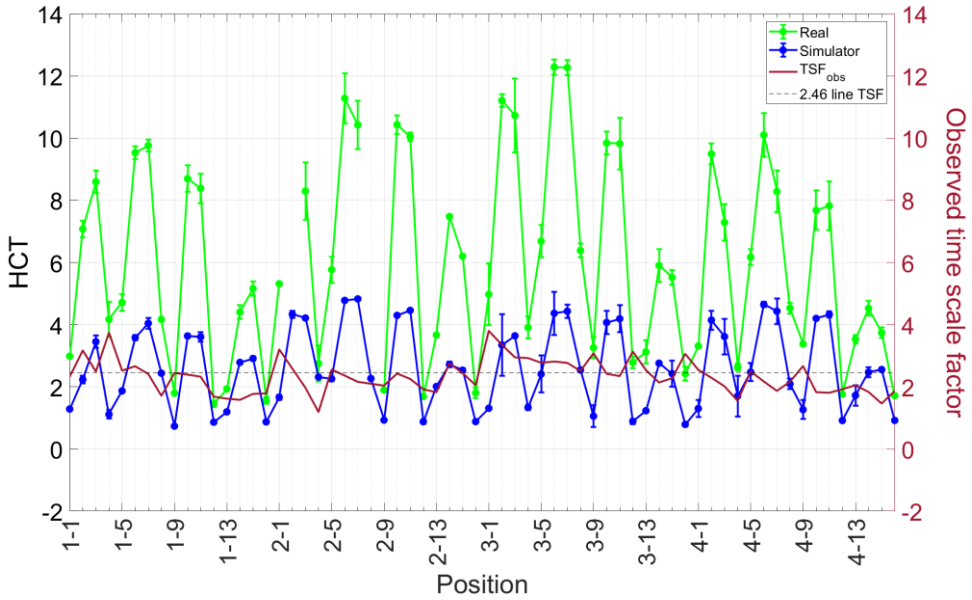

Figure 5-17, HCT and observed time scale factor analysis of Trial 1

Trials 2 and 3 – low air velocity

Trials 2 and 3 were conducted at a much slower airflow, where the fan speed was set to be 3 revolutions per second, generating 14 Pa pressure drop across the precooler, which is to test if the time scale approach is still valid under a very low airflow rate. Trial 3 is a replicate of trial 2, with swapped position between the kiwifruit and simulators. The four boxes of simulator packages were on the upper layer, and the kiwifruit packages were placed on the lower layer in trial 2. The simulator packages were on the lower layer, and the kiwifruit packages were on the upper layer in trial 3. Again, each trial had two cooling cycles as in previous experiments.

Figure 5-19 summarizes the derived temperature profiles of each product in trials 2 and 3, where the lines represent the average values from trials 2 and 3. The line colour, red, green, blue, and black, represent the product in box 1 to 4, respectively. The cross markers represent the kiwifruit, and the circle markers represent the simulator product. Again, no noticeable departure is observed between the cross markers and circle marks in Figure 5-19. In these two trials, some positions in box 1 cooled faster than boxes 2 to 4, such as positions 3, 4 and 12. The MAD analysis in Figure 5-18 is created to assist the comparison. Again, the MAD values generally fluctuate between 0.01 to 0.15 (equivalent to 0.2 to 3.6 °C difference). Within these 64 positions, only four positions have MAD greater than 0.1 (equates to 2.6 °C). The average value for these 64 positions is 0.05 (equivalent to 1.4 °C). This range of variation is acceptable.

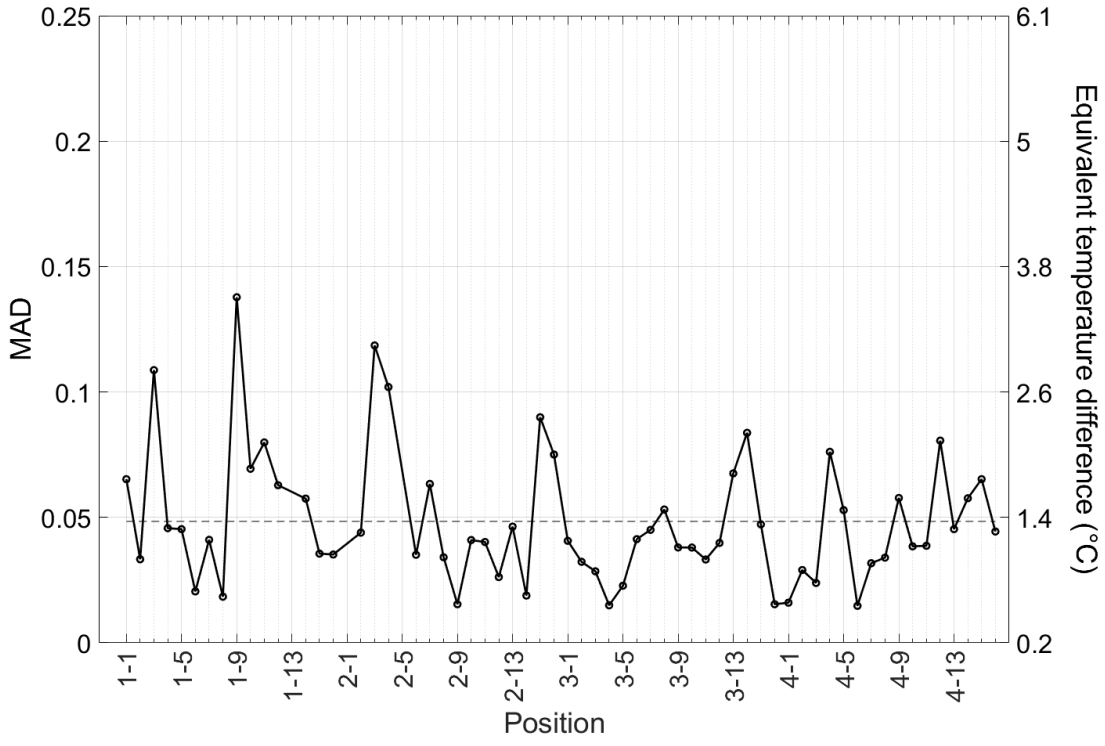

Figure 5-18, MAD analysis of Trial 2 and 3

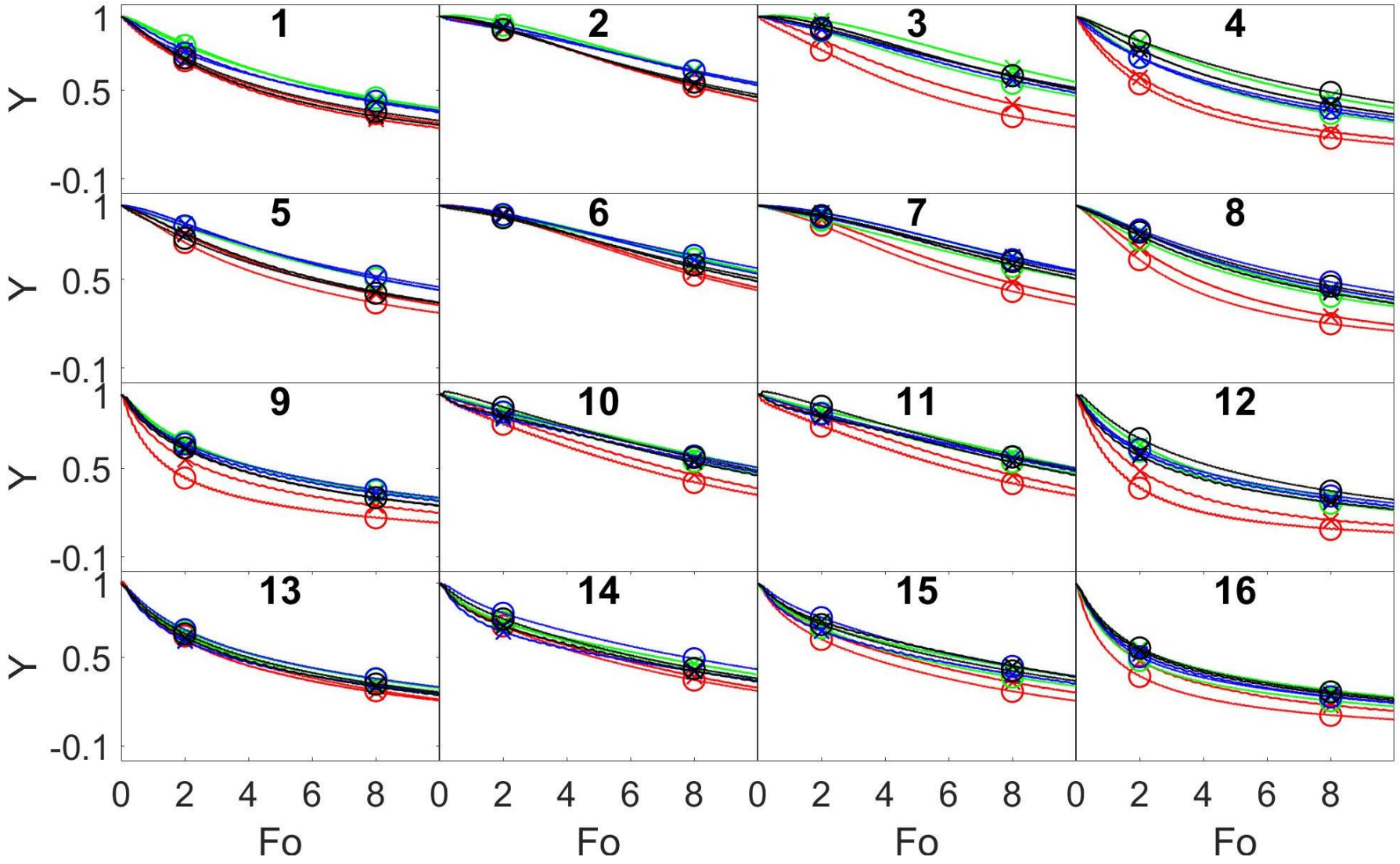

Figure 5-19, Summary of four boxes cooling in trial 2 and 3

The HCT analysis on actual time and scaling time were also conducted (Figure 5-20 and Figure 5-21), where the average HCT_{Fo} difference between real product and simulator was -0.010±0.247, and the observed TSF from HCT is 2.44±0.11. Both values overlapped with an acceptable variation range, (0 ± 0.21 and 2.46 ± 0.17, respectively).

It is noteworthy that both the HCT_{Fo} difference and observed TSF (the lines in red) shows a very slight trend of increase as product positions moved away further from the air inlet (see Figure 5-8 c). This trend is statistically significant, as the one-way ANOVA between HCT_{Fo} difference and the box have a p-value less than 0.05 (Table 5-3). This slight trend means the simulator needed a shorter time to reach half of its initial temperature than the kiwifruit as distance from air inlet increases. However, the effect of this slight trend is physically insignificant as no trend could be detected in the MAD analysis (Figure 5-18). Also, trials 2 and 3 were conducted at a relatively low-pressure drop condition (14 Pa), whereas a typical experiments have pressure drop of about 100 Pa across the packages of product, which means trial 1 is a more realistic analogy. No evident trend was be detected in HCT_{Fo} analysis of trial 1. Overall, trial 1, 2 and 3 shows acceptable temperature profile agreement between real product and simulator, which indicates the validity of the time scale approach at high and low-velocity airflow.

Table 5-3, Minitab 16 out of one-way ANOVA between HCT_{Fo} difference and Box position

Analysis of Variance

Source	DF	Adj SS	Adj MS	F-Value	P-Value
box	3	33.68	11.2269	22.59	0.000
Error	59	29.32	0.4970		
Total	62	63.00			

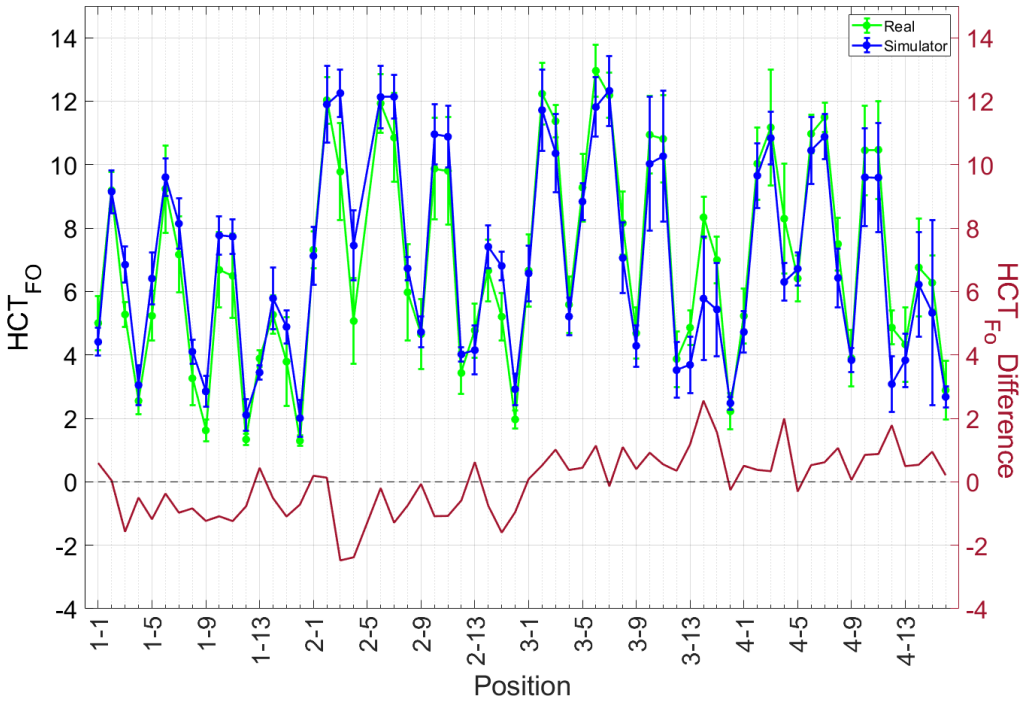

Figure 5-20, HCT_{Fo} analysis of Trials 2 and 3

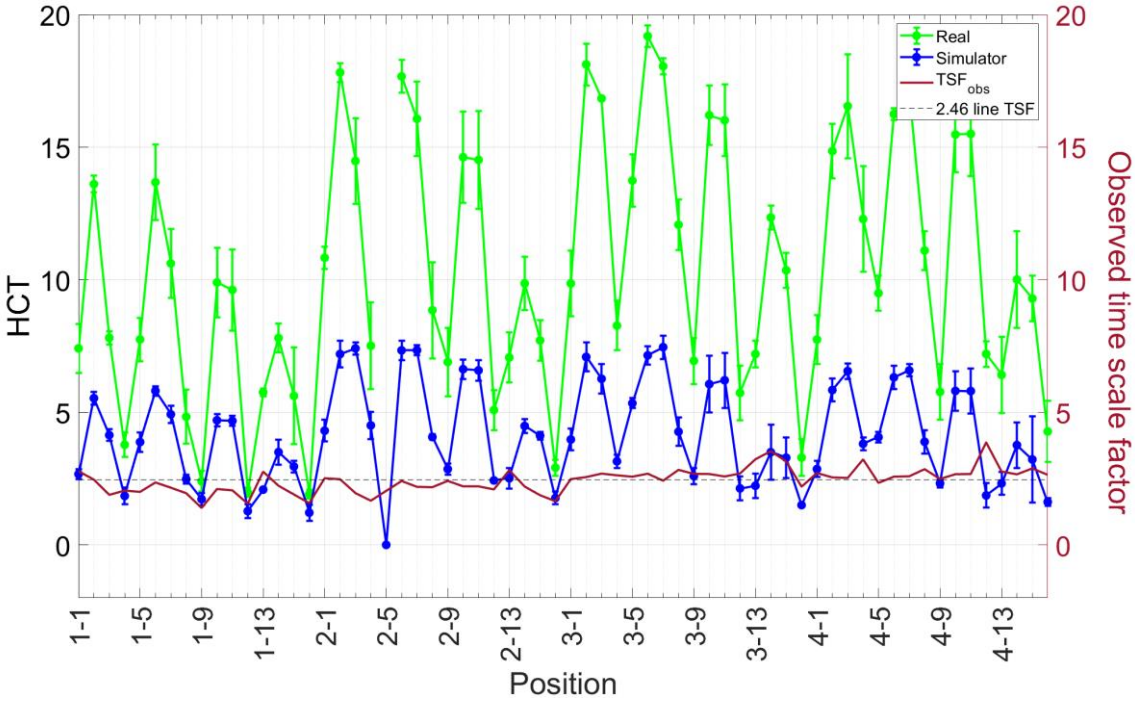

Figure 5-21, HCT and observed time scale factor analysis of Trial 2 and 3

5.2.4. Simulator and real kiwifruit experimental variation analysis

As mentioned, both trial 2 and 3 conducted two cooling cycling, which means four sets of experimental data could be used to analyse the experimental variation. Figure 5-22 and Figure 5-23 illustrate the kiwifruit and simulator experimental variation comparisons.

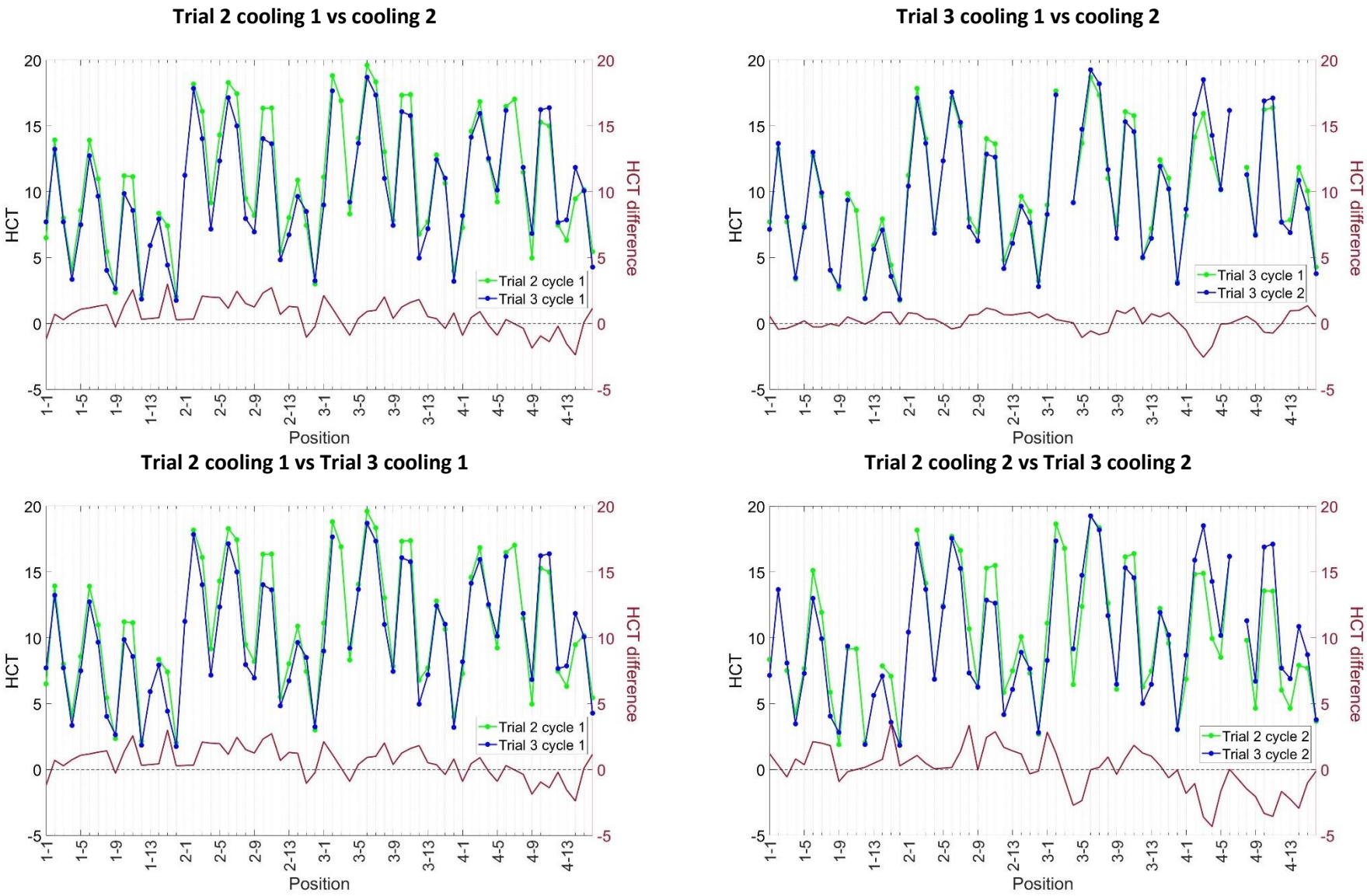

Figure 5-22, Experimental variation comparison for the kiwifruit

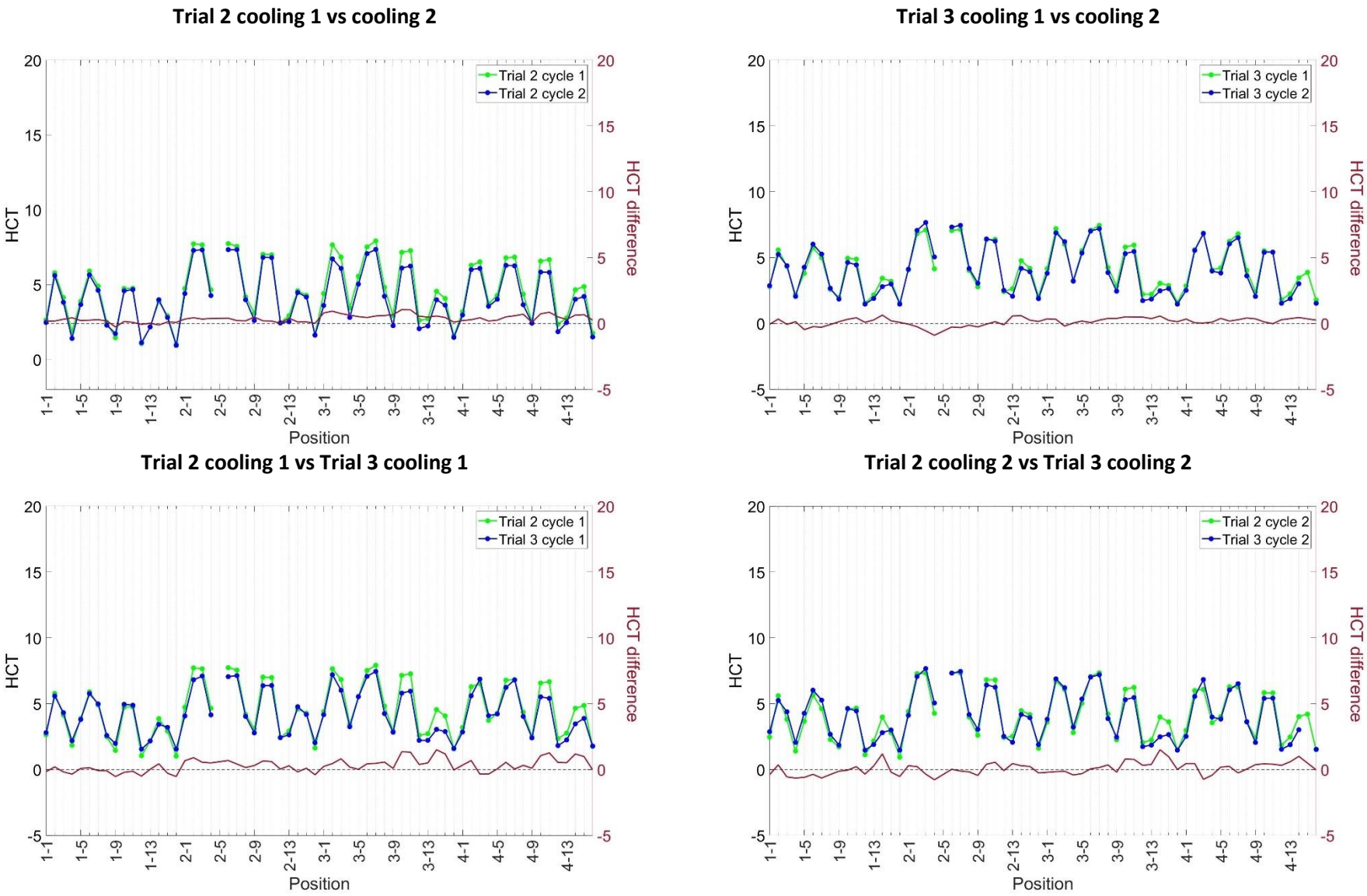

Figure 5-23, Experimental variation comparison for the simulator

Table 5-4 summarises the standard deviation and the equivalent 95% confident internal for each comparison. In theory, trial 3 is a replicate of trial 2 and cooling 2 is a replicate of cooling 1, and therefore the average HCT difference should theatrically be zero. Based on this, the overall difference between replicates can be quantified by calculating the standard deviation of HCT difference.

Table 5-4, Comparison matrix result: standard deviation (left) and equivalent 95% confident interval (right) for real product (left bottom) and simulator (right top)

	Trial 2 cooling 1	Trial 2 cooling 2	Trial 3 cooling 1	Trial 3 cooling 2
Trial 2 cooling 1		0.460|0.114	0.580|0.143	
Trial 2 cooling 2	1.206|0.305			0.484|0.121
Trial 3 cooling 1	1.341|0.339			0.328|0.082
Trial 3 cooling 2		1.766|0.455	0.767|0.192	

Although trial 3 was designed to be a replicate of trial 3, restacking of the kiwifruit and simulator was unavoidable between trial. Therefore, comparing the standard deviation between trial versus comparing standard deviation between cooling indicates whether the restacking play an important role in the experimental variation or not. Table 5-4 shows that both kiwifruit and simulator had smaller standard deviation if the products were not restacked. This suggests that a slight stacking difference in an experiment could cause noticeable experimental variation.

The equivalent 95% confidential interval of the standard deviation were calculated and are summarised in Table 5-4 (the right values). This 95% confidence interval means, between two well-controlled experiments with corresponding conditions (with or without stacking pattern change), the 95% of the HCT difference would be within the range. As a result, ±0.397 hours of HCT difference is a typical expected HCT variation in a well-controlled kiwifruit experiment (an average of 0.339 and 0.455 hours). The equivalent HCT_{Fo} for these acceptable HCT differences are ±0.21, which is used as a benchmark in section 5.2.3.2 for the HCT_{Fo} analysis.

Although the fluctuation of HCT difference within kiwifruit was greater than within simulators in Figure 5-22 and Figure 5-23, it is expected that the simulator will cool 2.46 times faster than the kiwifruit, and therefore the comparison need to be normalised. The average HCT value for kiwifruit through the 64 positions within these four cooling tests was 10.25 hours and was 4.25 hours for the simulator. The experimental variations are normalised by considering the 95% confidence interval as a percentage of the average HCT, and it is shown in Table 5-5. The

difference between the normalised experimental variation of kiwifruit and simulator is insignificant (p-value for t-test as 0.49). Nevertheless, having a stable and durable simulator that can be repeatedly used is still preferred and believed to achieve better consistency in the long run.

Table 5-5, Normalised experimental variation

	Kiwifruit	Simulator
Trial 2, cooling 1 vs cooling 2	2.98%	2.68%
Trial 3, cooling 1 vs cooling 2	1.87%	1.93%
Cooling 1, trial 2 vs trial 3	3.30%	3.36%
Cooling 2, trial 2 vs trial 3	4.44%	2.85%

It is notable to point out that in Figure 5-22, the HCT difference for kiwifruit can be as much as 3.5 hours. Likewise, in Figure 5-23, the HCT difference for the simulator can be 1.5 hours, which is equivalent to 3.69 hours with time scaling. These are not uncommon observation experimental outliers in a large scale experiment (Olatunji, Shim, & East, 2019).

5.3 Open package application – Apple simulator

Although the closed package system case study has already demonstrated the feasibility of the time scaled approach, a case study for an open package system was carried out to further demonstrate the application of the simulator development framework.

A standard Z-pack apple package (0.482 by 0.313 by 0.257 m; WLH) was used in this case study. Four layers of count size 70 Jazz apples were packed into the Z-pack. Pulp moulded interleaving packaging material, 'Friday' trays, were used to separate each layer. The details of the package can be found in East et al. (2003).

Figure 5-24, Standard Z-Pack apple package (Tanner, 1998)

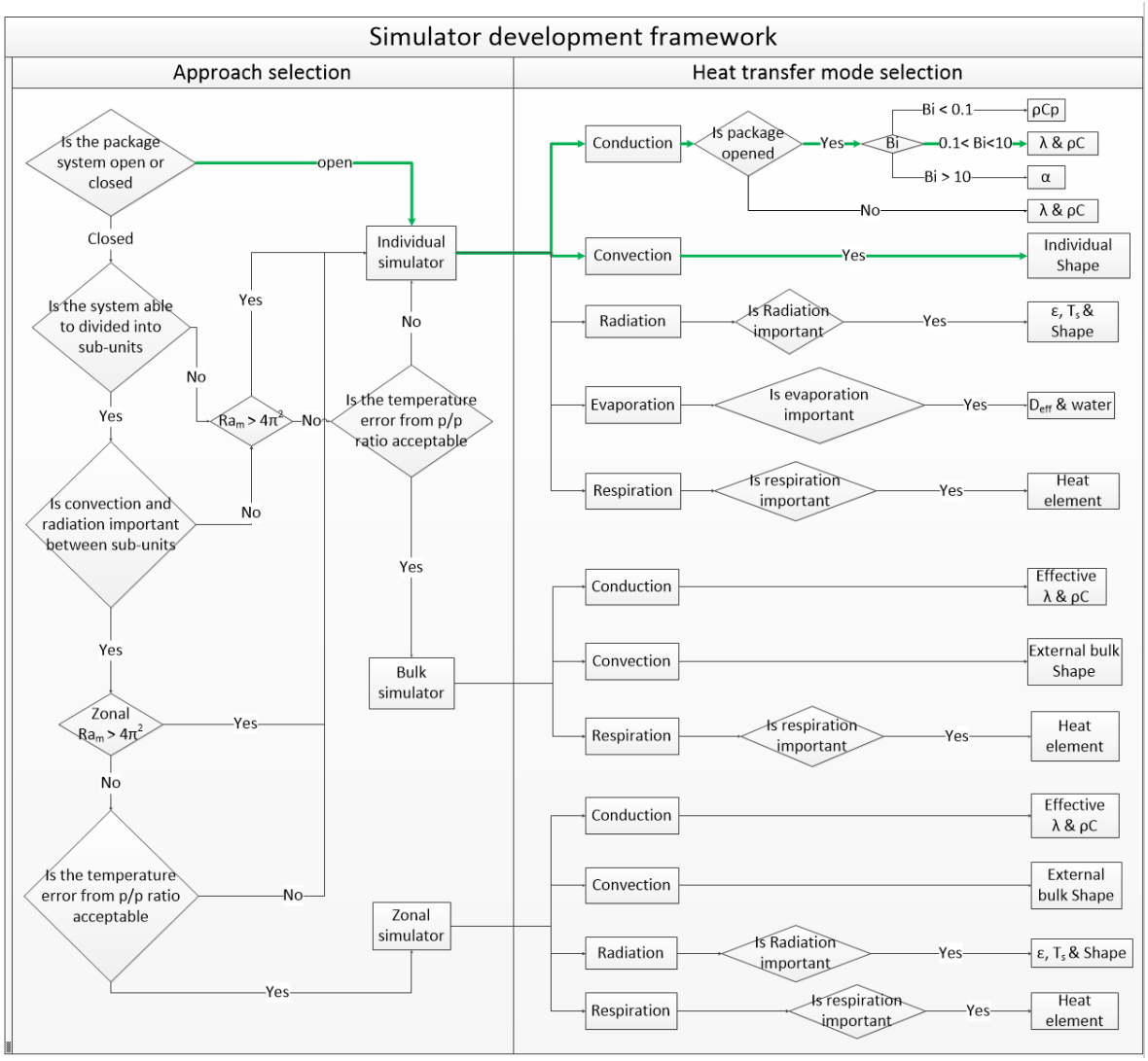

Figure 5-25, Apple simulator design decision tree

Figure 5-25 demonstrates the utilisation of the simulator development framework for apple simulator development. Apples are packed in an open package system, and therefore, individual simulators should be used. Based on the study of Tanner et al. (2002a), conduction and convection are the critical modes of heat transfer occurring in the system, and therefore, the Bi number and the shape of the apple is important to match. By calculation, the Bi number would be within 0.1 to 10, and therefore, the thermal conductivity and volumetric heat capacity need to be matched (appendix J).

Table 5-6 summarises the thermal properties of apple, which are based on the literature data (for detail see Table 2-3). The thermal properties of apples were not measured, as the study of apple

thermal properties is already well established (Ashrae, 2010; Rahman, 2009b). The table also shows that the simulator achieved the targeted thermal conductivity. From these values, the time scaling factor was calculated to be 2.43 ± 0.22.

Table 5-6, Thermal properties of apple

Properties	Apple	Simulator
Thermal conductivity ($Wm^{-1}K^{-1}$)	0.43±0.01	0.42±0.03 (n=3)
Heat capacity ($Jkg^{-1}K^{-1}$)	3793±35	972±10
Density ($kg\ m^{-3}$)	961±60	1547±13 (n=4)

As discussed in chapter 4, it is not easy to find commercially ready and easy to manufacture material for individual simulators without including significant amounts of water. For this reason, a time scaled approach was used. Following the time scaled approach, the thermal conductivity ($0.43\ W\ m^{-1}K^{-1}$) is the important thermal property to match to reproduce the same Bi number in the real fruit system. Using the methodology outlined in section 4.2.4, a 21% (vol) of aluminium particles in a polyester matrix can achieve the required thermal conductivity. Ten apple moulds were made from ten counts of 70 Jazz apples using the methodology developed in Section 4.2.1. Seventy apple simulators were then cast using the 21% aluminium particle/polyester material. Figure 5-26 shows the apple fruit simulators manufactured for this case study.

Figure 5-26, Pictures of apple and apple simulator

The thermal conductivity and density of the apple simulators were measured using the methods outlined in section 4.2.2. In addition, the specific heat capacity of the simulator was calculated based on the measured polyester and aluminium specific heat capacity mentioned in section 4.2.6.3. Comparisons of the thermal properties between apples and simulators are shown in Figure 5-25 demonstrates the utilisation of the simulator development framework for apple simulator development. Apples are packed in an open package system, and therefore, individual simulators should be used. Based on the study of Tanner, Cleland et al. (2002), conduction and convection are the critical modes of heat transfer occurring in the system, and therefore, the Bi number and the shape the apple is important to match. By calculation, the Bi number would be within 0.1 to 10, and therefore, the thermal conductivity and volumetric heat capacity need to be matched.

A single apple box cooling experiment was conducted, as shown in Figure 5-27. Refrigerated air was directed into the box via the package vents. The apple package was insulated on the top, bottom, and sides to ensure air only passed through the package via the vent. The products were cooled from 20 °C to the refrigerated air temperature (approximately 0°C). The cooling fan was set at 20 revolutions per second, resulting in a 139 Pa of pressure drop across the box. Similar to the previous kiwifruit experiments, each experiment was conducted for two cooling cycles. Sixteen products were instrumented, and the sensor pattern is shown in Figure 5-27 B (or products in yellow in Figure 5-27 A). In each case, the thermocouples were positioned with the aim to measure the temperature of the apple centre. A guide hole was created using a rod for the apple before pushing the thermocouples in the product. The hole depth was carefully created to ensure the thermocouples could reach the product centre. The guide hole was created by a 3.5 mm drill for the simulators, and thermal paste was used to fill the air gap between the thermocouple and the simulator material. Figure 5-27 B) shows the instrumented product position, and Figure 5-26 shows the pictures of how the thermocouples were positioned in the product.

A

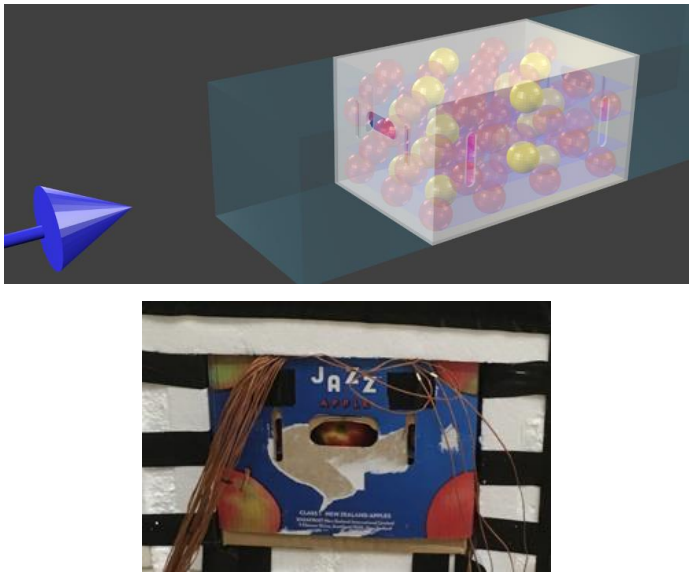

B

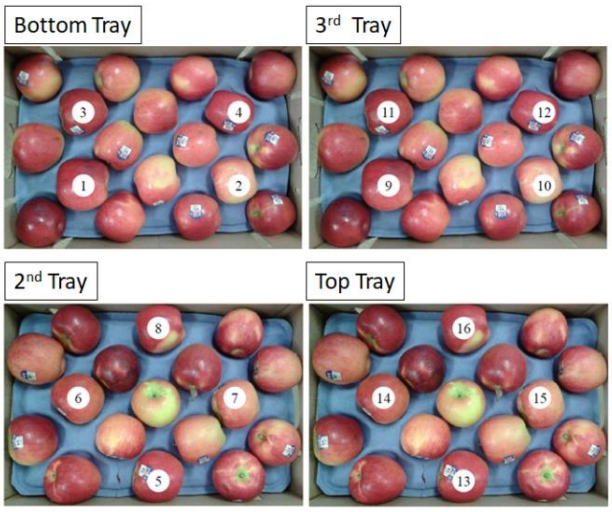

Figure 5-27, A) Experimental setup of apple cooling and B) sensor position

Figure 5-28 shows the measured temperature profiles of the real and the simulated fruit using scaled time. In general, no obvious departure was detected between the apples and the simulator, apart from at product positions 14 and 15 (at the top layer), where the MAD are also relatively large compared to other positions. These positions could potentially be experimental outliers. Given that the cooling air can only pass through the package via the vent holes, each 'Friday' tray acts as a resistance to the airflow; therefore, every slight shift of the product stacking could significantly change the airflow dynamics. The study of Łapiński et al. (2021) also shows that a change in stacking could lead to a 10-25% difference in heat transfer efficiency. The average MAD across these 16 positions is 0.062, equivalent to 1.2°C, which is an acceptable difference.

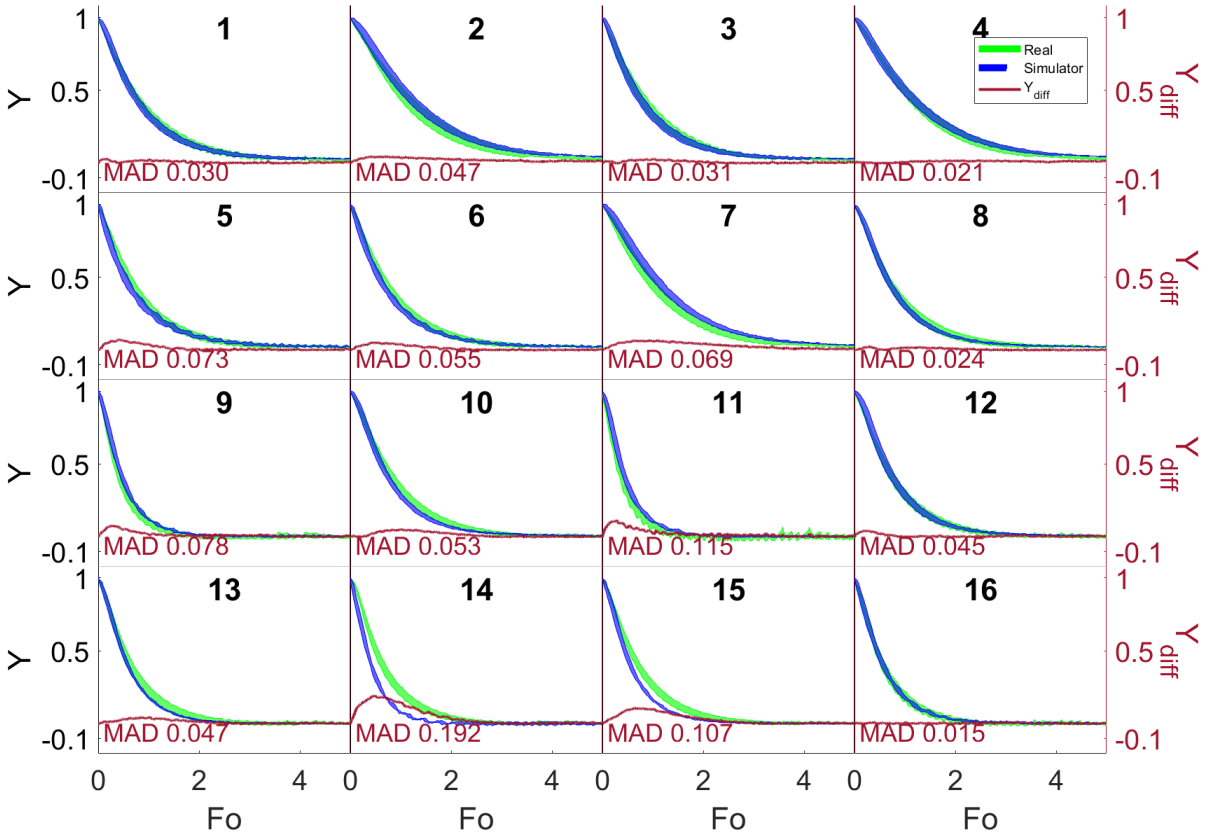

Figure 5-28, A) Measured temperature profiles of apple, simulators and the average difference in Y

Figure 5-29 shows the HCT_{Fo} and HCT analysis in real time and scaled time. In the HCT_{Fo} analysis, the simulator generally had the same HCT_{Fo} as the real product, apart from the product at positions 14 and 15, which has been already discussed. The products at position 7 also have a slightly larger deviation, but the deviation is smaller than the experimental variation. In general, the average HCT_{Fo} is 0.016 ± 0.040 (95% CI), which overlaps with the zero line. In the HCT analysis, although the observed TSF (time scale factors) are generally lower, the average observed TSF is 2.20±0.18, agrees with the theoretical TSF of 2.43±0.22. Overall, the experimental shows a similar performance between simulator and real apples under scaled time, further validating the possibility of the time scale approach.

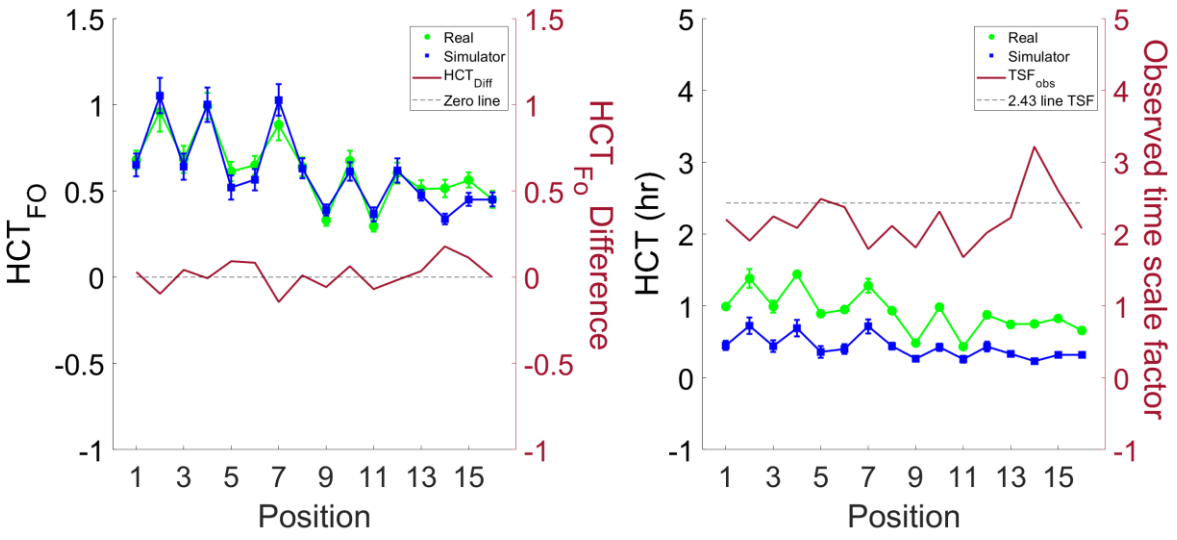

Figure 5-29, Comparison of HCT of real and simulator apples on Fo scale (left) and actual time (right); HCT_{Fo} difference between real product and simulator (left, right axis) and observed time scaled factor (right, right axis)

5.4 Summary and remarks

This chapter has theoretically and experimentally demonstrated the feasibility and applicability of time scaled simulators. The application of the simulator development framework was also demonstrated. Throughout the validation trials carried out in this work, the ease of use of the simulators was clearly noticeable. The work showed that time scaled simulators could provide a meaningful result with only a fraction of the original experimental time. In addition, the simulators are reusable, stable, and controllable, providing a good packaging development and research tool. While it was appropriate to develop individual time scaled simulators for kiwifruit and apples in this chapter, other fruit cooling scenarios exist where individual fruit manufacture is problematic.

An excellent example of this is in table grapes, where the fruit exists in clusters or punnets, and the scale of the fruit are an order of magnitude smaller. The simulator development framework suggests that bulk simulators might be a more appropriate strategy in these scenarios, which is the focus of the next chapter.

Chapter 6. Case study – Bulk simulator development

The previous chapter demonstrated the application of the simulator development framework and the feasibility of the time scaled approach. This chapter will demonstrate the application of the simulator development framework to bulk simulator development.

A simulator for a package of table grapes will be used as a case study. Figure 6-1 shows the Defor package configuration for table grapes (Figure 6-1, A). The footprint of the package is 508 x 406 x 120 mm (L, W, H). Table grapes (approximately 900g) are packed in zip-lock plastic carry bags, and nine bags are packed in the Defor box in a three-by-three configuration, as shown in Figure 6-1, B. Between the carton box and the bags of table grapes, there is a polyliner, a corrugated riffle sheet and an SO_2/moisture absorber.

a) b)

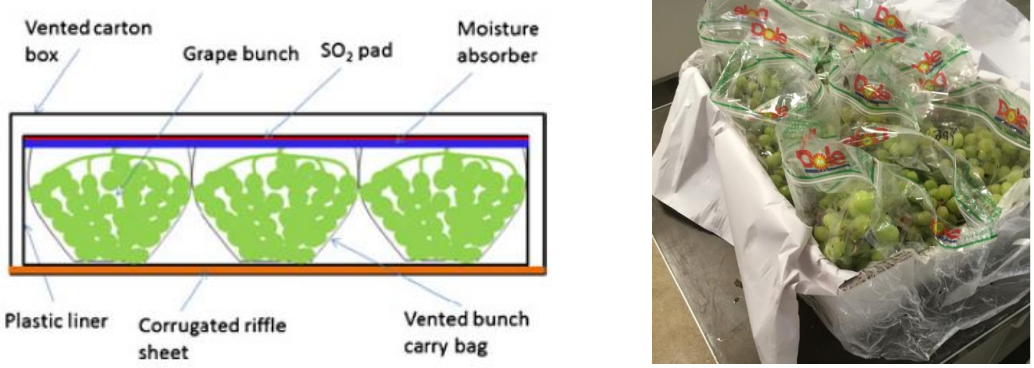

Figure 6-1, Defor packaging configuration, (a) the cross-section of table grape packaging, adapted from Delele et al. (2012) and (b) picture of a Defor box of table grapes

Although the time scaled simulator approach is generally suitable for most applications, the bulk simulator approach could be useful in cases where a large number of small scale fruit are packed, such as berries and cherries. For example, manufacturing large numbers of individual time scaled table grape berries may be intensive and challenging to achieve adequate dispersion of the different component materials using a manufacturing method as shown in Chapter 4. Instead, making a larger bulk collection of fruit would be easier and more convenient for experimental handling.

Chapter 3 has already discussed the effect of the package to produce size ratio (P/p ratio) on the appropriate use of the bulk approximation (porous medium approach). Produce packages with a ratio greater than or equal to 6.7 (often approximated to 10) P/p can be considered a porous

medium. In such cases, the production unit can be approximated as the bulk fruit volume. For example, a bag of table grapes has a P/p ratio of 10, which means a bulk table grape simulator is theoretically possible. Many studies that model the cooling of table grapes have successfully applied the porous medium approach (Delele et al., 2009; Delele et al., 2009a; Delele et al., 2012).

Chapter 3 also discussed the effect of the contour shape of the bulk simulator. In a conduction dominant system, the contour shape of the simulator should include as much air as possible to optimise the approximation of effective thermal conductivity. For example, if the combined Defor package of table grapes is perfectly sealed, there will be no internal airflow through the box. In such cases, a simulator of one overall bulk object can provide an adequate approximation, and a slab with matched effective thermal properties would be sufficient. The modelling study of Amos (1995) demonstrated this on a package of apples. However, if convection has a significant role during the cooling (i.e. airflow can occur between the packets of grapes), the air pockets directly influence the fruit cooling behaviour. Experimental studies suggest that convection could occurred inside a table grape package (Delele et al., 2012; Ngcobo et al., 2012).

6.1 Selection of simulator design approach

Figure 6-2 is the selection framework for the simulator design approach developed in chapter 3 and applied to the Defor box of table grapes. Since the P/p ratio for the table grape package is greater than 6.7 and the Defor box has a multilayer configuration (closed package system); two types of bulk simulators could be considered; 1. The porous medium approach, and 2. The zonal approach.

A zonal approach is a smaller version of the porous medium approach. The study of Ngcobo et al. (2012) shows that the surrounding polyliner contributes the most significant airflow restriction for refrigerated air (60 to 85%), and the table grape carry bags contribute less than 10%. This result suggests that the polyliner has resisted a significant amount of refrigerated air that only a small portion of refrigerated air can pass through the polyliner and then the table grape bag. This finding indicates that the porous medium approach (a bulk simulator representing the whole package of table grape) might not be suitable, as refrigerated air could potentially flow through the polyliner, between bags of table grape. A zonal simulator that represents a bag of table grape could be an option. The Darcy-Rayleigh number of a bag of table grapes is calculated to be 2.4 (smaller than $4\pi^2$), where the permeability is 1.43~2.44 x 10^{-8} m given by Delele et al. (2012), the

characteristic length is 0.06m (half-height of the package) and the maximum temperature gradient is 20 °C.

Overall, the flow of decisions for the simulator development are shown as the green lines in Figure 6-2. Conduction is considered important, and forced convection between bags of grapes is important; thus, the thermal conductivity, thermal mass, and external bag shape (contour) needs to be considered in the simulator development. Radiation and respiration are considered insignificant during precooling (Delele et al., 2012).

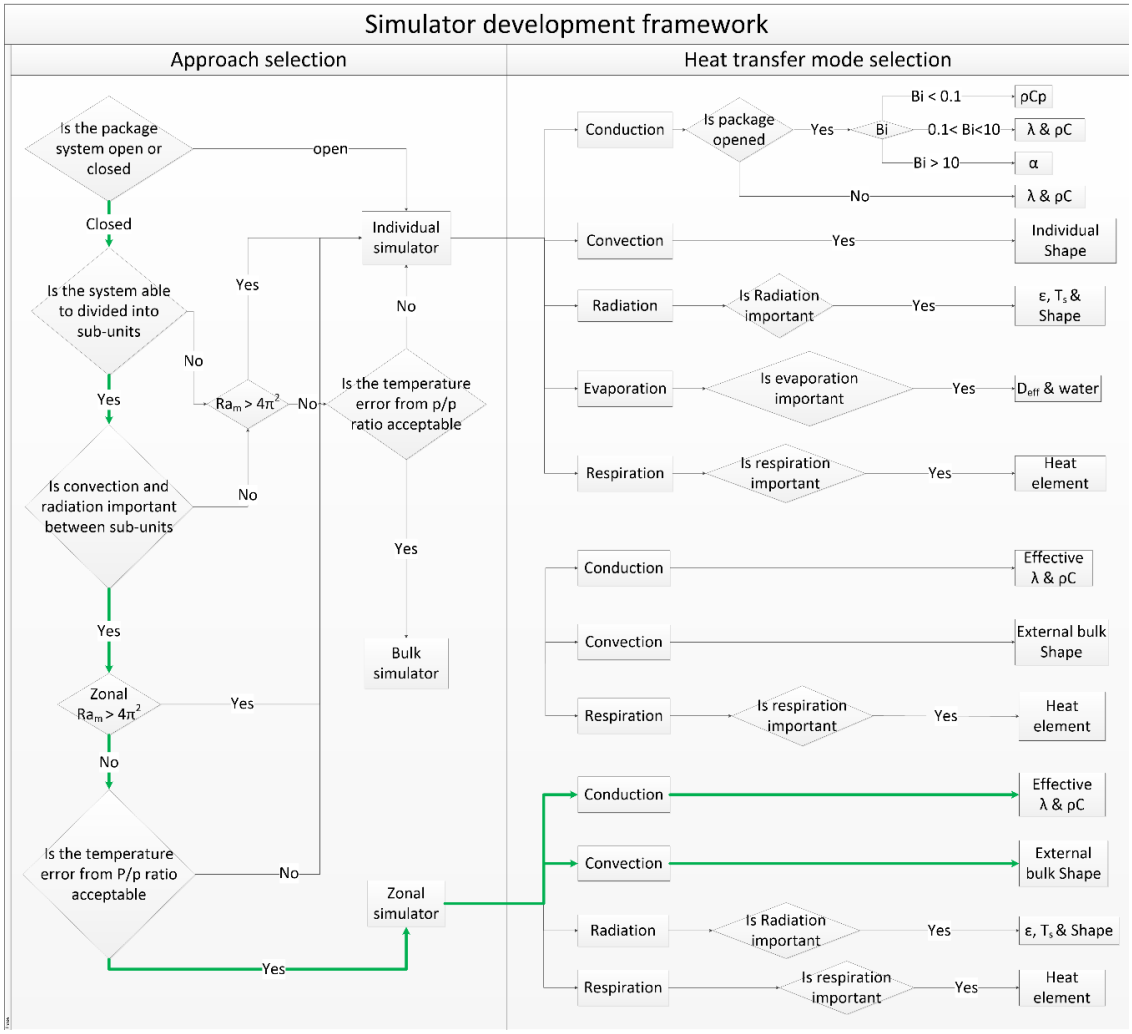

Figure 6-2, Table grape simulator decision tree

In chapter 4, it was shown that there are possible material combinations that match the thermal conductivity and thermal mass required for a bulk simulator (see appendix A). The effective thermal properties are dependent on the horticultural produce and its stacking pattern. Section

6.2.2 shows a detailed analysis of the table grape system. Although some material combinations may match the thermal properties of bulk grapes, the time scaled approach was applied using the combination of polyester resin with Q-cell. This decision avoided time spent on material handling and adapting casting methodology to new materials. However, using a time scaled approach still allows the evaluation of the bulk simulator concept. As a result, the volumetric heat capacity of the bulk grape bags was not matched. Table 6-1 summarises the thermal properties for table grapes (for more detail see Table 2-3).

Table 6-1, Table grape thermal properties based on literature values (from Table 2-3)

Properties	Table Grape
Thermal conductivity ($W\ m^{-1}K^{-1}$)	0.52±0.03
Specific heat capacity ($J\ kg^{-1}\ K^{-1}$)	3555±155
Density ($kg\ m^{-3}$)	1085±30

6.2 Simulator development

6.2.1 Shape

In this scenario, the shape of the bulk simulator is important, as it can affect the heat transfer features of the simulator in many ways. For example, the effective thermal mass can be affected by including a different number (or volume) of air pockets in the simulator; the effective thermal conductivity can be affected by the structure of berry, peduncle and pedicel; and the heat transfer coefficient of the simulator can be directly affected by the shape. In addition, appropriate reproduction of the shape of the individual bags of grapes will also allow flow of air through the box as would occur in the packaged system.

In order to achieve faithful geometry information, a Computed Tomography scan (CT; Brilliance 16P, Philips, Netherlands) was performed on a Defor box of table grapes (Figure 6-3). The shape of the table grape simulator and effective thermal conductivity were developed based on the CT scan image. This CT scanned package was then used for the cooling experiments. Thus, the table grape simulator should theoretically have the same shape as the table grapes used in the validation experiment. Practically, it is believed that the table grape inside the package would have

undergone slight movement during the handling. Nevertheless, this approach minimised the shape difference between the simulator and the experimental table grapes.

Figure 6-3 (left) shows the 3D reconstruction of the CT scans, consisting of 1492 scanned images, each taken at 0.4 mm intervals through the thickness of the box (in the direction of the longest box dimension). The pixel resolution of the scanned image was 750 by 750, and one pixel is equivalent to 0.651 by 0.651 by 0.4 mm (W, H and L corresponding to the package orientation).

Figure 6-4 shows the intensity histogram of the CT scan (the scan in Figure 6-3). In general, higher material density would result in a higher intensity reading. However, if the scanning object is too small or thin, the intensity of that object material could become low. Otsu's method was used to define each material intensity range (MathWorks Inc. , 2020). Theoretically, five different densities of material are presented in the scan: the cardboard package, polyliner, air, grape berry, and the peduncle, pedicel, and stem, which were considered one material. Therefore, four threshold levels should be defined (as red lines in Figure 6-4) to separate these materials. Otsu's method assumes the image histogram exhibits a multimodal distribution in the histogram, providing the corresponding peaks for segregation. This was not the case for the grape package system, as shown in Figure 6-4. The volume of the polyliner and the peduncle, pedicel and stem of the table grape was too small to be effectively separated. As a result, pixels with an intensity lower than 132 (1^{st} threshold) were considered to be air; pixels with intensity between 132 to 837 (2^{nd} and 3^{rd} thresholds) were considered to be the cardboard box and polyliner, and pixels with an intensity higher than 837 (4^{th} and 5^{th} thresholds) were considered to be table grapes, which included berries, peduncles, pedicels and stem. All pixels smaller than 837 (3rd threshold) were reset to zero to remove the cardboard box and polyliner in the image, resulting in the segregated table grapes in Figure 6-3 (right).

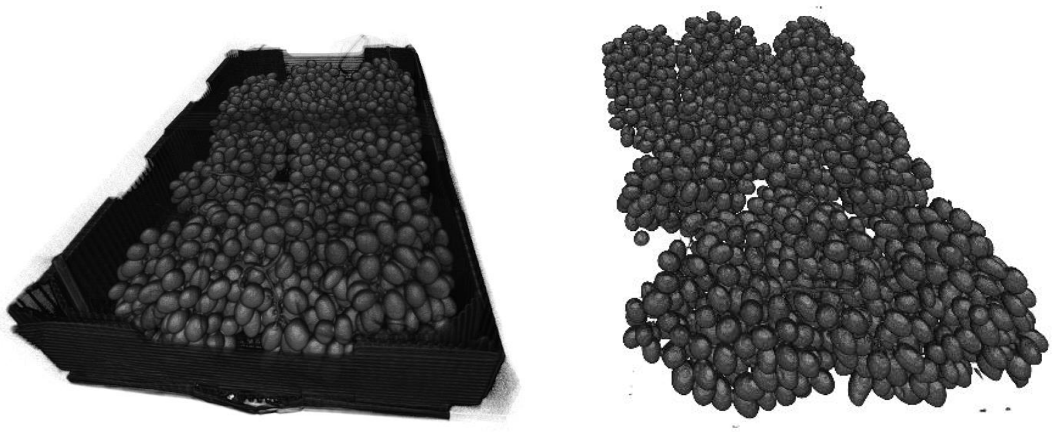

Figure 6-3, CT scan image of the table grape package (left: without segmentation, right: removed package material)

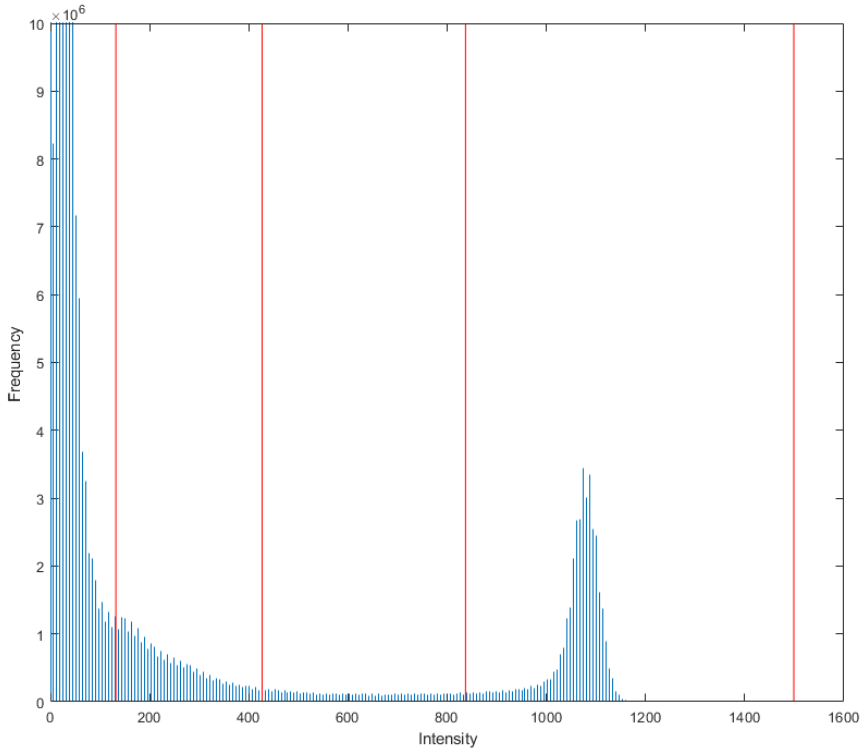

Figure 6-4, Intensity histogram of the CT scan

The image was then cleaned by assuming the table grapes are interconnected as one object, and any unconnected small objects are noise from previous segregation. For example, the dots in the right bottom corner of Figure 6-3 (right) were removed by this algorithm, resulting in a 1 % volume reduction which was considered to be insignificant.

Segmentation of overlapping objects is generally daunting, and segmenting the CT scan into nine well-defined bags of table grapes is challenging. Segmenting the table grapes based on the plastic bag was considered, but this approach was not used due to the resolution limit of the plastic bag (i.e. the film thickness was much smaller than the pixal resolution). The application of k-mean clustering was also considered. Pixels were converted into x, y and z coordinates, and the k-mean clustering approach was applied. Nevertheless, no precise segmentation was achieved. K-mean clustering on individual table grape centroids was considered; however, this would be programmatically and computationally intensive (segmentation of individual grape berries would be needed before the clustering). Finally, an adaptive watershed segmentation method was developed and used based on Chinea Valdés and Lorenzo-Ginori (2011) and MathWorks Inc. (2020a). Instead of applying watershed segmentation on separate individual grapes, which could not be validated later, the CT image was first converted into a bulk shape by merging all the possible air pockets and then applying the adaptive watershed to segment nine bags of table grapes.

Figure 6-5 shows the flowchart of the segmentation algorithm. The processed CT image (matrix A) was first binarised, and then binary dilation and erosion were performed. Both binary dilation and erosion rely on an inspecting matrix (matrix B). In binary dilution, every pixel equal to '1' in matrix A converts its matrix B equivalent surrounding into '1'. In binary erosion, matrix B is superimposed onto matrix A and moved around. If the pixels in the superimposed area are not all equal to '1', the pixels in the superimposed area will be converted to '0'. Matrix C is the product after binary dilation and erosion, which is the bulk shape of the table grape (Figure 6-6 left). Euclidean distance transformation and H-minima transformation were applied on matrix C to produce markers. Markers are the regional minima for the watershed separation. Figure 6-6 (right) shows the markers (the shadow inside the grape) and the corresponding separation.

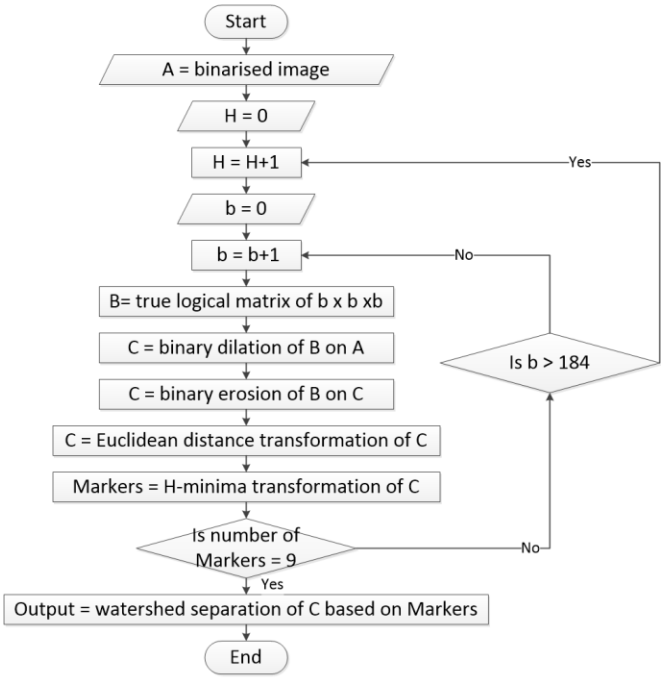

Figure 6-5, Adaptive watershed algorithm

The size of matrix B and the H value (the incremental threshold value in H-minima transformation) were iterated until nine marks were produced. In the binary dilation and erosion, a cube inspecting matrix was used (matrix B; b by b by b) as the simulator contour shape optimisation was not considered. Further study can be conducted on using other shapes of inspecting matrix for a smoother merging transition and then studying the contour shape's effect on simulator performance. The dimension of the Defor box package is 120 x 406 x 508 (H, W, L; equivalent to 184 by 623 by 11270 pixels). Therefore, the equivalent height of matrix B should not exceed the actual height of the package. For this reason, the size of matrix B was kept smaller than 184 by 184 by 184, as this means the matrix equivalent size becomes 119.7 by 119.7 by 73.6 mm (H, W, L). So when the value of b exceeded 184, the iteration was restarted with a new iterated H-value.

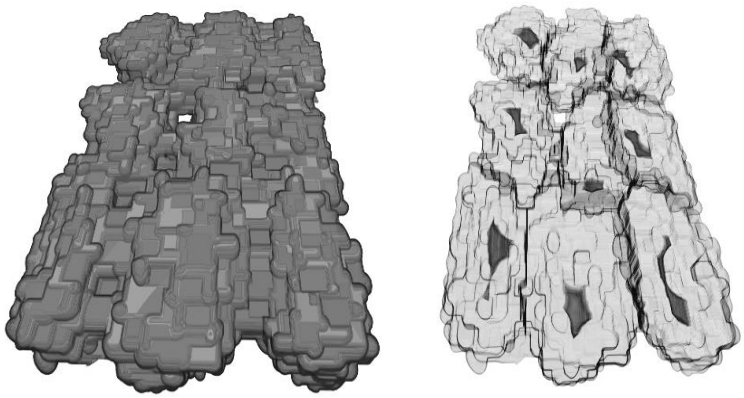

Figure 6-6, Bulk shape table grape (left) and segmented bulk shape table grape with markers (right)

Figure 6-6 (right) shows nine bulk shapes of segmented table grapes. The segmentation between the table grapes appears to be logical and reasonable. In order to validate the adequacy of the separation, the segmentation boundaries were applied to the table grape image (Figure 6-3, right). The mass of the separated table grape was calculated by multiplying all the pixels with the equivalent dimension (to become the equivalent volume), summing them all and multiplying by the density of the table grape berry (1079 $kg\ m^{-3}$; Table 2-3).

Table 6-2, Table grape weight measurement CT scan calculation vs Experimental

ID	CT calculation (kg)	Exp measurement (kg)	Difference (%)
1	1.162	1.246	7%
2	0.999	1.112	10%
3	0.670	0.683	2%
4	0.787	0.665	-18%
5	0.639	0.721	11%
6	0.849	0.890	5%
7	1.035	0.932	-11%
8	0.857	0.840	-2%
9	0.674	0.630	-7%
Total	7.670	7.719	1%

Table 6-2 compares the calculated values based on the CT scan and experimental measurements. It was expected that the accuracy of image segmentation would not be perfect. The maximum difference in mass was 18% (122 g) and the average difference was 8% (54 g); however, this was acceptable for this application. The total weight of the CT calculation is similar to the experimental measurement, with only a 1% difference, which is acceptable. The segmentation should not affect

the actual image volume, but some volume associated with one bag may have been transferred to another neighbouring bag.

6.2.2 Thermal properties

6.2.2.1 Effective thermal conductivity of bulk table grape

The time scale approach was used in this case study so determining the effective thermal conductivity of the bulk table grape was essential. The effective medium model (Equation 4-3) could be used to predict the effective thermal conductivity of a bag of table grapes. Also, finite-difference simulations were used to estimate the effective thermal conductivity because the CT scanned image was available.

$$\sum_{i=1}^{n} \frac{\lambda_e - \lambda_i}{\lambda_i + 2\lambda_e} = 0 \qquad \text{Equation 4-3}$$

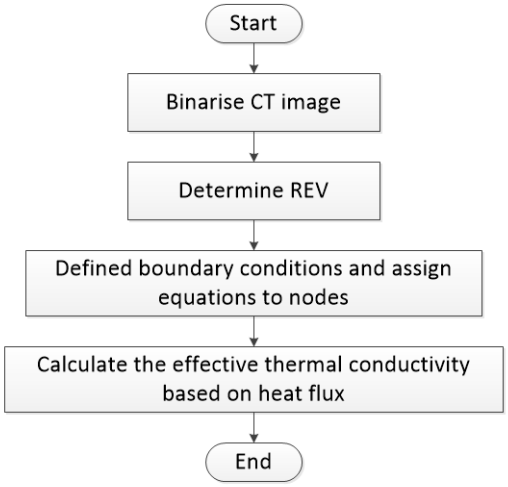

Figure 6-7, Flowchart for estimating effective thermal conductivity based on finite difference simulation

Figure 6-7 shows the flowchart for determining the effective thermal conductivity of the table grape. The CT scan image was first converted into a binary matrix, where '1' represents the table grape berry and '0' represent the air pockets between them. As the resolution of the CT scan is high and therefore the finite difference simulation could become computationally intensive, a representative element volume (REV) of the CT scan was determined.

Figure 6-8 shows the determination of REV for each bag of table grapes in the package. The actual volume fraction of air (p_d) can be calculated by the sum of air pixels inside divided by the sum of bulk table grape bag pixels (segmented from Figure 6-6). For calculating the volume fraction of REV, a 'window' in the centre of the image was defined, and the volume fraction could be calculated as the sum of table grape berry pixels divided by the sum of the 'window' pixels. The size of the 'window' was iterated from 5 by 5 by 5 to 150 by 150 by 150 pixels. As the window size grows larger, its volume fraction will become closer to the actual volume fraction. The REV can be determined when the window's volume fraction no longer changes as the 'window' size increases. In general, as shown in Figure 6-8 the minimum REV size was decided to be 100 by 100 by 100 pixels, although the volume fraction of REV still has a slight change above this window size. It is interesting to point out that all the REV volume fractions were above the actual volume fraction, which could be due to the definition of the bulk table grape edge (i.e., some air pockets at the surface of the grape bunches were included in the geometric shape).

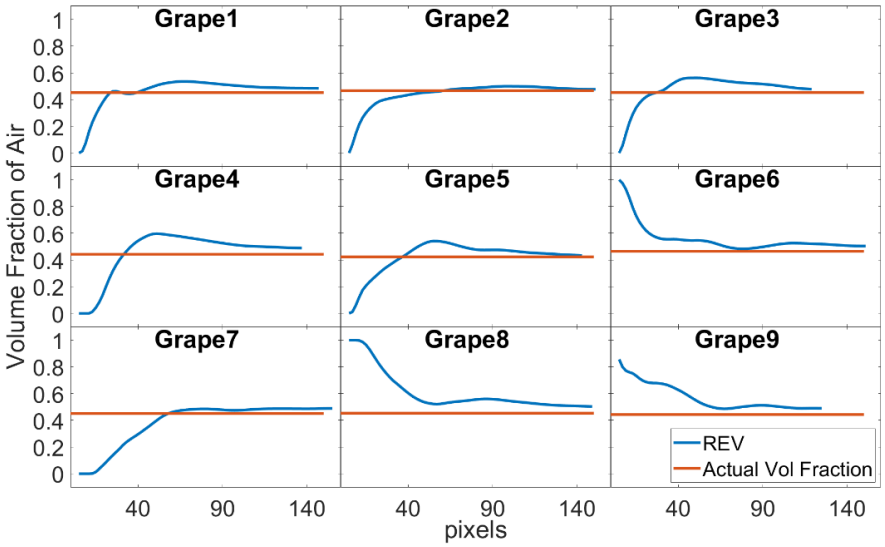

Figure 6-8, Determination of REV based on the 'window' size (pixels) vs air volume fraction

After the REV was determined, governing equations were assigned to each node (Figure 6-9). The Fourier equation can describe all the nodes not on the boundary (Equation 6-1). All the nodes on the side boundary were defined as no heat flow (Equation 6-2). The top and bottom boundary nodes were defined as a constant temperature (Equation 6-3). A 20°C temperature difference was applied (20 and 0 °C, respectively). Any pixel with a value of '1' was defined as a table grape, and the corresponding thermal properties were used. Likewise, any pixel with the value of '0'was

assigned air properties. Afterwards, the finite-difference solution was used to calculate the average heat flux at the top and bottom boundaries. This heat flux could be used to calculate the effective thermal conductivity (Equation 6-4).

Fourier equation

$$\frac{\partial T}{\partial t} = \frac{\lambda_{eff}}{\rho c} \nabla^2 T \qquad \text{Equation 6-1}$$

Side boundaries

$$\nabla T = 0 \,; \nabla T = 0 \qquad \text{Equation 6-2}$$

Top and bottom boundaries

$$T = T_c \qquad \text{Equation 6-3}$$

Thermal conductivity

$$\lambda = \frac{QL}{T_{bottom} - T_{top}} \qquad \text{Equation 6-4}$$

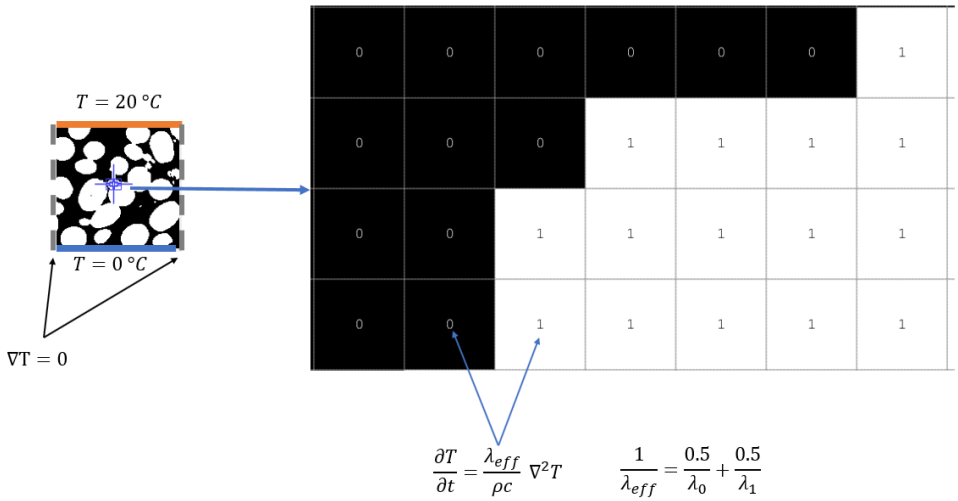

Figure 6-9, Cross-section of finite-difference for REV

Table 6-3 shows the prediction of effective thermal conductivity from the effective medium theory and finite-difference solution based on REV and the actual volumes of table grape. In general, the effective medium theory gives a lower prediction for REV than the actual volume, which is

expected, as the air volume fraction of REV is slightly lower than the actual. Although the average REV volume fraction is about 10% smaller than the actual volume fraction, REV's predicted effective thermal conductivity is 15% smaller. This observation suggests that the effective medium theory model is sensitive to the volume fraction. The calculated effective thermal conductivity from the finite-difference solution gives an even smaller value than the values given from the effective medium theory. Nevertheless, the calculated effective thermal conductivity from the finite-difference method was used for the simulator development. This is because the effective medium theory is an empirical model that does not consider the shape and structure of the dispersed phase (the air), whereas the finite-difference did consider these aspects of the bulk table grape and therefore, the finite-difference method should provide a more realistic value (Carson, 2002). Also, the CT scan image provides more than sufficient 'nodes' for the calculation to ensure the finite-difference calculation is adequate. Therefore, the effective medium theory model was used in this case to ensure that the finite-difference method provides similar ballpark values. On average, the effective thermal conductivity of bulk table grapes was determined to be 0.126±0.023 $W\ m^{-1}K^{-1}$.

Table 6-3 Effective thermal conductivity from EMT and Finite Differences

Table grape ID	REV p_d / actual p_d	Effective medium theory ($W\ m^{-1}\ K^{-1}$)		Finite-difference ($W\ m^{-1}\ K^{-1}$)
		$\boldsymbol{\lambda_{REV}}$	$\boldsymbol{\lambda_{Act}}$	λ_{REV}
1	0.500/0.452	0.174±0.007	0.205±0.009	0.119±0.002
2	0.499/ 0.466	0.175±0.007	0.196±0.008	0.130±0.001
3	0.498/ 0.453	0.176±0.007	0.204±0.009	0.125±0.001
4	0.506/ 0.442	0.171±0.007	0.211±0.009	0.116±0.002
5	0.466/ 0.423	0.196±0.008	0.224±0.010	0.148±0.001
6	0.523/ 0.464	0.160±0.006	0.197±0.008	0.117±0.002
7	0.477/ 0.450	0.189±0.008	0.206±0.009	0.138±0.000
8	0.540/ 0.453	0.150±0.006	0.204±0.009	0.113±0.002
9	0.498/ 0.443	0.176±0.007	0.210±0.009	0.107±0.002
Average	0.500/0.450	0.174±0.030	0.206±0.028	0.126±0.023

6.2.2.2 The volumetric heat capacity of bulk table grapes

The effective volumetric heat capacity can be calculated based on the volume fraction (Equation 6-5), and Table 6-4 shows the upper and lower value of each bag of table grapes, which

considered the variation of table grape berry's thermal properties(Table 2-3). The density and heat capacity of the table grape berry can be found in Table 2-3. It is noteworthy to point out the average difference between the upper and lower value is 270 $kJ\ m^{-3}K^{-1}$, which is approximately 15 to 20% and is due to the range of heat capacity and density data reported in literature for table grapes that was used in Equation 6-5. The average difference across all bags of table grape is 61 $kJ\ m^{-3}K^{-1}$ for upper value and 52 $kJ\ m^{-3}K^{-1}$ for lower value. This shows that the variation in volume fraction between bags is much smaller than the variation due to the uncertainty in thermal properties of the table grapes.

Note that the volumetric heat capacity is important for the time scale factor calculation, even if it is not matched in the simulator design. This difference potentially means each bag of table grapes has a different time-scaling timeframe. In order to handle this, the average volumetric heat capacity was used with the upper and lower values used as uncertainty bounds, so that the offset of volumetric heat capacity would be considered to be the experimental variation.

$$\rho Cp_{eff} = pd\ \rho Cp_1 + (1 - pd)\rho Cp_2 \qquad \text{Equation 6-5}$$

Table 6-4 Effective volumetric heat capacity of table grapes

Table grape ID	REV p_d / actual p_d	Upper value ρCp_{eff} $(kJ\ m^{-3}\ K^{-1})$	Lower value ρCp_{eff} $(kJ\ m^{-3}\ K^{-1})$
1	0.452	2069	1794
2	0.466	2073	1798
3	0.453	2077	1801
4	0.442	2044	1773
5	0.423	2210	1916
6	0.464	1974	1712
7	0.450	2164	1877
8	0.453	1903	1651
9	0.443	2077	1801
Average	0.450	2066	1791

6.2.3 Prototyping

Although quite a few thermoplastics and thermoset materials (Figure 4-2) could be used to match both the thermal conductivity and thermal mass of the bulk table grape, the simulator was manufactured using polyester resin with Q-cell filler. Because the properties were already

measured and known, and the casting behaviour is well-understood as described in the previous chapter, it made sense to use this material. If a fully matched bulk simulator is required in future work, it could be manufactured from thermoplastic by CNC machining.

6.2.3.1 Casting moulding development

The bulk table grape simulator has an irregular shape, so manufacturing using silicone moulds would be ideal due to their flexibility which aids in demoulding. Nevertheless, making a silicone mould for a bulk table grape simulator means two process steps are involved; a master simulator (positive mould) needs to be made first and then using this master simulator to make the silicone mould (negative mould). Creating the positive mould could be as complicated as creating a negative mould base on a CAD object (the Table grape shape from section 6.2.1). Therefore, it was interesting to explore alternative mould making methods based on the CAD drawing. Three rapid prototyping methods for mould making were tested: CNC machining, 3D extrusion printing and selective laser sintering (SLS) printing. The CNC machining was carried out using medium-density fibreboard (MDF, Lakepine Zero, New Zealand) and rigid polyurethane foam (Formathane, Forman, New Zealand). The 3D printing material for the mould making was carried out using PLA filament (Up Fila, Tiertime, China), and the SLS printing material for the mould making was nylon powder (Precimid 1170, Advanced Moulding Solutions, USA).

Figure 6-10 shows the photographs of the moulds made using the four materials. As shown in Figure 6-10, the table grape simulators were cast from serval parts instead of casting one entire bulk simulator. Casting one big piece of material could result in uneven temperature distribution causing significant shrinkage. Also, many undercut edges make the demoulding process very difficult. Undercuts are object edges that are not perpendicular to the mould parting line which causes issues with demoulding by trapping the cast material within the mould. The bulk table grape mould consisted of either, eight parts (for SLS and 3D printing method) or four parts (for CNC method) to reduce the effects of undercuts. The needle shown in Figure 6-10 B was used to make a guide hole for thermal conductivity measurements afterwards (the line source method as previously described in section 4.2.2).

In general, CNC machining soft materials, like MDF and rigid foam, for mould making has a relatively short manufacturing time (approximately 30 minutes), but the reusability of the mould is low. The MDF mould was broken after a single use (Figure 6-10 A). The MDF mould was made of a

stack of 25 mm MDF sheets glued together and then shaped by the CNC machine. The glued areas were generally the fracture point during demoulding. The rigid foam mould is also not a durable option, as it needs to be fully dismantled to retrieve the cast part. The mould material firmly adheres to the part, even if multiple layers of mould release agent were applied. As a result, the grape simulator needed to be sanded down to remove the remaining foam material.

The mould made from 3D extrusion and SLS printer had similar manufacturing times. It took approximately 60 to 80 hours to print a set of mould components. Even though the printing methods could generate undercuts on the moulds, the parts were relatively easy to be demoulded, and the moulds could be reused. It was challenging since defective parts were often produced in 3D extrusion or SLS printing, but the study of 3D printing improvement was outside of the project scope.

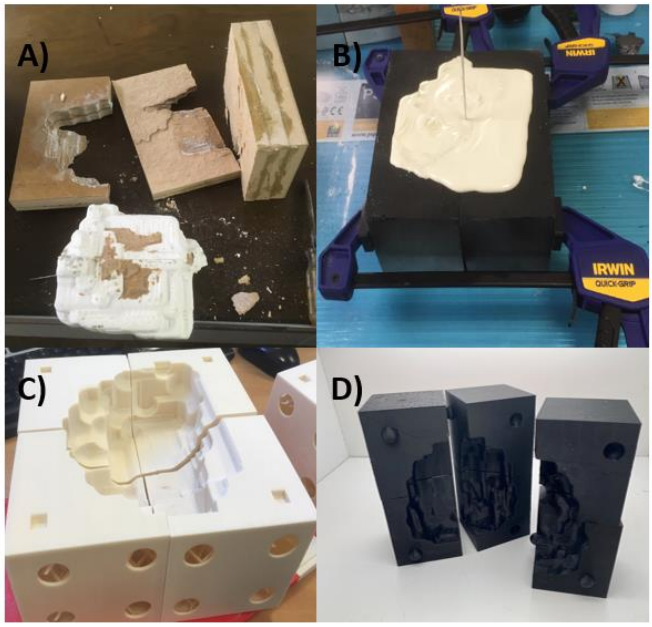

Figure 6-10, Pictures of the moulds, A) CNC MDF, B) CNC rigid foam, C) SLS Nylon D), and 3D print PLA

Table 6-5 shows the tolerance check of the simulator properties against expected values, where the table grape simulator volumes were calculated from the CT bulk table grape image (Figure 6-6 left; the sum of all pixels multiplied by the pixel dimensions). The simulator weights were directly measured, and the simulator volumes were calculated based on the simulator density (680 $kg\ m^{-3}$). In general, the bulk table grape simulator was about 7.3% smaller than the image

calculated value, which is expected as the polyester resin will shrink after casting, and this shrinkage is particularly significant in casting large objects.

Bulk table grape simulator 3 was 26.6% larger than the image calculated value due to a 3D printing error on the mould. The mould would have been remade in an ideal situation, and a new simulator cast from it. However, due to the limited supply of PLA filament and the availability of the 3D printer, the difference was accepted. In fact, a high percentage of 3D printing products were rejected due to defects. If many moulds are needed, an industrial-grade 3D printer should be considered.

Bulk table grape simulator 9 was 14.8% smaller than the image calculated value because the surface of the simulator was sanded to remove the residual foam material. The sanding process could remove a considerable amount of the simulator surface, resulting in a smaller volume. Overall, no prototype method and mould material could be recommended, as each method had significant disadvantages. Further studies could be conducted in the future to optimise the prototyping method.

Table 6-5, Manufacture tolerance check

ID	Simulator weight (kg)	Volume (m^3)	Volume from CT scan (m^3)	Difference (from CT volume)	Method and material
1	1.2391	0.00182	0.00194	5.9%	CNC/MDF
2	1.1148	0.00164	0.00169	3.0%	3D/PLA
3	1.0291	0.00151	0.00120	-26.6%	3D/PLA
4	0.8416	0.00124	0.00131	5.3%	3D/PLA
5	0.6781	0.00100	0.00108	7.9%	3D/PLA
6	0.9987	0.00147	0.00154	4.6%	3D/PLA
7	1.1291	0.00166	0.00183	9.2%	CNC/MDF
8	0.9028	0.00133	0.00144	8.1%	SLS/Nylon
9	0.6656	0.00098	0.00115	14.8%	CNC/Foam

6.2.3.2 Casting material

Based on the work summarised in chapter 4, polyester resin and Q-cell mixture were identified as suitable for this case study, although the time scaling approach must be adopted. The mixture composition for the bulk table grape was determined based on Figure 4-9, where 42% (vol) of Q-cell with 58% of polyester resin should achieve the targeted thermal conductivity. Table 6-6 summarises the individual table grape berry, the targeted effective properties for the table grape,

and the measured properties for the table grape simulator (detail of the measurement methods are shown in section 4.2.2.).

Table 6-6, Thermal properties summary of individual grape berry, bulk table grape and the simulator

Properties	Table grape berry	Bulk table grape	Simulator
Thermal conductivity ($W\ m^{-1}K^{-1}$)	0.523±0.026	0.126±0.023	0.164±0.007(n=18)
Specific heat capacity ($J\ kg^{-1}\ K^{-1}$)	3555±155	3471±236	1492±167 (n=1)
Density ($kg\ m^{-3}$)	1085±30	541±55	779±1 (n=2)
Volumetric heat capacity ($kJ\ m^{-3}\ K^{-1}$)	3861±275	1891±319	1162±132

6.3 Validation

Validation experiments were conducted on the same Defor package of real table grapes that were CT scanned as explained previously. This was compared with a package constructed using the bulk table grape simulators (Figure 6-11). Thermocouples were embedded in the approximate centre of the bag of the table grapes inside the berry (Figure 6-11, C), whereas thermocouples were embedded in defined positions in the bulk table grape simulators (Figure 6-11, D). Nine thermocouples were used on each of nine bags of table grapes. The number of thermocouples was minimised for cable management, as the wire can be easily pulled out of position from the table grape berry. Fifty-four thermocouples were embedded in the pre-drilled positions of the simulators, where each simulator had six thermal couples embedded to accommodate the uncertainty of the thermocouple position in the real table grape experiment. Thermocouples were placed 2 cm away from the approximate thermal centre in all directions (up, down, front, back and sides). Thermal paste was used to maximise thermal contact between the wire and the material. The thermocouples were secured by tape to minimise unnecessary movement. The packaging detail is as described in Figure 6-1. The bulk fruit simulators were placed inside the plastic bags and packed in the same arrangement as found during CT scanning, which mimics the air pocket patterns between the grapes and the nearby surface.

a)

b)

c)

d)

Figure 6-11, Experimental setup for table grape and bulk table grape simulator experimental, a) table grapes, b) bulk table grape simulator, c) thermocouple in table grape berry, and d) thermocouples in fixed positions

Figure 6-12 shows the cooling wind tunnel setup. The package of table grapes was placed on a wire mesh in a wind tunnel (1 by 0.8 by 0.4m, L, W, H). The table grape/simulator packs were initially equilibrated to approximately 20°C and then cooled with the refrigerated air (3.5 $m\ s^{-1}$ superficial air velocity, approximately 0 °C). After the first cooling cycle, the package was equilibrated to approximately 20 °C again without modification or movement. This equilibrated package was then cooled for a second time inside the wind tunnel. Three replicates of simulator cooling (6 heating/cooling cycles) were conducted, and one replicate of table grape cooling was conducted. The simulator cooling was replicated by fully disassembly and re-assembling of the thermocouples and packages. The re-assembled package was then used for the next cooling experiment. The replicates allowed investigation of the variation in data collected for true replicates, something that is very difficult to achieve with horticultural produce as thermocouple position is challenging to reproduce.

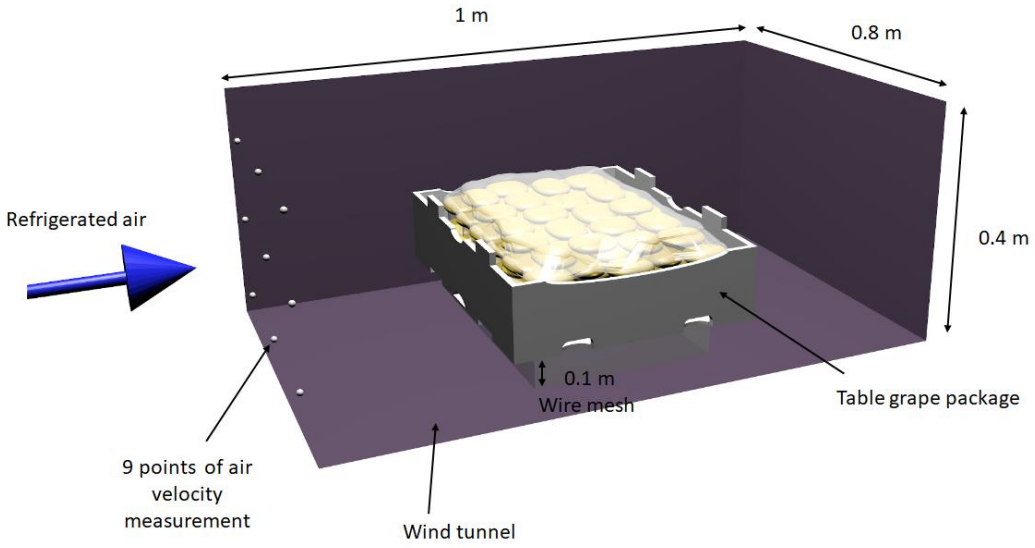

Figure 6-12 Experimental setups for the cooling wind tunnel experiments

Figure 6-13 compares table grape and bulk table grape simulator data under scaled time. The dimensionless temperature (Y) profile band for real table grapes (green) generally overlap the overall simulator cooling profiles (blue, red and yellow), apart from bags 3 and 8. The band considers the upper and lower thermal property values (for the Fo calculation) and the experimental variation within the two cooling cycles. In addition to this, the bands for simulators also consider the positional variations (6 thermocouples per bag of table grapes). On average, MAD between the table grape and the table grape simulator is 0.16 (excluding bag 3 and 8), which is equivalent to 3.35°C. This difference could be acceptable depending on the experimental purpose, such as comparing the cooling rates caused by different package/vent designs.

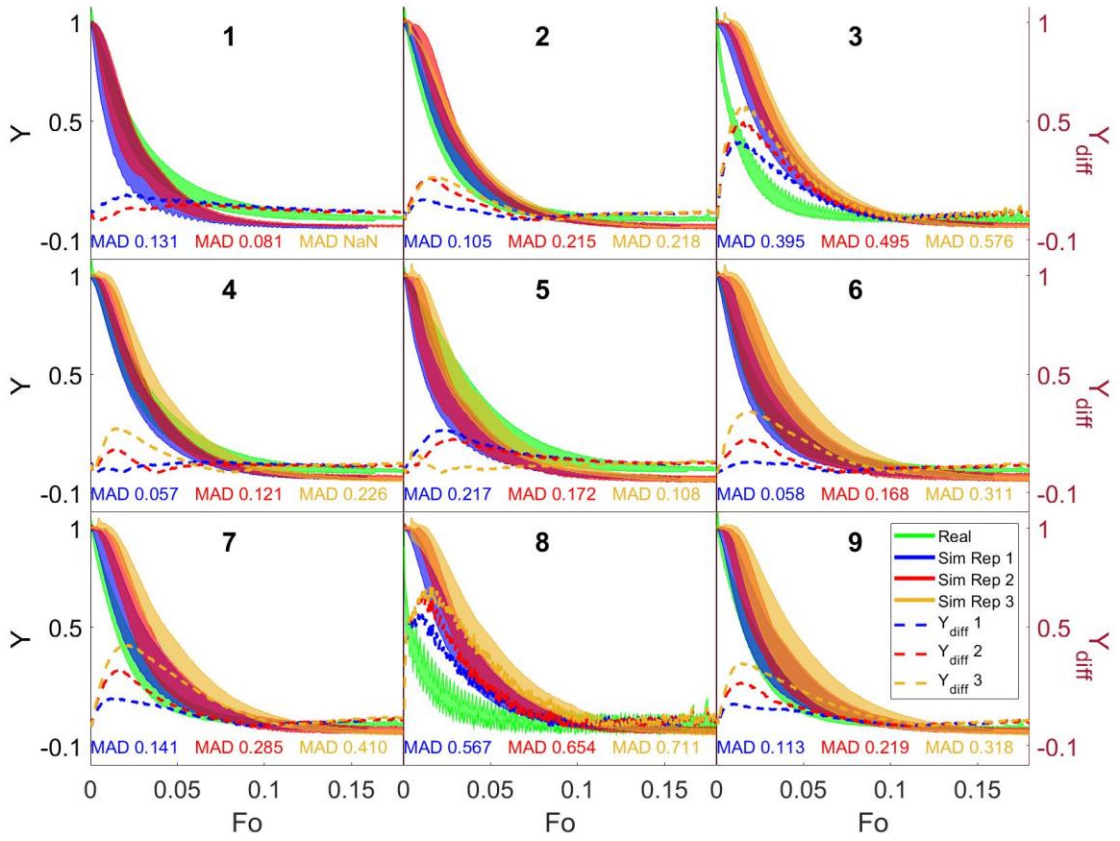

Figure 6-13 Derived temperature profile of real table grape, bulk table grape simulator and the average difference in Y

The fluctuation pattern of table grape data in bags 3 and 8 suggests displacement of the thermocouples in these two bags. The table grape package was carefully handled throughout the experiment, but unavoidable handling error can occur, showing the difficulty of ensuring good thermocouple placement. As a result, table grape bags 3 and 8 cooled faster than the bulk table grape simulator. The temperature fluctuation of bags 3 and 8 suggests a non-thermal equilibrium between the air pocket and table grape berry inside the bag and that the thermocouples in these bags could have been in the airspace within the grape bunches. Refrigerated air could potentially flow through the package layers or it may be sensitive to change due to the thermocouple end having very little thermal mass when not inserted in the fruit properly. The bulk simulator assumes thermal equilibrium inside the stack of the bulk product, so conduction is the dominant heat transfer mode, and effective thermal conductivity would be the important parameter.

Real table grapes were generally warmer than the bulk simulator at the same time scaled time, and the Y value of table grapes did not reach zero. This suggests that the heat of respiration could

be significant in table grape cooling. However, the bulk table grape simulator is limited to excluding this heat transfer mode. As a result, the simulator could cool faster (after time-scaling) than the table grapes.

Regardless of the limitation of non-thermal equilibrium and respiration heat, the bulk table grape simulator provides a reasonable approximation on the cooling of table grapes (as mentioned above). This suggests that the bulk table grape simulator is still a useful tool to simulate the cooling of table grapes and how operation or packaging configuration might influence cooling performance.

It is also worthwhile to consider the reproducibility of the bulk table grape simulator by comparing simulator replicates 1 to 3, in Figure 6-13. Although the bands generally overlap, the experimental variation could still be significant. For example, in bag 7, the simulator replicate one overlaps with replicate two. Replicate two also overlaps with replicate three; however, replicate three does not overlap with replicate one. Bags 6 and 8 have similar outcomes. Even though the thermocouple position and product thermal properties were controlled, experimental variation could still be significant. The experimental variation for a real product is likely to be even more substantial. The advantage of the time scaled bulk simulator is that it allows multiple controlled condition experiments to be conducted relatively quickly. In the case of package-design experiments, multiple tests can be performed to confirm the statistical significance of how package design influences precooling performance.

6.4 Summary and remarks

The simulator design framework was used to demonstrate the development of a bulk simulator for table grapes. A CT scanning process flowchart was established for developing irregularly shaped simulators. The product's bulk shape and effective thermal conductivity can be determined based on this data with a systematic process.

Time scaled bulk table grape simulators were developed and validated against real table grapes. Although the bulk table grape simulator did not provide behaviour that perfectly matched the cooling of real table grapes, the simulator provides a reasonable approximation. The bulk simulator provides more controllable packing scenarios and thermocouple placement, allowing experiments to be carried out more readily and reproducibly.

Chapter 7. Conclusions and future research

7.1 Conclusion

This research set out to develop a standard framework for fruit simulator development. This was demonstrated by applying this framework to manufacture kiwifruit simulators for forced air cooling optimisation purposes. The generalised framework was then tested by developing individual apple simulators and zonal bulk table grape simulators. All the developed simulators were validated against data collected for the targeted horticultural produce, and the results show good agreement. Overall, the main goal of this research work was achieved.

A literature review was conducted in chapter 2, which identified the need for a simulator in cooling experiment studies, and state of the art was reviewed. From this, the theoretical concept of time scaling for simulators by Redding et al. (2016) was discovered, and this concept was explored and tested extensively in this research work.

A comprehensive analysis was conducted to develop the understanding of heat transfer mechanisms during horticultural cooling in chapter 3, and based on that understanding, a simulator development framework was established. This guides developers which necessary thermal properties are important to include in simulator design for different applications. Ratios are proposed to quantify the significance of the heat transfer modes or simulator features. Biot (Bi) number can be used to evaluate the internal conduction of the product; and hence, to determine the corresponding matching thermal properties. The ratio of the product and ambient thermal conductivity can be used to determine the significance of the heat conduction via thermal contact; and hence, to determine if the simulator needs to be soft or not to mimic the contact area. Raleigh (Ra_m) number can be used to evaluate the significance of internal natural convection inside a closed system. The ratio of heat transfer coefficient to mass transfer coefficient could be used to evaluate the importance of evaporative heat transfer during cooling for an open package system. Furthermore, the package to product length ratio (P/p) can be adapted from porous medium model development, which provides guidelines for deciding on the use of bulk versus individual simulator approaches. If individual simulator is considered, the use of time scale approach could be a potential option to ease the material selection process.

A systematic material selection method was developed in chapter 4, where an algorithm was constructed for single-phase and multiphase material selections. By inputting a material database with their associated properties, the program can select suitable single-phase materials or iterate through the database to provide the possible material combinations with the suggested mixing ratio. Material combinations that met the general requirements for fruit simulators (individual and bulk) were then demonstrated by casting fabrication. Various types of mould material for the casting were tested. Although no recommendations for the mould material could be given as each material has its own advantage and disadvantages, the study provides some useful information for future studies.

Time scaled kiwifruit and apple individual simulators were developed in chapter 5. The kiwifruit simulator was developed first, and the framework was then further tested by developing the apple simulator. Overall, both simulators match the cooling performance of the corresponding products, and the results confirm the validity of the time scale approach in experimental studies.

The kiwifruit simulator was tested and validated in various experimental scales. The validation of the time scale simulators demonstrates the significant benefit for future cooling experiments, such as shortening the experimental time and providing a consistent, stable and durable testing product.

The experimental variation was also analysed for the kiwifruit simulator experiments in chapter 5, since multi experimental trials were conducted. Although the analysis shows that the simulator tends to have less experimental variation compared to real kiwifruit, the improvement is not statistically significant, and the improvement is not as significant as is believed by many studies (Pathare et al., 2012; Redding et al., 2016; Vigneault & Castro, 2005). Much of the variation caused by alterations in individual fruit orientation and stacking arrangements that would occur in real fruit would also be present when using individual simulators. Ideas such as fixing individual fruit simulators together in a solid formation may allow reduction of variation due to these effects. Other sources of variation such as the placement of polyliners relative to vents and fruit are likely to still contribute to differences in cooling rates to some extent.

A bulk table grape simulator was also developed, and outlined in chapter 6. Its design was also based on the simulator development framework outlined in Chapter 3. This was to test if the framework is suitable for a bulk simulator development. A process of using CT scanning to

reproduce the shape of the scanning object was developed, including an algorithm for cluster segmentation. Both the process and the algorithm can be used in other areas of study. The developed bulk table grape simulator from the CT scan was validated against the real table grape (the same grape package that was scanned). A reasonable match between the simulator and table grape was obtained, which further confirmed the usability of the simulator development framework.

The findings of this research provide a sound and systematic basis for development of fruit simulators and a valuable tool for optimisation of post-harvest systems. The resulting simulators can be used year round (non-seasonal), have fixed properties (can be used repeatedly without change) and can result in reduced variability or more controlled experiments. The concepts and frameworks developed in the work could also be expanded to other applications in the postharvest industry or the wider food sector.

7.2 Future research

This research leads to:

- Application of the fruit simulators or fruit simulator development framework to other heat transfer applications
- Extension of the fruit simulator framework to a wider range of applications where other (non-heat transfer related) properties require matching

7.2.1 Expansion of the simulator development framework

Potential application of the simulator on refrigerated container studies

In this research work, the simulator development framework was mainly focused on heat transfer applications, particularly in horticultural produce precooling. There are a number of other scenarios throughout the supply chain where heat transfer is a key consideration to operation and fruit quality. Container cooling and refrigerated transportation (Taher et al., 2021) are research areas becoming focused on and where simulators could be employed. Such systems have quite different air flow regimes, often much slower heat transfer dynamics and heat of respiration may also be important. The simulator design framework could be applied to these scenarios directly with minimal changes or extensions.

Expansion of the development framework

Beyond heat transfer applications, it is believed that the scope of the simulator development framework could be expanded for other simulator applications. For example, Figure 7-1 shows a generalised concept of the potential framework expansion (the list is not exhaustive). Each module under the simulator umbrella represents a series of logical decisions for selecting the important properties that should be considered in simulator design. For example, Figure 3-11 is the logical decision tree for the heat transfer module.

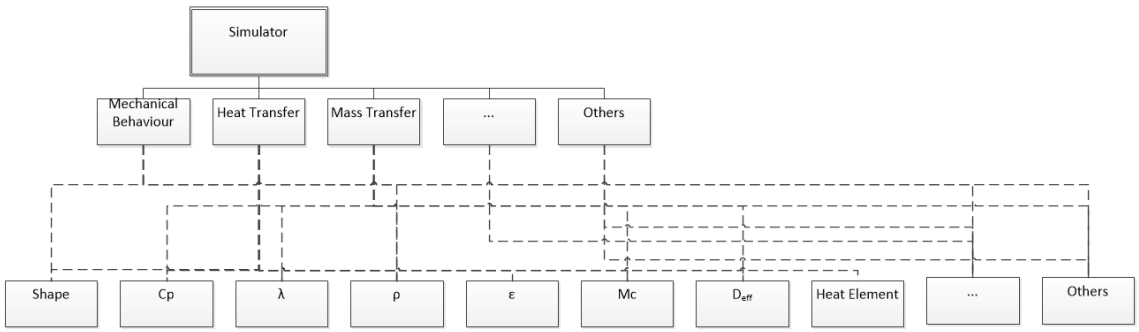

Figure 7-1, Expansion of simulator development framework

The first step would be to identify the key physical phenomena that are/could be important to reproduce in a simulator and what physical properties are relevant to them. All the important features would be listed (e.g., conduction in heat transfer), and all the relevant properties identified in the table. It is very important to identify relevant physical phenomena and the important properties required to reproduce them, as in mathematical modelling. The heat transfer simulator development carried out in this research provides an example of how this could be achieved. Table 6-2 summarises this process for heat transfer. It is not exhaustive, and as more studies are conducted, the framework can be expanded. Eventually, users can utilise the table for their single purpose or multi-purpose simulator development.

Table 7-1, Preliminary framework for properties selection

	Heat Transfer					...	Other modules
Properties	Conduction	Convection	Radiation	Evaporation	Respiration	...	Other Feature
ρ	√						
Cp	√						

λ	√						
ε			√	√			
Ts			√				
Shape		√					
D_{eff}				√			
Mc				√			
…							
Others							√

Traceability study application – Example of expansion

An example of the potential framework expansion can be demonstrated by the case study of using simulators to behave like real fruit to track fruit movement and mixing on a grading line.

Table 7-2 illustrates the potential use of Table 6-2 to extend the approach to this new simulator application. Given that the time scaled kiwifruit simulator already matches the thermal conductivity and shape; if density was also included, then the simulator can also be used for the traceability study. In fact, if the simulators are not required for multiple use, simulators that match just density and shape are required. This conclusion is reinforced by the study of Bollen, Riden, and Cox (2007) which suggests that matching density and shape can reasonably mimic the motion of the horticultural produce in a packing line.

Table 7-2, The example of utilising Table 6-2 for traceability fruit simulators

	Simulator	Heat Transfer					…	Mechanical behaviour
Properties	Time scale	Conduction	Convection	Radiation	Evaporation	Respiration	…	Motion behaviour
ρ	√	√						√
Cp		√						
λ	√	√						
ε				√	√			
Ts				√				
Shape	√		√					√
D_{eff}					√			
Mc					√			
…								
Others								

Figure 7-2 shows photographs of the traceability simulators produced as a side-project of this work. The simulators were manufactured using the same moulding and casting process outlined in

Chapter 4. The density of the kiwifruit fruit was matched by using the same thermoset polymer used for making heat transfer kiwifruit simulators. 400 simulators were manufactured. RFID tags were embedded inside the fruit during casting to identify the simulators at different points along the packing line. The colouring was applied on the simulator to aid retention time analysis and visual analysis to ensure simulated fruit were not packed with the real product.

Grading line characterisation experiments were conducted in a commercial packhouse during normal operation. The simulator fruit was dumped with the incoming real fruit from a bulk picking bin (Figure 7-2 right). Their position and dispersion along the line were then monitored over time. Overall, meaningful information was extracted from the use of the simulators for the commercial study. The result will not be discussed here, as it was outside of the project scope and interpretation of the results requires extra understanding of the packhouse operation.

Figure 7-2, Pictures of traceability study simulator(left) and its trialling experiment in a packhouse (right)

Potential fully matched simulator

In this project, most of the research was focused on time scale simulators, which matched the thermal conductivity, but varied the volumetric heat capacity. However, there are applications where a fully matched simulator (matching both volumetric heat capacity and thermal conductivity) would be more desirable. For example, using a simulator as a proxy of the surrounding horticultural produce condition, in which the simulator needs to have the same thermal conductivity and volumetric heat capacity as the surrounding produce (Defraeye et al., 2017; Redding et al., 2016). Defraeye et al. (2017) successfully developed an apple simulator made

of gel material. The authors demonstrated how the simulator could be used to reflect the temperature of surrounding apples and provide data on the temperature time history that fruit undergo during transport through the supply chain.

The previous chapters (Figure 4-3) have demonstrated the difficulty of finding non-water-based materials for fully matched simulator development, where the thermal conductivity was predicted based was on the Maxell-Eucken (ME) or Effective Medium Theory (EMT) models, which both reflect a simple dispersed particle structure – particles dispersed in a continuous matrix material. More complex structures that provide heat transfer and storage pathways could potentially provide new innovative simulator designs. To demonstrate this concept the hypothetical structures could be considered, as shown in Figure 7-3. Structure A is a simple layered structure. A material with high volumetric heat capacity could be used in the core of the simulator, acting as the thermal storage to increase the effective volumetric heat capacity. Then a low thermal conductivity material could be used for the external layer, acting as a thermal resistance to lower the effective thermal conductivity. This type of structure should theoretically be suitable for scenarios that approximate the first and third types of boundary conditions, where surface convection is significant and consistent. The series model for thermal conductivity prediction could be used for material selection of this structure, where the series model predicts the lowest possible effective thermal conductivity. However, whether this structure would significantly change the heat transfer pathway in the material conduction via contact is uncertain. As the simulator is not homogeneous, the pathway could be affected, affecting the effective thermal conductivity in the box or in even larger scale. Structures B and C could also be considered, where structures B and C provide some possibility to direct the heat flow pathways; hence provide a better uniform heat flow pathway.

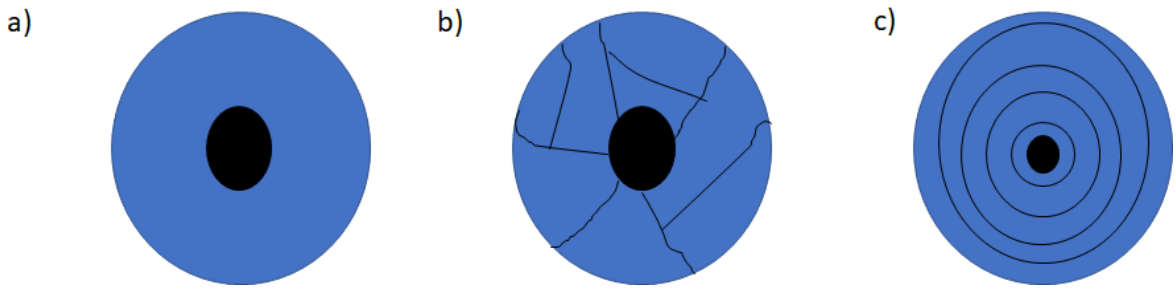

Figure 7-3, Hypothetical structures for full matched simulator based on the series model

If material combination structure is studied, a similar material selection framework that is demonstrated in Figure 4-1 could be used. Also, series and parallel models for thermal conductivity should be considered instead of using ME and EMT as these represent the most extreme effective thermal conductivity possible. Figure 7-4 shows the algorithm's output with a series and parallel model. As in Figure 4-1, each dot in the figure represents one particular combination at one mix ratio, using one predicted method. The dots inside the yellow box show there are several possible combinations to achieve the required volumetric heat capacity and thermal conductivity. Approximately 8000 combinations could be found. Perhaps parameterised structures modelled using finite elements could be a useful approach for design of internal structures, allowing optimisation to fully match the heat transfer behaviour of real fruit. Further development of this idea is not trivial and may present challenges in how the resulting structures would be manufactured. It is suggested as an interesting direction for future work.

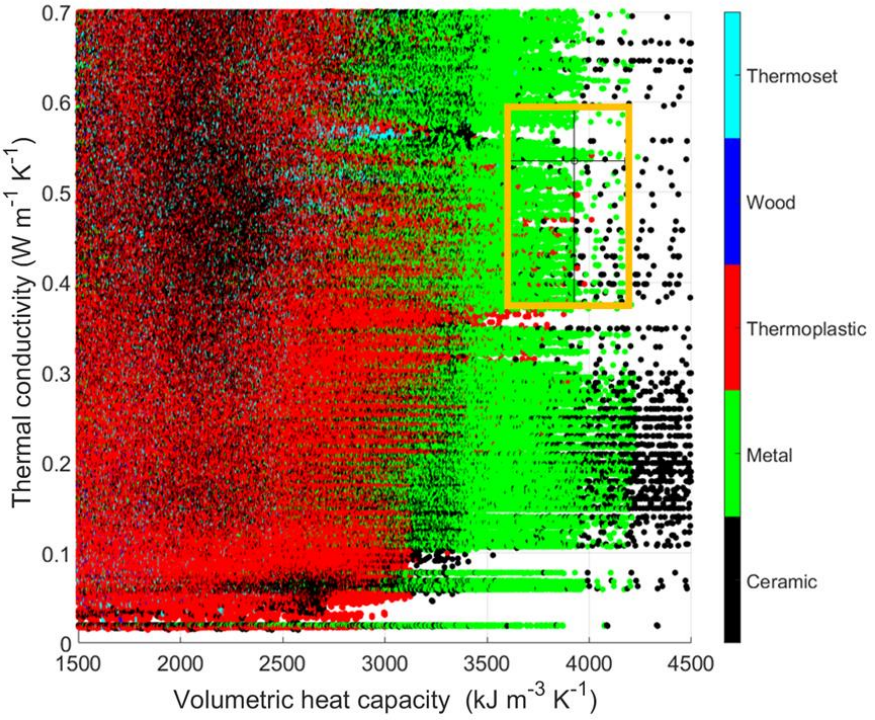

Figure 7-4, Material combinations based on series and parallel thermal conductivity models. The yellow box represents the range of properties required to match typical individual horticultural produce.

7.3 Final remarks

Although there is plenty of opportunity for future development of fruit simulators, this work has provided working simulators for kiwifruit, apples and grapes that could be routinely used in improving post-harvest operation and packaging design to improve cooling performance. The work has also provided a framework for the development and application of fruit simulators to replace real produce in experimental work.

Reference

Acevedo, C., Sánchez, E., & Young, M. E. (2007). Heat and mass transfer coefficients for natural convection in fruit packages. *Journal of Food Engineering, 80*(2), 655-661. doi:http://dx.doi.org/10.1016/j.jfoodeng.2006.07.001

Ahmed, J., & Rahman, M. (2009a). Thermal Conductivity Measurement of Foods. In *Food Properties Handbook, Second Edition*: CRC Press.

Ahmed, J., & Rahman, M. (2009b). Thermal Conductivity Data of Foods. In *Food Properties Handbook, Second Edition*: CRC Press.

Akhijahani, H. S., & Khodaei, J. (2013). Investigation of Specific Heat and Thermal Conductivity of Rasa Grape (Vitis vinifera L.) As a Function of Moisture Content. *World Applied Sciences Journal, 22*(7), 939-947.

Allais, I., & Alvarez, G. (2001). Analysis of heat transfer during mist chilling of a packed bed of spheres simulating foodstuffs. *Journal of Food Engineering, 49*(1), 37-47. doi:http://dx.doi.org/10.1016/S0260-8774(00)00182-5

Allais, I., Alvarez, G., & Flick, D. (2006). Modelling cooling kinetics of a stack of spheres during mist chilling. *Journal of Food Engineering, 72*(2), 197-209. doi:http://dx.doi.org/10.1016/j.jfoodeng.2004.11.010

Alvarez, G., & Trystram, G. (1995). Design of a new strategy for the control of the refrigeration process: fruit and vegetables conditioned in a pallet. *Food Control, 6*(6), 347-355. doi:http://dx.doi.org/10.1016/0956-7135(95)00046-1

Alvarez, G., & Flick, D. (1999a). Analysis of heterogeneous cooling of agricultural products inside bins: Part II: thermal study. *Journal of Food Engineering, 39*(3), 239-245. doi:http://dx.doi.org/10.1016/S0260-8774(98)00166-6

Alvarez, G., & Flick, D. (1999b). Analysis of heterogeneous cooling of agricultural products inside bins Part I: aerodynamic study. *Journal of Food Engineering, 39*(3), 227-237. doi:http://dx.doi.org/10.1016/S0260-8774(98)00164-2

Alvarez, G., Bournet, P., & Flick, D. (2003). Two-dimensional simulation of turbulent flow and transfer through stacked spheres. *International Journal of Heat and Mass Transfer, 46*(13), 2459-2469. doi:http://dx.doi.org/10.1016/S0017-9310(02)00546-X

Ambaw, A., Delele, M. A., Defraeye, T., Ho, Q. T., Opara, L. U., Nicolaï, B. M., & Verboven, P. (2013). The use of CFD to characterize and design post-harvest storage facilities: Past, present and future. *Computers and Electronics in Agriculture, 93*, 184-194. doi:http://dx.doi.org/10.1016/j.compag.2012.05.009

Ambaw, A., Fadiji, T., & Opara, U. L. (2021). Thermo-Mechanical Analysis in the Fresh Fruit Cold Chain: A Review on Recent Advances. *Foods, 10*(6), 1357.

Amos, N. D. (1995). *Mathematical modelling of heat transfer and water vapour transport in apple coolstores.* (Ph.D. thesis). Massey University,

Anderson, B. A., & Singh, R. P. (2005). Moisture Diffusivity in Tylose Gel (Karlsruhe Test Material). *Journal of Food Sceience 70*(5), E331-E337.

Ang, C. E. (2014). *Development of dry weight kiwi fruit analogue : food engineering project.* (Bachelor of Food Engineering). Massey University, Palmerston North, New Zealand.

Ashrae. (2010). *Thermal properties of foods* (SI ed ed.). Atlanta, GA: American Society of Heating, Refrigerating, and Air-Conditioning Engineers.

Becker, B. R., & Fricke, B. A. (1996). Transpiration and respiration of fruits and vegetables. *Science et Technique du Froid (France)*.

Ben Amara, S., Laguerre, O., & Flick, D. (2004). Experimental study of convective heat transfer during cooling with low air velocity in a stack of objects. *International Journal of Thermal Sciences, 43*(12), 1213-1221. doi:https://doi.org/10.1016/j.ijthermalsci.2004.04.004

Berry, T. M., Defraeye, T., Nicolai, B., & Opara, U. L. (2016). Multiparameter Analysis of Cooling Efficiency of Ventilated Fruit Cartons using CFD: Impact of Vent Hole Design and Internal Packaging. *Food and Bioprocess Technology, 9*(9), 1481-1493. doi:10.1007/s11947-016-1733-y

Bingol, G., Pan, Z., Roberts, J. S., Devres, Y. O., & Balaban, M. O. (2008). Mathematical modeling of microwave-assisted convective heating and drying of grapes. *International Journal of Agricultural and Biological Engineering, 1*(2), 46-54.

Bollen, A. F., Riden, C. P., & Cox, N. R. (2007). Agricultural supply system traceability, Part I: Role of packing procedures and effects of fruit mixing. *Biosystems Engineering, 98*(4), 391-400. doi:http://dx.doi.org/10.1016/j.biosystemseng.2007.07.011

Bonacina, C., Cominl, G., Fasano, A., & Primicerio, M. (1974). On the estimation of thermophysical properties in nonlinear heat-conduction problems. *International Journal of Heat and Mass Transfer, 17*(8), 861-867. doi:http://dx.doi.org/10.1016/0017-9310(74)90153-7

Brosnan, T., & Sun, D.-W. (2001). Precooling techniques and applications for horticultural products — a review. *International Journal of Refrigeration, 24*(2), 154-170. doi:http://dx.doi.org/10.1016/S0140-7007(00)00017-7

Burdon, J., & Lallu, N. (2011). 14 - Kiwifruit (Actinidia spp.). In E. M. Yahia (Ed.), *Postharvest Biology and Technology of Tropical and Subtropical Fruits* (pp. 326-362e): Woodhead Publishing.

Carson, J. K. (2002). *Prediction of the thermal conductivity of porous foods : a thesis submitted in partial fulfilment of the requirements for the degree of Doctor of Philosophy in Food Engineering, Massey University, Palmerston North, New Zealand, 2002*: 2002.

Carson, J. K., Lovatt, S. J., Tanner, D. J., & Cleland, A. C. (2003). An analysis of the influence of material structure on the effective thermal conductivity of theoretical porous materials using finite element simulations. *International Journal of Refrigeration, 26*(8), 873-880. doi:https://doi.org/10.1016/S0140-7007(03)00094-X

Carson, J. K., & East, A. R. (2017). The cold chain in New Zealand – A review. *International Journal of Refrigeration*. doi:https://doi.org/10.1016/j.ijrefrig.2017.09.019

Castro, L. R., Vigneault, C., & Cortex, L. A. B. (2004). Effect of container opening on air distribution during precooling of horticultural produce. *Transactions of ASAE, 47*(6), 2033-2038.

Castro, L. R., Vigneault, C., & Cortex, L. A. B. (2004a). Container opening design for horticultural produce cooling efficiency. *Food, Agriculture & Environment, 2*(1), 135-140. Retrieved from http://world-food.net/download/journals/2004-issue_1/f24.pdf

Castro, L. R., Vigneault, C., & Cortez, L. A. B. (2005). Cooling performance of horticultural produce in containers with peripheral openings. *Postharvest Biology and Technology, 38*(3), 254-261. doi:http://dx.doi.org/10.1016/j.postharvbio.2005.07.004

Cecen, V., Tavman, I. H., Kok, M., & Aydogdu, Y. (2009). Epoxy- and polyester-based composites reinforced with glass, carbon and aramid fabrics: Measurement of heat capacity and thermal conductivity of composites by differential scanning calorimetry. *Polymer Composites, 30*(9), 1299-1311. doi:10.1002/pc.20695

Chen, C. (2015). Determining the Leaf Emissivity of Three Crops by Infrared Thermometry. *Sensors (Basel, Switzerland), 15*(5), 11387-11401. doi:10.3390/s150511387

Chinea Valdés, L., & Lorenzo-Ginori, J. (2011). *Evaluation of Distance Transform-based alternatives for image segmentation of overlapping objects*.

Chuntranuluck, S. (1995). *Prediction of chilling times of foods subject to both convective and evaporative cooling at the product surface : a thesis presented in partial fulfilment of the*

requirements for the degree of Doctor of Philosophy in Biotechnology and Bioprocess Engineering at Massey University.

Chuntranuluck, S., Wells, C. M., & Cleland, A. C. (1998a). Prediction of chilling times of foods in situations where evaporative cooling is significant—Part 2. Experimental testing. *Journal of Food Engineering, 37*(2), 127-141. doi:http://dx.doi.org/10.1016/S0260-8774(98)00088-0

Chuntranuluck, S., Wells, C. M., & Cleland, A. C. (1998b). Prediction of chilling times of foods in situations where evaporative cooling is significant - Part 1. Method development. *Journal of Food Engineering, 37*(2), 111-125. Retrieved from http://www.scopus.com/inward/record.url?eid=2-s2.0-0032132276&partnerID=40&md5=eee43e8e68471e5d1480506dec96ddb4

Clay Mathematics Institute. (2018). Navier–Stokes Equation. Retrieved from http://www.claymath.org/millennium-problems/navier%E2%80%93stokes-equation

Cleland, A. C. (1977). *Heat transfer during freezing of foods and prediction of freezing times : a thesis presented in partial fulfilment of the requirements for the degree of Doctor of Philosophy in Biotechnology at Massey University*: 1977.

COMSOL Multiphysics. Heat Transfer Module User's Guide. In: COMSOL Multiphysics.

COMSOL Multiphysics v5.2. (Version 5.2): COMSOL Multiphysics. Retrieved from https://www.comsol.com/

Cuesta, F. J., & Lamúa, M. (2009). Fourier series solution to the heat conduction equation with an internal heat source linearly dependent on temperature: Application to chilling of fruit and vegetables. *Journal of Food Engineering, 90*(2), 291-299. doi:https://doi.org/10.1016/j.jfoodeng.2008.06.036

Curto[1], J., Ilangovan[1], A., Gaspar, P. D., Silva, P. D., & Alves, N. (2021). Numerical Study of the Impact on Cooling Behaviour of Vent-Holes Design of Fruit Packaging Boxes.

Das, M. K., Mukherjee, P. P., & Muralidhar, K. (2018). Equations Governing Flow and Transport in Porous Media. In M. K. Das, P. P. Mukherjee, & K. Muralidhar (Eds.), *Modeling Transport Phenomena in Porous Media with Applications* (pp. 15-63). Cham: Springer International Publishing.

Defraeye, T., Herremans, E., Verboven, P., Carmeliet, J., & Nicolai, B. (2012). Convective heat and mass exchange at surfaces of horticultural products: A microscale CFD modelling approach. *Agricultural and Forest Meteorology, 162-163*, 71-84. doi:https://doi.org/10.1016/j.agrformet.2012.04.010

Defraeye, T., Lambrecht, R., Tsige, A. A., Delele, M. A., Opara, U. L., Cronjé, P., . . . Nicolai, B. (2013). Forced-convective cooling of citrus fruit: Package design. *Journal of Food Engineering, 118*(1), 8-18. doi:http://dx.doi.org/10.1016/j.jfoodeng.2013.03.026

Defraeye, T., Verboven, P., & Nicolai, B. (2013a). CFD modelling of flow and scalar exchange of spherical food products: Turbulence and boundary-layer modelling. *Journal of Food Engineering, 114*(4), 495-504. doi:https://doi.org/10.1016/j.jfoodeng.2012.09.003

Defraeye, T., Lambrecht, R., Delele, M. A., Tsige, A. A., Opara, U. L., Cronjé, P., . . . Nicolai, B. (2014). Forced-convective cooling of citrus fruit: Cooling conditions and energy consumption in relation to package design. *Journal of Food Engineering, 121*, 118-127. doi:http://dx.doi.org/10.1016/j.jfoodeng.2013.08.021

Defraeye, T., Cronjé, P., Berry, T., Opara, U. L., East, A., Hertog, M., . . . Nicolai, B. (2015). Towards integrated performance evaluation of future packaging for fresh produce in the cold chain. *Trends in Food Science & Technology, 44*(2), 201-225. doi:http://dx.doi.org/10.1016/j.tifs.2015.04.008

Defraeye, T., Cronjé, P., Verboven, P., Opara, U. L., & Nicolai, B. (2015a). Exploring ambient loading of citrus fruit into reefer containers for cooling during marine transport using

computational fluid dynamics. *Postharvest Biology and Technology, 108*, 91-101. doi:http://dx.doi.org/10.1016/j.postharvbio.2015.06.004

Defraeye, T., Verboven, P., Opara, U. L., Nicolai, B., & Cronjé, P. (2015b). Feasibility of ambient loading of citrus fruit into refrigerated containers for cooling during marine transport. *Biosystems Engineering, 134*, 20-30.

Defraeye, T., Nicolai, B., Kirkman, W., Moore, S., Niekerk, S., Verboven, P., & Cronjé, P. (2016). Integral performance evaluation of the fresh-produce cold chain: A case study for ambient loading of citrus in refrigerated containers. *Postharvest Biology and Technology, 112*, 1-13. doi:http://dx.doi.org/10.1016/j.postharvbio.2015.09.033

Defraeye, T., Wu, W., Prawiranto, K., Fortunato, G., Kemp, S., Hartmann, S., . . . Nicolai, B. (2017). Artificial fruit for monitoring the thermal history of horticultural produce in the cold chain. *Journal of Food Engineering, 215*(Supplement C), 51-60. doi:https://doi.org/10.1016/j.jfoodeng.2017.07.012

Dehghannya, J., Ngadi, M., & Vigneault, C. (2008). Simultaneous Aerodynamic and Thermal Analysis during Cooling of Stacked Spheres inside Ventilated Packages. *Chemical Engineering & Technology, 31*(11), 1651-1659. doi:10.1002/ceat.200800290

Dehghannya, J., Ngadi, M., & Vigneault, C. (2010). Mathematical Modeling Procedures for Airflow, Heat and Mass Transfer During Forced Convection Cooling of Produce: A Review. *Food Engineering Reviews, 2*(4), 227-243. doi:10.1007/s12393-010-9027-z

Dehghannya, J., Ngadi, M., & Vigneault, C. (2011). Mathematical modeling of airflow and heat transfer during forced convection cooling of produce considering various package vent areas. *Food Control, 22*(8), 1393-1399. doi:https://doi.org/10.1016/j.foodcont.2011.02.019

Dehghannya, J., Ngadi, M., & Vigneault, C. (2012). Transport phenomena modelling during produce cooling for optimal package design: Thermal sensitivity analysis. *Biosystems Engineering, 111*(3), 315-324. doi:https://doi.org/10.1016/j.biosystemseng.2012.01.001

Delele, M. A., Tijskens, E., Atalay, Y. T., Ho, Q. T., Ramon, H., Nicolaï, B. M., & Verboven, P. (2008). Combined discrete element and CFD modelling of airflow through random stacking of horticultural products in vented boxes. *Journal of Food Engineering, 89*(1), 33-41. doi:https://doi.org/10.1016/j.jfoodeng.2008.03.026

Delele, M. A., Schenk, A., Ramon, H., Nicolaï, B. M., & Verboven, P. (2009). Evaluation of a chicory root cold store humidification system using computational fluid dynamics. *Journal of Food Engineering, 94*(1), 110-121. doi:https://doi.org/10.1016/j.jfoodeng.2009.03.004

Delele, M. A., Schenk, A., Tijskens, E., Ramon, H., Nicolaï, B. M., & Verboven, P. (2009a). Optimization of the humidification of cold stores by pressurized water atomizers based on a multiscale CFD model. *Journal of Food Engineering, 91*(2), 228-239. doi:http://dx.doi.org/10.1016/j.jfoodeng.2008.08.027

Delele, M. A., Ngcobo, K., Opara, U. L., & Meyer, C. J. (2012). Investigating the Effects of Table Grape Package Components and Stacking on Airflow, Heat and Mass Transfer Using 3-D CFD Modelling. *Food and Bioprocess Technology, 6*(9), 2571-2585. doi:10.1007/s11947-012-0895-5

Delele, M. A., Vorstermans, B., Creemers, P., Tsige, A. A., Tijskens, E., Schenk, A., . . . Verboven, P. (2012a). CFD model development and validation of a thermonebulisation fungicide fogging system for postharvest storage of fruit. *Journal of Food Engineering, 108*(1), 59-68. doi:http://dx.doi.org/10.1016/j.jfoodeng.2011.07.030

Delele, M. A., Ngcobo, M. E. K., Getahun, S. T., Chen, L., Mellmann, J., & Opara, U. L. (2013). Studying airflow and heat transfer characteristics of a horticultural produce packaging system using a 3-D CFD model. Part I: Model development and validation. *Postharvest*

Biology and Technology, 86, 536-545. doi:http://dx.doi.org/10.1016/j.postharvbio.2013.08.014

Delele, M. A., Ngcobo, M. E. K., Getahun, S. T., Chen, L., Mellmann, J., & Opara, U. L. (2013a). Studying airflow and heat transfer characteristics of a horticultural produce packaging system using a 3-D CFD model. Part II: Effect of package design. *Postharvest Biology and Technology, 86*, 546-555. doi:https://doi.org/10.1016/j.postharvbio.2013.08.015

Dincer, I. (1995). Air flow precooling of individual grapes. *Journal of Food Engineering, 26*(2), 243-249. doi:http://dx.doi.org/10.1016/0260-8774(94)00049-F

Downie, D., & Martin, J. (1980). An adiabatic calorimeter for heat-capacity measurements between 6 and 300 K. The molar heat capacity of aluminium. *The Journal of Chemical Thermodynamics, 12*(8), 779-786.

East, A. R., Sabarez, H. T., Tanner, D. J., & Cleland, D. J. (2003). Validation of a packaging design tool: Case study for apple packaging. In *Proceedings 21th International Congress of Regrigeration* (pp. 249). Washington DC: Int Inst Refrigeration.

East, A. R., & Smale, N. J. (2008). Combining a hybrid genetic algorithm and a heat transfer model to optimise an insulated box for use in the transport of perishables. *Vaccine, 26*(10), 1322-1334. doi:https://doi.org/10.1016/j.vaccine.2007.12.055

Emond, J.-P., Mercier, F., Sadfa, S., Bourré, M., & Gakwaya, A. (1996). Study of parameters affecting cooling rate and temperature distribution in forced-air precooling of strawberry. *Transactions of the ASAE, 39*(6), 2185-2191.

Feng, Y. T., & Han, K. (2012). An accurate evaluation of geometric view factors for modelling radiative heat transfer in randomly packed beds of equally sized spheres. *International Journal of Heat and Mass Transfer, 55*(23), 6374-6383. doi:https://doi.org/10.1016/j.ijheatmasstransfer.2012.06.025

Ferrua, M. J. (2007). *Modeling the forced-air cooling process of fresh horticultural products.* (DOCTOR OF PHILOSOPHY). UNIVERSITY OF CALIFORNIA, DAVIS.

Ferrua, M. J., & Singh, R. P. (2008). A nonintrusive flow measurement technique to validate the simulated laminar fluid flow in a packed container with vented walls. *International Journal of Refrigeration, 31*(2), 242-255. doi:http://dx.doi.org/10.1016/j.ijrefrig.2007.05.013

Ferrua, M. J., & Singh, R. P. (2009a). Modeling the forced-air cooling process of fresh strawberry packages, Part III: Experimental validation of the energy model. *International Journal of Refrigeration, 32*(2), 359-368. doi:http://dx.doi.org/10.1016/j.ijrefrig.2008.04.011

Ferrua, M. J., & Singh, R. P. (2009b). Modeling the forced-air cooling process of fresh strawberry packages, Part II: Experimental validation of the flow model. *International Journal of Refrigeration, 32*(2), 349-358. doi:http://dx.doi.org/10.1016/j.ijrefrig.2008.04.009

Ferrua, M. J., & Singh, R. P. (2009c). Modeling the forced-air cooling process of fresh strawberry packages, Part I: Numerical model. *International Journal of Refrigeration, 32*(2), 335-348. doi:http://dx.doi.org/10.1016/j.ijrefrig.2008.04.010

Ferrua, M. J., & Singh, R. P. (2009d). Design guidelines for the forced-air cooling process of strawberries. *International Journal of Refrigeration, 32*(8), 1932-1943. doi:https://doi.org/10.1016/j.ijrefrig.2009.07.011

Fordham, R., & Briggs, A. G. (1985). *Principles of vegetable crop production*: London : Collins, 1985.

Frederick, R. L., & Comunian, F. (1994). Air-cooling characteristics of simulated grape packages. *International Communications in Heat and Mass Transfer, 21*(3), 447-458. doi:http://dx.doi.org/10.1016/0735-1933(94)90012-4

FreshFacts. (2017). New Zealand Horticulture. Retrieved from http://www.freshfacts.co.nz/files/freshfacts-2017.pdf

Getahun, S., Ambaw, A., Delele, M., Meyer, C. J., & Opara, U. L. (2017). Analysis of airflow and heat transfer inside fruit packed refrigerated shipping container: Part I – Model development and validation. *Journal of Food Engineering, 203*, 58-68. doi:http://dx.doi.org/10.1016/j.jfoodeng.2017.02.010

Gillies, S., & Toivonen, P. (1995). Cooling method influences the postharvest quality of broccoli. *HortScience, 30*(2), 313-315.

Gruyters, W., Verboven, P., Diels, E., Rogge, S., Smeets, B., Ramon, H., . . . Nicolaï, B. M. (2018). Modelling Cooling of Packaged Fruit Using 3D Shape Models. *Food and Bioprocess Technology, 11*(11), 2008-2020. doi:10.1007/s11947-018-2163-9

Gunther, D., & Mogele, F. (2016). Additive manufacturing of casting tools using powder-binder-jetting technology. *New Trends 3D Print*, 53-86.

Han, J., Zhao, C., Yang, X., Qian, J., & Fan, B. (2015). Computational modeling of airflow and heat transfer in a vented box during cooling: Optimal package design. *Applied Thermal Engineering, 91*, 883-893. doi:http://dx.doi.org/10.1016/j.applthermaleng.2015.08.060

Han, J., Qian, J., Zhao, C., Yang, X., & Fan, B. (2017). Mathematical modelling of cooling efficiency of ventilated packaging: Integral performance evaluation. *International Journal of Heat and Mass Transfer, 111*, 386-397. doi:http://dx.doi.org/10.1016/j.ijheatmasstransfer.2017.04.015

Han, J., Zhao, C., Qian, J., Ruiz-Garcia, L., & Zhang, X. (2018). Numerical modeling of forced-air cooling of palletized apple: Integral evaluation of cooling efficiency. *International Journal of Refrigeration, 89*, 131-141. doi:https://doi.org/10.1016/j.ijrefrig.2018.02.012

He, S. Y., Feng, G. P., Yang, H. S., Wu, Y., & Li, Y. F. (2004). Effects of pressure reduction rate on quality and ultrastructure of iceberg lettuce after vacuum cooling and storage. *Postharvest Biology and Technology, 33*(3), 263-273. doi:http://dx.doi.org/10.1016/j.postharvbio.2004.03.006

Hellebrand, H. J., Beuche, H., & Linke, M. (2001). *Determination of thermal emissivity and surface temperature distribution of horticultural products.* Paper presented at the Sixth International Symposium on Fruit, Nut and Vegetable Production Engineering, Potsdam, Germany.

Hellebrand, H. J., Beuche, H., Linke, M., Herold, B., & Geyer, M. (2001a). *Chances and shortcomings of thermal imaging in the evaluation of horticultural products.* Paper presented at the International Conference" Physical Methods in Agriculture-Approach to Precision and Quality", Prague.

Hershko, V., & Nussinovitch, A. (1996). An empirical model for the stress‐strain relationships of hydrocolloid gels in tension mode. *Journal of texture studies, 26*(6), 675-684.

Hosseinzadeh, J., Feyzollahzadeh, M., & Afkari, A. H. (2013). The physical and chemical properties of kiwifruit harvested at four stages. *Bulgarian journal of Agricultural Science, 19*(1), 174-180. Retrieved from http://www.researchgate.net/publication/236109972_The_physical_and_chemical_properties_of_kiwifruit_harvested_at_four_stages

Hust, J. G., & Lankford, A. B. (1984). *Thermal conductivity of aluminum, copper, iron, and tungsten for temperatures from 1 K to the melting point*. Retrieved from

Icier, F., & Ilicali, C. (2005). The use of tylose as a food analog in ohmic heating studies. *Journal of Food Engineering, 69*(1), 67-77. doi:http://dx.doi.org/10.1016/j.jfoodeng.2004.07.011

IGI Global. (2015). *Handbook of research on advances and applications in refrigeration systems and technologies*.

Ihueze, C. C., & Mgbemena, C. E. (2017). Design for limit stresses of orange fruits (Citrus sinensis) under axial and radial compression as related to transportation and storage design. *Journal of the Saudi Society of Agricultural Sciences, 16*(1), 72-81. doi:https://doi.org/10.1016/j.jssas.2015.02.005

Ikegwu, O., & Ekwu, F. (2009). Thermal and physical properties of some tropical fruits and their juices in Nigeria. *Journal of Food technology, 7*(2), 38-42.

Jansen, K. M. B., Van Dijk, D. J., & Husselman, M. H. (1998). Effect of processing conditions on shrinkage in injection molding. *Polymer Engineering & Science, 38*(5), 838-846. doi:10.1002/pen.10249

Kittel, C. (2005). *Introduction to solid state physics* (8th ed ed.): Wiley.

Krantz, W. B. (2007). *Scaling analysis in modeling transport and reaction processes: a systematic approach to model building and the art of approximation*: John Wiley & Sons.

Laguerre, O., Amara, S. B., & Flick, D. (2006). Heat transfer between wall and packed bed crossed by low velocity airflow. *Applied Thermal Engineering, 26*(16), 1951-1960. doi:http://dx.doi.org/10.1016/j.applthermaleng.2006.01.011

Laguerre, O., Ben Amara, S., Alvarez, G., & Flick, D. (2008). Transient heat transfer by free convection in a packed bed of spheres: Comparison between two modelling approaches and experimental results. *Applied Thermal Engineering, 28*(1), 14-24. doi:http://dx.doi.org/10.1016/j.applthermaleng.2007.03.014

Laguerre, O., Ben Amara, S., Charrier-Mojtabi, M. C., Lartigue, B., & Flick, D. (2008a). Experimental study of air flow by natural convection in a closed cavity: Application in a domestic refrigerator. *Journal of Food Engineering, 85*(4), 547-560. doi:http://dx.doi.org/10.1016/j.jfoodeng.2007.08.023

Laguerre, O., Remy, D., & Flick, D. (2009). Airflow, heat and moisture transfers by natural convection in a refrigerating cavity. *Journal of Food Engineering, 91*(2), 197-210. doi:http://dx.doi.org/10.1016/j.jfoodeng.2008.08.029

Laguerre, O., Benamara, S., & Flick, D. (2010). Numerical simulation of simultaneous heat and moisture transfer in a domestic refrigerator. *International Journal of Refrigeration, 33*(7), 1425-1433. doi:http://dx.doi.org/10.1016/j.ijrefrig.2010.04.010

Lambrinos, G., Assimaki, H., Manolopoulou, H., Sfakiotaki, E., & Porlimgis, J. (1997). Air precooling and hydrocooling of Hayward Kiwifruit. *Acta Hort, 1997*(444), 561-566.

Łapiński, A., Śmierciew, K., Zou, H., & Butrymowicz, D. (2021). Measurement of Heat Transfer and Flow Resistance for a Packed Bed of Horticultural Products with the Implementation of a Single Blow Technique. *Processes, 9*(12), 2151.

Le Page, J.-F., Chevarin, C., Kondjoyan, A., Daudin, J.-D., & Mirade, P.-S. (2009). Development of an approximate empirical-CFD model estimating coupled heat and water transfers of stacked food products placed in airflow. *Journal of Food Engineering, 92*(2), 208-216. doi:http://dx.doi.org/10.1016/j.jfoodeng.2008.11.001

Llave, Y., Mori, K., Kambayashi, D., Fukuoka, M., & Sakai, N. (2016). Dielectric properties and model food application of tylose water pastes during microwave thawing and heating. *Journal of Food Engineering*. doi:http://dx.doi.org/10.1016/j.jfoodeng.2016.01.003

López, A., Molina-Aiz, F. D., Valera, D. L., & Peña, A. (2012). Determining the emissivity of the leaves of nine horticultural crops by means of infrared thermography. *Scientia Horticulturae, 137*, 49-58. doi:http://dx.doi.org/10.1016/j.scienta.2012.01.022

Lotfi, M., Heyd, R., Bakak, A., Hadaoui, A., & Koumina, A. (2021). Experimental Measurements on the Thermal Conductivity of Glycerol-Based Nanofluids with Different Thermal Contrasts. *Journal of Nanomaterials, 2021*, 3190877. doi:10.1155/2021/3190877

Marai, S., Ferrar, E., & Civelli, R. (2012). *Postharvest cold chain optimisation of little fruits.* Paper presented at the Proceedings of the 2012 COMSOL Conference, Milan.
Martins, M., Oliveira, l., Saraz, O., & Alexander, J. (2011). Numerical study of apple cooling in tandem arrangement. *Dyna, 78*(166), 158-165.
MathWorks Inc. . (2020). Multithresh. Retrieved from https://au.mathworks.com/help/images/ref/multithresh.html
MathWorks Inc. (2020a). Watershed. Retrieved from https://au.mathworks.com/help/images/ref/watershed.html
MatWeb, L. (2016). Property Search. Retrieved from http://www.matweb.com/
Maul, F., Vigneault, C., Sargent, S., Chau, K., & Caron, J. (1997). *Nondestructive sensor system ofr evaluation of cooling efficiency*. Paper presented at the Proceedings from the Sensors for nondestructive testing international Conference and Tour Holiday Inn International Drive resort, Orlando, Florida.
Mercier, S., Marcos, B., & Uysal, I. (2017). Identification of the best temperature measurement position inside a food pallet for the prediction of its temperature distribution. *International Journal of Refrigeration, 76*, 147-159. doi:https://doi.org/10.1016/j.ijrefrig.2017.01.025
Minh, T., Perry, J., & Bennett, A. (1969). Forced-air precooling of white potatoes in bulk. *ASHRAE transactions, 75*(2), 148-150.
Montanaro, G., Dichio, B., Xiloyannis, C., & Lang, A. (2012). Fruit transpiration in kiwifruit: environmental drivers and predictive model. *AoB plants, 2012*, pls036.
Moureh, J., Tapsoba, M., & Flick, D. (2009a). Airflow in a slot-ventilated enclosure partially filled with porous boxes: Part I – Measurements and simulations in the clear region. *Computers & Fluids, 38*(2), 194-205. doi:https://doi.org/10.1016/j.compfluid.2008.02.006
Moureh, J., Tapsoba, M., & Flick, D. (2009b). Airflow in a slot-ventilated enclosure partially filled with porous boxes: Part II – Measurements and simulations within porous boxes. *Computers & Fluids, 38*(2), 206-220. doi:https://doi.org/10.1016/j.compfluid.2008.02.007
Ngcobo, M. E. K., Delele, M. A., Opara, U. L., Zietsman, C. J., & Meyer, C. J. (2012). Resistance to airflow and cooling patterns through multi-scale packaging of table grapes. *International Journal of Refrigeration, 35*(2), 445-452. doi:http://dx.doi.org/10.1016/j.ijrefrig.2011.11.008
Ngcobo, M. E. K., Opara, U. L., & Thiart, G. D. (2012a). Effects of Packaging Liners on Cooling Rate and Quality Attributes of Table Grape (cv. Regal Seedless). *Packaging Technology and Science, 25*(2), 73-84. doi:10.1002/pts.961
Ngcobo, M. E. K., Delele, M. A., Opara, U. L., & Meyer, C. J. (2013a). Performance of multi-packaging for table grapes based on airflow, cooling rates and fruit quality. *Journal of Food Engineering, 116*(2), 613-621. doi:http://dx.doi.org/10.1016/j.jfoodeng.2012.12.044
Ngcobo, M. E. K., Delele, M. A., Opara, U. L., Thiart, G. D., & Meyer, C. J. (2013c). Heat transfer and external quality attributes of 'regal seedless' table grapes inside multi layered packaging during postharvest cooling and storage. In K. Hannweg & M. Penter (Eds.), *Acta Horticulturae* (Vol. 1007, pp. 189-196).
Nield, D. A. (2013). *Convection in porous media* (4th ed ed.). New York: Springer.
Norski Holdings Ltd. product Guide - Norski. In.
Norton, T., Tiwari, B., & Sun, D.-W. (2013). Computational Fluid Dynamics in the Design and Analysis of Thermal Processes: A Review of Recent Advances. *Critical Reviews in Food Science and Nutrition, 53*(3), 251-275. doi:10.1080/10408398.2010.518256
O'Sullivan, J. L. (2016). *Significant factors affecting the forced-air cooling process of polylined horticultural produce:.* (Ph.D. thesis). Massey University,

O'Sullivan, J., Ferrua, M. J., Love, R., Verboven, P., Nicolaï, B., & East, A. (2016a). Modelling the forced-air cooling mechanisms and performance of polylined horticultural produce. *Postharvest Biology and Technology, 120*, 23-35. doi:https://doi.org/10.1016/j.postharvbio.2016.05.008

O'Sullivan, J. L., Ferrua, M. J., Love, R., Verboven, P., Nicolai, B., & East, A. (2014). Airflow measurement techniques for the improvement of forced-air cooling, refrigeration and drying operations. *Journal of Food Engineering, 143*, 90-101. doi:http://dx.doi.org/10.1016/j.jfoodeng.2014.06.041

O'Sullivan, J. L., Ferrua, M. J., Love, R., Verboven, P., Nicolai, B., & East, A. (2016b). Modelling the forced-air cooling mechanisms and performance of polylined horticultural produce. *Postharvest Biology and Technology, 120*, 23-35. doi:http://dx.doi.org/10.1016/j.postharvbio.2016.05.008

O'Sullivan, J. L., Ferrua, M. J., Love, R., Verboven, P., Nicolaï, B., & East, A. (2017). Forced-air cooling of polylined horticultural produce: Optimal cooling conditions and package design. *Postharvest Biology and Technology, 126*, 67-75. doi:https://doi.org/10.1016/j.postharvbio.2016.11.019

Oberkampf, W. L., & Roy, C. J. (2010). *Verification and validation in scientific computing*: Cambridge, UK ; New York : Cambridge University Press, 2010.

Olatunji, J. R., Love, R. J., Shim, Y. M., Ferrua, M. J., & East, A. R. (2017). Quantifying and visualising variation in batch operations: A new heterogeneity index. *Journal of Food Engineering, 196*, 81-93. doi:http://dx.doi.org/10.1016/j.jfoodeng.2016.10.004

Olatunji, J. R. (2018). *An Integrated Modelling Approach to Inform Package Design for Optimal Cooling of Horticultural Produce.* (Ph.D. thesis). Massey University,

Olatunji, J. R., Shim, Y. M., & East, A. R. (2019). *Experimental Error in Large Scale Cooling Operations.* Paper presented at the IIR International Congress of Refrigeration, Montréal , Canada.

Oliveira, J., Lessio, B., Morgante, C., Santos, M., & Augusto, P. (2012). Specific heat (Cp) of tropical fruits: cajá, cashew apple, cocoa, kiwi, pitanga, soursop fruit and yellow melon. *International food research journal, 19*(3), 811-814.

Ozturk, H. M., & Ozturk, H. K. (2009). Effect of pressure on the vacuum cooling of iceberg lettuce. *International Journal of Refrigeration, 32*(3), 402-410. doi:http://dx.doi.org/10.1016/j.ijrefrig.2008.09.009

Pan, C., Kou, K., Jia, Q., Zhang, Y., Wu, G., & Ji, T. (2017). Improved thermal conductivity and dielectric properties of hBN/PTFE composites via surface treatment by silane coupling agent. *Composites Part B: Engineering, 111*, 83-90. doi:https://doi.org/10.1016/j.compositesb.2016.11.050

Panagiotis, A. M., Magdalini, K. K., & Mohammad Shafiur, R. (2009). Data and Models of Density, Shrinkage, and Porosity. In *Food Properties Handbook, Second Edition*: CRC Press.

Pathare, P., Opara, U. L., Vigneault, C., Delele, M. A., & Al-Said, F. (2012). Design of packaging vents for cooling fresh horticultural produce. *Food and Bioprocess Technology, 5*(6), 2031-2045. doi:10.1007/s11947-012-0883-9

Pham, A. T., Moureh, J., & Flick, D. (2018). Experimental characterization of heat transfer within a pallet of product generating heat. *Journal of Food Engineering*. doi:https://doi.org/10.1016/j.jfoodeng.2018.12.003

Pham, Q. *Thermal properties of unsalted MH1000 Tylose gel*. Retrieved from Sydney, Australia: http://www.ceic.unsw.edu.au/staff/Tuan_Pham/

Pham, Q. T. (2014). *Food Freezing and Thawing Calculations*: Springer.

Pinto, G., & Jiménez-Martín, A. (2001). Conducting aluminum-filled nylon 6 composites. *Polymer Composites, 22*(1), 65-70. doi:10.1002/pc.10517

Rahman, M., & Al-Saidi, G. (2009). Thermal Conductivity Prediction of Foods. In *Food Properties Handbook, Second Edition*: CRC Press.

Rahman, M. S. (2009b). *Food Properties Handbook, Second Edition*. Baton Rouge, UNITED STATES: CRC Press.

Razavi, S. M. A., & Parvar, M. B. (2007). Some physical and mechanical properties of kiwifruit. *International Journal of Food Engineering, 3*(6), 1-16. Retrieved from http://www.researchgate.net/publication/234155827_Some_Physical_and_Mechanical_Properties_of_Kiwifruit

Redding, G. P., Yang, A., Shim, Y. M., Olatunji, J., & East, A. (2016). A review of the use and design of produce simulators for horticultural forced-air cooling studies. *Journal of Food Engineering, 190*, 80-93. doi:http://dx.doi.org/10.1016/j.jfoodeng.2016.06.014

Riedel, L. (1960). Eine Prufsubstanz fiir gefrierversuche. *Kaltetechnik, 12*, 222-226.

Rolle, L., Torchio, F., Giacosa, S., & Río Segade, S. (2015). Berry density and size as factors related to the physicochemical characteristics of Muscat Hamburg table grapes (Vitis vinifera L.). *Food Chemistry, 173*, 105-113. doi:https://doi.org/10.1016/j.foodchem.2014.10.033

Roy, C. J., & Oberkampf, W. L. (2011). A comprehensive framework for verification, validation, and uncertainty quantification in scientific computing. *Computer Methods in Applied Mechanics and Engineering, 200*(25), 2131-2144. doi:https://doi.org/10.1016/j.cma.2011.03.016

Ryall, A. L. (1972). *Handling, transportation, and storage of fruits and vegetables*. Westport, Conn.: AVI Pub. Co.

Singh, R. P., Ferruh, E. d., & Mohammad Shafiur, R. (2009). Specific Heat and Enthalpy of Foods. In *Food Properties Handbook, Second Edition*: CRC Press.

Smale, N. J. (2004). *Mathematical modelling of airflow in shipping systems : model development and testing : a thesis presented in partial fulfilment of the requirements for the degree of Doctor of Philosophy in Food Technology at Massey University, Palmerston North, New Zealand*: 2004.

So, J.-H., Joe, S.-Y., Hwang, S.-H., Jun, S., & Lee, S.-H. (2021). Analysis of the Temperature Distribution in a Refrigerated Truck Body Depending on the Box Loading Patterns. *Foods, 10*(11), 2560.

Stankus, S. V., Savchenko, I. V., Baginskii, A. V., Verba, O. I., Prokop'ev, A. M., & Khairulin, R. A. (2008). Thermal conductivity and thermal diffusivity coefficients of 12Kh18N10T stainless steel in a wide temperature range. *High Temperature, 46*(5), 731-733. doi:10.1134/s0018151x08050222

Statistics New Zealand. (2019, 19 September 2019, 10:45am). Gross domestic product: June 2019 quarter. Retrieved from https://www.stats.govt.nz/information-releases/gross-domestic-product-june-2019-quarter#:~:text=New%20Zealand%20economy%20grows%200.5,the%20year%20ended%20June%202019.

STM Pro. Aluminium powder silver metal metallic. Retrieved from http://stmpro.co.nz/web/index.php/aluminium-powder-silver-metal-metallic-20kg.html#product_tabs_spcifications_tab

Stokely, K., Mazza, M. G., Stanley, H. E., & Franzese, G. (2010). Effect of hydrogen bond cooperativity on the behavior of water. *Proceedings of the National Academy of Sciences, 107*(4), 1301-1306. doi:10.1073/pnas.0912756107

Sweat, V. E. (1974). EXPERIMENTAL VALUES OF THERMAL CONDUCTIVITY OF SELECTED FRUITS AND VEGETABLES. *Journal of Food Science, 39*(6), 1080-1083. doi:10.1111/j.1365-2621.1974.tb07323.x

Taher, M. B., Ahachad, M., Mahdaoui, M., Zeraouli, Y., & Kousksou, T. (2021). A survey of computational and experimental studies on refrigerated trucks. *Journal of Energy Storage*, 103575.

Tanaka, F., Konishi, Y., Kuroki, Y., Hamanaka, D., & Uchino, T. (2012). The use of cfd to improve the performance of a partially loaded cold store. *Journal of Food Process Engineering, 35*(6), 874-880. doi:doi:10.1111/j.1745-4530.2011.00636.x

Tang, Z., Kang, H., Shen, Z., Guo, B., Zhang, L., & Jia, D. (2012). Grafting of Polyester onto Graphene for Electrically and Thermally Conductive Composites. *Macromolecules, 45*(8), 3444-3451. doi:10.1021/ma300450t

Tanner, D., & Amos, N. (2002). *Temperature variability during shipment of fresh produce.* Paper presented at the International Conference: Postharvest Unlimited 599.

Tanner, D. J. (1998). *Mathematical modelling for design of horticultural packaging : a thesis presented in partial fulfilment of the requirements for the degree of Doctor of Philosophy in Food Engineering at Massey University.* 1998, Available from EBSCOhost cat00245a database.

Tanner, D. J., Cleland, A. C., Opara, L. U., & Robertson, T. R. (2002a). A generalised mathematical modelling methodology for design of horticultural food packages exposed to refrigerated conditions: part 1, formulation. *International Journal of Refrigeration, 25*(1), 33-42. doi:http://dx.doi.org/10.1016/S0140-7007(01)00019-6

Tanner, D. J., Cleland, A. C., & Opara, L. U. (2002b). A generalised mathematical modelling methodology for the design of horticultural food packages exposed to refrigerated conditions Part 2. Heat transfer modelling and testing. *International Journal of Refrigeration, 25*(1), 43-53. doi:http://dx.doi.org/10.1016/S0140-7007(01)00018-4

Tanner, D. J., Cleland, A. C., & Robertson, T. R. (2002c). A generalised mathematical modelling methodology for design of horticultural food packages exposed to refrigerated conditions: Part 3, mass transfer modelling and testing. *International Journal of Refrigeration, 25*(1), 54-65. doi:http://dx.doi.org/10.1016/S0140-7007(01)00017-2

Thompson, A. K. (1996). *Postharvest technology of fruit and vegetables*. Oxford: Blackwell Science.

Tong, A. (2001). Improving the accuracy of temperature measurements. *Sensor Review, 21*(3), 193-198.

Tremeac, B., Hayert, M., & Le-Bail, A. (2008). Mechanical properties of tylose gel and chocolate in the freezing range. *International Journal of Refrigeration, 3*(1), 967-873.

Tu, J., Yeoh, G. H., & Liu, C. (2008). *Computational Fluid Dynamics : A Practical Approach* (Vol. 1st ed). Amsterdam: Butterworth-Heinemann.

Turk, R., & Celik, E. (1992). The effect of vacuum precooling on the half cooling period and quality characteristic of Iceberg lettuce. *Physiological Basis of Postharvest Technologies 343*, 321-324.

Tutar, M., Erdogdu, F., & Toka, B. (2009). Computational modeling of airflow patterns and heat transfer prediction through stacked layers' products in a vented box during cooling. *International Journal of Refrigeration, 32*(2), 295-306. doi:http://dx.doi.org/10.1016/j.ijrefrig.2008.05.003

Valente, M., Chambarel, A., Cordonnier, J., & Pumborios, M. (1996). Finite element modelling of heat transfer in avocados. [Modélisation des transferts de chaleur chez l'avocat par la méthode des éléments finis]. [archive]. *International agrophysics*, 123-129.

Van der Sman. (2008). Scale analysis and integral approximation applied to heat and mass transfer in packed beds. *Journal of Food Engineering, 85*(2), 243-251. doi:http://dx.doi.org/10.1016/j.jfoodeng.2007.07.031

Van der Sman, R. G. M. (2002). Prediction of airflow through a vented box by the Darcy–Forchheimer equation. *Journal of Food Engineering, 55*(1), 49-57. doi:https://doi.org/10.1016/S0260-8774(01)00241-2

Verboven, P., Flick, D., Nicolaï, B. M., & Alvarez, G. (2006). Modelling transport phenomena in refrigerated food bulks, packages and stacks: basics and advances. *International Journal of Refrigeration, 29*(6), 985-997. doi:http://dx.doi.org/10.1016/j.ijrefrig.2005.12.010

Vigncaull, C., Goycttc, B., & Raghavan, G. S. V. (1995). Continuous flow liquid-ice system tested on broccoli. *Canadian Society for Bioengineering, 37*(3), 225-230. Retrieved from http://csbe-scgab.ca/publications/cbe-journal/browse/7213-continuous-flow-liquid-ice-system-tested-on-broccoli

Vigneault, C., Bartz, J., & Sargent, S. (2000). Postharvest decay risk associated with hydrocooling tomatoes. *Plant disease, 84*(12), 1314-1318.

Vigneault, C., & Goyette, B. (2002). Design of plastic container opening to optimize forced-air precooling of fruits and vegetables. *Transactions of ASAE 38*(1), 73-76.

Vigneault, C., & Castro, L. R. (2005). Produce-simulator property evaluation for indirect airflow distribution measurement through horticultural crop package. *Journal of Food, Agriculture and Environment, 3*(2), 67-72. Retrieved from http://world-food.net/produce-simulator-property-evaluation-for-indirect-airflow-distribution-measurement-through-horticultural-crop-package/

Vigneault, C., Castro, L., & Cortez, L. A. B. (2005a). A new approach to measure air distribution through horticultural crop packages. *ISHS Acta Horticulturae, 682*, 2239-2245.

Vigneault, C., Goyette, B., & De Castro, L. R. (2006). Maximum slat width for cooling efficiency of horticultural produce in wooden crates. *Postharvest Biology and Technology, 40*(3), 308-313. doi:10.1016/j.postharvbio.2006.01.005

Vigneault, C., & de Castro, L. R. (2006a). Indirect measurement method for laminar to turbulent airflow through horticultural produce simulators. *Transactions of the ASABE, 49*(5), 1455-1461. Retrieved from <Go to ISI>://WOS:000242138500017

Vigneault, C., Castro, L., Goyette, B., Markarian, N., Charles, M., Bourgeois, G., & Foot, E. T. L. (2007). Indirect airflow distribution measurement method for horticultural crop package design. *Canadian Biosystems Engineering, 49*(3), 13-22.

Vigneault, C., Thompson, J., & Wu, S. (2009). Designing container for handling fresh horticultural produce. *Postharvest technologies for horticultural crops, 2*(2), 25-47.

Whitaker, S. (1969). ADVANCES IN THEORY OF FLUID MOTION IN POROUS MEDIA. *Industrial & Engineering Chemistry, 61*(12), 14-28. doi:10.1021/ie50720a004

Wills, R. B. H., McGlasson, B., Graham, D., & Joyce, D. (2007). *Postharvest : an introduction to the physiology and handling of fruit, vegetables and ornamentals*: Sydney : University of New South Wales Press, c2007.

Wood, F. W. (1975). US3892870 A.

Wu, W., Cronjé, P., Nicolai, B., Verboven, P., Opara, U. L., & Defraeye, T. (2018). Virtual cold chain method to model the postharvest temperature history and quality evolution of fresh fruit – A case study for citrus fruit packed in a single carton. *Computers and Electronics in Agriculture, 144*, 199-208. doi:https://doi.org/10.1016/j.compag.2017.11.034

Wu, W., & Defraeye, T. (2018). Identifying heterogeneities in cooling and quality evolution for a pallet of packed fresh fruit by using virtual cold chains. *Applied Thermal Engineering, 133*, 407-417. doi:https://doi.org/10.1016/j.applthermaleng.2017.11.049

Zhao, C.-J., Han, J.-W., Yang, X.-T., Qian, J.-P., & Fan, B.-L. (2016). A review of computational fluid dynamics for forced-air cooling process. *Applied Energy, 168*, 314-331. doi:http://dx.doi.org/10.1016/j.apenergy.2016.01.101

Zou, Q., Opara, L. U., & McKibbin, R. (2006a). A CFD modeling system for airflow and heat transfer in ventilated packaging for fresh foods:: II. Computational solution, software development, and model testing. *Journal of Food Engineering, 77*(4), 1048-1058. doi:http://dx.doi.org/10.1016/j.jfoodeng.2005.08.043

Zou, Q., Opara, L. U., & McKibbin, R. (2006b). A CFD modeling system for airflow and heat transfer in ventilated packaging for fresh foods: I. Initial analysis and development of mathematical models. *Journal of Food Engineering, 77*(4), 1037-1047. doi:http://dx.doi.org/10.1016/j.jfoodeng.2005.08.042

Appendix

Appendix A Potential material for bulk simulator

Material	Volumetric heat capacity ($kJ\ m\ K^{-1}$)	Thermal conductivity ($w\ m^{-1}\ K^{-1}$)
Eastman Tenite 105E3V36327 Acetate Clear, Trsp	1875.2	0.25
Eastman Tenite 360A4861307 Cellulose Acetate Propionate, Clear, Trsp	1772.7	0.25
Eastman Tenite 485E3720008 Cellulose Acetate Butyrate, Clear, Trsp	1758.0	0.25
Eastman Tenite 485E3720023 Butyrate Clear, Trsp	1699.4	0.25
Eastman Tenite 550E3V45510 Cellulose Acetate Butyrate, Water Clear, Trsp	1743.4	0.25
Eastman Tenite Acetate 105E1R26033 Clear, Trsp Cellulose Acetate	1866.9	0.25
Eastman Tenite Acetate 109E3V36324 Clear, Trsp Cellulose Acetate	1925.7	0.25
Eastman Tenite Acetate 109E3V46022 Natural, Trsp Cellulose Acetate	1881.6	0.25
Eastman Tenite Butyrate 264A3720013 Clear, Trsp Cellulose Acetate Butyrate	1734.6	0.25
Eastman Tenite Butyrate 264E4861310 Clear, Trsp Cellulose Acetate Butyrate	1749.3	0.25
Eastman Tenite Butyrate 285A2R30016 Natural, Trsp Cellulose Acetate Butyrate	1764.0	0.25
Eastman Tenite Butyrate 285A2R30023 Natural, Trsp Cellulose Acetate Butyrate	1719.9	0.25
Eastman Tenite Butyrate 438E0V16304 Clear, Trsp Cellulose Acetate Butyrate	1778.7	0.25
Eastman Tenite Butyrate 485A2R30023 Natural, Trsp Cellulose Acetate Butyrate	1705.2	0.25
Rotuba 855, Slow Burning Ethyl Cellulose	2200.0	0.22
Rotuba 856, Slow Burning Ethyl Cellulose	2180.0	0.22
Americas Styrenics Styron® 425 High Impact Polystyrene	2205.5	0.19
Americas Styrenics Styron® XL-8028 High Impact Polystyrene	1996.0	0.19
Arkema Group KYNAR® 1000 HD Polyvinylidene Fluoride Homopolymer - Injection Molding and Extrusion	2371.8	0.18
Arkema Group KYNAR® 460 Polyvinylidene Fluoride Homopolymer - Extrusion	2314.4	0.18

Arkema Group KYNAR® 710, 710 HDP Polyvinylidene Fluoride Homopolymer- Injection Molding	2385.2	0.18
Asahi Glass Fluon® P-63P PFA Perfluoropolymer	2215.5	0.25
Asahi Glass Fluon® P-66P PFA Perfluoropolymer	2252.3	0.25
Asahi Glass Fluon® PTFE	2257.5	0.25
Asahi Kasei Delpet® 560F Acrylic Molding Compound	1737.4	0.21
Asahi Kasei Leona® 1300S Nylon 66	1903.8	0.20
Asahi Kasei Leona® FR200 Nylon 66	1937.2	0.20
Ascend Performance Materials VYDYNE® 21SP Nylon, General Purpose	1938.0	0.24
Azoty Tarnow™ TARFLEN SG-1 PTFE	2150.0	0.25
Azoty Tarnow™ TARFLEN SM-K22G3 PTFE	2110.0	0.25
Bayer MaterialScience Apec® 1600 Polycarbonate	1853.0	0.17
Bayer MaterialScience Makroblend® DP UT3905 Polycarbonate + PBT, Impact Grade	2184.0	0.18
Bayer MaterialScience Makroblend® S 7916 Polycarbonate + PBT, Impact Grade	2256.0	0.19
Bayer MaterialScience Makroblend® S 7916/2 Polycarbonate + PBT, Impact Grade	2244.0	0.18
Bayer MaterialScience Makrolon® 1243 Polycarbonate	2040.0	0.17
Bayer MaterialScience Makrolon® 1837* Polycarbonate, Impact Grade	2023.0	0.17
Bayer MaterialScience Makrolon® 3158 Polycarbonate	1887.0	0.17
Chevron Phillips Ryton® R-4 04 PPS (Polyphenylene Sulfide)	1650.0	0.29
Diapolyacrylate Acrypet® IR H70 Impact Modified PMMA	1664.4	0.21
Diapolyacrylate Acrypet® MF-001 PMMA	1737.4	0.21
Dow AIM® 4800 High Impact Styrenic Resin	2163.2	0.18
Dow Prevail® 3150 ABS + Polyurethane	1586.2	0.19
Dow Retain® 8209 ABS + Polycarbonate	2368.1	0.22
Dow Tyril® 100 SAN	2150.4	0.19
Dow Tyril® 880B SAN	2319.2	0.20
DuPont Performance Polymers Crastin® 6129 NC010 Polybutylene Terephthalate (PBT)	2549.8	0.25
DuPont Performance Polymers Crastin® 6130 NC010 Polybutylene Terephthalate (PBT)	2470.3	0.25

DuPont Performance Polymers Crastin® FG6129 NC010 Polybutylene Terephthalate (PBT)	2528.9	0.25
DuPont Performance Polymers Crastin® FG6130 NC010 Polybutylene Terephthalate (PBT)	2480.5	0.25
DuPont Performance Polymers Crastin® FGS600F10 NC010 Polybutylene Terephthalate (PBT)	2530.5	0.21
DuPont Performance Polymers Crastin® FGS600F40 NC010 Polybutylene Terephthalate (PBT)	2553.1	0.21
DuPont Performance Polymers Crastin® HR5315HF NC010 Polybutylene Terephthalate (PBT)	2334.3	0.26
DuPont Performance Polymers Crastin® HR5330HF NC010 Polybutylene Terephthalate (PBT)	2413.4	0.28
DuPont Performance Polymers Crastin® S620F20 NC010 Polybutylene Terephthalate (PBT)	2541.0	0.21
DuPont Performance Polymers Crastin® SK601 NC010 Polybutylene Terephthalate (PBT)	2419.2	0.24
DuPont Performance Polymers Crastin® SK602 NC010 Polybutylene Terephthalate (PBT)	2498.5	0.24
DuPont Performance Polymers Crastin® SK603 NC010 Polybutylene Terephthalate (PBT)	2520.3	0.25
DuPont Performance Polymers Crastin® SK605 NC010 Polybutylene Terephthalate (PBT)	2499.9	0.28
DuPont Performance Polymers Crastin® SK612SF NC010 Polybutylene Terephthalate (PBT)	2508.0	0.24
DuPont Performance Polymers Crastin® SK615SF NC010 Polybutylene Terephthalate (PBT)	2508.5	0.28
DuPont Performance Polymers Crastin® SK645FR NC010 Polybutylene Terephthalate (PBT)	2560.0	0.26
DuPont Performance Polymers Crastin® SO653 NC010 Polybutylene Terephthalate (PBT)	2497.5	0.25
DuPont Performance Polymers Crastin® ST820 NC010 Polybutylene Terephthalate (PBT)	2362.5	0.20
DuPont Performance Polymers Hytrel® 5526 Polyester Elastomer TPC-ET	2352.7	0.19
DuPont Performance Polymers Hytrel® G4074 Polyester Elastomer TPC-ET	2265.3	0.26
DuPont Performance Polymers Sorona® MT3401 NC010 Polytrimethylene Terephthalate (PTT)	2394.0	0.20
DuPont Performance Polymers Zytel® 70G33HS1L NC010 Nylon 66	2460.3	0.22

DuPont Performance Polymers Zytel® 79G13L NC010 Nylon 66	2396.8	0.18
DuPont Performance Polymers Zytel® BM70G20HSLX BK537 Nylon 66	2320.0	0.20
DuPont Performance Polymers Zytel® FR50 NC010A Nylon 66	2490.0	0.22
DuPont Performance Polymers Zytel® LC6200 BK385 Nylon 612	2457.0	0.17
Eastman Eastar DN003 PCTG Copolyester	1648.2	0.19
Eastman Eastar GN101 PETG Copolyester	1651.0	0.19
Eastman Eastman AP005 Copolyester	1808.0	0.19
Ensinger ENSITEP® PBT Polybutylene Terephthalate - Extruded Products	1794.0	0.21
Ensinger ENSITEP® PET Polyethylene Terephthalate - Extruded Products	1614.6	0.29
Ensinger TECATRON™ GF 40 Polyphenylene sulfide (PPS)	1935.2	0.25
Evonik Corporation Trogamid® CX7323 Transparent Nylon	2390.4	0.25
Evonik Corporation Trogamid® CX9710 Transparent Nylon	2400.0	0.28
Evonik CYRO Acrylite® S-10 Acrylic Molding Compound	1749.3	0.19
Evonik CYRO Acrylite® SG Acrylic Sheet, Sign Grade	1719.9	0.19
Hippe PA 11 Nylon 11	2184.0	0.23
Hippe PA 12 Nylon 12	2142.0	0.23
Hippe PA 46 Nylon 46	2478.0	0.30
Hippe PA 6 Nylon 6	1710.0	0.23
Hippe PA 66 Nylon 66	1938.0	0.23
Hippe PBT Polybutylene Terephthalate	1573.0	0.21
Hippe PMMA	1734.6	0.19
Hippe POM Copolymer	2115.0	0.31
Hippe PTFE	2180.0	0.25
Kleerdex Elson® 405 AS DC Plate, PMMA/Acrylic, Clear Transparent	1749.3	0.21
Lucite International XL Sanitary Ware Acrylic Sheet	1749.3	0.21
Plaskolite Optix® PL-76 Acrylic Resin	1770.0	0.20
Plaskolite PL-24 Acrylic Resin	1737.4	0.20
Plaskolite West Optix® PL-25 Acrylic Resin	1785.0	0.20
Polikim EFALON® T-100 Virgin PTFE	2162.9	0.24
Polycasa XT 610 PMMA	1725.0	0.18

Polycasa XT 620 PMMA	1740.0	0.18
Polycasa XT 630 PMMA	1755.0	0.18
Polycasa XT PMMA	1749.3	0.18
Polyurethane, Rigid	1936.0	0.19
SABIC Innovative Plastics Cycoloy® EHA PC+ABS	2180.0	0.20
SABIC Innovative Plastics Lexan® 3412R PC	1585.4	0.21
SABIC Innovative Plastics Lexan® 3413R PC	1621.6	0.22
SABIC Innovative Plastics Lexan® 3414R PC	1580.8	0.22
SABIC Innovative Plastics Lexan® DMX1435 PC Copolymer (Asia Pacific)	1659.0	0.20
SABIC Innovative Plastics NORYL GTX GTX678 PPE+PA	1568.0	0.20
SBR	2068.0	0.17
Schwartz Technical Plastics LAMIGAMID® 100 Polyamide 6, Extruded, Dry	1903.8	0.23
Schwartz Technical Plastics LAMIGAMID® 200 Polyamide 66, Dry	1920.5	0.20
Schwartz Technical Plastics LAMIGAMID® 300 Cast Polyamide 6, Dry	1887.1	0.25
Schwartz Technical Plastics LAMIGAMID® 310 Cast Polyamide 6, Dry	1920.5	0.25
Schwartz Technical Plastics LAMIGAMID® 600 Polyoxymethylene	2087.8	0.27
Schwartz Technical Plastics LAMIGAMID® 700 Ultra High Molecular Weight Polyethylene	2185.0	0.33
Solvay Specialty Polymers Hylar® 460 PVDF Polyvinylidene Fluoride	2464.0	0.21
Solvay Specialty Polymers Solef® 1006 Polyvinylidene Fluoride (PVDF)	2130.0	0.20
Solvay Specialty Polymers Solef® 1008 PVDF Homopolymer	2136.0	0.20
Solvay Specialty Polymers Solef® 1015/0078 PVDF Homopolymer	2028.0	0.20
Solvay Specialty Polymers Solef® 11008 PVDF Copolymer	2136.0	0.19
Solvay Specialty Polymers Solef® 20810 PVDF Copolymer	2136.0	0.18
Solvay Specialty Polymers Solef® 31008 PVDF Copolymer	2112.0	0.18
Solvay Specialty Polymers Solef® 460/461 Polyvinylidene Fluoride (PVDF)	2358.4	0.20
Solvay Specialty Polymers Solef® 61010 PVDF Copolymer	2112.0	0.20
Spartech Polycast Cell Cast Acrylic	1737.4	0.19
Styron CALIBRE™ 200 10 Polycarbonate, General Purpose	2232.1	0.30
Zell-Metall Engineering Plastics Zellamid 1100	1920.5	0.28

Zell-Metall Engineering Plastics Zellamid 250 GF 30 (PA6.6 + 30% glass fiber)	2025.0	0.27
Park Electrochemical Nelco® N4000-12 SI® High Speed/Low Loss, CAF Resistant Laminate and Prepreg	2011.4	0.29
Park Electrochemical Nelco® N4000-13 SI® High-Speed Multifunctional Epoxy Laminate and Prepreg	2327.0	0.29

Appendix B Norski resin Data Sheets

Resin

NORSKI
EPOXIES • RESINS • GLUES • FILLERS

SAFETY DATA SHEET

Issue Date 14-Aug-2017 **Revision Date** 14-Aug-2017 **Version** 1

Section 1: PRODUCT IDENTIFIER AND CHEMICAL IDENTITY

Product identifier
Product Name Gelcoat

Description White Liquid

Other means of identification
UN Number UN1866

Recommended use of the chemical and restrictions on use
Recommended Use

Details of the supplier of the safety data sheet
Manufacturer
Norski Holdings Ltd
10 Northpoint Street
Pimmerton
Wellington 5247
New Zealand

For further information, please contact
Contact Point +64 (04) 233 6184
E-mail address Enquiries@norski.co.nz

Emergency telephone number
Emergency Telephone +64 0800 500 341

Section 2: HAZARD(S) IDENTIFICATION

Regulatory information

EPA New Zealand HSNO approval code or group standard HSR002495 Group Standard Additives, Process Chemicals and Raw Materials (Flammable) Group Standard 2006

Dangerous Goods Class 3 PG III

GHS Classification

Flammable liquids	Category 3 (HSNO - 3.1C)
Reproductive toxicity	Category 2 (HSNO - 6.8B)
Acute toxicity - Inhalation (Dusts/Mists)	Category 4 (HSNO - 6.1D)
Specific target organ toxicity (repeated exposure)	Category 1 (HSNO - 6.9A)
Specific target organ toxicity (single exposure)	Category 3 (HSNO - 6.1E)
Skin corrosion/irritation	Category 2 (HSNO - 6.3A)
Serious eye damage/eye irritation	Category 2 (HSNO - 6.4A)
Skin sensitisation	Category 1A (HSNO - 6.5B)
Acute aquatic toxicity	Category 2 (HSNO - 9.1D)
Chronic aquatic toxicity	Category 3 (HSNO - 9.1C)

Page 1 of 11

NORSKI
EPOXIES • RESINS • GLUES • FILLERS

Label elements

Signal word DANGER

H226 - Flammable liquid and vapour
H315 - Causes skin irritation
H317 - May cause an allergic skin reaction
H319 - Causes serious eye irritation
H332 - Harmful if inhaled
H335 - May cause respiratory irritation
H361 - Suspected of damaging fertility or the unborn child
H372 - Causes damage to organs through prolonged or repeated exposure
H401 - Toxic to aquatic life
H412 - Harmful to aquatic life with long lasting effects

Precautionary Statements - Prevention
Obtain special instructions before use
Do not handle until all safety precautions have been read and understood
Use personal protective equipment as required
Use only outdoors or in a well-ventilated area
Wash face, hands and any exposed skin thoroughly after handling
Contaminated work clothing should not be allowed out of the workplace
Wear protective gloves
Do not breathe dust/fume/gas/mist/vapours/spray
Do not eat, drink or smoke when using this product
Avoid release to the environment
Keep away from heat/sparks/open flames/hot surfaces. - No smoking
Keep container tightly closed
Ground/bond container and receiving equipment
Use only non-sparking tools
Take precautionary measures against static discharge
Use explosion-proof electrical/ ventilating/ lighting/ equipment
Keep cool

Precautionary Statements - Response
IF exposed or concerned: Get medical advice/attention
Specific treatment (see supplemental first aid instructions on this label)
IF IN EYES: Rinse cautiously with water for several minutes. Remove contact lenses, if present and easy to do. Continue rinsing
If eye irritation persists: Get medical advice/attention
If skin irritation or rash occurs: Get medical advice/attention
IF ON SKIN (or hair): Remove/Take off immediately all contaminated clothing. Rinse skin with water/shower Wash contaminated clothing before re-use
IF INHALED: Remove victim to fresh air and keep at rest in a position comfortable for breathing
In case of fire: Use CO_2, dry chemical, or foam for extinction
Precautionary Statements - Storage
Store locked up
Store in a well-ventilated place. Keep container tightly closed
Precautionary Statements - Disposal
Dispose of contents/container to an approved waste disposal plant

Other hazards
This product contains crystalline silica (quartz) in a non-respirable form. Inhalation of crystalline silica is unlikely to occur from exposure to this product
Avoid dust formation Sanding and grinding dust may be harmful if inhaled

Section 3: COMPOSITION AND INFORMATION ON INGREDIENTS

Substance

Not applicable

Mixture

Chemical Name	CAS No		Weight-%
Styrene	100-42-5		30-<60
Crystalline silica	14808-60-7		1-<2.5
2-Hydroxy-4-methoxybenzophenone	131-57-7		<0.25
Cobalt octoate	136-52-7		<0.25
Non-hazardous ingredients		Balance	

Section 4: FIRST AID MEASURES

Description of first aid measures

General advice	Show this safety data sheet to the doctor in attendance. Immediate medical attention is required. IF exposed or concerned: Get medical advice/attention.
Emergency telephone number	Poisons Information Centre, New Zealand: 0800 764 766
Inhalation	Remove to fresh air. IF exposed or concerned: Get medical advice/attention. Get medical attention immediately if symptoms occur.
Skin contact	Wash with soap and water. May cause an allergic skin reaction. In the case of skin irritation or allergic reactions see a doctor. Get medical attention if irritation develops and persists. Wash off immediately with soap and plenty of water for at least 15 minutes.
Eye contact	Rinse immediately with plenty of water, also under the eyelids, for at least 15 minutes. Keep eye wide open while rinsing. Do not rub affected area. Remove contact lenses, if present and easy to do. Continue rinsing. Get medical attention if irritation develops and persists.
Ingestion	Do NOT induce vomiting. Clean mouth with water and drink afterwards plenty of water. Never give anything by mouth to an unconscious person. Call a doctor.
Self-protection of the first aider	Remove all sources of ignition. Ensure that medical personnel are aware of the material(s) involved, take precautions to protect themselves and prevent spread of contamination. Use personal protective equipment as required. See section 8 for more information. Avoid direct contact with skin. Use barrier to give mouth-to-mouth resuscitation. Avoid contact with skin, eyes or clothing. Wear personal protective clothing (see section 8).

Most important symptoms and effects, both acute and delayed

Itching. Rashes. Hives. Burning sensation.

Indication of any immediate medical attention and special treatment needed

May cause sensitisation in susceptible persons. SEEK URGENT MEDICAL ATTENTION

Section 5: FIREFIGHTING MEASURES

Suitable Extinguishing Media

Suitable extinguishing media
Carbon dioxide (CO_2). Dry chemical. Alcohol-resistant foam. Water spray.

Unsuitable extinguishing media
Do not use water jetstream

Specific hazards arising from the chemical

Flammable. Risk of ignition. Keep product and empty container away from heat and sources of ignition. In the event of fire, cool tanks with water spray. Fire residues and contaminated fire extinguishing water must be disposed of in accordance with local regulations. Product is or contains a Sensitiser. May cause sensitisation by skin contact.

Special protective actions for fire-fighters

Wear self-contained breathing apparatus and protective suit. Use personal protective equipment as required.

Hazchem code •3WE.

Section 6: ACCIDENTAL RELEASE MEASURES

Personal precautions, protective equipment and emergency procedures

Personal precautions
Evacuate personnel to safe areas. Use personal protective equipment as required. See section 8 for more information. Avoid contact with skin, eyes or clothing. Ensure adequate ventilation. Keep people away from and upwind of spill/leak. ELIMINATE all ignition sources (no smoking, flares, sparks or flames in immediate area). Pay attention to flashback. Take action to prevent static discharges. All equipment used when handling the product must be grounded. Do not touch or walk through spilled material.

Ventilate the area. Refer to protective measures listed in Sections 7 and 8.

For emergency responders
Use personal protection recommended in Section 8.

Environmental precautions

Refer to protective measures listed in Sections 7 and 8. Prevent further leakage or spillage if safe to do so. Prevent product from entering drains.

Methods and material for containment and cleaning up

Methods for containment
Stop leak if you can do it without risk. Do not touch or walk through spilled material. A vapour suppressing foam may be used to reduce vapours. Dam far ahead of spill to collect run-off water. Keep out of drains, sewers, ditches and waterways. Absorb with earth, sand or other non-combustible material and transfer to containers for later disposal.

Methods for cleaning up
Take action to prevent static discharges. Dam up. Soak up with inert absorbent material. Pick up and transfer to properly labelled containers.

Precautions to prevent secondary hazards

Prevention of secondary hazards
Clean contaminated objects and areas thoroughly observing environmental regulations.

Reference to other sections
See section 8 for more information. See section 13 for more information.

Section 7: HANDLING AND STORAGE

Precautions for safe handling

Advice on safe handling
Use personal protection equipment. Avoid contact with skin and eyes. Avoid breathing vapours or mists. Keep away from heat, hot surfaces, sparks, open flames and other ignition sources. No smoking. Take action to prevent static discharges. Use grounding and bonding connection when transferring this material to prevent static discharge, fire or explosion. Use with local exhaust ventilation. Use spark-proof tools and explosion-proof equipment. Keep in an area equipped with sprinklers. Use according to package label instructions. Handle in accordance with good industrial hygiene and safety practice. Avoid contact with skin, eyes or clothing. Do not eat, drink or smoke when using this product. Remove contaminated clothing and shoes. Ensure adequate ventilation. Take off contaminated clothing and wash it before reuse. In case of insufficient ventilation, wear suitable respiratory equipment.

General Hygiene Considerations
When using do not eat, drink or smoke. Regular cleaning of equipment, work area and clothing is recommended. Do not eat, drink or smoke when using this product. Contaminated work clothing should not be allowed out of the workplace. Wash hands before breaks and immediately after handling the product. Wash hands before breaks and after work. Wear suitable gloves and eye/face protection. Avoid contact with skin, eyes or clothing. Wash contaminated clothing before re-use.

Conditions for safe storage, including any incompatibilities

Storage Conditions
Keep containers tightly closed in a dry, cool and well-ventilated place. Keep away from heat, sparks, flame and other sources of ignition (i.e. pilot lights, electric motors and static electricity). Keep in properly labelled containers. Do not store near combustible materials. Keep in an area equipped with sprinklers. Store in accordance with the particular national regulations. Store in accordance with local regulations. Store locked up. Keep out of the reach of children. Store separately. Hazardous polymerisation may take place during a fire due to heat. Closed containers could violently rupture. Do not store at temperatures above 27C.

Incompatible materials
Strong acids. Strong bases. Strong oxidising agents.

Section 8: EXPOSURE CONTROLS AND PERSONAL PROTECTION

Control parameters

Exposure Limits

Chemical Name	New Zealand
Styrene 100-42-5	TWA: 50 ppm TWA: 213 mg/m$_3$ STEL: 100 ppm STEL: 426 mg/m$_3$ Skin*
Crystalline silica 14808-60-7	TWA: 0.2 mg/m$_3$

Biological occupational exposure limits

Chemical Name	New Zealand
Styrene 100-42-5	1 g/L urine end of shift Mandelic acid

Appropriate engineering controls

Engineering Controls	Ensure adequate ventilation, especially in confined areas.

Individual protection measures, such as personal protective equipment

Eye/face protection	Tight sealing safety goggles. Face protection shield.
Skin and body protection	Antistatic footwear. Wear fire resistant or flame retardant clothing. Gloves made of plastic or rubber. Suitable protective clothing. Apron.
Respiratory protection	Where respiratory protection is required, use a respirator selected and in accordance with AS/NZS 1715 and AS/NZS 1716.
Environmental exposure controls	Do not allow into any sewer, on the ground or into any body of water.

Section 9: PHYSICAL AND CHEMICAL PROPERTIES

Information on basic physical and chemical properties

Physical state	liquid
Appearance	clear Hazy
Colour	clear
Odour	Characteristic Styrene
Odour threshold	No information available

Property	Values	Remarks •Method
pH		No information available
Melting point / freezing point		No information available
Boiling point/boiling range	145 °C	(based on components)
Flash point	31 °C	Tag Closed Cup
Evaporation rate	0.49	
Flammability (solid, gas)		No information available
Flammability Limit in Air		
Upper flammability limit:	6.1 %	
Lower flammability limit:	1.1 %	
Vapour pressure	6	hPa, 20°C Derived from solvent
Vapour density	3.6	Derived from solvent
Relative density	0.95	
Water solubility		insoluble
Solubility(ies)	-	No information available
Partition coefficient		No information available
Auto-ignition temperature	490 °C	Derived from solvent
Decomposition temperature		No information available
Kinematic viscosity	316 mm2/s	
Dynamic viscosity	> 300 mPa s	No information available
Explosive properties	No information available	
Oxidising properties	No information available	

Other Information

VOC Content (%)	No information available
Density	No information available

* This information may be derived from the components in the preparation.

Section 10: STABILITY AND REACTIVITY

Reactivity
No Data Available.

Chemical stability

Stable under normal conditions.

Explosion data

Sensitivity to Mechanical Impact	None.
Sensitivity to Static Discharge	May be ignited by heat, sparks or flames.

Possibility of Hazardous Reactions
HAZARDOUS POLYMERISATION MAY OCCUR UPON DEPLETION OF INHIBITOR.

Conditions to avoid

Heat, flames and sparks.

Incompatible materials

Strong acids. Strong bases. Strong oxidising agents.

Hazardous Decomposition Products

Decomposition products can include and are not limited to:Styrene.

Section 11: TOXICOLOGICAL INFORMATION

Acute toxicity

Information on likely routes of exposure

Product Information

Inhalation	Specific test data for the substance or mixture is not available. May cause irritation of respiratory tract.
Eye contact	Specific Test Data for the substance is not available. Irritating to the eyes based on components. Causes serious eye irritation.
Skin contact	Specific Test Data for the substance is not available. Causes skin irritation. May cause sensitisation by skin contact. Repeated or prolonged contact may cause allergic reaction reactions in very susceptible people.
Ingestion	Specific Test Data for the substance is not available. Ingestion may cause gastrointestinal irritation, nausea vomiting and diarrhoea.

Numerical measures of toxicity - Product Information

The following values are calculated based on chapter 3.1 of the GHS document
Converted acute toxicity point estimates may have been used when only acute toxicity hazard classification is available.

ATEmix (inhalation-vapour) 30.60
ATEmix (inhalation-dust/mist) 3.90
0% of the mixture consists of ingredient(s) of unknown toxicity
0 % of the mixture consists of ingredient(s) of unknown acute oral toxicity
0 % of the mixture consists of ingredient(s) of unknown acute dermal toxicity
0 % of the mixture consists of ingredient(s) of unknown acute inhalation toxicity (gas)
0 % of the mixture consists of ingredient(s) of unknown acute inhalation toxicity (vapour)
0 % of the mixture consists of ingredient(s) of unknown acute inhalation toxicity (dust/mist)

Chemical Name	Oral LD50	Dermal LD50	Inhalation LC50
Styrene	= 5000 mg/kg (Rat)	-	= 11.8 mg/L (Rat) 4 h
Crystalline silica	-	-	-
2-Hydroxy-4-methoxybenzophenone	= 7400 mg/kg (Rat)	-	-

See section 16 for terms and abbreviations

Delayed and immediate effects as well as chronic effects from short and long-term exposure

Skin corrosion/irritation
Classification based on individual ingredients of the mixture. Irritating to skin

Serious eye damage/eye irritation
Classification based on individual ingredients of the mixture. Irritating to eyes.

Sensitisation
May cause sensitisation by skin contact.

Germ cell mutagenicity
No information available.

Carcinogenicity

Chemical Name	New Zealand
Crystalline silica - 14808-60-7	Known or presumed human carcinogen if in fine respirable dust only

Reproductive toxicity
Contains a known or suspected reproductive toxin.

STOT - single exposure
May cause respiratory irritation.

STOT - repeated exposure
Causes damage to organs through prolonged or repeated exposure.

Aspiration hazard
No information available.

See section 16 for terms and abbreviations

Section 12: ECOLOGICAL INFORMATION

Ecotoxicity

Ecotoxicity

Unknown Aquatic Toxicity 0.04060791% of the mixture consists of components(s) of unknown hazards to the aquatic environment

Chemical Name	Fish
Styrene	19.03 - 33.53 mg/L LC50 96 h Lepomis macrochirus static 6.75 - 14.5 mg/L LC50 96 h Pimephales promelas static 3.24 - 4.99 mg/L LC50 96 h Pimephales promelas flow-through 58.75 - 95.32 mg/L LC50 96 h Poecilia reticulata static

Chemical Name	Crustacea
Styrene	3.3 - 7.4 mg/L EC50 48 h Daphnia magna

Chemical Name	Algae/aquatic plants
Styrene	0.46 - 4.3 mg/L EC50 72 h Pseudokirchneriella subcapitata static 0.15 - 3.2 mg/L EC50 96 h Pseudokirchneriella subcapitata static 1.4 mg/L EC50 72 h Pseudokirchneriella subcapitata 0.72 mg/L EC50 96 h Pseudokirchneriella subcapitata

Persistence and degradability

No information available.

Bioaccumulative potential

Chemical Name	Partition coefficient
Styrene	2.95

Mobility

Mobility in soil

No information available.

Mobility

No information available.

Other adverse effects

Endocrine Disruptor Information .

Section 13: DISPOSAL CONSIDERATIONS

Waste Treatment Methods

Waste from Residues/unused products

Section 14: TRANSPORT INFORMATION

Road transport

UN Number	UN1866
Proper shipping name	RESIN SOLUTION
Description	UN1866, RESIN SOLUTION, 3, III
Hazard Class	3
Packing Group	III
Special Precautions for users	223, *
Hazchem code	•3Y.
IERG	14

IMDG

UN/ID no	UN1866
Proper shipping name	RESIN SOLUTION
Description	UN1866, RESIN SOLUTION, 3, III, (31°C C.C.)
Hazard Class	3
Packing Group	III
EmS-No	F-E, S-E
Special Precautions for users	223, 955

Transport in Bulk According to Annex II of MARPOL and the IBC CODE
No information available

IATA

UN/ID no	UN1866
Proper shipping name	Resin solution
Description	UN1866, Resin solution, 3, III
Hazard Class	3
Packing Group	III
ERG Code	3L

Section 15: REGULATORY INFORMATION

Safety, health and environmental regulations/legislation specific for the substance or mixture

New Zealand
Regulatory information

EPA New Zealand HSNO approval code or group standard	HSR002495 Group Standard Additives, Process Chemicals and Raw Materials (Flammable) Group Standard 2006

International Inventories

AICS - Australian Inventory of Chemical Substances	Listed or exempt
DSL - Canadian Domestic Substances List	Listed or exempt
IECSC - China Inventory of Existing Chemical Substances	Listed or exempt
EINECS/ELINCS - European Inventory of Existing Chemical Substances/European List of Notified Chemical Substances	Listed or exempt
ENCS - Japan Existing and New Chemical Substances	Listed or exempt
KECL - Korean Existing and Evaluated Chemical Substances	Listed or exempt
NZIoC - New Zealand Inventory of Chemicals	Listed or exempt
PICCS - Philippines Inventory of Chemicals and Chemical Substances	Listed or exempt
CICR - Turkey Chemical Inventory Control Regulation	No information available
NCSR - Taiwan National Chemical Substance Registry	No information available
TSCA - United States Toxic Substances Control Act Section 8(b) Inventory	Listed or exempt

For confirmation on the European REACh status contact the Allnex Compliance group at PSRA-Customer-Requests@allnex.com

International Regulations

Ozone-depleting substances (ODS) Not applicable

Persistent Organic Pollutants Not applicable

Export Notification requirements Not applicable

Section 16: ANY OTHER RELEVANT INFORMATION

Legend Section 8: EXPOSURE CONTROLS AND PERSONAL PROTECTION

TWA	TWA (time-weighted average)	STEL	STEL (Short Term Exposure Limit)
Ceiling	Maximum limit value	*	Skin designation
C	Carcinogen		

Disclaimer

This information is given without any warranty or representation. We do not assume any legal responsibility for same, nor do we give permission, inducement, or recommendation to practice any patented invention without a license. It is offered solely for your consideration, investigation, and verification. Before using any product, read its label.

End of Safety Data Sheet

Catalyst

EPOXIES • RESINS • GLUES • FILLERS

SAFETY DATA SHEET

Issue Date 14-Aug-2017 **Revision Date** 14-Aug-2017 **Version** 1

Section 1: PRODUCT IDENTIFIER AND CHEMICAL IDENTITY

Product identifier
Product Name CUROX M-200 (NA1) CATALYST

Description Clear Liquid

Other means of identification
UN Number UN3105

Recommended use of the chemical and restrictions on use
Recommended Use Industrial and Professional use only.

Details of the supplier of the safety data sheet
Manufacturer
Norski Holdings Ltd
10 Northpoint Street
Plimmerton
Wellington 5247
New Zealand

For further information, please contact
Contact Point +64 (04) 233 6184
E-mail address Enquiries@norski.co.nz

Emergency telephone number
Emergency Telephone +64 0800 500 341

Section 2: HAZARD(S) IDENTIFICATION

EPA New Zealand HSNO approval code or group standard HSR002630
Group Standard: Oxidising substances (class 5.1.1) and organic peroxides (class 5.2) (Organic peroxides, Corrosive) Group Standard 2006.

GHS Classification

Flammable liquids	Category 4 (HSNO - 3.1D)
Organic peroxides	Type D (HSNO - 5.2D)
Acute toxicity - Oral	Category 4 (HSNO - 6.1D)
Skin corrosion/irritation	Category 1 B (HSNO - 8.2B)
Serious eye damage/eye irritation	Category 1 (HSNO - 8.3A)
Chronic aquatic toxicity	Category 2 (HSNO - 9.1B)

NORSKi®
EPOXIES • RESINS • GLUES • FILLERS

Label elements

Signal word Danger

Hazard statements
H227 - Combustible liquid
H242 - Heating may cause a fire
H302 - Harmful if swallowed
H314 - Causes severe skin burns and eye damage
H411 - Toxic to aquatic life with long lasting effects

Precautionary Statements - Prevention
Wash face, hands and any exposed skin thoroughly after handling
Do not eat, drink or smoke when using this product
Do not breathe dust/fume/gas/mist/vapours/spray
Wear protective gloves/protective clothing/eye protection/face protection
Avoid release to the environment
Keep away from heat/sparks/open flames/hot surfaces. - No smoking
Keep/Store away from clothing/combustible materials
Keep only in original container
Precautionary Statements - Response
Immediately call a POISONS INFORMATION CENTRE or doctor Specific
treatment (see supplemental first aid instructions on this label)
IF IN EYES: Rinse cautiously with water for several minutes. Remove contact lenses, if present and easy to do. Continue rinsing Immediately call a POISONS INFORMATION CENTRE or doctor
IF ON SKIN (or hair): Remove/Take off immediately all contaminated clothing. Rinse skin with water/shower Wash contaminated clothing before re-use
IF INHALED: Remove victim to fresh air and keep at rest in a position comfortable for breathing Immediately call a POISONS INFORMATION CENTRE or doctor "

Rinse mouth
Do NOT induce vomiting
Collect spillage
Precautionary Statements - Storage
Store locked up
Store at temperatures not exceeding .?1 °C/ .?2 °F. Keep cool
Store away from other materials
Protect from sunlight
Precautionary Statements - Disposal
Dispose of contents/container to an approved waste disposal plant

Other hazards
No hazard identified

Section 3: COMPOSITION AND INFORMATION ON INGREDIENTS

Substance

Not applicable

Mixture

Chemical Name	CAS No		Weight-%
Dimethyl phthalate	131-11-3		60-100
Methyl ethyl ketone peroxide	1338-23-4		30-<60
Methyl ethyl ketone	78-93-3		5-<10
Hydrogen peroxide	7722-84-1		1-<5
Non-hazardous ingredients		Balance	

Section 4: FIRST AID MEASURES

Description of first aid measures

General advice

Show this Safety Data Sheet to the Doctor in attendance. Immediate medical attention is required.

Emergency Telephone Number:

Poison Information Centre New Zealand 0800 764 766

Inhalation

Remove to Fresh Air. If breathing has stopped, give artificial respiration. Get Medical Attention Immediately. If not breathing give artificial respiration. Do not use mouth to mouth method if victim ingested or inhaled the substance; give artificial respiration with the aid of a pocket mask equipped with a one- way valve or other proper respiratory device. If breathing is difficult trained personnel should give oxygen. Delayed pulmonary oedema may occur. Get immediate medical advice/attention. Get immediate medical attention if symptoms occur.

Skin Contact

Wash off immediately with soap and plenty of water while removing all contaminated clothes and shoes. Get immediate medical advice/attention. Wash off immediately with soap and plenty of water for at least 15 minutes. Get medical attention if irritation develops and persists. If skin irritation persists, call a doctor.

Eye Contact

Rinse immediately with plenty of water, also under the eyelids, for at least 15 minutes. Keep eye wide open while rinsing. Do not rub affected area. Remove contact lenses, if present and easy to do. Continue rinsing. Get immediate medical advice/attention.

Ingestion

Do NOT induce vomiting. Clean mouth with water and drink afterwards plenty of water. Never give anything by mouth to an unconscious person. Immediate medical attention is required. Call a doc

Self Protection of First Aider

Ensure that medical personnel are aware of the material(s) involved, take precautions to protect themselves and prevent spread of contamination. Use personal protective equipment as required. See section 8 for more information. Remove all sources of ignition. Wear personal protective clothing (see section 8). Avoid contact with skin, eyes or clothing. Avoid direct contact with skin. Use barrier to give mouth-to-mouth resuscitation.

Most Important Symptoms and Acute and Delayed Symptoms

Burning

Indication of any Immediate Medical Attention and Special Treatment Needed.

Note to Doctors

Product is a corrosive material. Use of gastric lavage or emesis is contra-indicated. Possible perforation of stomach or esophagus should be investigated. Do not give chemical antidotes. Asphyxia from glottal oedema may occur. Marked decrease in blood pressure may occur with moist rales, frothy sputum, and high pulse pressure.

Section 5: FIREFIGHTING MEASURES

Use extinguishing measures that are appropriate to local circumstances and the surrounding environment. Water spray or fog is preferred; if water not available use dry chemical, CO2 or regular foam. Flood fire area with water from a distance. Use water or fog; do not use straight streams. Move containers from fire area if you can do it without risk. Cool containers with flooding quantities of water until well after fire is out. Dry chemical. Carbon dioxide (CO2). Water spray. Alcohol-resistant foam.

Unsuitable extinguishing media

Do not use water jetstream

Specific hazards arising from the chemical

Keep product and empty container away from heat and sources of ignition. Risk of ignition. These substances will accelerate burning when involved in a fire. Some may burn rapidly with flare burning effect. Some may decompose explosively when heated or involved in a fire. May ignite combustibles (wood paper, oil, clothing, etc.). Run-off may create fire or explosion hazard. In the event of fire, cool tanks with water spray. The product causes irritation of eyes, skin and mucous membranes. Thermal decomposition can lead to release of irritating and toxic gases and vapours.

Special protective actions for fire-fighters

Firefighters should wear self-contained breathing apparatus and full firefighting turnout gear. Use personal protection equipment. Oxidiser. May ignite combustibles (wood paper, oil, clothing, etc.). Some may burn rapidly with flare burning effect. Do not move cargo or vehicle if cargo has been exposed to heat. Move containers from fire area if you can do it without risk. Fight fire from maximum distance or use unmanned hose holders or monitor nozzles. ALWAYS stay away from tanks engulfed in fire. For massive fire, use unmanned hose holders or monitor nozzles; if this is impossible withdraw from area and let fire burn.

Hazchem code 2WE.

Section 6 Accidental Release Measures

Personal precautions, protective equipment and emergency procedures

Personal precautions
Ensure adequate ventilation. Avoid contact with skin, eyes or clothing. Evacuate personnel to safe areas. Keep people away from and upwind of spill/leak. ELIMINATE all ignition sources (no smoking, flares, sparks or flames in immediate area). Do not touch damaged containers or spilled material unless wearing appropriate protective clothing. See section 8 for more information. Stop leak if you can do it without risk. DO NOT CLEAN UP OR DISPOSE OF, EXCEPT UNDER SUPERVISION OF A SPECIALIST. Use personal protective equipment as required. Take action to prevent static discharges. Do not touch or walk through spilled material. Attention! Corrosive material.

Keep combustibles (wood, paper, oil, etc.) away from spilled material. ELIMINATE all ignition sources (no smoking, flares, sparks or flames in immediate area). Ventilate the area. Refer to protective measures listed in Sections 7 and 8.

For emergency responders

Use personal protection recommended in Section 8.

Methods and material for containment and cleaning up

Methods for containment
Prevent further leakage or spillage if safe to do so. Stop leak if you can do it without risk. Do not touch or walk through spilled material. Dam far ahead of liquid spill for later disposal.

Methods for cleaning up

Cover liquid spill with sand, earth or other non-combustible absorbent material. Cover powder spill with plastic sheet or tarp to minimise spreading. Take up with inert, damp, non-combustible material using clean non-sparking tools and place into loosely covered plastic containers for later disposal. Flush area with flooding quantities of water. Prevent product from entering drains.
Take action to prevent static discharges. Dam up. Soak up with inert absorbent material. Pick up and transfer to properly labelled containers

Prevention of secondary hazards
Clean contaminated objects and areas thoroughly observing environmental regulations.

Reference to other sections
See section 8 for more information. See section 13 for more information.

Section 7: HANDLING AND STORAGE

Precautions for safe handling

Advice on safe handling
Use personal protection equipment. Avoid contact with skin, eyes or clothing. Keep away from heat, hot surfaces, sparks, open flames and other ignition sources. No smoking. Do not eat, drink or smoke when using this product. Remove contaminated clothing and shoes. Use only with adequate ventilation. Do not breathe vapour or mist. Take action to prevent static discharges. Use with local exhaust ventilation. Handle in accordance with good industrial hygiene and safety practice. Ensure adequate ventilation. In case of insufficient ventilation, wear suitable respiratory equipment. Handle product only in closed system or provide appropriate exhaust ventilation. Take off contaminated clothing and wash it before reuse.

General Hygiene Considerations

When using do not eat, drink or smoke. Regular cleaning of equipment, work area and clothing is recommended. Avoid contact with skin, eyes or clothing. Wash hands thoroughly after handling. Keep away from food, drink and animal feeding stuffs. Do not eat, drink or smoke when using this product. Remove and wash contaminated clothing and gloves, including the inside, before re-use. Contaminated work clothing should not be allowed out of the workplace. Wash hands before breaks and immediately after handling the product. Wash hands before breaks and after work. Wear suitable gloves and eye/face protection.

Conditions for safe storage, including any incompatibilities

Storage Conditions

Keep containers tightly closed in a dry, cool and well-ventilated place. Keep away from heat, sparks, flame and other sources of ignition (i.e. pilot lights, electric motors and static electricity). Keep in properly labelled containers. Do not store near combustible materials. Store in accordance with the particular national regulations. Store in accordance with local regulations. Keep out of the reach of children. Protect from moisture. Store locked up. Store separately. Ambient transport organic peroxides are recommended to be stored temperatures below 30C/ 86F to maintain product quality.

Incompatible materials
Organic material. Combustible material. Hydrocarbons. Strong acids. Strong bases. Strong oxidising agents.

Note that this product must be stored as an Organic Peroxide and not a Combustible Liquid.

Section 8: EXPOSURE CONTROLS AND PERSONAL PROTECTION

Control parameters

Exposure Limits

Chemical Name	New Zealand
Dimethyl phthalate 131-11-3	TWA: 5 mg/m³
Methyl ethyl ketone peroxide 1338-23-4	Ceiling: 0.2 ppm Ceiling: 1.5 mg/m³
Methyl ethyl ketone 78-93-3	TWA: 150 ppm TWA: 445 mg/m³ STEL: 300 ppm STEL: 890 mg/m³
Hydrogen peroxide 7722-84-1	TWA: 1 ppm TWA: 1.4 mg/m³

Biological occupational exposure limits

Chemical Name	New Zealand
Methyl ethyl ketone 78-93-3	2 mg/L urine end of shift MEK

Appropriate engineering controls

Engineering Controls Ensure adequate ventilation, especially in confined areas.

Individual protection measures, such as personal protective equipment

Eye/face protection	Tight sealing safety goggles. Face protection shield.
Skin and body protection	Gloves made of plastic or rubber. Suitable protective clothing. Apron. Wear chemical resistant clothing such as gloves, apron, boots or whole bodysuits made from neoprene, as appropriate. Antistatic footwear.
Hand Protection	Wear suitable gloves.
Respiratory protection	Where respiratory protection is required, use a respirator selected and in accordance with AS/NZS 1715 and AS/NZS 1716.
Environmental exposure controls	No information available.

Section 9: PHYSICAL AND CHEMICAL PROPERTIES

Information on basic physical and chemical properties

Physical state	liquid
Appearance	clear
Colour	colourless
Odour	Slight Pungent
Odour threshold	No information available

Property	Values	Remarks •Method
pH	< 7	
Melting point / freezing point		No information available
Boiling point/boiling range		No information available
Flash point	68 °C	Approximately Seta Closed Cup ISO 3679
Evaporation rate		No information available
Flammability (solid, gas)		No information available
Flammability Limit in Air		
Upper flammability limit:	No information available	
Lower flammability limit:	No information available	
Vapour pressure	500	hPa, 50°C
Vapour density		No information available
Relative density	1.15	
Water solubility		Miscible
Solubility(ies)	-	No information available
Partition coefficient		No information available
Auto-ignition temperature	281 °C	
Decomposition temperature	60	SADT
Kinematic viscosity		No information available
Dynamic viscosity		No information available
Explosive properties	No information available	
Oxidising properties	Not applicable	

Other Information

VOC Content (%)	No information available
Density	No information available

* This information may be derived from the components in the preparation.

Section 10: STABILITY AND REACTIVITY

Reactivity
No Data Available.

Chemical stability

Organic peroxide. MAY CAUSE FIRE.

Explosion data
Sensitivity to Mechanical Impact None.
Sensitivity to Static Discharge May be ignited by heat, sparks or flames.

Possibility of Hazardous Reactions

Possibility of Hazardous Reactions
None under normal processing.

Conditions to avoid

Heat, flames and sparks.

Incompatible materials

Organic material. Combustible material. Hydrocarbons. Strong acids. Strong bases. Strong oxidising agents.

Hazardous Decomposition Products

Self-accelerating decomposition may occur if the specific control temperature is not maintained. Decomposition products can include and are not limited to:. Methyl ethyl ketone peroxide.

Section 11: TOXICOLOGICAL INFORMATION

INHALATION

Specific test data for the substance or mixture is not available. Corrosive by inhalation. (based on components). Inhalation of corrosive fumes/gases may cause coughing, choking, headache, dizziness, and weakness for several hours. Pulmonary oedema may occur with tightness in the chest, shortness of breath, bluish skin, decreased blood pressure, and increased heart rate. Inhaled corrosive substances can lead to a toxic oedema of the lungs. Pulmonary oedema can be fatal.

EYE CONTACT

Specific test data for the substance or mixture is not available. Causes burns. (based on components). Corrosive to the eyes and may cause severe damage including blindness. Risk of serious damage to eyes.

SKIN CONTACT

Specific test data for the substance or mixture is not available. Corrosive. (based on components). Causes burns

INGESTION

Specific test data for the substance or mixture is not available. Causes burns. (based on components). Ingestion causes burns of the upper digestive and respiratory tracts. May cause severe burning pain in the mouth and stomach with vomiting and diarrhoea of dark blood. Blood pressure may decrease. Brownish or yellowish stains may be seen around the mouth. Swelling of the throat may cause shortness of breath and choking. May cause lung damage if swallowed.

Numerical measures of toxicity - Product Information

The following values are calculated based on chapter 3.1 of the GHS document
Converted acute toxicity point estimates may have been used when only acute toxicity hazard classification is available.

ATEmix (oral) 1,137.00
ATEmix (dermal) 40,000.00
ATEmix (inhalation-vapour) 239.00
ATEmix (inhalation-dust/mist) 67.00
0% of the mixture consists of ingredient(s) of unknown toxicity
0 % of the mixture consists of ingredient(s) of unknown acute oral toxicity
0 % of the mixture consists of ingredient(s) of unknown acute dermal toxicity
0 % of the mixture consists of ingredient(s) of unknown acute inhalation toxicity (gas)
0 % of the mixture consists of ingredient(s) of unknown acute inhalation toxicity (vapour)
0 % of the mixture consists of ingredient(s) of unknown acute inhalation toxicity (dust/mist)

Chemical Name	Oral LD50	Dermal LD50	Inhalation LC50
Dimethyl phthalate	= 6800 mg/kg (Rat)	-	-
Methyl ethyl ketone peroxide	= 470 mg/kg (Rat) = 407 mg/kg (Rat)	-	= 200 ppm (Rat) 4 h
Methyl ethyl ketone	= 2737 mg/kg (Rat) = 2483 mg/kg (Rat)	= 6480 mg/kg (Rabbit) = 5000 mg/kg (Rabbit)	= 11700 ppm (Rat) 4 h
Hydrogen peroxide	= 1518 mg/kg (Rat)	= 4060 mg/kg (Rat) = 2000 mg/kg (Rabbit)	= 2 g/m³ (Rat) 4 h

See section 16 for terms and abbreviations

Delayed and immediate effects as well as chronic effects from short and long-term exposure

Skin corrosion/irritation
Classification based on data available for ingredients. Causes burns.

Serious eye damage/eye irritation
Classification based on individual ingredients of the mixture. Risk of serious damage to eyes. Causes burns.

Sensitisation
No information available.

Germ cell mutagenicity
No information available.

Carcinogenicity

Chemical Name	New Zealand
Hydrogen peroxide - 7722-84-1	Suspected human carcinogen

Reproductive toxicity
No information available.

STOT - single exposure
No information available.

STOT - repeated exposure
No information available.

Aspiration hazard
No information available.

Section 12: ECOLOGICAL INFORMATION

Ecotoxicity

Unknown Aquatic Toxicity 0% of the mixture consists of components(s) of unknown hazards to the aquatic environment

Chemical Name	Fish
Dimethyl phthalate	49.5 mg/L LC50 96 h Lepomis macrochirus 39 mg/L LC50 96 h Pimephales promelas flow-through 37 - 69 mg/L LC50 96 h Lepomis macrochirus static 100 - 220 mg/L LC50 96 h Leuciscus idus static 56 mg/L LC50 96 h Oncorhynchus mykiss flow-through 121 mg/L LC50 96 h Pimephales promelas static
Methyl ethyl ketone	3130 - 3320 mg/L LC50 96 h Pimephales promelas flow-through
Hydrogen peroxide	16.4 mg/L LC50 96 h Pimephales promelas 10.0 - 32.0 mg/L LC50 96 h Oncorhynchus mykiss static 18 - 56 mg/L LC50 96 h Lepomis macrochirus static

Chemical Name	Crustacea
Dimethyl phthalate	33 mg/L EC50 48 h Daphnia magna
Methyl ethyl ketone	520 mg/L EC50 48 h Daphnia magna 4025 - 6440 mg/L EC50 48 h Daphnia magna Static 5091 mg/L EC50 48 h Daphnia magna
Hydrogen peroxide	18 - 32 mg/L EC50 48 h Daphnia magna Static 7.7 mg/L EC50 24 h Daphnia magna

Chemical Name	Algae/aquatic plants
Dimethyl phthalate	142 mg/L EC50 96 h Pseudokirchneriella subcapitata static 20.6 - 45.8 mg/L EC50 96 h Pseudokirchneriella subcapitata 26.1 mg/L EC50 96 h Skeletonema costatum 28.4 - 71 mg/L EC50 72 h Pseudokirchneriella subcapitata 204 mg/L EC50 72 h Desmodesmus subspicatus
Hydrogen peroxide	2.5 mg/L EC50 72 h Chlorella vulgaris

Persistence and degradability

No information available.

Bioaccumulative potential

Chemical Name	Partition coefficient
Dimethyl phthalate	2.12
Methyl ethyl ketone	0.29

Mobility

Mobility in soil

No information available.

Mobility

No information available.

Other adverse effects
No information available.
Endocrine Disruptor Information .

Chemical Name	EU - Endocrine Disrupters Candidate List	EU - Endocrine Disruptors - Evaluated Substances	Endocrine disrupting potential
Dimethyl phthalate	Group III Chemical	-	-

Section 13: DISPOSAL CONSIDERATIONS

Waste Treatment Methods

Waste from Residues/unused products

Refer to all federal state and local Regulations prior to disposal of container and unused contents by re-use recycle or disposal.

Contaminated Packaging

Disposal should be in accordance with applicable regional national, and local laws and regulations. Observe all label precautions until container is cleaned reconditioned or destroyed. Refer to all
federal state and local regulations prior to
regulations prior to disposal of container and unused contents by re -use recycle and disposal.

Section 14 : Transport Information

Proper shipping name	ORGANIC PEROXIDE TYPE D, LIQUID
Description	UN3105, ORGANIC PEROXIDE TYPE D, LIQUID (Methyl ethyl ketone peroxide, Hydrogen peroxide), 5.2
Hazard Class	5.2
Special Precautions for users	122, 274, 323
Hazchem code	2WE.
IERG	32

IMDG

UN/ID no	UN3105
Proper shipping name	ORGANIC PEROXIDE TYPE D, LIQUID
Description	UN3105, ORGANIC PEROXIDE TYPE D, LIQUID (Methyl ethyl ketone peroxide, Hydrogen peroxide), 5.2
Hazard Class	5.2
EmS-No	F-J, S-R
Special Precautions for users	122, 274

Transport in Bulk According to Annex II of MARPOL and the IBC CODE
No information available

IATA
UN/ID no
Proper shipping name

Description

Hazard Class

Section 15: REGULATORY INFORMATION

Safety, health and environmental regulations/legislation specific for the substance or mixture

New Zealand Regulatory information

Classified as Hazardous according to the Hazardous Substances (Minimum Degrees of Hazard) Regulations 2001, New Zealand. See section 8 for national exposure control parameters.

EPA New Zealand HSNO approval code or group standard HSR002630
Group Standard: Oxidising substances (class 5.1.1) and organic peroxides (class 5.2) (Organic peroxides, Corrosive) Group Standard 2006.

This Group Standard contains all trigger quantities for New Zealand HSNO requirements.

International Inventories

AICS - Australian Inventory of Chemical Substances	Listed or exempt
DSL - Canadian Domestic Substances List	Listed or exempt
IECSC - China Inventory of Existing Chemical Substances	Listed or exempt
EINECS/ELINCS - European Inventory of Existing Chemical Substances/European List of Notified Chemical Substances	Listed or exempt
ENCS - Japan Existing and New Chemical Substances	Listed or exempt
KECL - Korean Existing and Evaluated Chemical Substances	Listed or exempt
NZIoC - New Zealand Inventory of Chemicals	Listed or exempt
PICCS - Philippines Inventory of Chemicals and Chemical Substances	Listed or exempt
CICR - Turkey Chemical Inventory Control Regulation	No information available
NCSR - Taiwan National Chemical Substance Registry	No information available
TSCA - United States Toxic Substances Control Act Section 8(b) Inventory	Listed or exempt

For confirmation on the European REACh status contact the Allnex Compliance group at PSRA-Customer-Requests@allnex.com

International Regulations

Ozone-depleting substances (ODS) Not applicable

Persistent Organic Pollutants Not applicable

Export Notification requirements Not applicable

Section 16: ANY OTHER RELEVANT INFORMATION

Revision Date 14-Aug-2017

Revision Note New Format

Key or legend to abbreviations and acronyms used in the safety data sheet

Legend Section 8: EXPOSURE CONTROLS AND PERSONAL PROTECTION

TWA	TWA (time-weighted average)	STEL	STEL (Short Term Exposure Limit)
Ceiling	Maximum limit value	*	Skin designation
C	Carcinogen		

Disclaimer

This information is given without any warranty or representation. We do not assume any legal responsibility for same, nor do we give permission, inducement, or recommendation to practice any patented invention without a license. It is offered solely for your consideration, investigation, and verification. Before using any product, read its label.

End of Safety Data Sheet

User Guide

POLYESTER RESIN

PRODUCT DESCRIPTION

A general purpose resin for repair work and hand laid fibreglass laminations normally used with 'Norski Chopped Strand Mat'

AREAS OF USE

Polyester Resin and Chopped strand mat are used in so many areas that it is impossible to list all the areas that it can be used.

Typically, a mould is created, then after the polyester resin and chopped strand mat are applied to the mould and then cured, the article is removed allowing another article to be produced using the same mould.

Moulds can be large or small and the resulting product is a lightweight, waterproof shell (or skin) Whilst this product is used heavily in the marine environment, it's uses have spread far and wide nowadays. Some examples of articles produced are , horse floats, campervan and caravan siding, boats and boat parts, different car panels and spoilers,

Alternatively, repairs can be undertaken to article manufactured originally from polyester resin and chopped strand mat.

The process referred to in these instructions is a repair undertaken to an article that was originally manufactured in a mould using polyester resin and chopped strand mat

PROPERTIES (at 20°C)

Colour- Blue. Changes colour to green when catalyst added,
Toxicity: toxic - see precautions.
Finish: Satin/Opaque

Coverage*:** One litre of catalysed resin will wet out one meter^2 of 450g ***chopped strand matt.
(250 ml for one sq. meter of ***Glass Cloth***).

***Drying Time*:** Refer curing table later in this document.
Recoating: Up to 7 days at 20 °C.
Pot Life: Refer curing table later in this document.
Mixing Ratio: 1-2% hardener by volume.
Thinning: Can only be thinned with Norski Polyester Thinners - nothing else.

Norski Holdings Ltd, 10 Northpoint St, Plimmerton Wellington 5024
Phone 04 233 6184, Facsimile 04 233 6173, Website www.norski.co.nz

EPOXIES • RESINS • GLUES • FILLERS

Weight per Litre: 1. 0kg
Volume Solids: N/A

***Flash Point*: 30** °C (closed cup)
Clean Up: Norski Cleaning Fluid/Acetone.
UN Number: 1866 HAZCHEM 3 Y

Norski have measuring equipment, rollers, and accessories available for sale to complete your job, please refer to our website or give us a call.

PREPARATION

Thorough cleaning is essential for adhesion. Remove all grease, oils, dust and other contaminants. Loose or flaking paint should be sanded back to a stable condition. First roughen smooth surfaces by sanding with medium sandpaper. The surface to be treated must also be dry before commencing. NOTE: Surfaces such as polystyrene foam need to he previously coated with a sealing product to isolate the foam from attack by the polyester.

After the polyester catalyst is mixed into the blue resin, the colour changes to green as the chemical reaction begins, then becomes translucent/opaque when cured.

Important: The mixing ratio of catalyst to Polyester Resin is between 1 and 2% of resin by volume. *For example,* 100 mls of Polyester Resin will require 1 -2mls of catalyst. The following table indicates the approximate gel times that can be expected. Increasing the volume (mass) and/or % of catalyst will further reduce the working time available.

% cotalyst by volume	*Approximate gel time (in minutes for 100 mls)*			
	15 °C	20 °C	25 °C	30 °C
1%	57	41	25	20
2%	37	26	16	11

Note Do not mix up more resin than can be applied within 15 minutes at 20°C

APPLICATION (undertaking a patch repair)

As the areas of use are many and varied, the following is a general guide only.

1. Using a brush, wet the surface surrounding the cracks or holes with a thin coat of mixed resin and immediately lay on the pre-wetted out fibreglass matt patch or glass cloth by pressing it onto the resin.

Norski Holdings Ltd, 10 Northpoint St, Plimmerton Wellington 5024
Phone 04 233 6184, Facsimile 04 233 6173, Website www.norski.co.nz

EPOXIES • RESINS • GLUES • FILLERS

2. Apply more mixed resin with the brush using a stippling action until the whole area appears clear. Resin starved patches will show as obvious white spots and must be recoated before the resin sets, otherwise these dry spots will have to he cut out later with a sharp knife.

3. After the patch has cured, a filler coat may be applied by adding Norski Filler Powder to a small quantity of mixed resin. A paste or putty-like consistency can he obtained which can then be trowelled or screeded on.

4. This filler coat will even out the texture of the fibreglass matt which can then be sanded smooth and painted if desired. If the texture or profile is not a cosmetic consideration, a second coat of mixed resin can he applied without the talc

TRANSPORTATION

Flammable liquid
Dangerous Goods Class 3.2.
Pack sizes available 20Kg, 4Kg, 2Kg, 1 Kg, 500ml and 250 ml

PRECAUTIONS

Precautions are as follows:-

1. If using any type of Norski Polyester Resin, Norski Gelcoat or Norski Flowcoat use only Norski Polyester Catalyst. *DO NOT USE ACCELERATOR*.

2. Treat all Norski Polyester Resin and Catalyst as FLAMMABLE.

3. Keep away from naked flame.

4. Polyester Catalyst is extremely dangerous to the eyes and can cause permanent damage. If splashed into the eyes, flush immediately with clean running water for at least 10 minutes and see a doctor.

5. Wear protective glasses and rubber gloves when mixing and DO NOT rub the eyes with contaminated hands or clothing

6. Wash thoroughly after handling.

7. Keep out of reach of children at all times.

8. **DO NOT** store solvent or resin soaked rags in a confined spaces as spontaneous combustion can occur.

Norski Holdings Ltd, 10 Northpoint St, Plimmerton Wellington 5024
Phone 04 233 6184, Facsimile 04 233 6173, Website www.norski.co.nz

EPOXIES • RESINS • GLUES • FILLERS

FIRST AID

If poisoning occurs, contact a Doctor or the POISONS INFORMATION CENTRE
IF SWALLOWED DO NOT INDUCE VOMITING.

DO NOT INHALE VAPOUR, USE WITH ADEQUATE VENTILATION.
STORE IN A COOL PLACE.

SAFETY PRECAUTIONS: Do not use near fire or flames. Harmful or fatal if swallowed Use disposable gloves to avoid skin contamination. If resin comes into contact with skin, wash uncured resin off with soap and water. Wear safety glasses to avoid eye contamination. Mixed formulation contains Epoxy Resin and Amines. If swallowed do not induce vomiting. Give a glass of water. Contact a Doctor or the Poisons National Information Centre on 0800 764 766 (Urgent information only). Eye Contamination: Hold eyes open and flood with water for at least 15 minutes. See a Doctor immediately.

WARRANTY

Because the use of this product is beyond the control of the manufacturer, no liability or responsibility can be accepted for any loss or damage arising from its application or use. Liability for faulty material is limited to product replacement only.

Norski Holdings Ltd, 10 Northpoint St, Plimmerton Wellington 5024
Phone 04 233 6184, Facsimile 04 233 6173, Website www.norski.co.nz

Appendix C Thermal conductivity probe

The theory of the line source method (thermal conductivity probe) refers to Ahmed and Rahman (2009a)

The thermal conductivity of the sample is found from:

$$\lambda = \frac{Q}{4\pi S} \qquad \text{Eq C-1}$$

$$S = \frac{(\theta_2 - \theta_1)}{Ln\left(\frac{t_2}{t_1}\right)} \qquad \text{Eq C-2}$$

$$Q = 6.0\ W\ m^{-1}$$

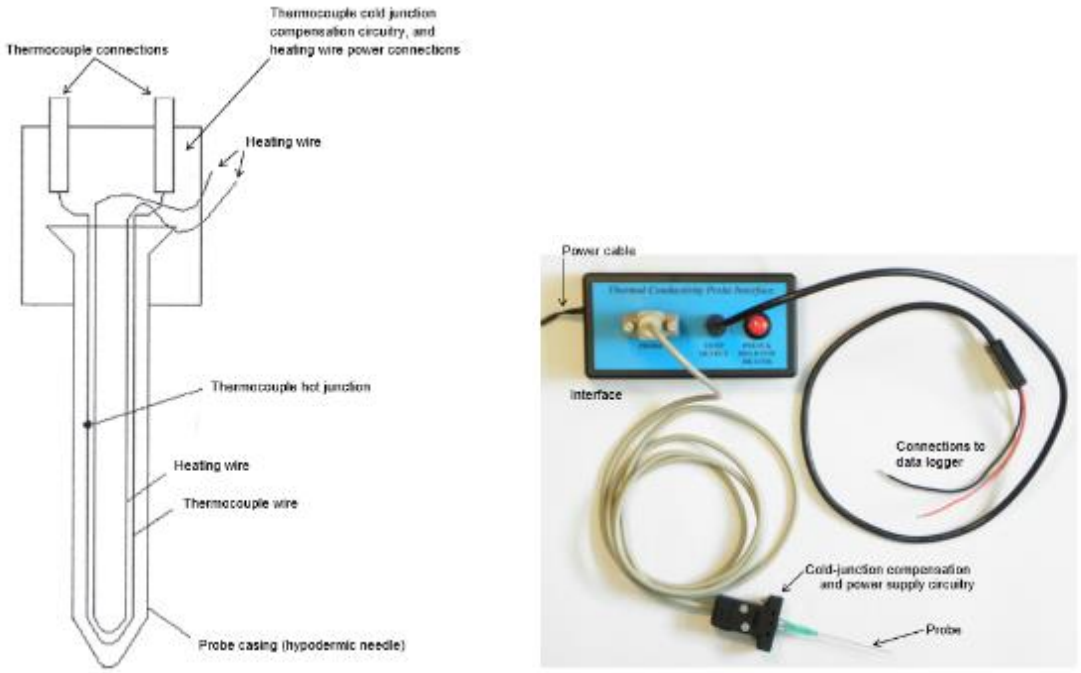

Figure 5, Picture of the thermal conductivity probe

Table C-1, Thermal conductivity prob calibration

Glycerol Literature value [1]	Measured value Glycerol
$0.284\ W\ m^{-1}K^{-1}$	$0.273 \pm 0.018\ W\ m^{-1}K^{-1}$

1 Lotfi et al. (2021)

Appendix D Thermal Paste R 001 Technical data sheet

A NEW FORCE IN CHEMICAL MANUFACTURING

Unit 2, 14-16 Lee Holm Road
St Marys NSW 2760
Australia

Ph: 1300 738 250 (Australia)
Ph: +61 2 9833 9766 (International)
Fax: 02 9623 3670

sales@chemtools.com.au
www.chemtools.com.au

TECHNICAL DATA SHEET

October 2015

PRODUCT NAME

R001 Thermally Conductive Grease – Heatsink Compound

PRODUCT RANGE

Part Number	Available Size
CT-R001-SI-S10-PT	10cc Syringe
CT-R001-SI-S30-PT	30cc Syringe
CT-R001-50	50 Gram Tube
CT-R001-150	150 Gram Tube
CT-R001-1KG	1 Kilo Pail
CT-R001-4KG	4 Kilo Pail

Refer to SDS for product safety guidelines

R001 Thermally Conductive Grease – Heatsink Compound

Chemtools® R001 Thermally Conductive Grease is a non-toxic, metal oxide filled silicone grease, which provides a highly efficient and highly thermally conductive compound designed to operate over a wide temperature range. The formulation is designed for use in applications where long term high temperature stability is required.

COMMON USES:

- Diodes
- Transistors
- Heat sinks
- Semi-conductors
- Thermostats
- Power resistors
- Radiators

FEATURES & BENEFITS

- Good Thermal Conductivity.
- Non-Electrically Conductive.
- Wide Operating Temperature Range.
- Low Creep and Low Bleed Characteristics.
- Easy Application, Low Toxicity, Economic.

TYPICAL SPECIFICATION:

Thermo Conductive Constituent:	Metal oxide powders
Carrier:	Silicones
Appearance:	White Paste
Odour:	None
Thermal Conductivity:	0.9 W/mK
Thermal Resistance:	0.12 °C-cm2/W
Density:	2.1 g/cm3
Temperature Range:	-50 to +200°C
Weight Loss:	-0.6% after 200hrs @ 150°C
Bleed:	0.4%
Dielectric Strength:	18kV/mm
Permittivity:	3.6 @ 1MHz
Electrical Resistance:	3 x 1014Ω

SHELF LIFE:
>3 years (Please refer to storage conditions below)

DIRECTIONS FOR USE:
Clean all surfaces before use. Ensure good coverage. The surface of all components should be free of dirt, contaminants and old grease.

STORAGE:
Store in a cool, dry place, in tightly closed original containers at a room temperature between 5°C and 40°C. Do not place in direct sunlight or near any heat source. Do not return any used material to its original container.

DISPOSAL:
All products should be disposed of in accordance with local regulations.

PRECAUTIONS:
This product generally present little hazard in normal handling if ordinary care is exercised. If spilled, cover with inert, absorbent material and remove. Flush the area with water. None of these materials should be used, stored, or transported until the handling precautions and recommendations as stated in the Safety Data Sheets (SDS) for this and all other products being used are understood by all persons who will work with the material.

WARRANTY:
All products purchased from or supplied by Chemtools® are subject to terms and conditions set out in the contract. Chemtools® warrants only that its products meet the specifications designated as such herein, or in other publications. All other information supplied by Chemtools® is considered accurate, but is furnished upon the express condition. The customer shall make its own assessment to determine the product's suitability for a particular purpose. Chemtools® makes no other warranty, either expressed or implied, including those regarding such other information, the data upon which the same is based, or the results to be obtained from the use thereof; that any product shall be merchantable or fit for any particular purpose; or that the use of such other information or products will not infringe any patent.

Appendix E STEM Pro Aluminium powder Specification

S.T.M. PRO SPECIAL EFFECTS

Material Safety Data Sheet

CAP 75B ALUMINIUM POWDER

Infosafe No.	APSHE	**Version No.**	2.1	**ISSUED Date**	13/04/2012 **Status** ISSUED by STM PRO

1. IDENTIFICATION OF THE MATERIAL AND SUPPLIER

Product Name
CAP 75B ALUMINIUM POWDER

Product Code
ACAP710002

Company Name
STM PRO Special Effects New Zealand

Address
PO BOX 27-204,
Wellington 6041
New Zealand

Emergency Tel.
111

Email
info@stmpro.co.nz

Recommended Use
Industrial application

2. HAZARDS IDENTIFICATION

Hazard Classification
Not classified as Hazardous according to the Hazardous Substances (Minimum Degrees of Hazard) Regulations 2001, New Zealand.
Not classified as Dangerous Goods for transport according to the New Zealand Standard NZS 5433:2007 Transport of Dangerous Goods on Land.

3. COMPOSITION/INFORMATION ON INGREDIENTS

Chemical Characterization
Solid

Ingredients

Name	CAS	Proportion
Aluminium	7429-90-5	60-100 %
Other ingredients determined not to be hazardous		Balance

4. FIRST AID MEASURES

Inhalation

If inhaled, remove affected person from contaminated area. Keep at rest until recovered. If symptoms develop and/or persist seek medical attention.

Ingestion
Do not induce vomiting. Wash out mouth thoroughly with water. Seek medical attention.

Skin
Remove all contaminated clothing immediately. Wash affected area thoroughly with soap and water. If symptoms develop seek medical attention.

Eye
If in eyes, hold eyelids apart and flush the eyes continuously with running water. Continue flushing for several minutes until all contaminants are washed out completely. If symptoms develop and/or persist seek medical attention.

First Aid Facilities
Eyewash and normal washroom facilities.

Advice to Doctor
Treat symptomatically.

Other Information
For advice in an emergency, contact a Poisons Information Centre or a doctor at once. (0800 764 766)

5. FIRE FIGHTING MEASURES

Suitable Extinguishing Media
Dry chemical, carbon dioxide, sand or earth may be used for small fires only.

Hazards from Combustion Products
Under fire conditions this product may emit toxic and/or irritating fumes and gases .

Specific Hazards
Dust clouds may present an explosion hazard in the presence of an ignition source. In contact with acids, can liberate flammable hydrogen gas which can form explosive mixtures in air. In contact with water releases flammable gases which may ignite spontaneously.

Precautions in connection with Fire
Fire fighters should wear Self-Contained Breathing Apparatus (SCBA) operated in positive pressure mode and full protective clothing to prevent exposure to vapours or fumes. Water spray may be used to cool down heat-exposed containers. Fight fire from safe location. This product should be prevented from entering drains and watercourses.

Unsuitable Extinguishing Media
Do not use water jet.

6. ACCIDENTAL RELEASE MEASURES

Emergency Procedures
Increase ventilation. Evacuate all unprotected personnel. Wear respiratory protection and full protective clothing to minimise exposure. Wear sufficient respiratory protection and full protective clothing to prevent exposure. Sweep up material avoiding dust generation or dampen spilled material with water to avoid airborne dust, then transfer material to a suitable container. Wash surfaces well with soap and water. Seal all wastes in labelled plastic containers for subsequent recycling or disposal. Dispose of waste according to the applicable local and national regulations. If contamination of sewers or waterways occurs inform the local water and waste management authorities in accordance with local regulations.

7. HANDLING AND STORAGE

Precautions for Safe Handling
Avoid inhalation of dust, and skin or eye contact. Use only in a well ventilated area. Keep containers sealed when not in use. Prevent the build up of dust in the work

atmosphere. Maintain high standards of personal hygiene ie. washing hands prior to eating, drinking, smoking or using toilet facilities.

Conditions for Safe Storage
Store in a cool, dry, well-ventilated area, out of direct sunlight and moisture. Store in suitable, labelled containers. Keep containers tightly closed. Store away from incompatible materials. Ensure that storage conditions comply with applicable local and national regulations.

8. EXPOSURE CONTROLS/PERSONAL PROTECTION

National Exposure Standards

Substance	Regulations	Exposure Duration	Exposure Limit	Units	Notes
Aluminium	NZ OELs List	TWA	10	mg/m3	**Metal dust**

Biological Limit Values
No biological limits allocated.

Engineering Controls
Use with good general ventilation. If dusts are produced, local exhaust ventilation should be used.

Respiratory Protection
If engineering controls are not effective in controlling airborne exposure then an approved respirator with a replaceable filter should be used.
Reference should be made to Australian Standards AS/NZS 1715, Selection, Use and Maintenance of Respiratory Protective Devices; and AS/NZS 1716, Respiratory Protective Devices, in order to make any necessary changes for individual circumstances.

Eye Protection
Safety glasses with side shields, chemical goggles or full-face shield as appropriate should be used. Final choice of appropriate eye/face protection will vary according to individual circumstances. Eye protection devices should conform to relevant regulations.
Eye protection should conform with Australian/New Zealand Standard AS/NZS 1337 - Eye Protectors for Industrial Applications.

Hand Protection
Wear gloves of impervious material such as butyl rubber, PVC or laminated film gloves. Final choice of appropriate gloves will vary according to individual circumstances i.e. methods of handling or according to risk assessments undertaken.
Reference should be made to AS/NZS 2161.1: Occupational protective gloves - Selection, use and maintenance.

Body Protection
Suitable protective workwear, e.g. cotton overalls buttoned at neck and wrist is recommended. Chemical resistant apron is recommended where large quantities are handled.

9. PHYSICAL AND CHEMICAL PROPERTIES

Form
Solid

Appearance
Silver- white grit

Odour
Odourless

Melting Point
680°C

Boiling Point
2450-2467°C

Solubility in Water
Insoluble in water

Specific Gravity
2.70

pH Value
Not applicable

Vapour Pressure
Not applicable

Vapour Density (Air=1)
Not applicable

Evaporation Rate
Not applicable

Colour
Silver- white

Flash Point
Not applicable

Flammability
Not flammable

Auto-Ignition Temperature
Not applicable

Explosion Limit - Upper
Not available

Explosion Limit - Lower
Not available

10. STABILITY AND REACTIVITY

Chemical Stability
Stable under normal conditions of storage and handling.

Conditions to Avoid
Heat, open flames and other sources of ignition.

Incompatible Materials
Oxidising agents, water, bases, acids and halogenated organic compounds

Hazardous Decomposition Products
Thermal decomposition may result in the release of toxic and/or irritating fumes .

Hazardous Reactions
Aluminium reacts with water, acids and bases.

Hazardous Polymerization
Will not occur.

11. TOXICOLOGICAL INFORMATION

Toxicology Information
No toxicity data available for this material.

Inhalation
Inhalation of dusts may irritate the respiratory system.

Ingestion
Ingestion of this product may irritate the gastric tract causing nausea and vomiting.

Skin
Skin contact may cause mechanical irritation resulting in redness and itching.

Eye
Eye contact may cause mechanical irritation. May result in mild abrasion.

Chronic Effects
Chronic exposure to this material may aggravate existing respiratory disorders and lung disorders such as bronchitis, emphysema and asthma. Onset and progression are related to dust concentrations and duration of exposure.

12. ECOLOGICAL INFORMATION

Ecotoxicity
No ecological data available for this material.

Persistence / Degradability
Not available

Mobility
Not available

Bioaccumulative Potential
Not available

Environmental Protection
Prevent this material entering waterways, drains and sewers.

13. DISPOSAL CONSIDERATIONS

Disposal Considerations
The disposal of the spilled or waste material must be done in accordance with applicable local and national regulations.
Product Disposal:
This product can be disposed through a licensed commercial waste collection service. Dispose of waste according to the applicable local and national regulations.This product is non-hazardous and therefore the New Zealand HSNO regulations regarding disposal do not apply, however other regulations may apply. It can be disposed in a licensed landfill facility. As the product is a non-hazardous solid substance, it can be disposed in a licensed landfill facility after authorization.
Container Disposal:
The product is non-hazardous, therefore, the packaging may be re-used or recycled if it has been treated to remove any residual contents of the substance. Any wash-off water from the container cleaning process should be sent to a suitable waste water treatment plant before discharge into the environment.In New Zealand, the packaging (that may or may not hold any residual substance) that is lawfully disposed of by householders or other consumers through a public or commercial waste collection service is a means of compliance with regulations.

14. TRANSPORT INFORMATION

Transport Information
Not classified as Dangerous Goods for transport according to the New Zealand Standard NZS 5433:2007 Transport of Dangerous Goods on Land.
Not classified as Dangerous Goods by the criteria of the International Maritime Dangerous Goods Code (IMDG Code) for transport by sea.

Not classified as Dangerous Goods by the criteria of the International Air Transport Association (IATA) Dangerous Goods Regulations for transport by air.

IMDG Marine Pollutant
No

15. REGULATORY INFORMATION

Regulatory Information
Not classified as Hazardous according to the Hazardous Substances (Minimum Degrees of Hazard) Regulations 2001, New Zealand.

End of MSDS

Appendix F Q-cell data sheet

ADHESIVE TECHNOLOGIES NZ LTD.
17 Corban Avenue, Henderson, Auckland ■ P.O. Box 21169, Henderson, Auckland 8, New Zealand
Phone: +64 9 838-6961 ■ Facsimile: +64 9 836-4849 ■ Website: www.adhesivetechnologies.co.nz

Safety Data Sheet - NZ Supplement Sheet

Product Name	**409 Q-cell**	
NZ Supplier	**Adhesive Technologies NZ ltd** 17 Corban Avenue Henderson Auckland 09 838 6961 **Website:** www.adhesivetechnologies.co.nz	
Emergency Contact Numbers	National Poisons Centre 0800 764 766 (0800 POISON)	New Zealand Fire Service– 111
HSNO Approval Number	Not classified	
Signal Word	Not Applicable	
Issue Date	16/09/2021	

This supplement must be read in conjunction with the attached Safety Data Sheet (SDS)

SAFETY DATA SHEET

SECTION 1: IDENTIFICATION OF THE SUBSTANCE/MIXTURE AND OF THE COMPANY/UNDERTAKING

1.1 Product identifier

Product Name	**Q-Cel® Inorganic microspheres 5000, 6000, 7000, 9000 series**

1.2 Relevant identified uses of the substance or mixture and uses advised against

Identified use(s)	Specialty engineering additive in plastics. E.g. it is added to modify the density, impact resistance, wear resistance, provide thermal or acoustic insulation in plastics and thermoset systems.

1.3 Details of the supplier of the safety data sheet

Company Identification	Potters Industries LLC P. O. Box 841 Valley Forge, PA 19482 USA
Telephone	+1 610-651-4700
E-Mail (competent person)	sds.uk@pqcorp.com

1.4 Emergency telephone number

Emergency Phone No.	Potters Industries LLC +1 610-651-4200 ChemTrec (800) 424-9300

SECTION 2: HAZARDS IDENTIFICATION

2.1 Classification of the substance or mixture

GHS Classification	Not classified as dangerous for supply/use.

2.2 Label elements

Hazard pictogram(s)	
Signal word(s)	Not applicable.
Hazard statement(s)	Not applicable
Precautionary statement(s)	Not applicable

SECTION 3: COMPOSITION/INFORMATION ON INGREDIENTS

Ingredient(s)	%W/W	CAS No.	EINECS No. / REACH Registration	Hazard symbol(s) and hazard statement(s)
Amorphous Sodium Borosilicate	>99.9	50815-87-7	Exempt	
Proprietary anticake coating	<1			

SECTION 4: FIRST AID MEASURES

4.1 Description of first aid measures

Eye Contact	Irrigate with eyewash solution or clean water, holding the eyelids apart, for at least 15 minutes. If symptoms persist, obtain medical attention.

Skin Contact	Wash affected skin with plenty of water. If symptoms occur obtain medical attention.
Inhalation	In case of accident by inhalation: remove casualty to fresh air and keep at rest. If symptoms develop, obtain medical attention.
Ingestion	Get medical advice/attention.
4.2 Most important symptoms and effects, both acute and delayed	Dust may cause irritation.
4.3 Indication of any immediate medical attention and special treatment needed	Flush the contaminated area of body with large amounts of water.

SECTION 5: FIRE-FIGHTING MEASURES

5.1 Extinguishing media	
Suitable Extinguishing Media	As appropriate for surrounding fire.
Unsuitable extinguishing Media	None known.
5.2 Special hazards arising from the substance or mixture	Non-combustible.

SECTION 6: ACCIDENTAL RELEASE MEASURES

6.1 Personal precautions, protective equipment and emergency procedures	Wear suitable protective clothing. Wear eye/face protection. An approved dust mask should be worn if dust is generated during handling. See Also Section 8.
6.2 Environmental precautions	Floats on water.
6.3 Methods and materials for containment and cleaning up	Caution - spillages may be slippery. Avoid generation of dust. Use vacuum equipment for collecting spilt materials, where practicable. Transfer to a container for disposal or recovery.
6.4 Reference to other sections	Not applicable.

SECTION 7: HANDLING AND STORAGE

7.1 Precautions for safe handling	Avoid contact with skin, eyes or clothing. Avoid generation of dust. Wash thoroughly after handling. Wear protective equipment to comply with good occupational hygiene practice. Do not eat, drink or smoke at the work place.
7.2 Conditions for safe storage, including any incompatibilities	Keep container tightly closed and dry. In case of high humidity or storage for extended periods of time, use plastic bags to enclose product containers to avoid caking.

SECTION 8: EXPOSURE CONTROLS/PERSONAL PROTECTION

8.1 Control parameters

SUBSTANCE.	Occupational Exposure Limits
	UK EH40: Dust Total inhalable: WEL 10mg/m3 8h TWA. Respirable: WEL 4mg/m3 8h TWA. ACGIH: Particulates not otherwise classified Inhalable TLV 10mg/m3 8h TWA. Respirable: TLV 3mg/m3 8h TWA. OSHA: Inert or Nuisance Dust Total dust : PEL 15mg/m3 8h TWA. Respirable fraction : PEL 5mg/m3 8h TWA.

8.2 Exposure controls

8.2.1 Appropriate engineering controls	Use only with adequate ventilation to keep exposures (airborne levels of dust, fume, vapour etc) below recommended exposure limits.
8.2.2 Personal Protection	
Respiratory protection	Avoid inhalation of dusts. Wear suitable respiratory protective equipment if exposure to levels above the occupational exposure limit is likely.
Eye/face protection	Chemical goggles (EN 166).
Skin protection	Wear suitable protective clothing and gloves. For example PVC or rubber gloves.
8.2.3 Environmental Exposure Controls	Local exhaust recommended.

SECTION 9: PHYSICAL AND CHEMICAL PROPERTIES

9.1 Information on basic physical and chemical properties

Appearance	Powder. White.
Odour	Odourless.
pH (Value)	Not applicable.
Freezing Point (°C)	Not applicable.
Melting Point (°C)	Not applicable.
Boiling Point (°C)	Not applicable.
Flash Point (°C) [Closed cup]	Not applicable.
Evaporation rate	Not applicable.
Flammability (solid, gas)	Not applicable.
Explosive Limit Ranges	Not applicable.
Vapour pressure (Pascal)	
Vapour Density (Air=1)	Not applicable.
Density (g/ml)	Not applicable.
Solubility (Water)	Soluble.
Solubility (Other)	Not available.
Partition Coefficient	Not available.
Auto Ignition Point (°C)	Not applicable.
Decomposition Temperature (°C)	Not applicable.
Viscosity (mPa. s)	Not applicable.
Explosive properties	Not applicable.
Oxidising Properties	Not applicable.
9.2 Other information	Not applicable.

SECTION 10: STABILITY AND REACTIVITY

10.1 Reactivity	Avoid contact with strong acids
10.2 Chemical stability	Stable.
10.3 Possibility of hazardous reactions	None known.
10.4 Conditions to avoid	None known.
10.5 Incompatible materials	Strong acids
10.6 Hazardous decomposition product(s)	None known.

SECTION 11: TOXICOLOGICAL INFORMATION

11.1 Information on toxicological effects

Acute toxicity

Ingestion	Avoid ingestion. May be harmful if swallowed.

Inhalation	When a similar material was tested for respiratory toxicity in a 6-month intratracheal study in rats, no mortalities, untoward reaction, or observation correlated with exposure to the material. Minimal multifocal inflammation of the lung occurred in 90% of males and 80% of females. No appreciable increase in fibrous tissue was present in these lesions.
Skin Contact	When tested for primary irritation potential, this material caused mild eye irritation and slight skin irritation.
Eye Contact	When tested for primary irritation potential, this material caused mild eye irritation and slight skin irritation.
Sensitisation	It is not a skin sensitiser.
Carcinogenicity	IARC, NTP, OSHA, ACGIH do not list this product or any components thereof as known or suspected carcinogen.

SECTION 12: ECOLOGICAL INFORMATION

12.1 Toxicity	No data available on mixture. The following data is reported for sodium silicates: a 96 hour median tolerance for fish (Gambusia affnis) of 2320 ppm; a 96 hour median tolerance for water fleas (Daphnia magna) of 247 ppm.
12.2 Persistence and degradability	No data available on mixture.
12.3 Bioaccumulative potential	No data available on mixture.
12.4 Mobility in soil	No data available on mixture.
12.5 Results of PBT and vPvB assessment	Not classified as PBT or vPvB.

SECTION 13: DISPOSAL CONSIDERATIONS

13.1 Waste treatment methods	The waste is considered to be non hazardous. Disposal should be in accordance with local, state or national legislation.

SECTION 14: TRANSPORT INFORMATION

14.1 UN number	Not applicable
14.2 Proper Shipping Name	Not classified as dangerous for transport. Not classified as hazardous under DOT or US Transport Recommendations. Goods are not regulated for transport via IATA International Maritime Dangerous Goods (IMDG) Code: Not classified as hazardous ADR/RID Class : Not classified as dangerous for transport.
14.3 Transport hazard class(es)	Not applicable.
14.4 Packing group	Not applicable.
14.5 Environmental hazards	Not applicable.
14.6 Special precautions for user	Not applicable.
14.7 Transport in bulk according to Annex II of MARPOL73/78 and the IBC Code	Not applicable.

SECTION 15: REGULATORY INFORMATION

15.1 Safety, health and environmental regulations/legislation specific for the substance or mixture

TSCA Inventory Status: Reported/Included.
AICS Inventory Status: Reported/Included.
DSL/NDSL Inventory Status: Reported/Included.

German Water Hazard Classification VwVwS: WGK class 1 (low hazard to water).
1,0,0

SECTION 16: OTHER INFORMATION

Reviewed and reconfirmed, no significant changes.

This SDS was last reviewed: 10/2019
The following sections contain revisions or new statements:

Q-Cel® Hollow Microspheres

Typical[1] Properties

Q-Cel® Lightweight hollow microspheres offer latitude in manufacturing low density products. These single cell hollow microspheres appear as a white free flowing powder. The spheres are hydrophobic in nature. As filler, the primary function is to reduce resin usage and density but can enhance other properties as well.

TYPICAL PROPERTIES OF Q-CEL® ULTRA-LIGHT HOLLOW MICROSPHERES								
Q-Cel® Grades	Density (g/cm³)			Particle Size (µm)		Crush Strength (Isostatic)		
	True[2]	Effective[3]	Bulk[4]	Mean	D90	Psi	Bar	Mpa
6014	0.16	0.14	0.08	<105	<190	250	17	1.7
6019	0.21	0.19	0.11	<80	<150	500	34	3.4
6019S	0.215	0.19	0.11	<70	<135	500	34	3.4
6717		0.19	0.10	<52	<105	500	34	3.4
7019	0.22	0.19	0.21	<80	<150	500	34	3.4
7023S	0.26	0.23	0.26	<85	<135	750	52	5.2
5028	0.29	0.25	0.16	<75	<120	750	52	5.2
6036	0.40	0.35	0.21	<70	<115	1000	68	6.8
7040S	0.46	0.40	0.26	<60	<95	2000	138	13.8
6042S	0.49	0.42	0.26	<60	<100	2000	138	13.8
6048	0.54	0.47	0.27	<60	<105	3000	207	20.7
5070S		0.70	0.42	<45	<53	3500	242	24.2

[1] Typical values, not for specification purposes
[2] True Density is the particle density as measured by Gas Displacement
[3] Effective Density is the particle density as measured by liquid displacement
[4] Bulk Density is the weight as measured in a container (bin, silo, bag...) and includes the interstitial air

Q-Cel® Lightweight hollow microspheres have a density approximately one-fifth of most thermoset resins. On equal weight basis, the Q-Cel® hollow microspheres occupy five times more volume than an equivalent weight resin. They can displace heavy fillers, such as calcium carbonate, talc and clays, thus lowering the weight of composites materials. Spheres have the lowest surface area, thus the lowest resin demand. Lower viscosities are common allowing less resin to be used, increase the volume produced, usually resulting in cost savings in many applications.

- Q-Cel® 6014.k is recommended for any resin system where low viscosity and low shear processing conditions are used.
- Q-Cel 6019.k—7019.k—7023S.k and 5028.k are suited for many applications including fiberglass reinforced composites, urethanes foams, putties, cultured marble and adhesives. They also provide other desirable properties such as improved finishing characteristics and better thermal shock resistance. Application method involve trowelling, spray-up and casting where processing and/or viscosity produce a medium shear environment.
- Q-Cel® 6717 & 6019S.k are characterised by a low density and reduced particle size. They are particularly suited in applications where surface finishing and aesthetic properties are critical.

Q-Cel® High Strength products: As the density of Q-Cel® products increases, spheres size decrease and maximum working pressure increases. The Q-Cel® 6036—7040S—6042S—6048 and 5070S allow the formulators to choose the minimum density product that will survive pumping and moderate shear. High strength Q-Cel microspheres have ideal properties in low densities SMC and PVC plastisol formulations. Experience show that surface properties of Class A formulations have been enhanced by incorporating 6042S. Also improvement in flexural modulus is often noticed in parts containing Q-Cel®.

Q-Cel® reduced Alkalinity products: The Q-Cel® "5000" & "7000" series have reduced alkalinity compared to the "6000" series. They are intended for use in alkaline sensitive thermoset resins and in some formulations have provided improved stability and viscosity.

Product/ Service Information

Packaging:

Q-Cel® Hollow Microspheres are available in boxes with plastic liners and various bulk boxes or bags to suit our customer's requirements. The package weight depends on the density of the Q-Cel® grade. Details of packaging options are available as a separate document.
Samples in sufficient quantity for testing are available on request.

Safety Information:

Q-Cel® Solid Glass Microspheres are moderately alkaline, and prolonged exposure may irritate the respiratory tract. In dusty environments, the use of a NIOSH-approved mask or respirator is recommended. Material Safety Data Sheets (MSDS) can be supplied on request.

Storage:

Our packaging is designed to protect damages during shipment and handling. Some cautions are given for a proper storage:
Store micro-spheres containers in dry conditions.
Partially used containers should be tightly closed, not left open to the atmospheres for extended periods,
The products are hydroscopic and will tend to agglomerate upon prolonged exposure to moisture and humidity.

Other Product Range:

Sphericel® Ultra-Fine Hollow Glass Microspheres
Spheriglass® Solid Glass Microspheres
Spheriwhite® Colour-Enhancing Solid Glass Microspheres
Luxsil® Hollow Glass Microspheres for cosmetic applications
Spacer Beads Solid Glass Microspheres for the bonding lines
A & P series Technical Quality Solid Glass Microspheres
Q-Cel® ONG Hollow Microspheres for Oil Well Cementing

For further information about our range of Solid & Hollow Glass Microspheres, please contact us:

Potters Europe

Pontefract Road
Barnsley
South Yorkshire S71 1EJ
United Kingdom

Phone: +44 (0)1226 704 516
Fax: +44 (0)1226 207 615
E-mail: PQHS-Sales@pottersgroup.com
www.potterseurope.com

Ref: 3-03-042-1-12

Appendix G Input material database

Material	Thermal conductivity	Density	Heat capacity	Material Type	Material Typ
CeramTec CD 101 Silicon Carbide, SiC-ZrB2	100	3260	0.6	Ceramic	Carbide
CeramTec CD 110 Silicon Carbide, SSiC	100	3100	0.6	Ceramic	Carbide
CeramTec Rocar® SiG Silicon Carbide, SiSiC	115	3070	0.7	Ceramic	Carbide
CeramTec Rocar® ST Silicon Carbide, SSiC	100	3110	0.6	Ceramic	Carbide
COI Ceramics Nicalon™ CG SiCO Ceramic Fiber	2.97	2550	0.71	Ceramic	Carbide
COI Ceramics Nicalon™ HI SiC Low O Ceramic Fiber	7.77	2740	0.67	Ceramic	Carbide
COI Ceramics Nicalon™ HI Type S SiC Ceramic Fiber	18.4	3100	0.7	Ceramic	Carbide
CoorsTek ACI-Co10 Tungsten Carbide	85	14500	0.213	Ceramic	Carbide
CoorsTek ACI-Co6 Tungsten Carbide	100	14900	0.209	Ceramic	Carbide
CoorsTek ACI Ni10 Tungsten Carbide	75	14400	0.215	Ceramic	Carbide
CoorsTek ACI-Ni6 Tungsten Carbide	82	14900	0.21	Ceramic	Carbide
CoorsTek Pure SiC™ HR CVD Silicon Carbide, > 99.9995%	115	3210	0.665	Ceramic	Carbide
CoorsTek Reaction Bonded Silicon Carbide, SCRB (SC-2)	125	3100	0.7	Ceramic	Carbide
CoorsTek SC-DSG (SC-35) Graphite Loaded Sintered Silicon Carbide	125	2800	0.82	Ceramic	Carbide
CoorsTek SC-DSLP (SC-50) Liquid Phase Sintered Silicon Carbide	80	3180	0.8	Ceramic	Carbide
Goodfellow Tungsten Carbide/Cobalt	70	14900	0.34	Ceramic	Carbide
Sapco S.SiC Silicon Carbide	100	3100	1	Ceramic	Carbide
Sapco Si.SiC Silicon Carbide	160	3100	1.1	Ceramic	Carbide
Silicon Carbide, Reaction-Bonded, SiSiC	140	3000	0.7	Ceramic	Carbide
Specialty Materials SCS-6 Silicon Carbide Monofilament	150	3000	0.71	Ceramic	Carbide
Clay, Soft Shale	1.67	2450	0.837	Ceramic	Clay
Autoclaved aerated concrete, 0.500 g/cc density	0.17	500	1	Ceramic	Concrete
Autoclaved aerated concrete, 0.600 g/cc density	0.195	600	1	Ceramic	Concrete
Autoclaved aerated concrete, 0.700 g/cc density	0.22	700	1	Ceramic	Concrete
Autoclaved aerated concrete, 0.800 g/cc density	0.245	800	1	Ceramic	Concrete
Autoclaved aerated concrete, 0.900 g/cc density	0.285	900	1	Ceramic	Concrete
Autoclaved aerated concrete, 1.000 g/cc density	0.315	1000	1	Ceramic	Concrete
Autoclaved aerated concrete, 2.100 g/cc density	1.345	2100	1	Ceramic	Concrete
Concrete, 1 4 Dry	0.75	2300	0.657	Ceramic	Concrete
Concrete, Cinder	0.34	1600	0.657	Ceramic	Concrete
Concrete, Lightweight	0.21	950	0.657	Ceramic	Concrete
Concrete; Stone, 1-2-4 Mix	1.46	2300	0.88	Ceramic	Concrete
Portland Cement	0.53	2010	0.736	Ceramic	Concrete
Portland Cement with Treated Silica Fume	0.33	1730	0.788	Ceramic	Concrete
Portland Cement with Untreated Silica Fume	0.35	1720	0.782	Ceramic	Concrete
Portland Cement with Untreated Silica Fume and Silane	0.61	1970	0.98	Ceramic	Concrete
96% Silica Consolidated Reconstructed Glass	1.38	2180	0.75	Ceramic	Glass
Accuratus MACOR Machinable Glass Ceramic	1.5	2520	0.79	Ceramic	Glass
AGY ZenTron® S-2 Generic S-Glass Fiber	1.25	2460	0.737	Ceramic	Glass
Aremco Aremcolox™ Macor® Machinable Glass Ceramic Machinable Ceramic, MGC	1.46	2520	0.79	Ceramic	Glass
C-Glass Fiber, Generic	1.1	2540	0.787	Ceramic	Glass
Copper Bromide, CuBr, Cubic	1.25	4980	0.381	Ceramic	Glass
Copper Chloride, CuCl, Cubic (Nantokite)	0.84	4140	0.49	Ceramic	Glass
Copper Iodide, CuI, Cubic (Marshite)	1.68	5630	0.276	Ceramic	Glass
Corning Pyroceram® Glass Ceramic	3.39	2600	0.974	Ceramic	Glass
E-Glass Fiber, Generic	1.3	2570	0.81	Ceramic	Glass
Mateck Cesium Iodide, CsI	1.1	4510	0.2	Ceramic	Glass
Mateck Glass (BK7 Schott or analogous)	1.11	2510	0.858	Ceramic	Glass
Mateck Thallium Bromoiodide TlBr-TlI (KRS-5)	0.54	7370	0.151	Ceramic	Glass
Phosphorus (III) Bromide, PBr3	0.117	2800	0.281	Ceramic	Glass
S-2 Glass® Fiber	1.45	2460	0.737	Ceramic	Glass
Saint-Gobain Puropsil® B Infrared Grade Low [OH] Optical Fused Quartz	2	2210	0.75	Ceramic	Glass
Saint-Gobain Vitreosil® CFQ/TSC Optical Fused Quartz	1.38	2200	0.75	Ceramic	Glass
Schott F2 Glass	0.78	3600	0.557	Ceramic	Glass
Schott K10 Glass	1.12	2520	0.77	Ceramic	Glass
Schott KZFS12 Glass	0.71	3840	0.54	Ceramic	Glass
Schott LF5 Glass	0.866	3220	0.657	Ceramic	Glass
Schott LITHOSIL-Q Glass	1.31	2200	0.79	Ceramic	Glass
Schott LITHOTEC-CAF2 Glass	9.71	3180	0.854	Ceramic	Glass
Schott N-BAF10 Glass	0.78	3750	0.56	Ceramic	Glass
Schott N-BAF4 Glass	1.02	2890	0.74	Ceramic	Glass
Schott N-BAF51 Glass	0.67	3330	0.84	Ceramic	Glass
Schott N-BAF52 Glass	0.96	3050	0.68	Ceramic	Glass
Schott N-BAK1 Glass	0.795	3190	0.687	Ceramic	Glass
Schott N-BAK2 Glass	0.92	2860	0.69	Ceramic	Glass
Schott N-BAK4 Glass	0.88	3050	0.68	Ceramic	Glass
Schott N-BALF4 Glass	0.85	3110	0.69	Ceramic	Glass
Schott N-BALF5 Glass	1.05	2610	0.81	Ceramic	Glass
Schott N-BASF2 Glass	0.94	3150	0.66	Ceramic	Glass
Schott N-BK10 Glass	1.32	2390	0.81	Ceramic	Glass
Schott N-F2 Glass	1.05	2650	0.81	Ceramic	Glass
Schott N-FK5 Glass	0.925	2450	0.808	Ceramic	Glass
Schott N-FK51A Glass	0.76	3680	0.69	Ceramic	Glass
Schott N-K5 Glass	0.95	2590	0.783	Ceramic	Glass
Schott N-KF9 Glass	1.04	2500	0.86	Ceramic	Glass
Schott N-KZFS11 Glass	0.81	3200	0.69	Ceramic	Glass
Schott N-KZFS2 Glass	0.81	2550	0.83	Ceramic	Glass
Schott N-KZFS4 Glass	0.84	3000	0.76	Ceramic	Glass
Schott N-KZFS5 Glass	0.95	3040	0.73	Ceramic	Glass
Schott N-KZFS8 Glass	1.05	3200	0.76	Ceramic	Glass
Schott N-LAF2 Glass	0.67	4300	0.51	Ceramic	Glass
Schott N-LAF21 Glass	0.83	4280	0.55	Ceramic	Glass
Schott N-LAF33 Glass	0.8	4360	0.57	Ceramic	Glass
Schott N-LAF34 Glass	0.56	4240	0.8	Ceramic	Glass

Schott N-LAF35 Glass	0.8	4120	0.57	Ceramic	Glass
Schott N-LAF36 Glass	0.79	4430	0.54	Ceramic	Glass
Schott N-LAF7 Glass	0.83	3730	0.62	Ceramic	Glass
Schott N-LAK10 Glass	0.86	3690	0.64	Ceramic	Glass
Schott N-LAK21 Glass	0.88	3740	0.59	Ceramic	Glass
Schott N-LAK33A Glass	0.81	4220	0.55	Ceramic	Glass
Schott N-LAK34 Glass	0.82	4020	0.52	Ceramic	Glass
Schott N-LAK8 Glass	0.84	3750	0.62	Ceramic	Glass
Schott N-LAK9 Glass	0.908	3510	0.649	Ceramic	Glass
Schott N-LASF31a Glass	0.79	5510	0.44	Ceramic	Glass
Schott N-LASF40 Glass	0.81	4430	0.55	Ceramic	Glass
Schott N-LASF41 Glass	0.79	4850	0.49	Ceramic	Glass
Schott N-LASF43 Glass	0.81	4260	0.55	Ceramic	Glass
Schott N-LASF44 Glass	0.82	4440	0.53	Ceramic	Glass
Schott N-LASF45 Glass	1.02	3630	0.66	Ceramic	Glass
Schott N-LASF46A Glass	0.91	4450	0.54	Ceramic	Glass
Schott N-LASF9 Glass	0.79	4410	0.53	Ceramic	Glass
Schott N-PK51 Glass	0.65	3860	0.62	Ceramic	Glass
Schott N-PK52A Glass	0.73	3700	0.67	Ceramic	Glass
Schott N-PSK3 Glass	0.99	2910	0.682	Ceramic	Glass
Schott N-PSK53A Glass	0.64	3570	0.59	Ceramic	Glass
Schott N-SF1 Glass	1	3030	0.75	Ceramic	Glass
Schott N-SF10 Glass	0.96	3050	0.74	Ceramic	Glass
Schott N-SF11 Glass	0.95	3220	0.71	Ceramic	Glass
Schott N-SF14 Glass	1	3120	0.75	Ceramic	Glass
Schott N-SF15 Glass	1.04	2920	0.76	Ceramic	Glass
Schott N-SF2 Glass	1.14	2720	0.79	Ceramic	Glass
Schott N-SF4 Glass	0.95	3150	0.76	Ceramic	Glass
Schott N-SF5 Glass	1	2860	0.77	Ceramic	Glass
Schott N-SF57 Glass	0.99	3530	0.66	Ceramic	Glass
Schott N-SF6 Glass	0.96	3370	0.69	Ceramic	Glass
Schott N-SF66 Glass	0.8	4000	0.54	Ceramic	Glass
Schott N-SF8 Glass	1.03	2900	0.77	Ceramic	Glass
Schott N-SK14 Glass	0.851	3440	0.636	Ceramic	Glass
Schott N-SK16 Glass	0.818	3580	0.578	Ceramic	Glass
Schott N-SK2 Glass	0.776	3550	0.595	Ceramic	Glass
Schott N-SK4 Glass	0.83	3540	0.57	Ceramic	Glass
Schott N-SK5 Glass	0.99	3300	0.56	Ceramic	Glass
Schott N-SSK2 Glass	0.81	3530	0.58	Ceramic	Glass
Schott N-SSK8 Glass	0.84	3270	0.64	Ceramic	Glass
Schott N-ZK7 Glass	1.04	2490	0.77	Ceramic	Glass
Schott P-LASF47 Glass	0.85	4540	0.55	Ceramic	Glass
Schott P-PK53 Glass	0.64	2830	0.77	Ceramic	Glass
Schott P-SF67 Glass	0.79	4240	0.53	Ceramic	Glass
Schott P-SF8 Glass	1.02	2900	0.79	Ceramic	Glass
Schott P-SK57 Glass	1.01	3010	0.76	Ceramic	Glass
Schott SF10 Glass	0.741	4280	0.465	Ceramic	Glass
Schott SF2 Glass	0.735	3860	0.498	Ceramic	Glass
Schott SF4 Glass	0.65	4790	0.41	Ceramic	Glass
Schott SF57 Glass	0.62	5510	0.36	Ceramic	Glass
Schott SF6 Glass	0.673	5180	0.389	Ceramic	Glass
Silver Iodide, AgI, (Miersite)	0.42	5670	0.232	Ceramic	Glass
Vanadyl Trichloride, VOCl3	0.139	1830	0.519	Ceramic	Glass
Boron Nitride, Cubic BN, (Borazone)	20	3490	0.793	Ceramic	Nitride
CeramTec Alunit® HS Aluminum Nitride	170	3330	0.738	Ceramic	Nitride
CeramTec CeramCool® Alunit® Aluminum Nitride	180	3330	0.738	Ceramic	Nitride
CeramTec SL 200 BG Silicon Nitride, Si3N4-Y2O3	21	3210	0.7	Ceramic	Nitride
CeramTec SL 303 Silicon Nitride, SiAlON+SiC	19	3250	0.7	Ceramic	Nitride
Momentive Performance Materials HBC Hot-Pressed Boron Nitride	25.5	1950	0.808	Ceramic	Nitride
Momentive Performance Materials HBN Hot-Pressed Boron Nitride	46	2100	0.808	Ceramic	Nitride
Momentive Performance Materials HBR Hot-Pressed Boron Nitride	44	2000	0.808	Ceramic	Nitride
Momentive Performance Materials HBT Hot-Pressed Boron Nitride	21	1750	0.808	Ceramic	Nitride
Momentive Performance Materials PolarTherm® PT110 Boron Nitride (BN) Powder	275	2250	0.794	Ceramic	Nitride
Alumina, alpha Al2O3, 99.5%	30	3900	0.88	Ceramic	Oxide
Carpenter Advanced Ceramics CAC975 97.5% Alumina	21.6	3790	0.891	Ceramic	Oxide
Carpenter Advanced Ceramics CAC995 99.5% Alumina	23.5	3890	0.891	Ceramic	Oxide
Carpenter Advanced Ceramics CAC998 99.8% Alumina	29	3920	0.791	Ceramic	Oxide
Carpenter Advanced Ceramics MS Grade Zirconia	3.08	5740	0.47	Ceramic	Oxide
Carpenter Advanced Ceramics TS Grade Zirconia	3.05	5730	0.47	Ceramic	Oxide
Carpenter Advanced Ceramics ZrX-GBP Zirconia	3.1	5740	0.5	Ceramic	Oxide
CeramTec 547 Cordierite (2MgO-2Al2O3-5SiO2)	1.6	2300	0.7	Ceramic	Oxide
CeramTec 645 Steatite (MgO-SiO2)	5.5	2700	1.1	Ceramic	Oxide
CeramTec 771 94% Alumina (Al2O3)	27.7	3600	0.9	Ceramic	Oxide
CeramTec 965 Toughened Alumina (Al2O3-ZrO2)	21	4200	0.7	Ceramic	Oxide
CeramTec AT 79 Alumina, 99.6%	30	3950	0.9	Ceramic	Oxide
CeramTec B 40 Alumina, 99.1%	28	3820	0.9	Ceramic	Oxide
CeramTec B 601 Alumina, 98.5%	24	3830	0.9	Ceramic	Oxide
CeramTec CeramCool® Rubalit® 708 Alumina, 96%	24	3780	0.8	Ceramic	Oxide
CeramTec DC 25 Dispersion Ceramic, Al2O3-ZrO2	17	4370	0.7	Ceramic	Oxide
CeramTec DN 70 Dispersion Ceramic, Al2O3-ZrO2	15	4010	0.8	Ceramic	Oxide
CeramTec MZ 111 Zirconia, ZrO2-Y2O3	2.5	6080	0.4	Ceramic	Oxide
CeramTec MZ 429 Zirconia, ZrO2-Y2O3	2.5	6050	0.4	Ceramic	Oxide
CeramTec RK 87 Alumina, 99.8%	30	3960	0.9	Ceramic	Oxide
CeramTec Rubalit® 708 HP Alumina, 96% (High Performance)	24	3780	0.78	Ceramic	Oxide
CeramTec Rubalit® A 1894 Alumina, 94%	18	3700	0.9	Ceramic	Oxide
CeramTec Rubalit® A 1896 brown Alumina	24	3820	0.9	Ceramic	Oxide

CeramTec Rubalit® A 1898 Alumina, 98%	26	3800	0.9	Ceramic	Oxide
CeramTec Rubalit® HSS Alumina, 75% (High Strength Substrate)	22	4350	0.69	Ceramic	Oxide
CeramTec Rubalit® IS 95 Alumina	24	3730	0.9	Ceramic	Oxide
CeramTec V 38 Alumina, 96.0% Al2O3-SiO2	20	3750	0.9	Ceramic	Oxide
CeramTec V 679 Alumina, 99.7%	30	3900	0.9	Ceramic	Oxide
CeramTec Ziralit Zirconia Toughened Alumina (ZTA), Al2O3•ZrO2	13	3800	0.8	Ceramic	Oxide
CeramTec ZN 40 Zirconia, ZrO2-MgO	3	5740	0.4	Ceramic	Oxide
CoorsTek AD-85 Alumina (nom. 85% Al2O3)	16	3420	0.92	Ceramic	Oxide
CoorsTek AD-90 Alumina (nom. 90% Al2O3)	16.7	3600	0.92	Ceramic	Oxide
CoorsTek AD-94 Alumina (nom. 94% Al2O3)	22.4	3700	0.88	Ceramic	Oxide
CoorsTek AD-96 Alumina (nom. 96% Al2O3)	24.7	3720	0.88	Ceramic	Oxide
CoorsTek AD-998 Alumina(nom. 99.8% Al2O3)	30	3920	0.88	Ceramic	Oxide
CoorsTek Dura-Z™ MgO Partially Stabilized Zirconia	2.2	5720	0.4	Ceramic	Oxide
CoorsTek FG-995 Alumina (nom. 98.5% Al2O3)	27.5	3800	0.88	Ceramic	Oxide
CoorsTek PlasmaPure™ Alumina (nom. 99.8% Al2O3)	30	3930	0.88	Ceramic	Oxide
CoorsTek TTZ (Dura-Z™) MgO Partially Stabilized Zirconia	2.2	5720	0.6	Ceramic	Oxide
CoorsTek Yttria Partially Stabilized Zirconia, YZTP, Sintered	2.2	6020	0.4	Ceramic	Oxide
CoorsTek YZTP Yttria Partially Stabilized Zirconia, Hipped	2.2	6070	0.4	Ceramic	Oxide
CoorsTek Zirconia-Toughened Alumina, ZTA	27	4050	0.885	Ceramic	Oxide
Cordierite	2.5	2300	0.9	Ceramic	Oxide
Corundum, Aluminum Oxide, Alumina, 99.9%, Al2O3	38	3960	0.8015	Ceramic	Oxide
Fused Quartz	1.7	2200	0.71	Ceramic	Oxide
Goodfellow Ruby, Al2O3	37.5	3980	0.75	Ceramic	Oxide
Magnesia Stabilized Zirconia	2.6	5775	0.5	Ceramic	Oxide
MarkeTech MC-LD and MC-MD Ultra High Temperature Machinable Ceramics	1	3425	0.5	Ceramic	Oxide
Mateck Fused Silica UV-VIS Grade (SiO2)	1.35	2210	0.728	Ceramic	Oxide
Mateck Quartz Crystalline (SiO2)	9.11	2650	0.741	Ceramic	Oxide
Morgan Advanced Ceramics Deranox™ 970 Alumina	24	3740	0.88	Ceramic	Oxide
Morgan Advanced Ceramics Deranox™ 975 Alumina	24	3800	0.88	Ceramic	Oxide
Morgan Advanced Ceramics Deranox™ 995 Alumina	25.6	3890	0.88	Ceramic	Oxide
Morgan Advanced Ceramics HIP Vitox™ Bio-compatible Alumina	30.4	3980	0.8	Ceramic	Oxide
Mullite, 3Al2O3-2SiO2	3.5	2800	0.95	Ceramic	Oxide
SAES Getters Nd:YAG Solid State Laser Crystals (Nd-doped Y3Al5O12)	13	4550	0.59	Ceramic	Oxide
Sapco 95% Aluminum Oxide	20	3700	0.88	Ceramic	Oxide
Sapco 98% Aluminum Oxide	25	3900	0.88	Ceramic	Oxide
Sapco 99.7% Aluminum Oxide	30	3930	0.8	Ceramic	Oxide
Sapco 99.9% Aluminum Oxide	30	3970	0.8	Ceramic	Oxide
Sapco C 220 Steatite	2.6	2600	0.9	Ceramic	Oxide
Sapco C 221 Steatite	2.6	2700	0.9	Ceramic	Oxide
Sapco C 410 Steatite	2.1	2200	0.9	Ceramic	Oxide
Sapco Partially Stabilized TZP Zirconia (YSZ)	2	6050	0.4	Ceramic	Oxide
Skamol Group Exfoliated/Loose Vermiculite Loose Vermiculite	0.069	2600	1.03	Ceramic	Oxide
Steatite (Magnesium Silicon Oxide)	3	2500	1	Ceramic	Oxide
UBE Tyranno Grade LoxM Ceramic High Temperature Fiber	1.35	2480	0.735	Ceramic	Oxide
UBE Tyranno Grade S Ceramic High Temperature Fiber	0.97	2350	0.737	Ceramic	Oxide
UBE Tyranno Grade ZMI Ceramic High Temperature Fiber	2.52	2480	0.709	Ceramic	Oxide
Vermiculite, Magnesium Aluminum Iron Silicate	0.0635	2500	1.08	Ceramic	Oxide
Zinc Oxide, ZnO, Cubic	23.4	5680	0.494	Ceramic	Oxide
Zircar Ceramics MICROSIL Microporous Insulation	0.019	230	0.795	Ceramic	Oxide
Zircar Refractory Composites RS-99R Refractory Sheet	0.65	2100	1.05	Ceramic	Oxide
Zircar Refractory Composites RS-A Refractory Sheet	0.65	1600	1.05	Ceramic	Oxide
Zircar Refractory Composites RS-A3 Refractory Sheet	0.65	1700	1.05	Ceramic	Oxide
Copper Germanium Phosphide, CuGe2P3	3.8	4320	0.429	Ceramic	Phosphide/Pnictide
Gallium Antimonide, GaSb	27	5620	0.32	Ceramic	Phosphide/Pnictide
Gallium Arsenide, GaAs	50	5320	0.325	Ceramic	Phosphide/Pnictide
Indium Antimonide, InSb	16	5780	0.144	Ceramic	Phosphide/Pnictide
Indium Arsenide, InAs	29	5660	0.268	Ceramic	Phosphide/Pnictide
Mateck Gallium Arsenide (GaAs)	46	5320	0.35	Ceramic	Phosphide/Pnictide
Cadmium Selenide, CdSe, Cubic	9	5670	0.255	Ceramic	Sulfide/Chalcogenide
Cadmium Sulfide, CdS, Cubic (Hawleyite)	20	4830	0.33	Ceramic	Sulfide/Chalcogenide
Cadmium Telluride, CdTe, Cubic	5.85	5860	0.205	Ceramic	Sulfide/Chalcogenide
Copper Germanium Selenide, Cu2GeSe3	2.4	5570	0.34	Ceramic	Sulfide/Chalcogenide
Copper Germanium Sulfide, Cu2GeS3, High Temperature Form	1.2	4450	0.51	Ceramic	Sulfide/Chalcogenide
Copper Tin Selenide, Cu2SnSe3	3.5	5940	0.31	Ceramic	Sulfide/Chalcogenide
Copper Tin Sulfide, Cu2SnS3	2.8	5020	0.44	Ceramic	Sulfide/Chalcogenide
Mateck Cadmium Telluride (CdTe)	4.1	5860	0.209	Ceramic	Sulfide/Chalcogenide
Mateck Laser Grade Zinc Selenide, ZnSe CVD	16	5270	0.339	Ceramic	Sulfide/Chalcogenide
Mateck Window Grade Zinc Selenide, ZnSe	14.1	5260	0.367	Ceramic	Sulfide/Chalcogenide
Mercury Selenide, HgSe (Tiemannite)	1	8250	0.178	Ceramic	Sulfide/Chalcogenide
Mercury Telluride, HgTe (Coloradoite)	2	8170	0.164	Ceramic	Sulfide/Chalcogenide
Zinc Selenide, ZnSe	14	5420	0.339	Ceramic	Sulfide/Chalcogenide
Zinc Sulfide, ZnS, Sphalerite (Zincblende)	25.1	4080	0.472	Ceramic	Sulfide/Chalcogenide
Zinc Telluride, ZnTe, Cubic	10.8	6120	0.264	Ceramic	Sulfide/Chalcogenide
AISI 1012 Steel, cold drawn	49.8	7870	0.472	Metal	Carbon Steel
AISI 1021 Steel, cold drawn	49.8	7860	0.472	Metal	Carbon Steel
AISI 1021 Steel, cold rolled, 25 mm (1 in.) round	51.9	7860	0.472	Metal	Carbon Steel
AISI 1080 Steel, oil quenched from 815°C (1500°F), tempered at 480°C (900°F)	47.7	7850	0.49	Metal	Carbon Steel
AISI 11L17 Steel, cold drawn, 19-32 mm (0.75-1.25 in) round	49.8	7850	0.481	Metal	Carbon Steel
Steel, 0.5% C	54	7833	0.465	Metal	Carbon Steel
Steel, 1% C	43	7801	0.473	Metal	Carbon Steel
Steel, 1.5% C	36	7753	0.486	Metal	Carbon Steel
Steel, AISI 1010	63.9	7832	0.434	Metal	Carbon Steel
Steel, AISI 1010	64	7830	0.434	Metal	Carbon Steel
Steel, Plain	60.5	7854	0.434	Metal	Carbon Steel

Dura-Bar 100-70-03 Continuously Cast Ductile Iron Bar Stock ASTM A536	32.3	6920	0.506	Metal	Cast Iron
Dura-Bar 80-55-06 Continuously Cast Ductile Iron Bar Stock ASTM A536	24.2	6920	0.506	Metal	Cast Iron
Dura-Bar G2 Continuously Cast Gray Iron Bar Stock ASTM A48	53.3	7200	0.506	Metal	Cast Iron
Assab Steels VANADIS 10 Cold Work Steel	14	7420	0.46	Metal	Chrome-moly Steel
Assab Steels VANADIS 4 Cold Work Steel	26	7560	0.46	Metal	Chrome-moly Steel
Molybdenum Disilicide, MoSi2	66.2	6230	0.437	Metal	Intermetallic
60-40 Soft Solder (60 Sn-40Pb) - ASTM B 32 Grade Sn60	49.8	8600	0.173	Metal	Lead Alloy
Arsenical Lead Cable-Sheathing Alloy, UNS L50310, Cable Sheath, Extruded at 425°C (800°F), Water Quenched	33	11300	0.129	Metal	Lead Alloy
Lead, Pb	33	11400	0.1145	Metal	Lead Alloy
Pure Lead (Corroding Lead), UNS L50042, Sand Cast	35	11400	0.129	Metal	Lead Alloy
Pure Lead (Soft, Refined) (UNS L50005)	34.9	11700	0.13	Metal	Lead Alloy
EOS MS1 Maraging Steel for DMLS 3D Printing	17.6	8050	0.45	Metal	Marraging Steel
Special Metals UDIMAR® alloy 300 Fe-Ni Maraging Steel	19.6	8000	0.335	Metal	Marraging Steel
Antimony, Sb	18.6	6620	0.206	Metal	Pure Element
Arsenic, As	50.2	5720	0.33	Metal	Pure Element
Barium, Ba	18.4	3660	0.285	Metal	Pure Element
Boron, B	27.4	2600	1.28	Metal	Pure Element
Bromine, Br2	0.123	3100	0.35	Metal	Pure Element
Cadmium, Cd	92	8640	0.23	Metal	Pure Element
Calcium, Ca; Rolled	126	1540	0.632	Metal	Pure Element
Cerium, Ce	109	6700	0.188	Metal	Pure Element
Cesium, Cs	36	1890	0.209	Metal	Pure Element
Chromium, Cr; As-Swaged	69.1	7190	0.461	Metal	Pure Element
Dysprosium, Dy	10	8540	0.175	Metal	Pure Element
Iron Thermocouple Wire Type J - Standard	73.9	7860	0.473	Metal	Pure Element
Iron, Fe	76.2	7870	0.44	Metal	Pure Element
Lanthanum, La	14	6170	0.1795	Metal	Pure Element
AKS With Thoria Tungsten Alloy (UNS R07911)	6.2	15900	0.146	Metal	Refractory Metal
Goodfellow Tungsten 60/Copper 40 Alloy	228	13000	0.24	Metal	Refractory Metal
Rhenium, Re; Annealed	39.6	21000	0.138	Metal	Refractory Metal
Tantalum, Ta; Cold Worked	54.4	16600	0.153	Metal	Refractory Metal
Tantalum, Ta; Sintered, Cast (UNS R05210)	57.5	16700	0.139	Metal	Refractory Metal
Tantalum, Ta; Soft	57.5	16700	0.142	Metal	Refractory Metal
Tantalum, UNS R05200	59.4	16600	0.138	Metal	Refractory Metal
Tungsten, W	163	19300	0.134	Metal	Refractory Metal
Tungsten, W; Hard Unalloyed	174	19300	0.132	Metal	Refractory Metal
X12CrMoS17 Stainless Steel for medical instruments	26.1	7800	0.46	Metal	Special-Purpose Steel
X12CrNi177 Austenitic Stainless Steel for medical instruments	16.2	8000	0.5	Metal	Special-Purpose Steel
X20Cr13 Stainless Steel for medical instruments	30	7800	0.46	Metal	Special-Purpose Steel
X20CrNi172 Stainless Steel for medical instruments	20.2	7800	0.46	Metal	Special-Purpose Steel
X25CrNi2520 Austenitic Stainless Steel for medical instruments	17.5	7800	0.5	Metal	Special-Purpose Steel
X6CrNiTi1810 Austenitic Stainless Steel for medical instruments	16.1	8000	0.5	Metal	Special-Purpose Steel
202 Stainless Steel, Annealed Bar	16.3	7860	0.5	Metal	Stainless Steel
205 Austenitic Stainless Steel (UNS S20500)	16.2	7800	0.5	Metal	Stainless Steel
301 Stainless Steel	16.3	8030	0.5	Metal	Stainless Steel
308 Stainless steel, annealed, sheet and strip	15.2	8000	0.5	Metal	Stainless Steel
317LN High-Nitrogen Austenitic Stainless Steel, Annealed Plate, Sheet, Strip, UNS S31753	14	8000	0.5	Metal	Stainless Steel
330 Stainless Steel, annealed sheet	12.5	8000	0.46	Metal	Stainless Steel
403 Stainless Steel, tempered, bar	24.9	7800	0.46	Metal	Stainless Steel
405 Stainless Steel, annealed, sheet	27	7800	0.46	Metal	Stainless Steel
410 Cb Martensitic Stainless Steel (UNS S41040)	24.8	7730	0.46	Metal	Stainless Steel
439 Ferritic Stainless Steel (UNS S43900)	24.2	7700	0.46	Metal	Stainless Steel
444 Ferritic Stainless Steel, 18Cr-2Mo (UNS S44400)	26.8	7800	0.46	Metal	Stainless Steel
446 Stainless Steel, Annealed Sheet	21.6	7800	0.46	Metal	Stainless Steel
660 Stainless Steel (A286) short time tensile test	12.6	7920	0.46	Metal	Stainless Steel
661 Stainless Steel	12.3	8250	0.435	Metal	Stainless Steel
AISI Type 302B Stainless Steel, annealed sheet	15.9	8000	0.5	Metal	Stainless Steel
AISI Type 304L Stainless Steel	15.15	8000	0.5	Metal	Stainless Steel
AISI Type 310S Stainless Steel	14.2	8000	0.5	Metal	Stainless Steel
AISI Type 316L Stainless Steel, annealed sheet	14.95	8000	0.5	Metal	Stainless Steel
AISI Type 430Ti Stainless Steel annealed 1.6 mm thickness	24.2	7800	0.46	Metal	Stainless Steel
AISI Type 450 Stainless Steel, 25 mm diameter bar, solution annealed	20.7	7800	0.46	Metal	Stainless Steel
AISI Type 651 (19-9 DL) Stainless Steel	13.5	7940	0.42	Metal	Stainless Steel
AISI Type S21800 Stainless Steel	20.7	7610	0.48	Metal	Stainless Steel
AISI Type S24100 Stainless Steel 25 mm annealed bar at RT	20.7	7780	0.48	Metal	Stainless Steel
AK Steel 420 Martensitic Stainless steel	24.9	7740	0.46	Metal	Stainless Steel
ATI Allegheny Ludlum 309 Austenitic Stainless Steel	17.15	8030	0.502	Metal	Stainless Steel
ATI Allegheny Ludlum 310 Austenitic Stainless Steel	16.25	8030	0.502	Metal	Stainless Steel
ATI Allegheny Ludlum 430 Ferritic Stainless Steel	24.95	7700	0.46	Metal	Stainless Steel
ATI Allegheny Ludlum AL 20™ Sheet and Strip Specialty Steel	12.2	8080	0.5	Metal	Stainless Steel
ATI Allegheny Ludlum AL 2205™ Duplex Stainless Steel, Plate > 0.1875" Duplex Stainless Steel, UNS S31803	19	7880	0.42	Metal	Stainless Steel
ATI Allegheny Ludlum AL 409HP™ Ferritic Stainless Steel, UNS S40930	25	7760	0.477	Metal	Stainless Steel
ATI Allegheny Ludlum AL 433™ Ferritic Stainless Steel, Annealed	20.9	7800	0.46	Metal	Stainless Steel
ATI Allegheny Ludlum AL 4565™ Corrosion Resistant Stainless Steel	14	8000	0.535	Metal	Stainless Steel
ATI Allegheny Ludlum Stainless Steel AL 904L™ Alloy (UNS N08904)	11.5	7900	0.46	Metal	Stainless Steel
ATI Allegheny Ludlum Stainless Steel Type 321 (UNS S32100)	16.3	7920	0.5	Metal	Stainless Steel
ATI Allegheny Ludlum Stainless Steel Type 347 (UNS S34700)	16.3	7960	0.5	Metal	Stainless Steel
ATI Allegheny Ludlum Type 316 Stainless Steel, UNS S31600	14.6	8030	0.45	Metal	Stainless Steel
ATI Allegheny Ludlum Type 332 Stainless Steel, UNS N08800	11.6	8030	0.5	Metal	Stainless Steel
Bohler-Uddeholm M314 EXTRA Pre-hardened Holder Stainless Steel	18	7640	0.46	Metal	Stainless Steel

Bohler-Uddeholm POLMAX® 420 Modified - Stainless Mold Steel	16	7810	0.46	Metal	Stainless Steel
Carpenter Custom 450® Stainless Steel, Annealed	15	7750	0.477	Metal	Stainless Steel
Carpenter Custom 450® Stainless Steel, Condition H900 (Age Hardened 482°C)	15	7760	0.477	Metal	Stainless Steel
Crucible Steel 440C Chromium Steel	2.02	7640	0.46	Metal	Stainless Steel
EDRO #8 Premium 420 Stainless Mold Steel	22.9	7810	0.46	Metal	Stainless Steel
EDRO UltraChem® #15 Precipitation Hardening Stainless Mold Steel	16.1	7860	0.46	Metal	Stainless Steel
EOS PH1 Precipitation Hardening Stainless Steel for DMLS 3D Printing	14.75	7800	0.465	Metal	Stainless Steel
Industeel CLC 17.12.2 Ti Titanium Stabilized 18Cr-11Ni-2Mo Austenitic Stainless Steel	15	8000	0.5	Metal	Stainless Steel
Industeel CLC 18.10 Nb Niobium Stabilized 18Cr-10Ni Austenitic Stainless Steel	15	7950	0.5	Metal	Stainless Steel
Industeel CLC 18.9 L General Purpose 18Cr-9Ni Austenitic Stainless Steel	15	7900	0.5	Metal	Stainless Steel
Industeel SIRIUS 314 25% Cr - 1.8% Si Heat Resistant Stainless Steel	14	7900	0.5	Metal	Stainless Steel
Industeel SOLEIL C5 13% Cr 4 Ni Martensitic Stainless Steel with Improved Toughness	26	7700	0.46	Metal	Stainless Steel
Industeel URANUS® B25 6 Mo Cost Saving Super-Austenitic Stainless Steel with PREN = 42	13	8000	0.48	Metal	Stainless Steel
Industeel URANUS® B26 6 Mo High Performance Super-Austenitic Stainless Steel with PREN = 43	13	8100	0.45	Metal	Stainless Steel
Industeel URANUS® B28 High Nickel Super-Austenitic Stainless Steel	12	8000	0.45	Metal	Stainless Steel
Industeel URANUS® B6 Multipurpose Austenitic Stainless Steel with PREN = 34	17	8050	0.5	Metal	Stainless Steel
Industeel URANUS® B66 High Strength Super-Austenitic Stainless Steel with PREN = 54	12	8200	0.45	Metal	Stainless Steel
Industeel VIRGO 15.5PH 15Cr-5Ni-3Cu Precipitation Hardening Martensitic Stainless Steel (480°C (900°F) - 1 hour - air cooling)	14	7800	0.46	Metal	Stainless Steel
Industeel VIRGO 39 16% Cr, 5% Ni, Martensitic Stainless Steel	20	7700	0.46	Metal	Stainless Steel
Latrobe CSS-42L™ VIM-VAR High Performance Carburizing Stainless Steel; Bearing and Gear Steel	15.3	7940	0.452	Metal	Stainless Steel
Outokumpu 353MA® High Temperature Austenitic Stainless Steel	11.3	7900	0.45	Metal	Stainless Steel
Outokumpu 4021 Martensitic Stainless Steel	30	7700	0.46	Metal	Stainless Steel
Outokumpu 4529 Austenitic Stainless Steel	12	8100	0.45	Metal	Stainless Steel
Outokumpu 4713 High Temperature Ferritic Stainless Steel	20.5	7700	0.43	Metal	Stainless Steel
Sandvik 1802 Precision Wire	22	7700	0.46	Metal	Stainless Steel
Sandvik 1C256 Seamless tube and pipe	21	7700	0.5	Metal	Stainless Steel
Sandvik 1C356 Seamless tube and pipe	19	7700	0.5	Metal	Stainless Steel
Sandvik 2C48 Seamless tube and pipe	20	7600	0.475	Metal	Stainless Steel
Sandvik 2RE10 Seamless tube and pipe	13	7900	0.47	Metal	Stainless Steel
Sandvik 2RE69 Seamless tube and pipe	13	7900	0.485	Metal	Stainless Steel
Sandvik 316 Plate, Sheet and Coil	15	8000	0.485	Metal	Stainless Steel
Sandvik 321 Plate, Sheet and Coil	14	7900	0.465	Metal	Stainless Steel
Sandvik 904L-2RK65 Billet	12	8000	0.46	Metal	Stainless Steel
Sandvik Bioline 1RK91 Precision Wire	14	7900	0.455	Metal	Stainless Steel
Sandvik F44-254 SMO Billet	10	8000	0.485	Metal	Stainless Steel
Sandvik SAF 2507 Bar Steel	14	7800	0.49	Metal	Stainless Steel
Sandvik Sanicro 28 Seamless tube and pipe	10	8000	0.46	Metal	Stainless Steel
Sandvik SANMAC 304/304L Bar Steel	15	7900	0.475	Metal	Stainless Steel
Special Metals INCOLOY® 25-6M0 Super Austenitic Stainless Steel (UNS N08926)	11.5	8030	0.5	Metal	Stainless Steel
Special Metals INCOLOY® 27-7MO Super-Austenitic Stainless Steel	10.1	8020	0.454	Metal	Stainless Steel
Special Metals INCOLOY® alloy 832 Stainless Steel	14.2	7750	0.472	Metal	Stainless Steel
Stainless Steel, AISI 304	14.9	7900	0.477	Metal	Stainless Steel
Type 317LM Austenitic Stainless Steel, Annealed Bar, Plate, UNS S31725	14.6	8000	0.46	Metal	Stainless Steel
Type 410S Martensitic Stainless Steel, Annealed Forgings, UNS S41008	26.9	7730	0.46	Metal	Stainless Steel
Tin, Sn	63.2	6525	0.2345	Metal	Tin Alloy
AISI Type H11 Hot Work Tool Steel, air or oil quenched from 995-1025°C	42	7800	0.46	Metal	Tool Steel
Assab Steels ASP 60 Cold Work Steel	21	7890	0.418	Metal	Tool Steel
Assab Steels ASSAB XW-5 Cold Work Steel	20.5	7670	0.46	Metal	Tool Steel
Bohler-Uddeholm BÖHLER K294 MICROCLEAN AISI A11 Powder Metal Tool Steel	20.4	7420	0.46	Metal	Tool Steel
Bohler-Uddeholm BÖHLER M261 Extra Plastic Lens Mold Steel	25	7820	0.46	Metal	Tool Steel
Bohler-Uddeholm BÖHLER M268 VMR® Plastic Mold Steel	34.3	7850	0.46	Metal	Tool Steel
Bohler-Uddeholm BÖHLER S290 MICROCLEAN® High Speed Steel	19	8300	0.41	Metal	Tool Steel
Bohler-Uddeholm BÖHLER S390 MICROCLEAN® High Speed Steel	17	8100	0.418	Metal	Tool Steel
Bohler-Uddeholm BÖHLER S400(M7) High Speed Steel	19	8300	0.46	Metal	Tool Steel
Bohler-Uddeholm BÖHLER S401(M1) High Speed Steel	19	8000	0.46	Metal	Tool Steel
Bohler-Uddeholm BÖHLER S500(m42) High Speed Steel	20	8100	0.431	Metal	Tool Steel
Bohler-Uddeholm BÖHLER S590 MICROCLEAN® High Speed Steel	22	8050	0.418	Metal	Tool Steel
Bohler-Uddeholm BÖHLER S692/S693 MICROCLEAN® PM M4 High Speed Steel	20	7900	0.439	Metal	Tool Steel
Bohler-Uddeholm BÖHLER W302 SUPERIOR® Premium H13 Tool Steel	14.95	7800	0.46	Metal	Tool Steel
Bohler-Uddeholm M238 VMR® P20 Plastic Lens Mold Steel	34	7850	0.46	Metal	Tool Steel
Bohler-Uddeholm SUPERIOR® H13 Hot Work Tool Steel	25.9	7810	0.46	Metal	Tool Steel
Industeel CLC 1.2316 Prehardened (300HB) and Corrosion Resistant Mold Steel	24.3	7750	0.46	Metal	Tool Steel
Industeel TENASTEEL® Cold Work Tool Steel	21	7750	0.46	Metal	Tool Steel
International Mold Steel DH31-EX Die Cast & Forging Steel	26	7800	0.435	Metal	Tool Steel
3D Systems DuraForm® EX Impact-Resistant Plastic for SLS® Systems	0.51	1010	1.75	Polymer	Rapid Prototyping Polymer
3D Systems DuraForm® PA Nylon for SLS® Systems	0.7	1000	1.64	Polymer	Rapid Prototyping Polymer
Eastman Tenite 105E3V36327 Acetate Clear, Trsp	0.25	1280	1.465	Polymer	Renewable/Recycled Polymer

Eastman Tenite 360A4861307 Cellulose Acetate Propionate, Clear, Trsp	0.25	1210	1.465	Polymer	Renewable/Recycled Polymer
Eastman Tenite 485E3720008 Cellulose Acetate Butyrate, Clear, Trsp	0.25	1200	1.465	Polymer	Renewable/Recycled Polymer
Eastman Tenite 485E3720023 Butyrate Clear, Trsp	0.25	1160	1.465	Polymer	Renewable/Recycled Polymer
Eastman Tenite 550E3V45510 Cellulose Acetate Butyrate, Water Clear, Trsp	0.25	1190	1.465	Polymer	Renewable/Recycled Polymer
Eastman Tenite Acetate 105E1R26033 Clear, Trsp Cellulose Acetate	0.25	1270	1.47	Polymer	Renewable/Recycled Polymer
Eastman Tenite Acetate 109E3V36324 Clear, Trsp Cellulose Acetate	0.25	1310	1.47	Polymer	Renewable/Recycled Polymer
Eastman Tenite Acetate 109E3V46022 Natural, Trsp Cellulose Acetate	0.25	1280	1.47	Polymer	Renewable/Recycled Polymer
Eastman Tenite Butyrate 264A3720013 Clear, Trsp Cellulose Acetate Butyrate	0.25	1180	1.47	Polymer	Renewable/Recycled Polymer
Eastman Tenite Butyrate 264E4861310 Clear, Trsp Cellulose Acetate Butyrate	0.25	1190	1.47	Polymer	Renewable/Recycled Polymer
Eastman Tenite Butyrate 285A2R30016 Natural, Trsp Cellulose Acetate Butyrate	0.25	1200	1.47	Polymer	Renewable/Recycled Polymer
Eastman Tenite Butyrate 285A2R30023 Natural, Trsp Cellulose Acetate Butyrate	0.25	1170	1.47	Polymer	Renewable/Recycled Polymer
Eastman Tenite Butyrate 438E0V16304 Clear, Trsp Cellulose Acetate Butyrate	0.25	1210	1.47	Polymer	Renewable/Recycled Polymer
Eastman Tenite Butyrate 485A2R30023 Natural, Trsp Cellulose Acetate Butyrate	0.25	1160	1.47	Polymer	Renewable/Recycled Polymer
Goodfellow Cellophane, Rayophane Regenerated Cellulose Fiber	0.06	1525	1.4	Polymer	Renewable/Recycled Polymer
Rotuba 855, Slow Burning Ethyl Cellulose	0.22	1100	2	Polymer	Renewable/Recycled Polymer
Rotuba 856, Slow Burning Ethyl Cellulose	0.22	1090	2	Polymer	Renewable/Recycled Polymer
Americas Styrenics Styron® 425 High Impact Polystyrene	0.185	1002.5	2.2	Polymer	Thermoplastic
Americas Styrenics Styron® 6010 High Impact Polystyrene	0.168	1130	1.9	Polymer	Thermoplastic
Americas Styrenics Styron® 666D Polystyrene	0.123	1040	2.1	Polymer	Thermoplastic
Americas Styrenics Styron® XL-8023VC High Impact Polystyrene	0.134	962	1.79	Polymer	Thermoplastic
Americas Styrenics Styron® XL-8028 High Impact Polystyrene	0.188	998	2	Polymer	Thermoplastic
Arkema Group KYNAR FLEX® 2800-00 Polyvinylidene Fluoride Copolymer - Extrusion	0.162	1780	1.34	Polymer	Thermoplastic
Arkema Group KYNAR® 1000 HD Polyvinylidene Fluoride Homopolymer - Injection Molding and Extrusion	0.18	1770	1.34	Polymer	Thermoplastic
Arkema Group KYNAR® 460 Polyvinylidene Fluoride Homopolymer - Extrusion	0.18	1760	1.315	Polymer	Thermoplastic
Arkema Group KYNAR® 710, 710 HDP Polyvinylidene Fluoride Homopolymer- Injection Molding	0.18	1780	1.34	Polymer	Thermoplastic
Arkema Group VOLTALEF® 302 PCTFE	0.135	2135	0.9	Polymer	Thermoplastic
Asahi Glass Fluon® P-63P PFA Perfluoropolymer	0.251	2110	1.05	Polymer	Thermoplastic
Asahi Glass Fluon® P-66P PFA Perfluoropolymer	0.251	2145	1.05	Polymer	Thermoplastic
Asahi Glass Fluon® PTFE	0.251	2150	1.05	Polymer	Thermoplastic
Asahi Kasei Delpet® 560F Acrylic Molding Compound	0.21	1190	1.46	Polymer	Thermoplastic
Asahi Kasei Leona® 1300S Nylon 66	0.2	1140	1.67	Polymer	Thermoplastic
Asahi Kasei Leona® 90G60 Nylon 66	0.3	1710	1.84	Polymer	Thermoplastic
Asahi Kasei Leona® FR200 Nylon 66	0.2	1160	1.67	Polymer	Thermoplastic
Ascend Performance Materials VYDYNE® 21SP Nylon, General Purpose	0.24	1140	1.7	Polymer	Thermoplastic
Azoty Tarnow™ TARFLEN SG-1 PTFE	0.25	2150	1	Polymer	Thermoplastic
Azoty Tarnow™ TARFLEN SM-K22G3 PTFE	0.25	2110	1	Polymer	Thermoplastic
BASF Ultrason E 3010 PES	0.18	1370	1	Polymer	Thermoplastic
Bayer MaterialScience Apec® 1600 Polycarbonate	0.171	1090	1.7	Polymer	Thermoplastic
Bayer MaterialScience Apec® DP 1-9359/5 Polycarbonate	0.167	1065	1.7	Polymer	Thermoplastic
Bayer MaterialScience Apec® DP 1-9389 Polycarbonate	0.163	1040	1.7	Polymer	Thermoplastic
Bayer MaterialScience Apec® DP1-9389/5 Polycarbonate	0.163	1120	1.7	Polymer	Thermoplastic
Bayer MaterialScience Desmopan® 3385A Polyurethane	0.14	1115	1.7	Polymer	Thermoplastic
Bayer MaterialScience Desmopan® 481 Polyurethane	0.139	1110	1.7	Polymer	Thermoplastic
Bayer MaterialScience Desmopan® 790 Polyurethane	0.14	1120	1.7	Polymer	Thermoplastic
Bayer MaterialScience Desmopan® 9385 Polyurethane	0.133	1050	1.7	Polymer	Thermoplastic
Bayer MaterialScience Desmopan® DP 1080A Polyurethane	0.141	1125	1.7	Polymer	Thermoplastic
Bayer MaterialScience Makroblend® DP 7645 Polycarbonate + PET, Impact Grade	0.165	1200	1.76	Polymer	Thermoplastic
Bayer MaterialScience Makroblend® DP UT3905 Polycarbonate + PBT, Impact Grade	0.179	1200	1.82	Polymer	Thermoplastic
Bayer MaterialScience Makroblend® KU 2-7912/5 Polycarbonate + PBT, Impact Grade	0.167	1200	1.78	Polymer	Thermoplastic
Bayer MaterialScience Makroblend® S 7916 Polycarbonate + PBT, Impact Grade	0.185	1200	1.88	Polymer	Thermoplastic
Bayer MaterialScience Makroblend® S 7916/2 Polycarbonate + PBT, Impact Grade	0.184	1200	1.87	Polymer	Thermoplastic
Bayer MaterialScience Makrolon® 1239 Polycarbonate, Blow Molding/Extrusion Grade	0.2	1200	1.17	Polymer	Thermoplastic
Bayer MaterialScience Makrolon® 1243 Polycarbonate	0.173	1200	1.7	Polymer	Thermoplastic
Bayer MaterialScience Makrolon® 1837* Polycarbonate, Impact Grade	0.173	1190	1.7	Polymer	Thermoplastic
Bayer MaterialScience Makrolon® 3158 Polycarbonate	0.173	1110	1.7	Polymer	Thermoplastic
Bayer MaterialScience Makrolon® 3258 Polycarbonate, General Purpose, Mold Release, Biocompatibility	0.2	1200	1.2	Polymer	Thermoplastic
Bayer MaterialScience Makrolon® 8325 Polycarbonate	0.22	1350	1.13	Polymer	Thermoplastic
Bayer MaterialScience Makrolon® 9415(Z) Polycarbonate	0.21	1270	1.13	Polymer	Thermoplastic
Borealis BorPEX™ ME2510 Medium Density Polyethylene Compound for Crosslinked Pipes (Pex-B (Silane))	0.41	935	2.1	Polymer	Thermoplastic
Celanese Celanex® 2500 PBT	0.133	1210	1.92	Polymer	Thermoplastic
Celanese Celcon® M140 POM	0.155	1305	2.21	Polymer	Thermoplastic
Celanese FORTRON 214 PPS	3.46	1255	1.83	Polymer	Thermoplastic
Celanese GUR® 2122 PE-UHMW, Specialty	0.41	930	1.84	Polymer	Thermoplastic
Celanese GUR® 4113 PE-UHMW	0.41	935	1.84	Polymer	Thermoplastic

Celanese GUR® GHR 8110 PE-HD	0.41	950	1.84	Polymer	Thermoplastic
Celanese Hostaform® C 52021 POM	0.19	1305	2.06	Polymer	Thermoplastic
Celanese Hostaform® C 9021 K POM, Tribological	0.195	1335	2.06	Polymer	Thermoplastic
Chevron Phillips Ryton® R10 5002C PPS Polyphenylene Sulfide	0.56	2000	0.772	Polymer	Thermoplastic
Chevron Phillips Ryton® R10 5004A PPS Polyphenylene Sulfide	0.6	2000	0.7825	Polymer	Thermoplastic
Chevron Phillips Ryton® R10 7006A PPS Polyphenylene Sulfide	0.56	2000	0.7865	Polymer	Thermoplastic
Chevron Phillips Ryton® R-4 04 PPS (Polyphenylene Sulfide)	0.29	1650	1	Polymer	Thermoplastic
Cool Polymers Coolpoly® D1202 Thermally Conductive Polypropylene	5	1380	1.3	Polymer	Thermoplastic
Cool Polymers Coolpoly® D3606 Thermally Conductive Polyamide 4,6	1.5	1650	1.5	Polymer	Thermoplastic
Cool Polymers Coolpoly® D3608 Thermally Conductive High Temperature Polyamide (HTN)	1.6	1700	1.03	Polymer	Thermoplastic
Cool Polymers Coolpoly® D4302 Thermally Conductive Polybutylene Terephthalate	2.6	1470	1.31	Polymer	Thermoplastic
Cool Polymers Coolpoly® D5108 Thermally Conductive Polyphenylene Sulfide	10	1800	0.9	Polymer	Thermoplastic
Cool Polymers Coolpoly® D5110 Thermally Conductive Polyphenylene Sulfide	1.5	1450	1.05	Polymer	Thermoplastic
Cool Polymers Coolpoly® D5112 Thermally Conductive Polyphenylene Sulfide	6.5	1730	0.9	Polymer	Thermoplastic
Cool Polymers Coolpoly® D5502 Thermally Conductive Liquid Crystalline Polymer	1.5	1700	1	Polymer	Thermoplastic
Cool Polymers Coolpoly® D5506 Thermally Conductive Liquid Crystalline Polymer	10	1800	0.97	Polymer	Thermoplastic
Cool Polymers Coolpoly® D8102 Thermally Conductive Thermoplastic Elastomer	3	1300	1.3	Polymer	Thermoplastic
Cool Polymers Coolpoly® E1201 Thermally Conductive Polypropylene	10	1200	1.5	Polymer	Thermoplastic
Cool Polymers Coolpoly® E2 Thermally Conductive Liquid Crystalline Polymer	20	1840	0.9	Polymer	Thermoplastic
Cool Polymers Coolpoly® E3603 Thermally Conductive Polyphthalamide (PPA)	20	1560	1.05	Polymer	Thermoplastic
Cool Polymers Coolpoly® E3607 Thermally Conductive Polyamide (PA6)	14	1600	1.1	Polymer	Thermoplastic
Cool Polymers Coolpoly® E4301 Thermally Conductive Polybutylene Terephthalate	14	1410	1.27	Polymer	Thermoplastic
Cool Polymers Coolpoly® E4501 Thermally Conductive Polycarbonate	4	1280	1.41	Polymer	Thermoplastic
Cool Polymers Coolpoly® E5101 Thermally Conductive Polyphenylene Sulfide	20	1700	0.9	Polymer	Thermoplastic
Cool Polymers Coolpoly® E5105 Thermally Conductive Polyphenylene Sulfide	4.5	1490	1.15	Polymer	Thermoplastic
Cool Polymers Coolpoly® E8101 Thermally Conductive Thermoplastic Elastomer	15	1250	1.4	Polymer	Thermoplastic
Diapolyacrylate Acrypet® IR H70 Impact Modified PMMA	0.209	1140	1.46	Polymer	Thermoplastic
Diapolyacrylate Acrypet® MF-001 PMMA	0.209	1190	1.46	Polymer	Thermoplastic
Dow AIM® 4800 High Impact Styrenic Resin	0.181	1001.5	2.16	Polymer	Thermoplastic
Dow Isoplast® 302 Polyurethane (PUR-RT), Clear Amorphous Polymer	0.23	1170	2.25	Polymer	Thermoplastic
Dow Prevail® 3150 ABS + Polyurethane	0.19	1030	1.54	Polymer	Thermoplastic
Dow Retain® 8209 ABS + Polycarbonate	0.221	1190	1.99	Polymer	Thermoplastic
Dow Tyril® 100 SAN	0.193	1024	2.1	Polymer	Thermoplastic
Dow Tyril® 125 SAN	0.113	992	1.68	Polymer	Thermoplastic
Dow Tyril® 880B SAN	0.195	1040	2.23	Polymer	Thermoplastic
DuPont Performance Polymers Crastin® 6129 NC010 Polybutylene Terephthalate (PBT)	0.25	1220	2.09	Polymer	Thermoplastic
DuPont Performance Polymers Crastin® 6130 NC010 Polybutylene Terephthalate (PBT)	0.25	1205	2.05	Polymer	Thermoplastic
DuPont Performance Polymers Crastin® BM6450XD BK560 Polybutylene Terephthalate (PBT)	0.15	1120	2.21	Polymer	Thermoplastic
DuPont Performance Polymers Crastin® FG6129 NC010 Polybutylene Terephthalate (PBT)	0.25	1210	2.09	Polymer	Thermoplastic
DuPont Performance Polymers Crastin® FG6130 NC010 Polybutylene Terephthalate (PBT)	0.25	1210	2.05	Polymer	Thermoplastic
DuPont Performance Polymers Crastin® FGS600F10 NC010 Polybutylene Terephthalate (PBT)	0.21	1205	2.1	Polymer	Thermoplastic
DuPont Performance Polymers Crastin® FGS600F40 NC010 Polybutylene Terephthalate (PBT)	0.21	1210	2.11	Polymer	Thermoplastic
DuPont Performance Polymers Crastin® HR5315HF NC010 Polybutylene Terephthalate (PBT)	0.26	1255	1.86	Polymer	Thermoplastic
DuPont Performance Polymers Crastin® HR5330HF NC010 Polybutylene Terephthalate (PBT)	0.28	1395	1.73	Polymer	Thermoplastic
DuPont Performance Polymers Crastin® S620F20 NC010 Polybutylene Terephthalate (PBT)	0.21	1210	2.1	Polymer	Thermoplastic
DuPont Performance Polymers Crastin® SK601 NC010 Polybutylene Terephthalate (PBT)	0.24	1280	1.89	Polymer	Thermoplastic
DuPont Performance Polymers Crastin® SK602 NC010 Polybutylene Terephthalate (PBT)	0.24	1315	1.9	Polymer	Thermoplastic
DuPont Performance Polymers Crastin® SK603 NC010 Polybutylene Terephthalate (PBT)	0.25	1355	1.86	Polymer	Thermoplastic
DuPont Performance Polymers Crastin® SK605 NC010 Polybutylene Terephthalate (PBT)	0.28	1445	1.73	Polymer	Thermoplastic
DuPont Performance Polymers Crastin® SK612SF NC010 Polybutylene Terephthalate (PBT)	0.24	1320	1.9	Polymer	Thermoplastic
DuPont Performance Polymers Crastin® SK615SF NC010 Polybutylene Terephthalate (PBT)	0.28	1450	1.73	Polymer	Thermoplastic

DuPont Performance Polymers Crastin® SK642FR NC010 Polybutylene Terephthalate (PBT)	0.27	1475	1.74	Polymer	Thermoplastic
DuPont Performance Polymers Crastin® SK645FR NC010 Polybutylene Terephthalate (PBT)	0.26	1600	1.6	Polymer	Thermoplastic
DuPont Performance Polymers Crastin® SO653 NC010 Polybutylene Terephthalate (PBT)	0.25	1350	1.85	Polymer	Thermoplastic
DuPont Performance Polymers Crastin® ST820 NC010 Polybutylene Terephthalate (PBT)	0.2	1125	2.1	Polymer	Thermoplastic
DuPont Performance Polymers Hytrel® 3078 Polyester Elastomer TPC-ET	0.15	1005	2.15	Polymer	Thermoplastic
DuPont Performance Polymers Hytrel® 4068 Polyester Elastomer TPC-ET	0.16	1070	2.14	Polymer	Thermoplastic
DuPont Performance Polymers Hytrel® 5526 Polyester Elastomer TPC-ET	0.19	1115	2.11	Polymer	Thermoplastic
DuPont Performance Polymers Hytrel® 5556 Polyester Elastomer TPC-ET	0.16	1110	2.11	Polymer	Thermoplastic
DuPont Performance Polymers Hytrel® 6356 Polyester Elastomer TPC-ET	0.15	1140	2.15	Polymer	Thermoplastic
DuPont Performance Polymers Hytrel® 6359FG NC010 Polyester Elastomer TPC-ET	0.14	1130	2.16	Polymer	Thermoplastic
DuPont Performance Polymers Hytrel® 6646 NC010 Polyester Elastomer TPC-ET	0.15	1150	2.15	Polymer	Thermoplastic
DuPont Performance Polymers Hytrel® 7246 Polyester Elastomer TPC-ET	0.15	1185	2.15	Polymer	Thermoplastic
DuPont Performance Polymers Hytrel® 8238 Polyester Elastomer TPC-ET	0.15	1205	2.15	Polymer	Thermoplastic
DuPont Performance Polymers Hytrel® G4074 Polyester Elastomer TPC-ET	0.26	1105	2.05	Polymer	Thermoplastic
DuPont Performance Polymers Hytrel® G4774 Polyester Elastomer TPC-ET	0.16	1100	2.1	Polymer	Thermoplastic
DuPont Performance Polymers Hytrel® G5544 Polyester Elastomer TPC-ET	0.15	1135	2.11	Polymer	Thermoplastic
DuPont Performance Polymers Hytrel® HTR4275 BK316 Polyester Elastomer TPC-ET	0.15	1085	2.1	Polymer	Thermoplastic
DuPont Performance Polymers Hytrel® HTR8163HVBK Polyester Elastomer TPC-ET	0.16	1135	2.09	Polymer	Thermoplastic
DuPont Performance Polymers Hytrel® HTR8441 BK316 Polyester Elastomer TPC-ET	0.16	1100	2.15	Polymer	Thermoplastic
DuPont Performance Polymers Minlon® 11C140 NC010 Nylon 66	0.27	1360	1.9	Polymer	Thermoplastic
DuPont Performance Polymers Minlon® 22C NC010 Nylon 66	0.25	1365	2.1	Polymer	Thermoplastic
DuPont Performance Polymers Minlon® 73GM40 NC010 Nylon 6	0.23	1460	2.07	Polymer	Thermoplastic
DuPont Performance Polymers Minlon® 73M40 NC010 Nylon 6	0.27	1365	1.94	Polymer	Thermoplastic
DuPont Performance Polymers Sorona® 3301 NC010 Polytrimethylene Terephthalate (PTT)	0.2	1220	2.1	Polymer	Thermoplastic
DuPont Performance Polymers Sorona® MT3401 NC010 Polytrimethylene Terephthalate (PTT)	0.2	1140	2.1	Polymer	Thermoplastic
DuPont Performance Polymers Zytel® 101 NC010 Nylon 66	0.16	1060	2.79	Polymer	Thermoplastic
DuPont Performance Polymers Zytel® 101F NC010 Nylon 66	0.16	1055	2.79	Polymer	Thermoplastic
DuPont Performance Polymers Zytel® 103FHS NC010 Nylon 66	0.16	1075	2.79	Polymer	Thermoplastic
DuPont Performance Polymers Zytel® 151 NC010 Nylon 612	0.18	980	2.75	Polymer	Thermoplastic
DuPont Performance Polymers Zytel® 158 NC010 Nylon 612	0.19	980	2.8	Polymer	Thermoplastic
DuPont Performance Polymers Zytel® 330 NC010 Nylon	0.22	1180	2.46	Polymer	Thermoplastic
DuPont Performance Polymers Zytel® 70G13HS1L NC010 Nylon 66	0.16	1230	2.37	Polymer	Thermoplastic
DuPont Performance Polymers Zytel® 70G25HSL NC010 Nylon 66	0.21	1330	2.09	Polymer	Thermoplastic
DuPont Performance Polymers Zytel® 70G25HSLR NC010 Nylon 66	0.21	1235	2.09	Polymer	Thermoplastic
DuPont Performance Polymers Zytel® 70G30HSL BK039B Nylon 66	0.285	1285	2.29	Polymer	Thermoplastic
DuPont Performance Polymers Zytel® 70G30L NC010 Nylon 66	0.21	1290	2.29	Polymer	Thermoplastic
DuPont Performance Polymers Zytel® 70G33HS1L NC010 Nylon 66	0.22	1390	1.77	Polymer	Thermoplastic
DuPont Performance Polymers Zytel® 70G35EF NC010 Nylon 66 + Nylon 6	0.24	1320	2.13	Polymer	Thermoplastic
DuPont Performance Polymers Zytel® 70G35HSL NC010 Nylon 66	0.24	1325	2.13	Polymer	Thermoplastic
DuPont Performance Polymers Zytel® 70G35HSLRA4 BK267 Nylon 66	0.22	1340	2.3	Polymer	Thermoplastic
DuPont Performance Polymers Zytel® 70G43L NC010 Nylon 66	0.25	1390	2.05	Polymer	Thermoplastic
DuPont Performance Polymers Zytel® 70G50HSLA BK039B Nylon 66	0.385	1485	1.87	Polymer	Thermoplastic
DuPont Performance Polymers Zytel® 7335F NC010 Nylon 6	0.16	1050	2.7	Polymer	Thermoplastic
DuPont Performance Polymers Zytel® 73G15L NC010 Nylon 6	0.19	1150	2.47	Polymer	Thermoplastic
DuPont Performance Polymers Zytel® 73G30HSL NC010 Nylon 6	0.26	1280	2.28	Polymer	Thermoplastic
DuPont Performance Polymers Zytel® 73G30T NC010 Nylon 6	0.23	1325	2.2	Polymer	Thermoplastic
DuPont Performance Polymers Zytel® 73G45 BK263 Nylon 6	0.26	1420	2.1	Polymer	Thermoplastic
DuPont Performance Polymers Zytel® 73G50HSLA BK416 Nylon 6	0.26	1410	2.05	Polymer	Thermoplastic
DuPont Performance Polymers Zytel® 77G33L NC010 Nylon 612	0.26	1320	2.13	Polymer	Thermoplastic
DuPont Performance Polymers Zytel® 79G13L NC010 Nylon 66	0.18	1120	2.14	Polymer	Thermoplastic
DuPont Performance Polymers Zytel® 80G14A NC010A Nylon 66	0.19	1190	2.35	Polymer	Thermoplastic
DuPont Performance Polymers Zytel® 80G33HS1L NC010 Nylon 66	0.22	1225	2.2	Polymer	Thermoplastic
DuPont Performance Polymers Zytel® 80G33L NC010 Nylon 66	0.22	1220	2.2	Polymer	Thermoplastic
DuPont Performance Polymers Zytel® BM70G20HSLX BK537 Nylon 66	0.2	1160	2	Polymer	Thermoplastic
DuPont Performance Polymers Zytel® EFE1068 NC010T Nylon 66	0.14	1045	2.79	Polymer	Thermoplastic
DuPont Performance Polymers Zytel® FE270038 BK267 Nylon 66	0.26	1380	2.28	Polymer	Thermoplastic
DuPont Performance Polymers Zytel® FE270050 BK099 Nylon 66	0.21	1285	2.29	Polymer	Thermoplastic
DuPont Performance Polymers Zytel® FE5382 BK276 Nylon 612	0.26	1220	2.13	Polymer	Thermoplastic
DuPont Performance Polymers Zytel® FG408L NC010 Nylon 66	0.16	1020	2.6	Polymer	Thermoplastic
DuPont Performance Polymers Zytel® FG70G30HSR3 BK309 Nylon 66	0.22	1285	2.22	Polymer	Thermoplastic
DuPont Performance Polymers Zytel® FN727 NC010A Nylon 6	0.16	945	2.7	Polymer	Thermoplastic
DuPont Performance Polymers Zytel® FR50 NC010A Nylon 66	0.22	1500	1.66	Polymer	Thermoplastic
DuPont Performance Polymers Zytel® FR70G25V0 NC010 Nylon 66	0.22	1420	1.91	Polymer	Thermoplastic

DuPont Performance Polymers Zytel® FR70M30V0 NC010 Nylon 66	0.23	1510	1.7	Polymer	Thermoplastic
DuPont Performance Polymers Zytel® LC6200 BK385 Nylon 612	0.17	910	2.7	Polymer	Thermoplastic
DuPont Performance Polymers Zytel® PLS 93G35DH1 BK549 Nylon 6	0.28	1320	2.1	Polymer	Thermoplastic
DuPont Performance Polymers Zytel® RS 30G30HSL BK038A Nylon 610	0.26	1235	2.28	Polymer	Thermoplastic
DuPont™ 100 FEP Fluorinated Ethylene Propylene	0.2	2150	0.24	Polymer	Thermoplastic
DuPont™ Teflon® PTFE 7A Granular Molding Powder	0.275	2160	1.4	Polymer	Thermoplastic
DuPont™ Teflon® PTFE 9B Granular Molding Powder	0.275	2150	1.4	Polymer	Thermoplastic
DuPont™ Tefzel® 210 Resin Modified ETFE	0.24	1700	0.25	Polymer	Thermoplastic
Eastman Eastar 15086 Copolyester	0.2	1300	1.1	Polymer	Thermoplastic
Eastman Eastar DN003 PCTG Copolyester	0.19	1230	1.34	Polymer	Thermoplastic
Eastman Eastar GN101 PETG Copolyester	0.19	1270	1.3	Polymer	Thermoplastic
Eastman Eastman AP005 Copolyester	0.19	1130	1.6	Polymer	Thermoplastic
Ensinger ENSITEP® PBT Polybutylene Terephthalate - Extruded Products	0.21	1380	1.3	Polymer	Thermoplastic
Ensinger ENSITEP® PET Polyethylene Terephthalate - Extruded Products	0.29	1380	1.17	Polymer	Thermoplastic
Ensinger TECATRON™ GF 40 Polyphenylene sulfide (PPS)	0.251	1640	1.18	Polymer	Thermoplastic
Evonik Corporation Trogamid® CX7323 Transparent Nylon	0.25	960	2.49	Polymer	Thermoplastic
Evonik Corporation Trogamid® CX9710 Transparent Nylon	0.28	960	2.5	Polymer	Thermoplastic
Evonik CYRO Acrylite® S-10 Acrylic Molding Compound	0.19	1190	1.47	Polymer	Thermoplastic
Evonik CYRO Acrylite® SG Acrylic Sheet, Sign Grade	0.19	1170	1.47	Polymer	Thermoplastic
Evonik CYRO CYROLITE G-20 Acrylic-Based Multipolymer Molding Compound	0.22	1110	1.3	Polymer	Thermoplastic
Evonik CYRO XT® Polymer 2000-5052 Acrylic-Based Multipolymer Molding Compound	0.22	1120	1.3	Polymer	Thermoplastic
Hippe PA 11 Nylon 11	0.23	1040	2.1	Polymer	Thermoplastic
Hippe PA 12 Nylon 12	0.23	1020	2.1	Polymer	Thermoplastic
Hippe PA 46 Nylon 46	0.3	1180	2.1	Polymer	Thermoplastic
Hippe PA 6 Nylon 6	0.23	1140	1.5	Polymer	Thermoplastic
Hippe PA 66 Nylon 66	0.23	1140	1.7	Polymer	Thermoplastic
Hippe PBT Polybutylene Terephthalate	0.21	1300	1.21	Polymer	Thermoplastic
Hippe PC Polycarbonate	0.19	1200	1.2	Polymer	Thermoplastic
Hippe PE 300 Polyethylene	0.39	955	1.85	Polymer	Thermoplastic
Hippe PEEK Polyetheretherketone	0.25	1320	0.32	Polymer	Thermoplastic
Hippe PET Polyethylene Terephthalate	0.24	1370	1.1	Polymer	Thermoplastic
Hippe PMMA	0.19	1180	1.47	Polymer	Thermoplastic
Hippe POM Copolymer	0.31	1410	1.5	Polymer	Thermoplastic
Hippe PP Polypropylene	0.22	910	1.7	Polymer	Thermoplastic
Hippe PS Polystyrene	0.18	1050	1.3	Polymer	Thermoplastic
Hippe PTFE	0.25	2180	1	Polymer	Thermoplastic
Hippe PVC-U Polyvinyl Chloride	0.155	1400	0.875	Polymer	Thermoplastic
Hippe PVDF	0.11	1790	1.2	Polymer	Thermoplastic
Kleerdex Elson® 405 AS DC Plate, PMMA/Acrylic, Clear Transparent	0.21	1190	1.47	Polymer	Thermoplastic
Kleerdex Elson® 407AS DC Plate, Polycarbonate, Clear	0.2	1200	1.26	Polymer	Thermoplastic
KYDEX® 100 Acrylic/PVC Thermoplastic Sheet	0.16	1350	1.21	Polymer	Thermoplastic
Lucite International XL Sanitary Ware Acrylic Sheet	0.209	1190	1.47	Polymer	Thermoplastic
LyondellBasell Moplen HP400H Polypropylene Homopolymer	0.202	900	1.7	Polymer	Thermoplastic
Micropol Isoplas P381 Crosslinkable Polyethylene	0.431	944	1.9	Polymer	Thermoplastic
Micropol Isoplas P471 Crosslinkable Polyethylene	0.431	947	2	Polymer	Thermoplastic
Micropol Isoplas P501 Crosslinkable Polyethylene	0.46	952	2.1	Polymer	Thermoplastic
Micropol Isoplas P602 Crosslinkable Polyethylene	0.431	964	2	Polymer	Thermoplastic
Micropol Isoplas P651 Crosslinkable Polyethylene	0.46	960	2.1	Polymer	Thermoplastic
Mitsui AURUM® JCL3030 Thermoplastic Polyimide Resin, Amorphous, Wear/Friction Grade	0.488	1420	0.92	Polymer	Thermoplastic
Mitsui AURUM® JGN3030 Thermoplastic Polyimide Resin, Amorphous	0.349	1560	0.96	Polymer	Thermoplastic
Mitsui TPX® MX002 Methylpentene Copolymer	0.167	835	1.97	Polymer	Thermoplastic
Mitsui TPX® MX004 Methylpentene Copolymer	0.167	834	1.97	Polymer	Thermoplastic
Mitsui TPX® RT18 Methylpentene Copolymer, Transparent Grade	0.167	833	1.97	Polymer	Thermoplastic
PDMS	0.15	970	1.5	Polymer	Thermoplastic
Pearl Engineering PEPLPET B101H Monofilament Resin	0.242	1400	1.1	Polymer	Thermoplastic
Plaskolite Optix® PL-76 Acrylic Resin	0.2	1180	1.5	Polymer	Thermoplastic
Plaskolite PL-24 Acrylic Resin	0.2	1190	1.46	Polymer	Thermoplastic
Plaskolite West Optix® PL-25 Acrylic Resin	0.2	1190	1.5	Polymer	Thermoplastic
Polikim EFALON® T-100 Virgin PTFE	0.2405	2150	1.006	Polymer	Thermoplastic
Polycasa CAST PMMA	0.19	1190	2.16	Polymer	Thermoplastic
Polycasa PETG	0.2	1270	1.1	Polymer	Thermoplastic
Polycasa PS	0.16	1050	1.8	Polymer	Thermoplastic
Polycasa SAN	0.17	1080	1.38	Polymer	Thermoplastic
Polycasa XT 610 PMMA	0.18	1150	1.5	Polymer	Thermoplastic
Polycasa XT 620 PMMA	0.18	1160	1.5	Polymer	Thermoplastic
Polycasa XT 630 PMMA	0.18	1170	1.5	Polymer	Thermoplastic
Polycasa XT PMMA	0.18	1190	1.47	Polymer	Thermoplastic
Polyester	0.2	1345	1.15	Polymer	Thermoplastic
Polyethylene, HD	0.43	959	2	Polymer	Thermoplastic
Polyethylene, LD	0.38	925	1.55	Polymer	Thermoplastic
Polyethylene, MD	0.4	929	1.7	Polymer	Thermoplastic
Polypropylene	0.15	880	1.88	Polymer	Thermoplastic
Polystyrene	0.14	1045	1.25	Polymer	Thermoplastic
Polyurethane, Rigid	0.19	1100	1.76	Polymer	Thermoplastic
Premix Thermoplastics PRETHERM TPE 1050 Thermoplastic Elastomer, Boron Nitride / SEBS compound	1.6	1330	0.58	Polymer	Thermoplastic
Premix Thermoplastics PRETHERM TPE 1075 Thermoplastic Elastomer, Boron Nitride / SEBS compound	5.3	1600	1.25	Polymer	Thermoplastic
Pyrogel® XT Aerogel	0.02	200	0.84	Polymer	Thermoplastic
Rubber, Soft	0.13	1100	2.01	Polymer	Thermoplastic

SABIC Innovative Plastics Cycoloy® EHA PC+ABS	0.2	1090	2	Polymer	Thermoplastic
SABIC Innovative Plastics Lexan® 101 PC	0.29	1195	1.25	Polymer	Thermoplastic
SABIC Innovative Plastics Lexan® 103 PC	0.19	1195	1.25	Polymer	Thermoplastic
SABIC Innovative Plastics Lexan® 104R PC	0.195	1195	1.25	Polymer	Thermoplastic
SABIC Innovative Plastics Lexan® 121 PC	0.25	1195	1.25	Polymer	Thermoplastic
SABIC Innovative Plastics Lexan® 123R PC (Asia Pacific)	0.19	1195	1.26	Polymer	Thermoplastic
SABIC Innovative Plastics Lexan® 141 PC	0.27	1195	1.25	Polymer	Thermoplastic
SABIC Innovative Plastics Lexan® 203 PC	0.29	1195	1.26	Polymer	Thermoplastic
SABIC Innovative Plastics Lexan® 223R PC	0.25	1195	1.26	Polymer	Thermoplastic
SABIC Innovative Plastics Lexan® 223S PC (Asia Pacific)	0.25	1200	1.26	Polymer	Thermoplastic
SABIC Innovative Plastics Lexan® 243 PC	0.27	1195	1.26	Polymer	Thermoplastic
SABIC Innovative Plastics Lexan® 244R PC	0.27	1200	1.26	Polymer	Thermoplastic
SABIC Innovative Plastics Lexan® 3412R PC	0.21	1355	1.17	Polymer	Thermoplastic
SABIC Innovative Plastics Lexan® 3413R PC	0.22	1435	1.13	Polymer	Thermoplastic
SABIC Innovative Plastics Lexan® 3414R PC	0.22	1520	1.04	Polymer	Thermoplastic
SABIC Innovative Plastics Lexan® 4501 PPC	0.21	1195	1.25	Polymer	Thermoplastic
SABIC Innovative Plastics Lexan® 4701R PPC	0.21	1195	1.26	Polymer	Thermoplastic
SABIC Innovative Plastics Lexan® 500 PC	0.2	1260	1.21	Polymer	Thermoplastic
SABIC Innovative Plastics Lexan® 503 PC	0.2	1250	1.21	Polymer	Thermoplastic
SABIC Innovative Plastics Lexan® DMX1435 PC Copolymer (Asia Pacific)	0.2	1185	1.4	Polymer	Thermoplastic
SABIC Innovative Plastics Lexan® FL900 PC	0.15	1190	1.17	Polymer	Thermoplastic
SABIC Innovative Plastics Lexan® FL900S PC (Europe-Africa-Middle East)	0.15	950	0.28	Polymer	Thermoplastic
SABIC Innovative Plastics Lexan® FL910 PC	0.13	1185	1.19	Polymer	Thermoplastic
SABIC Innovative Plastics Lexan® FL930 PC	0.16	1360	1.04	Polymer	Thermoplastic
SABIC Innovative Plastics Lexan® IFX3420Z PC (Asia Pacific)	0.19	1200	1.25	Polymer	Thermoplastic
SABIC Innovative Plastics Lexan® PK2870 PC	0.2	1200	1.25	Polymer	Thermoplastic
SABIC Innovative Plastics LNP KONDUIT OX11314 PPS (Asia Pacific)	1.56	1890	1.44	Polymer	Thermoplastic
SABIC Innovative Plastics LNP KONDUIT OX11315 PPS (Asia Pacific)	9.25	1760	1.26	Polymer	Thermoplastic
SABIC Innovative Plastics LNP KONDUIT PX11311 PA 6 (Asia Pacific)	1.545	1740	1.42	Polymer	Thermoplastic
SABIC Innovative Plastics NORYL GTX GTX678 PPE+PA	0.2	1120	1.4	Polymer	Thermoplastic
SBR	0.17	1100	1.88	Polymer	Thermoplastic
Schwartz Technical Plastics LAMIGAMID® 100 Polyamide 6, Extruded, Dry	0.23	1140	1.67	Polymer	Thermoplastic
Schwartz Technical Plastics LAMIGAMID® 1200 Cast Polyamide 12, Dry	0.25	1030	2.5	Polymer	Thermoplastic
Schwartz Technical Plastics LAMIGAMID® 200 Polyamide 66, Dry	0.2	1150	1.67	Polymer	Thermoplastic
Schwartz Technical Plastics LAMIGAMID® 300 Cast Polyamide 6, Dry	0.25	1130	1.67	Polymer	Thermoplastic
Schwartz Technical Plastics LAMIGAMID® 310 Cast Polyamide 6, Dry	0.25	1150	1.67	Polymer	Thermoplastic
Schwartz Technical Plastics LAMIGAMID® 510 Polyethylene Terephthalate	0.21	1370	1.05	Polymer	Thermoplastic
Schwartz Technical Plastics LAMIGAMID® 600 Polyoxymethylene	0.27	1430	1.46	Polymer	Thermoplastic
Schwartz Technical Plastics LAMIGAMID® 700 Ultra High Molecular Weight Polyethylene	0.33	950	2.3	Polymer	Thermoplastic
Schwartz Technical Plastics LAMIGAMID® 710 High Density Polyethylene	0.14	955	2.3	Polymer	Thermoplastic
Solvay Specialty Polymers Halar® 300 ECTFE Fluoropolymer	0.151	1680	0.946	Polymer	Thermoplastic
Solvay Specialty Polymers Hylar® 460 PVDF Polyvinylidene Fluoride	0.205	1760	1.4	Polymer	Thermoplastic
Solvay Specialty Polymers Hylar® MP10 PVDF Polyvinylidene Fluoride	0.205	1780	1.5	Polymer	Thermoplastic
Solvay Specialty Polymers Solef® 1006 Polyvinylidene Fluoride (PVDF)	0.2	1775	1.2	Polymer	Thermoplastic
Solvay Specialty Polymers Solef® 1008 PVDF Homopolymer	0.2	1780	1.2	Polymer	Thermoplastic
Solvay Specialty Polymers Solef® 1015/0078 PVDF Homopolymer	0.2	1690	1.2	Polymer	Thermoplastic
Solvay Specialty Polymers Solef® 11008 PVDF Copolymer	0.19	1780	1.2	Polymer	Thermoplastic
Solvay Specialty Polymers Solef® 20810 PVDF Copolymer	0.18	1780	1.2	Polymer	Thermoplastic
Solvay Specialty Polymers Solef® 31008 PVDF Copolymer	0.18	1760	1.2	Polymer	Thermoplastic
Solvay Specialty Polymers Solef® 460/461 Polyvinylidene Fluoride (PVDF)	0.2	1760	1.34	Polymer	Thermoplastic
Solvay Specialty Polymers Solef® 61010 PVDF Copolymer	0.2	1760	1.2	Polymer	Thermoplastic
Spartech Polycast Cell Cast Acrylic	0.187	1190	1.46	Polymer	Thermoplastic
Styron CALIBRE™ 200 10 Polycarbonate, General Purpose	0.3	1105	2.02	Polymer	Thermoplastic
Styron Magnum™ 342EZ ABS, Medium Impact	0.15	1020	2	Polymer	Thermoplastic
Styron Magnum™ 344HP ABS	0.155	1060	2.12	Polymer	Thermoplastic
Total 3802 B HDPE, cable, sheet, pipe, injection molding	0.4	948	2	Polymer	Thermoplastic
Total 3802 Blue MDPE pipe, injection molding	0.4	941	2	Polymer	Thermoplastic
Total 3802 YCF MDPE pipe grade	0.4	940	2	Polymer	Thermoplastic
Total Lacqtene® 2001 TBK 46 HDPE pipe	0.4	955	2	Polymer	Thermoplastic
Total Xsene® XS10 B HDPE, pipe, injection molding	0.4	959	2	Polymer	Thermoplastic
Total Xsene® XS10 H HDPE, pipe, injection molding	0.4	950	2	Polymer	Thermoplastic
Zell-Metall Engineering Plastics Zellamid 1100	0.28	1150	1.67	Polymer	Thermoplastic
Zell-Metall Engineering Plastics Zellamid 250 GF 30 (PA6.6 + 30% glass fiber)	0.27	1350	1.5	Polymer	Thermoplastic
3M Dyneon™ Aflas® FA-150L PTFE Fluoroelastomer	0.2	1550	1.67	Polymer	Thermoplastic
3M Dyneon™ Fluorel™ FE-5610Q Fluoroelastomer VF2 + HFP Dipolymer	0.24	1800	1.65	Polymer	Thermoplastic
ACC QSil 216 QSI Quantum Silicones Transparent Liquid Silicone Rubber	0.18	1015	1.26	Polymer	Thermoset
Atom Adhesives AA-DUCT 905 Epoxy Adhesive	0.602	2350	0.3	Polymer	Thermoset
Bulk Molding Compounds BMC 940 Vinyl Ester Bipolar Plate Material	13.4	1890	0.846	Polymer	Thermoset
Dow VORANOL™ 4240 Polyether Polyol	0.151	1020	1.67	Polymer	Thermoset
Dow VORANOL™ 4701 Polyether Polyol	0.151	1020	1.67	Polymer	Thermoset
Dow VORANOL™ VORACTIV™ 6340 Catalytically Active Polyether Polyol	0.163	1020	1.84	Polymer	Thermoset
Natural Rubber, Not Vulcanized (NR, IR, Polyisoprene)	0.14	930	0.45	Polymer	Thermoset
Natural Rubber, Vulcanized (NR, IR, Polyisoprene)	0.15	950	0.44	Polymer	Thermoset

Park Electrochemical Nelco® N4000-11 Multifunctional 743:743 Laminate and Prepreg	0.5	1960	1.295	Polymer	Thermoset
Park Electrochemical Nelco® N4000-12 High Speed/Low Loss, CAF Resistant Laminate and Prepreg	0.4	1900	1.21	Polymer	Thermoset
Park Electrochemical Nelco® N4000-12 SI® High Speed/Low Loss, CAF Resistant Laminate and Prepreg	0.29	1780	1.13	Polymer	Thermoset
Park Electrochemical Nelco® N4000-13 High-Speed Multifunctional Epoxy Laminate and Prepreg	0.35	1910	1.21	Polymer	Thermoset
Park Electrochemical Nelco® N4000-13 SI® High-Speed Multifunctional Epoxy Laminate and Prepreg	0.294	1790	1.3	Polymer	Thermoset
Park Electrochemical Nelco® N4000-2 Multifunctional Epoxy Laminate and Prepreg	0.3505	1920	1.295	Polymer	Thermoset
Park Electrochemical Nelco® N4000-29 Multifunctional Epoxy	0.46	1990	0.92	Polymer	Thermoset
Park Electrochemical Nelco® N4000-7 EF® Halogen-Free Epoxy	0.47	1920	0.962	Polymer	Thermoset
Park Electrochemical Nelco® N4000-7 FR-4 Epoxy Laminate and Prepreg	0.525	1970	1.21	Polymer	Thermoset
Park Electrochemical Nelco® N4350-13 RF Microwave Performance, Modified Epoxy	0.35	1770	1.21	Polymer	Thermoset
Park Electrochemical Nelco® N7000-2 HT/N7000-3 Toughened Polyimide Laminate and Prepreg	0.45	1700	1.05	Polymer	Thermoset
Park Electrochemical Nelco® N8000Q Cyanate Ester Epoxy Laminate and Prepreg	0.44	1730	0.999	Polymer	Thermoset
Parker Chomerics CHO-THERM® 1671 High Power Thermally Conductive Electrical Insulator Pad	2.6	1550	1	Polymer	Thermoset
Parker Chomerics CHO-THERM® 1674 Commercial Grade Thermally Conductive Electrical Insulator Pad	1	2450	1	Polymer	Thermoset
Parker Chomerics CHO-THERM® 1678 High Power Thermally Conductive Electrical Insulator Pad	2	1550	1	Polymer	Thermoset
Parker Chomerics CHO-THERM® T441 0.20 mm Commercial Grade Thermally Conductive Electrical Insulator Pad	1.1	2450	1	Polymer	Thermoset
Parker Chomerics CHO-THERM® T444 Commercial Grade Thermally Conductive Electrical Insulator Pad	0.4	1700	1	Polymer	Thermoset
Parker Chomerics CHO-THERM® T500 High Power Thermally Conductive Electrical Insulator Pad	2.1	1600	1	Polymer	Thermoset
Parker Chomerics CHO-THERM® T609 Commercial Grade Thermally Conductive Electrical Insulator Pad	1.5	2100	1	Polymer	Thermoset
Saint-Gobain COHRlastic® R10404 Firm Thermally Conductive Conformable Silicone Rubber Sponge	0.108	1110	1.26	Polymer	Thermoset
Saint-Gobain COHRlastic® R10470 Firm General-Purpose Silicone Sponge Rubber	0.108	692	1.26	Polymer	Thermoset
Saint-Gobain COHRlastic® R10470 Medium General-Purpose Silicone Sponge Rubber	0.108	471	1.26	Polymer	Thermoset
Saint-Gobain COHRlastic® R10480 Soft Low Compression Set Silicone Sponge Rubber	0.108	332	1.26	Polymer	Thermoset
Hardwood	0.16	720	1.255	Wood	Hardwood
Oak	0.17	545	2.385	Wood	Hardwood
Particleboard, HD	0.17	1000	1.3	Wood	MISC Wood
Particleboard, LD	0.078	590	1.3	Wood	MISC Wood
Plywood	0.12	545	1.215	Wood	MISC Wood
Paper	0.18	930	1.34	Wood	Paper
Douglas Fir, Plywood	0.12	550	1.2	Wood	Softwood
Fir	0.11	415	2.72	Wood	Softwood
particle board	0.14	800	1.3	Wood	Softwood
Softwood	0.12	510	1.38	Wood	Softwood
Yellow Pine	0.15	640	2.805	Wood	Softwood
American Beech Wood	0.173	712.5	0.39	Wood	Wood and Natural Products
American Yellow Birch Wood	0.173	731.5	0.39	Wood	Wood and Natural Products

Appendix H Ra_m example calculation

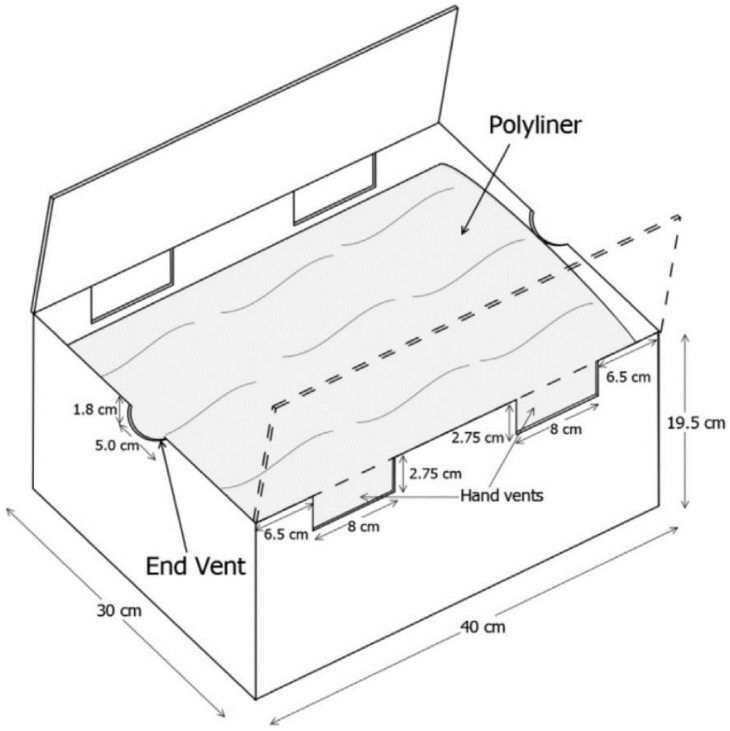

- Given that the kiwifruit box is 0.2 by 0.3 by 0.4 m
- The characteristic length of kiwifruit is 0.054 m (average of LWD)
- The volume fraction of air inside the kiwifruit box is approximately 0.55 (Olatunji, 2018)

$$K = \frac{D_{eq}^2\, p^2}{180(1-p)^2} = \frac{0.054^2 \times 0.55^2}{180\,(1-0.55)^2} = 2.42 \times 10^{-5}\, m^2$$

$$Ra_m @\, 20°C = K\,\frac{g\beta\Delta TL}{v\,\alpha_{air}} = 2.42 \times 10^{-5}\,\frac{9.81 \times \frac{1}{293} \times 20 \times 0.054}{1.80 \times 10^{-5} \times 2.07 \times 10^{-5}} = 2348 > 4\pi^2$$

$$Ra_m @\, 1°C = K\,\frac{g\beta\Delta TL}{v\,\alpha_{air}} = 2.42 \times 10^{-5}\,\frac{9.81 \times \frac{1}{274} \times 1 \times 0.054}{1.80 \times 10^{-5} \times 2.07 \times 10^{-5}} = 125 > 4\pi^2$$

Appendix I Master fruit for silicon mould

Picture of silicon moulds

Kiwifruit

ID	Weight (grams)	DL (mm)	Dx (mm)	Dy (mm)
1	103.20	71	50	52
2	98.00	58	51	54
3	96.60	61	47	55
4	101.60	63	51	52
5	99.50	64	47	53
6	106.30	65	50	53
7	98.00	61	46	54
8	103.70	61	50	54
9	99.00	62	50	54
10	105.50	63	50	54

Apple

ID	Weight (grams)
1	242.4
2	248.8
3	247.7
4	230.9
5	245.9
6	257.3
7	262.2
8	247.8
9	258.2
10	224.0

Appendix J $\boldsymbol{Bi}$ calculation for Apple

Given from Ashrae (2010) that apple has:

- Characteristic length 53-70 mm
- Thermal conductivity 0.37 – 0.47 $W\ m^{-1}\ K^{-1}$
- Heat transfer coefficient from 10.2 – 56.8 $W\ m^{-2}\ K^{-2}$ (from 0 – 5 $m\ s^{-1}$)

$$Bi_{max} = \frac{56.8\ \times 70\ \times 10^{-3}}{0.37} = 10.7$$

$$Bi_{min} = \frac{10.2\ \times 53\ \times 10^{-3}}{0.47} = 1.1$$

Appendix K Pictures of simulator instrumentation

Kiwifruit

Apple

Appendix L MATLAB coding

Q-cell size calculation

Input :

```
I = imread('image.jpeg'); % load image
[centersBright, radiiBright] = imfindcircles(I,[15
100],'ObjectPolarity','bright'); % define image


figure (1) % draw defined circles
imshow(I)
viscircles(centersBright, radiiBright,'Color','b');
set (figure(1),'color', 'w')

figure(2) % draw probaility
C = 0.737; % resolution
histogram(2*radiiBright*C,'Normalization','probability'),xlabel('Size[um
- uncalibrated]'),ylabel('Probability')

set (figure(2),'color', 'w')
set (gca, 'fontsize', 20)
```

output:

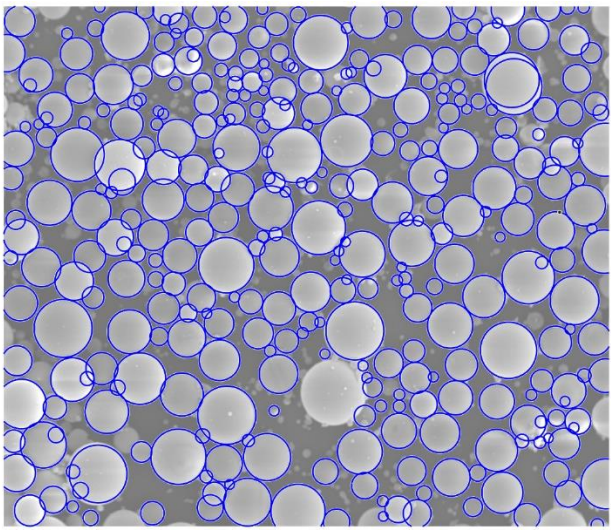

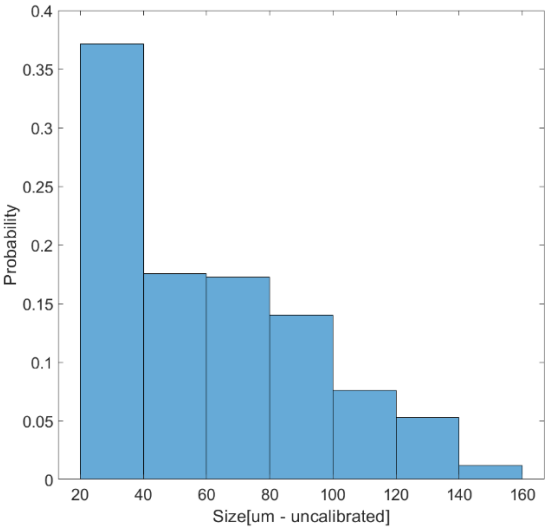

Material selection

```
% insert material data%
[num,txt]=xlsread('data_input.xlsx');

Name=txt(:,1);
K=num(:,1);
rho=num(:,2);
cp=num(:,3);
rhocp=rho.*cp;
material(:,1)=txt(:,1);
material(:,2)=txt(:,6);
material(:,3)=txt(:,7);
material_type=unique(txt(:, 6));
for i=1:size(material_type,1)
   material_type(i, 2)={num2str(i)};
end

%material title
c=size (K);
d=c (1,1);

%method

% parallel =3;
% maxwell=1;
% effective medium=2;
% series=4;
% colormap

figure(1)
f2=fastscatter(rho.*cp, K, typeC);
f2.MarkerSize=20;
ylim([0 0.7])
xlim ([1500 4500])
material_type2=material_type;

colorbar ('Ticks', [1.5:6.5], 'TickLabels', { material_type2{:, 1}, 'Thermoset'}, 'AxisLocation','in')
colormap(colM)


hold on
Err=errorbar (num2(end, 1), num2(end, 4), num2(end, 5), num2(end, 6), num2(end,2), num2(end,3), 'o',
'color', 'k');
text (num2(end, 1)+50, num2(end, 4)-0.01, 'Individual', 'fontsize', 15)

Err=errorbar (2062, 0.25, 0.08, 0.08, 500, 500, 'o', 'color', 'k');
text (2062+50, 0.28, 'Bulk', 'fontsize', 15)

xlabel ('Volumetric heat capacity (kJ m^-^3 K^-^1)')
ylabel ('Thermal conductivity (W m^-^1 K^-^1)')
```

```
set (figure(1), 'position', [100 100 1000 1000], 'color', 'w')
set (gca, 'fontsize', 20)
a=1;
for i=1:d
   check(i,1)=rho(i)*cp(i);
   if rho(i)*cp(i) >=2062-500 & rho(i)*cp(i) <=2062+500
      if K(i)>=0.25-0.08 & K(i)<=0.25+0.08

         SingBulk(a).K=K(i);
         SingBulk(a).rhocp=rho(i)*cp(i);
         SingBulk(a).Kc=material(i, 1);
           a=a+1;
       end
   end
end
 b=1;a=1; z=1;
for i=0:d-1
       progress=(i/(d-1))*100;


     for n=1:d
        clc
        disp(progress)
        toc
        for j=5:5:45

        %volume fraction
           pd=j/100;

            %thermal conductivity prediction
            % [ke]=superfunction (Kc, Kd, pd, type)
            % maxwelleucken =1;
            % tsao=2;
            % kopelman=3;
            % effectivemedium=4;
            data(j/5).rhocp(i*d+n).rhocp=(1-
pd)*rhocp(i+1,1)+pd*rhocp(n,1);
                  for method =1:4

data(j/5).method(method).prediction(i*d+n).K=superfunction(K(i+1,1
), K (n,1),pd,method);

                        if data(j/5).rhocp(i*d+n).rhocp >=3383 &
data(j/5).rhocp(i*d+n).rhocp <=3913
                              if
data(j/5).method(method).prediction(i*d+n).K>=0.42 &
data(j/5).method(method).prediction(i*d+n).K<=0.44
             select(b).K=data(j/5).method(method).prediction(i*d+n).K;
             select(b).rhocp=data(j/5).rhocp(i*d+n).rhocp;
```

```
                select(b).pd=pd;
                select(b).method=method;
                select(b).Kc=material(i+1, 1);
                select(b).Kd=material(n, 1);
                b=b+1;
            end
        end

    end

  end
 end
end
tmpx=[]; tmpy=[]; tmpc=[];
for i=1:9
for n=1:2
  if n<=2
    hold on
    tmpx=[tmpx, data(i).rhocp.rhocp];
    tmpy=[tmpy, data(i).method(n).prediction.K];
    tmpc=[tmpc, (data(i).material.type)];
  end
 end
end
tmp=[tmpx', tmpy', tmpc'];
tmp=unique(tmp,'rows');
figure (2)
set(gcf,'Renderer','OpenGL');
f1=fastscatter(tmp(:, 1), tmp(:, 2), tmp(:, 3), 'FaceAlpha',.03,'EdgeAlpha',.03, 'AlphaData', 0.03);
alpha (0.1)
f1.MarkerSize=20;
ylim([0 0.7])
xlim ([1500 4500])

colorbar ('Ticks', [1.5:7.5], 'TickLabels', { material_type{:, 1}, 'Thermoset'}, 'AxisLocation','in')
colormap(colM)

hold on
Err=errorbar (num2(:, 1), num2(:, 4), num2(:, 5), num2(:, 6), num2(:,2), num2(:,3), 'o', 'color', 'k');
text (num2(end, 1)+50, num2(end, 4)-0.01, txt2(end), 'fontsize', 15)

Err=errorbar (2062, 0.25, 0.08, 0.08, 500, 500, 'o', 'color', 'k');
text (2062+50, 0.25-0.01, 'Bulk', 'fontsize', 15)

tmp2=tmp;
tmp2(:, 1)=round(tmp2(:, 1),-2);
rhocp=unique(tmp2(:, 1));
 rData=[];
for i=1:size(rhocp,1)
   [r, ~]=ismember(tmp2(:, 1), rhocp(i));
```

```
    rhocp(i, 2)=min(tmp2(r,2));
    clc
    disp (i)
end

hold on

plot(rhocp(:, 1), rhocp(:, 2), 'LineWidth', 5, 'color', 'b')
colorbar ('Ticks', [1.5:6.5], 'TickLabels', { material_type2{:, 1}, 'Thermoset'}, 'AxisLocation','in')
colormap(colM)



xlabel ('Volumetric heat capacity  (kJ m^-^3 K^-^1)')
ylabel ('Thermal conductivity (W m^-^1 K^-^1)')
set (figure(2), 'position', [100 100 1000 1000], 'color', 'w')

set (gca, 'fontsize', 20)
```

Table grape image analysis

```
load('info.mat');
load('chile_grape.mat');
voxel_size = [info.PixelSpacing; info.SliceThickness]';
dx=voxel_size(1)/1000;
dy=voxel_size(2)/1000;
dz=0.4/1000;
level=multithresh(chile_grape, 4);
chileGrape=chile_grape;
chileGrape1=chile_grape;
chileGrape(chileGrape<=level(3))=0;
volumeViewer(chileGrape)
chileGrape1(chileGrape1<=500)=0;
chileGrape=clean(chileGrape);
chileGrape1=clean(chileGrape1);
count=1;
ic=30;

  % 11= 8 objects

count=0;
imask=10

chileclose=imclose (logical (chileGrape), ones ([ic ic ic]));

chileclose1=imclose (logical (chileGrape1), ones ([ic ic ic]));

D = -bwdist(~chileclose); % intensifier the pixel near the center of
mass, while reudce the the pixel intneisty near the eldge

D1 = -bwdist(~logical(chileGrape));

mask = imextendedmin(D, imask); % H-minima transform to generate maker

[L nmask]=bwlabeln(mask);

D2 = imimposemin(D,mask);

Ld2 = watershed(D2);

chileclose1(Ld2 == 0) = 0;

 [L1, n]=bwlabeln(chileclose1);

 disp (['imask ', num2str(imask), 'number of L1 ', num2str(max(L1(:)))])

 count=count+1;

data(count).L1=L1;

data(count).imask=imask;

data(count).object=max(data(count).L1(:));
```

```
for j=1:max(data(count).L1(:))
   data(count).chile(j).grape=chileGrape1;
   data(count).chile(j).grape (data(count).L1~=j)=0;
   [L n]=bwlabeln(logical (data(count).chile(j).grape));
   stat=regionprops3(L);
   A=stat.Volume;
   A=find(A==max(A));
   data(count).chile(j).grape(L~=A)=0;
   data(count).chile(j).mass=sum(sum(sum(logical(data(count).chile(j).grape))))*dx*dy*dz*1070;
end
data(count).totalMass=sum([data(count).chile(:).mass]);

for j=1:9
   chile(j).grape=chileGrape1;
   chile(j).grape (L1~=j)=0;
   [L n]=bwlabeln(logical (chile(j).grape));
   stat=regionprops3(L);
   A=stat.Volume;
   A=find(A==max(A));
   chile(j).grape(L~=A)=0;

   clean_level=0;

   zdel=[];

   parfor i=1:size(chile(j).grape,1)
      if sum(sum(logical(chile(j).grape(i,:,:))))==clean_level

         zdel=[zdel, i];
            end
       end

      chile(j).grape(zdel,:,:)=[];

   ydel=[];

   parfor i=1:size(chile(j).grape,2)
      if sum(sum(logical(chile(j).grape(:,i,:))))==clean_level

         ydel=[ydel, i];
      end
   end

   chile(j).grape(:,ydel,: )=[];

   xdel=[];

   parfor i=1:size(chile(j).grape,3)
```

```
      if sum(sum(logical(chile(j).grape(:,:,i))))==clean_level

        xdel=[xdel, i];
      end
    end
    tic

    chile(j).grape(:,:, xdel)=[];

  end

closevalue=[200];
for i=1:9
    chile(i).grapeLogical=logical (chile(i).grape);
    for j=1:size (closevalue,2)

      chile(i).grapeClose=imclose(chile(i).grapeLogical, ones([closevalue(j) closevalue(j)
closevalue(j)]));
      chile(i).grapeClose=imfill(chile(i).grapeClose,'holes');
      chile(i).grapepd=sum(chile(i).grapeLogical(:))/sum(chile(i).grapeClose(:));
      chile(i).closevalue=closevalue(j);
      chile(i).package=logical(chile(i).grape)+logical(chile(i).grapeClose);

chile(i).package_pd=sum(sum(sum(chile(i).package==1)))/sum(sum(sum(chile(i).package~=0)));%
air void
      chile(i).mass=sum(sum(sum(logical(chile(i).grape))))*dx*dy*dz*1070;
      save('chile.mat', 'chile', '-v7.3')
    end

end

  for i=1:9

     a=chile(i).grapeClose;

     A(i).sum=sum(a(:))*dx*dy*dz;

end
```

Effective Thermal conductivity

```
voxel_size = [info.PixelSpacing; info.SliceThickness]';
p=globalData;
scale=p.scale;
Ttop=p.Ttop;
Tbottom=p.Tbottom;
dx=voxel_size(1)/scale/1000;
dy=voxel_size(2)/scale/1000;
dz=0.4/scale/1000;
gk=0.5;
tic

% volume REV

for i=1:9
   n=1;
   [x, y, z]=size(chile(i).grape);

   chile(i).grapeReshape=chile(i).grape;
   chile(i).grapeClose=imclose (chile(i).grapeReshape, ones (30,30,30));
   chile(i).grapeClose=imfill (chile(i).grapeClose, 'holes');
   chile(i).package=logical(chile(i).grapeReshape)+logical(chile(i).grapeClose);


chile(i).package_pd=sum(sum(sum(chile(i).package==1)))/sum(sum(sum(chile(i).package~=0)));%
air void
   C=regionprops3(logical(chile(i).package));
   Cx=round(C.Centroid(2));
   Cy=round(C.Centroid(1));
   Cz=round(C.Centroid(3));

   for Rsize=2:round(min(size(chile(i).package))/2-25)

      chile(i).REV(n).data=chile(i).package(Cx-Rsize:Cx+Rsize, Cy-Rsize:Cy+Rsize, Cz-Rsize:Cz+Rsize);
      chile(i).REV(n).size=size(chile(i).REV(n).data,1);
      chile(i).REV(n).pd=sum(sum(sum(chile(i).REV(n).data
==1)))/sum(sum(sum(chile(i).REV(n).data~=0)));
      n=n+1;
   end
end
%%
% col={'b', 'g', 'r', 'y', 'm'};
% mak={'x', 'o', 'v', '<', '>'};
% com=nchoosek(1:5,2);

yaxis=[1 4 7];
```

```
[~, pos]=tight_subplot(3,3,0,0.1, 0.1);
figure (1)
  for i=1:9
   subplot ('position', pos{i})
   plot ([chile(i).REV(:).size], [chile(i).REV(:).pd], 'LineWidth', 3) %,'Color', col{com(i, 1)}, 'Marker',
mak{com(i,2)}});
   hold on
   plot ([0:10:150], chile(i).package_pd*ones(1, 16) , 'LineWidth', 3)%,'Color', col{com(i, 1)},
'Marker', mak{com(i,2)})
   hold on
   ti=title (['Grape', num2str(i)], 'Position', [75.0004 0.9 0]);
   ylim([0 1])

   if i<7
      xlim([0 160])
      xticklabels([])
      xticks([-10:50:160])
   elseif i>=7
      xlim([0 160])
      xticks([-10:50:160])


   end

   if i==8
      xlabel('pixels')
   end

   if i==4
      ylabel('Volume Fraction of Air')
   end

   if ismember(i, yaxis)
      ylim([-0.1 1.1])
      yticks([0:0.2:1])

   else
      ylim([-0.1 1.1])

      yticks([0:0.2:1])
      yticklabels([])

    end

   set(gca, 'FontSize', 25)
   if i==9
      legend ('REV', 'Actual Vol Fraction')
```

```
    end
    end
     set (figure(1), 'position',  [10 100 1500 1500], 'color', 'w')
  stop
   %%
for i=1:9
    n=50;
    % REV (50)
    % chile(i).REV(n).data=ones (3,3,3);
    [x1, y1, z1]=size(chile(i).REV(n).data);
    [K, rhocp]=thermalproperties(chile(i).REV(n).data, 1);
    [x y z] = ind2sub(size(chile(i).REV(n).data),find(chile(i).REV(n).data<=100));
    j=[1:x1*y1*z1]';
    T=[];
    T=sparse (T);
    parfor a=1:size(j,1)

       tmp=zeros(1, x1*y1*z1+1);
       if x(a)==1 | x(a)==x1
          tmp(a)=1;
       else
          rhocpj=rhocp(x(a),y(a),z(a));

          kbdx=(gk/K(x(a)-1, y(a), z(a))+gk/K(x(a),y(a),z(a)))^-1;

          kadx=(gk/K(x(a)+1, y(a), z(a))+gk/K(x(a),y(a),z(a)))^-1;

          %top heat transfer
          tmp(a-1)=kbdx/rhocpj*(1/dx^2);
          % bottom heat transfer
          tmp(a+1)=kadx/rhocpj*(1/dx^2);


          if y(a)-1>=1
             % left heat transfer
             kbdy=(gk/K(x(a), y(a)-1, z(a))+gk/K(x(a),y(a),z(a)))^-1;
             tmp(a-x1)=kbdy/rhocpj*(1/dy^2);
          else
             kbdy=0;

          end

          if y(a)+1<=y1
             % right heat transfer
             kady=(gk/K(x(a), y(a)+1, z(a))+gk/K(x(a),y(a),z(a)))^-1;
             tmp(a+x1)=kady/rhocpj*(1/dy^2);
          else
             kady=0;
```

```
    end

    if z(a)-1>=1
       % front heat transfer
       kbdz=(gk/K(x(a), y(a), z(a)-1)+gk/K(x(a),y(a),z(a)))^-1;
       tmp(a-x1*y1)=kbdz/rhocpj*(1/dz^2);
    else
       kbdz=0;
    end

    if z(a)+1<=z1
       % back heat transfer
       kadz=(gk/K(x(a), y(a), z(a)+1)+gk/K(x(a),y(a),z(a)))^-1;
       tmp(a+x1*y1)=kadz/rhocpj*(1/dz^2);
    else
       kadz=0;
    end


     tmp(a)=-kbdx/rhocpj/(dx^2)-kadx/rhocpj/(dx^2)...
          -kbdy/rhocpj/(dy^2)-kady/rhocpj/(dy^2)...
          -kbdz/rhocpj/(dz^2)-kadz/rhocpj/(dz^2);
    end

     tmp(end)=a;
   tmp=sparse (tmp);
   T=[T; tmp];

end

toc
T1=sortrows(T, size(T,2));
T1(:, end)=[];

Answer(i).Tmatrix=T1;

b=zeros(x1, y1, z1);
b(1, :, :)=Ttop;

b(end, :, :)=Tbottom;
b=reshape (b, x1*y1*z1,1);
T=T1\b;

T_m=reshape(T, x1, y1, z1);
Answer(i).T=T_m;
```

```
    kfx=(gk/K(1:end-1, :, :)+gk/K(2:end, :, : )).^-1;

    fluxX=kfx(1:end-1, :, :)./dx.*(T_m(1:end-2, :, :)-T_m(2:end-1, :, :));
    Answer(i).Qtop=mean(mean(mean(fluxX(1, :, :))));
    Answer(i).Qbottom=mean(mean(mean(fluxX(end, :, :))));
    dX=dx*x1;
    dT=Ttop-Tbottom;
    Answer(i).k1=Answer(i).Qtop*dX/dT;
    Answer(i).k2=Answer(i).Qbottom*dX/dT;
    clc
    disp(['i = ', num2str(i)])
    toc

end
```